Ulm University |Germany

A Detailed Investigation of Heterometal-Incorporated Polyoxovanadate Nanocluster Based Films: Material Properties and Sustainable Applications for Energy Storage Systems

Kumulative Disseration zur Erlangung des Doktorgrades Dr. rer. nat.

der Fakultät für Naturwissenschaften an der Universität

Ulm

vorgelegt von

M.Sc. Nikhil Arya

Born in Lucknow, India

2024

Dekan der Fakultät für Naturwissenschaften

Prof. Kay-E. Gottschalk

Gutachter:innen

Dr. Montaha Anjass

Prof. Dr. Sven Rau

Tag der Promotion

04.04.2025

"Every work has got to pass through hundreds of difficulties before succeeding. Those that persevere will see the light, sooner or later"

-Swami Vievekananda

Abstract

Molecular metal oxides, known as polyoxometalates (POMs), have exhibited exceptional catalytic properties and recently garnered interest for their application in energy conversion and storage systems, owing to their ability to store and transfer multiple electrons. This study represents the first demonstration of redox-driven, reversible electrodeposition of molecular vanadium oxide clusters ($K_5\{V_{12}\}$, $\{V_{12}\}$, and $\{V_{18}\}$), leading to the formation of thin films. The schematic (**Figure i**) represents a systematic depiction of the controlled electrochemical deposition approach, highlighting its physicochemical characteristics, and subsequent applications. A comprehensive investigation of the deposition mechanism indicates that the reduction potential plays a crucial role in determining the process's reversibility.

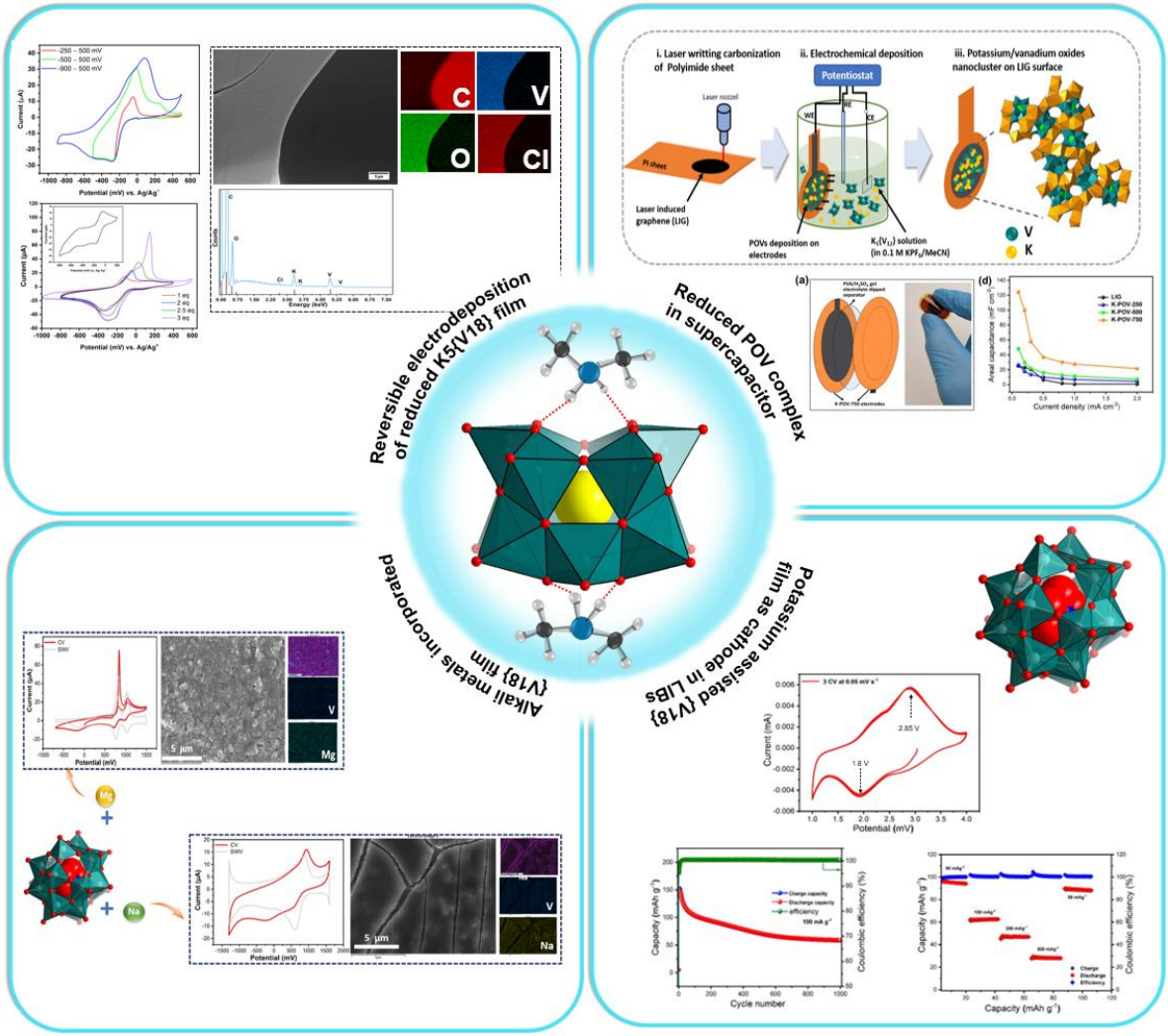

Figure i: Schematic overview illustrating the key experimental investigation conducted in this thesis.

Electrochemical quartz crystal microbalance (EQCM) measurements, combined with X-ray photoelectron spectroscopy (XPS) analysis, reveal the redox behavior and oxidation states of vanadium within the deposited films as a function of the applied potential range. The

multielectron reduction of the polyoxovanadate cluster is confirmed, enabling the potassium ion (K^+)-bridged reversible formation of potassium vanadium oxide thin films ($K_5\{V_{12}\}$).

At the specific applied reduction potentials range, the re-oxidation of the polyoxovanadate and complete stripping of the thin film was observed. However, the electrodeposition at higher cathodic potentials diminished the electrochemical reversibility and increased the stripping overpotential. We demonstrate the electrochemical performance of the deposited films, highlighting their potential applicability in potassium-ion battery (PIB) systems.

To enhance the electrochemical performance of the flexible energy storage systems, here we present a sustainable approach for tunning the electronic and electrochemical properties of hierarchically porous laser-induced graphene (LIG) substrate by electrochemically immobilizing reduced $K_5\{V_{12}\}$ complexes. Detailed spectroscopic studies reveal the correlation between the orientation of deposited clusters and the amorphous regions of the LIG. We also investigated, how the cluster deposition significantly decreases the grain boundary defects in the nanographitic lattice. The optimized electrode shows a fivefold increase in areal capacitance (C_A) of 125 mF/cm^2 at 0.1 mA/cm^2 compared to the undoped LIG electrode.

To evaluate the potential of POVs as electrode materials, we focused on the in-situ functionalization of $\{V_{18}\}$ cluster K^+ cations to enhance structural stability. The synthesized $K_5\{V_{18}\}$ film, deposited directly onto C-Al foil without additional additives, shows significant structural and electronic improvements. Partial reduction of vanadium from V^{5+} to V^{4+} (also up to V^{3+}) enables reversible multi-electron storage with outstanding structural stability. Electrochemical tests reveal a high specific capacity of 240 mAh/g at a current density of 50 mA/g, with excellent redox stability over 1000 galvanostatic charge-discharge (GCD) cycles, indicating strong potential as a cathode material for lithium-ion batteries (LIBs).

Table of Contents

Abstract.....V

Table of Contents.....VI

List of Figures.....IX

List of Tables.....XII

List of Abbreviation.....XIII

List of Compounds.....XV

Notations.....XV

Scientific Contributions.....XVI

Conferences and Conference Contributions.....XVII

1. Introduction.....1

1.1 Polyoxometalates (POMs).....1

1.1.1 General overview of Polyoxometalates.....1

1.1.2 A detailed discussion of the chemical and microstructural properties of Polyoxometalates.....2

1.2 Vanadium-based polyoxometalates.....5

1.2.1 Classification and detailed molecular structural properties.....5

1.2.2 Overview of the {V_{12}} and {V_{18}} POVs structures.....6

1.3 Immobilization of polyoxometalates into conductive substrates.....12

1.3.1 Electrodeposition.....13

1.3.2 Mechanism of electrochemical immobilization of POVs.....16

1.3.3 In-situ electrodeposition of potassium assisted reduced {V_{12}} and {V_{18}} film on a conductive surface.....19

1.4 POM-based redox active thin films and composites for energy storage.....20

1.4.1 Lithium-ion batteries/ post-Lithium-ion batteries.....20

1.4.2 The mechanism of charge storage in POM-based electrodes.....23

1.4.3 Electrochemical double-layer supercapacitors (EDLSCs) and pseudo-capacitors.....24

1.4.4 POM composites for high-performance supercapacitors electrode.....26

2. Objective 28

3. Results and Discussion 31

3.1 Reversible electrodeposition of K_5V_{12} for multi-electron storage.....31

3.1.1 Electrochemical characterization of the K_5V_{12} reduction.....31

3.1.2 Formation of a high redox active thin film of K_5V_{12}..... 33

3.1.3 The structural and elemental composition of reduced K_5V_{12}.....37

3.2 Reduced K_5V_{12} nanocomposites on porous graphene for supercapacitor.....39

3.2.1 Electrodeposition of K_5V_{12} on a nanoporous LIG surface.....39

3.2.2 Material characterization of the POVs modified LIG electrode 42

3.2.3 Mechanism of charge storage of POVs modified LIG electrode 47

3.3 In-situ alkali metal functionalization of POVs nanocluster……..…. …..49
3.3.1 In-situ alkali metal functionalization of {V_{12}}…...……..49
3.3.2 In-situ nanostructured EDOT/{V_{12}} complexes……...……..50
3.3.3 In-situ alkali metal functionalization of {V_{18}}…...……..54
3.4 Electrochemical performance of different POV-based thin supramolecular films as electrode material in battery and supercapacitor……..…..….....59
3.4.1 K_5{V_{12}}-based redox active film for (post-) lithium-ion batteries ……59
3.4.2 Potassium-functionalized reduced {V_{18}} thin film for Li-ion battery…62
3.4.3 Reduced K_5V_{12} nanocluster deposition for flexible supercapacitors…….65
3.5 Enhancing Si-dominant anodes: impact of polyacrylic acid neutralization degree on low-cost micron-sized silicon anodes for high-energy Li-ion full cells..……69
3.6 Enhancing Mg deposition and dissolution from ionic liquids: the impact of additives on Mg-ion battery applications……..……..…..….....74
4. Summary and Outlook..……..……..77
4.1 High-performance reversible electrodeposited potassium-bridged molecular vanadium cluster for energy storage……...77
4.2 Highly porous Laser-induced graphene surface modification by the reduced polyoxovanadate (K_5{V_{12}})……..78
4.3 Challenges and approaches for integrating carbon-additive and binder-free potassium-stabilized vanadium oxides thin film as cathode materials in LIBs and (Post-) lithium-ion batteries ……79
4.4 Preliminary results of Mg^{2+} and Na^{+} cation interactions with {V_{18}} nanocluster *via* electrochemical deposition……..80
5. References..……..……82
6. Publications ..……..……89
6.1 Publication 1…….....89
6.2 Publication 2……...106
6.3 Publication 3……...138
6.4 Publication 4……...167
7. Curriculum Vitae ..……..……..……..188
Acknowledgement……..……..……..189
Declaration of honesty in academic work……..……..190

List of Figures

Figure i: Schematic overview of the thesis work …..……..II

Figure 1: The two octahedral units connection …..……...2

Figure 2: Polyhedral structures of different POM clusters …..……..…..3

Figure 3 Schematic representation of the synthesis mechanism of large polynuclear POM anion.…..4

Figure 4 Self-assembly process involved during $\{V_{12}\}$ synthesis ……7

Figure 5 Schematic representation of a $\{V_{12}\}$ polyoxovanadate cluster incorporating potassium ions ……....9

Figure 6 Schematic representation of the polyhedral $[VO_6]$ assembly in dodecavanadate cluster……10

Figure 7 Schematic representation of a three-electrode cell configuration with an ionic electrolyte connected to the potentiostat workstation ……..…...14

Figure 8 Schematic representation of $K_5\{V_{12}\}$ cluster polymeric fragmentation into two half clusters ……...……..……...17

Figure 9 Polyhedral view of the $((DMA)_2[V_{12}O_{32}Cl]^{3-})=\{V_{12}\}$ cluster ……..20

Figure 10 Schematic representation of the working principle of the lithium-ion battery cell ……...21

Figure 11 Schematic representation of the charge-discharge mechanism in polyoxovanadate …….....……...24

Figure 12 Schematic view of a symmetric supercapacitor at a charged state……..…25

Figure 13 CVs of $K_5\{V_{12}\}$ at different cathodic switching potentials ……32

Figure 14 EQCM measurement of $K_5\{V_{12}\}$……..……34

Figure 15 High-resolution XPS spectra of **(a)** $K_5\{V_{12}\}$ cluster and reduced $K_5\{V_{12}\}$ films ..35

Figure 16 EDX elemental mapping of the $K_5\{V_{12}\}$ based film deposited ……..36

Figure 17 Pulsed electrodeposition profile of $K_5\{V_{12}\}$ at three different reduction potentials ……..38

Figure 18 Average thickness of the deposited film vs deposition potential ……..…….38

Figure 19 Schematic representation of LIG electrode fabrication and electrochemical immobilization of $K_5\{V_{12}\}$……40

Figure 20 cyclic voltammetry response during $K_5\{V_{12}\}$ deposition on LIG ……..41

Figure 21 SEM images of pristine LIG electrode ……..……43

Figure 22 Micro-Raman spectrum of LIG electrode ……..…...……..44

Figure 23 XPS survey spectra of pristine LIG and K-POV-750 electrode ……46

Figure 24 Quantitative analysis of charge storage mechanism ……...48

Figure 25 Pulsed electrodeposition profile of the $\{V_{12}\}$ cluster ……49

Figure 26 Surface morphology of $\{V_{12}\}/KPF_6$ deposited film ……...……51

Figure 27 CSCA pulsed deposition profile for $K_5\{V_{12}\}$ with EDOT polymer……52

Figure 28 Detail XPS spectra in the S2p region deposited PEDOT/ $K_5\{V_{12}\}$ complex …….53

Figure 29 CSCA profile of the $\{V_{18}\}$ cluster electrodeposition ……54

Figure 30 SEM characterization of $K_x\{V_{18}\}$ deposited films ……55

Figure 31 SEM and EDX analysis of $\{V_{18}\}$/ PEDOT complex ……..57

Figure 32 Detail XPS spectra in the S2p, V2p, and O1s region of $\{V_{18}\}$/ PEDOT complex..58

Figure 33 CV performance of the synthesized $K_5\{V_{12}\}$ film ……60

Figure 34 Differential capacity vs voltage (dQ/dV) curve ……..61

Figure 35 Electrochemical performance of the synthesized $K_x\{V_{18}\}$ ……62

Figure 36 CV, voltage capacity profile, and cyclic stability performance of $K_x\{V_{18}\}$ film…64

Figure 37 Cyclic voltammograms of K-POV-250, K-POV-500, and K-POV-750 electrodes… ……...……67

Figure 38 Adhesion of non-calendered (shaded orange) and calendered (orange) electrodes ……..……69

Figure 39 cross-section TEM image of the $Li_{0.7}$PAA electrode show Si particles surrounded……70

Figure 40 XPS detail measurements in the Si 2p, C 1s and O 1s regions from pristine electrodes ……..……72

Figure 41 The cycling performance at 1C, with C/3 check-up cycles every 50th cycle ……..73

Figure 42 Cyclic voltammograms showing Mg deposition on a Pt working electrode using……..74

Figure 43 Cyclic voltammograms (CV) of WS_2/PANI-40 | 0.1 M $Mg(TFSI)_2$ +……....75

Figure 44 Electrochemical study and material properties of the obtained $Mg_x\{V_{18}\}$ and $Na_x\{V_{18}\}$ ……..……...80

List of Tables

Table 1. Results of EDX analysis of synthesized K-POV electrodes.……43

Table 2. Results of quantitative XPS analysis for the expected elements in LIG and K-POV electrodes……..47

Table 3. Elemental composition of the deposited film from 3 CV cycles in different concentration ratios of $\{V_{18}\}$: EDOT……...……56

List of Abbreviation

CV	Cyclic voltammetry
DMA	Dimethyl ammonium
POMs	Polyoxometalates
TM	Transition metal
MeCN	Acetonitrile,
DMF	N, N-dimethylformamide
NMP	N-methyl-2-pyrrolidone
DMSO	Dimethyl sulfoxide
P	Phosphorus
Si	Silicon
S	Sulphur
Na	Sodium
Si	Potassium
Mg	Magnesium
V	Vanadium
W	Tungsten
Mo	Molybdenum
Fe	Iron
Co	Cobalt
Cu	Copper
WE	Working electrode
RE	Reference electrode
CE	Counter electrode
KSCN	potassium thiocyanate
M	Molar concentration
LIBs	Lithium-ion batteries
SWNTs	Single-wall carbon nanotubes
GO	Graphene oxide
EQCM	Electrochemical quartz crystal microbalance

FTIR	Fourier-transform infrared spectroscopy
CEI	Cathode electrolyte interphase
SWV	Square wave voltammetry

List of Compounds

Table **(a):** List of compounds

Formula	Abbreviation
$(n\text{Bu}_4\text{N})_4\,[\text{V}_4\text{O}_{12}]$	$\text{TBA}_4\{\text{V}_4\}$
$(\text{nBu}_4\text{N})(\text{NO}_3)$	Tetrabutylammonium nitrate
(EtOAc)	Ethyl acetate
$(n\text{Bu}_4\text{N})\text{PF}_6$	Tetrabutylammonium hexafluorophosphate
$\text{Mg}(\text{ClO}_4)_2$	Magnesium perchlorate
NaPF_6	Sodium hexafluorophosphate
KPF_6	Potassium hexafluorophosphate
$(n\text{Bu}_4\text{N})_3[(\text{C}_2\text{H}_8\text{N})_2\text{V}_{12}\text{O}_{32}\text{Cl}]$	$\{\text{V}_{12}\}$
$\text{K}_5(\text{CH}_3\text{CN})_3[\text{V}_{12}\text{O}_{32}\text{Cl}]$	$\text{K}_5\{\text{V}_{12}\}$
$\text{Mg}(\text{BH}_4)_2$,	Magnesium borohydride
Mg(TFSI)_2	Magnesium(II) bis(trifluoromethanesulfonyl)imide
MPPip-TFSI	1-Methyl-1-propylpiperidinium bis(trifluoromethylsulfonyl)imide
DEGDE	Diethylene glycol diethyl ether
dFBn	Difluorobenzene

Notation

In this work, cluster nomenclature follows the standard square bracket notation used in polyoxometalate chemistry, e.g., $(n\text{Bu}_4\text{N})_4\,[\text{V}_4\text{O}_{12}]$. To enhance readability and avoid lengthy cluster formulas, an abbreviated curly bracket notation is applied for certain compounds. In this simplified form, only the number of metal centers is indicated, while representing the entire cluster unit along with its corresponding charge. For instance, the above formula is reduced to $\{\text{V}_4\}$.

Single polyhedral units are denoted using the square bracket [MOx], where M represents the addenda atom and x denotes the coordination number (x = 4–7). To avoid the complexity, the charge is omitted when the primary focus is on structural information.

Scientific Contributions

List of Publications

The following research articles were published as a result of work performed during the years of study and in the course of this doctoral thesis:

(NA1) Arya, Nikhil, Tom Philipp, Simon Greiner, Michael Steiner, Christine Kranz, and Montaha Anjass. "Reversible electrodeposition of potassium-bridged molecular vanadium oxides: a new approach towards multi-electron storage." *Angewandte Chemie International Edition* 62, no. 35 (2023): e202306170.

(NA2) Arya, Nikhil, Sirshendu Dinda, Thomas Diemant, Ke Wang, Maximilian Fichtner, and Montaha Anjass. "Tuning the Electronic and Electrochemical Properties of 3D Porous Laser-Induced Graphene by Electrochemically Induced Deposition of Polyoxovanadate Nanoclusters for Flexible Supercapacitors." *Advanced Functional Materials* (2024): 2410943.

(NA3) Kloker, Gabriele, Dragoljub Vrankovic, **Nikhil Arya**, Thomas Diemant, and Montaha Anjass. "Enabling Si-dominant Anodes: Influence of Neutralization Degree of Polyacrylic Acid on Low-Cost Micron-Sized Silicon Anode in High-Energy Li-Ion Full Cell." *Batteries & Supercaps*: e202400330.

(NA4) Elkhafif, Omar W., Hagar K. Hassan, Motahira Hashmi, **Nikhil Arya**, Montaha Anjass, and Timo Jacob. "Boosting Mg deposition and dissolution from ionic liquids–The role of different additives for applications in Mg-ion batteries." *Journal of Energy Storage* 105 (2025): 114636.

Conferences and Conference Contributions

Date	Conference Name	Venue	Types of contribution
05/07/2021-08/07/2021	1st Graduate School Electrochemical Energy Storage (GS-EES) Summer School	Digital	Poster
15/09/2021-16/09/2021	10th Biennial Meeting of HIU	Ulm	Poster
04/07/2022-08/07/2022	2nd Graduate School Electrochemical Energy Storage (GS-EES) Summer School	Ulm	Research talks and Poster
07/09/2022-07/09/2022	17. Koordinationschemie-Treffen Jena	Jena	Poster
11/06/2023-12/06/2023	12th HIU-Biennial Meeting 2023	Ulm	Poster
24/07/2023-28/07/2023	3rd Graduate School Electrochemical Energy Storage (GS-EES) Summer School	Bad Liebenzell	Research talks and Poster
10/04/2024-11/09/2024	Advanced Battery Conference Münster	Münster	Participation

1. Introduction

Due to the huge demand for clean renewable energy, the energy storage and conversion systems have become key areas of interest in modern-day research. Next-generation energy storage systems must prioritize sustainability, performance, and high efficiency to meet the demands of today's world. As a result, a significant amount of research has been carried out in the last two decades. These advancements primarily focus on rechargeable batteries (secondary batteries) and supercapacitors. The redox-active electrode material is a crucial element in these energy storage devices. Therefore, it is essential to create a new class of electrode materials that possess optimal material properties, including exceptional chemical stability, accessibility, long life cycles, and promising performance.

Recently, there has been a rise in the use of layered metal oxide-based materials (such as $LiNi_xCo_yMn_zO_2$) as cathode materials for rechargeable batteries.[1] These materials have gained popularity due to their remarkable electrochemical stability, excellent reversibility, and impressive discharge capacity. Nevertheless, cathodes that contain high amounts of nickel (Ni), cobalt (Co), and manganese (Mn) encounter various challenges, such as expensive materials, structural flaws, and potential safety hazards.[2] Consequently, it is imperative to create a new class of metal oxide materials that are cost-effective to synthesize and possess a wide range of functional capabilities.

Recently, there has been a growing interest in polyoxometalates (POM), a type of early transition metal oxides, due to their potential as materials for energy storage and conversion.[3] The unique molecular crystal architecture and the multiple-oxidation state of these compounds drove widespread interest from many researchers. These materials offer the ability for well-defined molecular structural tunning and provide a novel bottom-up approach for heteroatom functionality to construct a multi-electron transfer electrode material for energy storage devices.[4]

1.1 Polyoxometalates (POMs)

1.1.1 General overview of Polyoxometalates

The word polyoxometalates first came into highlight by Berzelius in 1826.[5] The unique properties of the POM materials include that their structural framework can easily tuned up to

the molecular level with different elements of the periodic table. In general, POMs are clusters of anionic metal oxides composed of early transitional metal oxide building blocks. Their usual formula is $[M_xO_y]^{n-}$, where M represents the addenda atom. This atom often belongs to the group of early transition metals, such as vanadium (V), tungsten (W), molybdenum (Mo), or niobium (Nb), and is in a high oxidation state (d^1, d^0). The metal centers and the oxo ligands surrounding them are the fundamental units ($[MO_z]^{m-}$, $z = 4 - 7$) that compose the bigger polyoxometalate. The MO_z units, which are often octahedral, tetrahedral, or pyramidal in shape, are linked together by bridging μ-Oxo ligands. The MO_z units can be joined by corner-sharing (with one μ-Oxo ligand), edge-sharing (with two μ-Oxo ligands), or rarely face-sharing (with three μ-Oxo ligands), as seen in **Figure 1**.[6] The wide range of building block geometries and types of connection results in a diverse array of POM nanostructures that exhibit a broad range of physical characteristics. Indeed, the majority of these nanostructures have been intentionally engineered to be compatible with a particular use or purpose. POMs are appealing for a variety of applications, including (photo-) catalysis, medicine, and energy storage due to their wide range of physical characteristics and ability to be adjusted.[7–15]

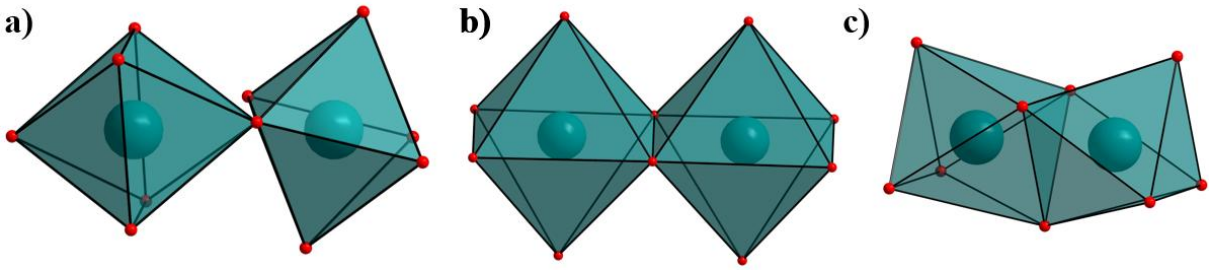

Figure 1: The two octahedral units $[MO_6]$ connect **a)** one μ^2-Oxo ligand *via* corner-sharing, **b)** two μ^2-Oxo ligands *via* edge-sharing, and **c)** three μ^2-Oxo ligands *via* face-sharing. Color scheme: red: oxygen, green: octahedral units $[MO_6]$, and center addenda atom.

1.1.2 Detailed discussion of the chemical and microstructural properties of Polyoxometalates

A categorization system has been developed in scientific literature to gain a more comprehensive understanding of a significant classification of POM and to categorize clusters based on their characteristics and compositions.[16] Polyoxometalates can be divided into two main categories: isopolyoxometalates and heteropolyoxometalates. Isopolyoxometalates are compounds that have a generic chemical formula $[M_xO_y]^{n-}$ and are made up of a single type of addenda atoms, such as V, Mo, and W. They are frequently less stable than their counterparts and offer a limited range of options because of their relatively modest number of potential

constituents.[6] The Lindqvist structure $[M_6O_{19}]^{n-}$ primarily consists of six metal units, making it a widely studied isopolyoxometalate (refer to **Figure 2a**).[17]

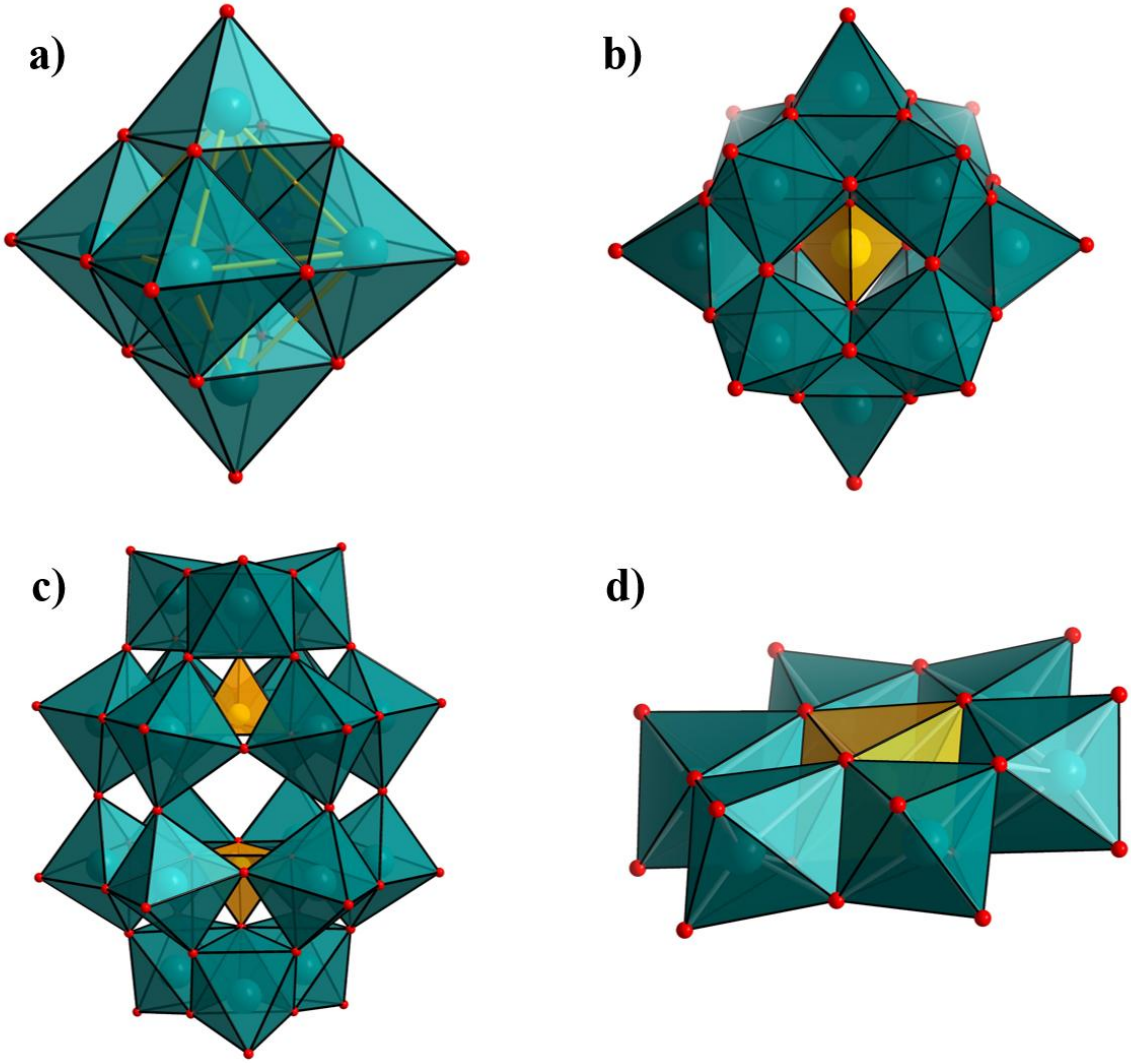

Figure 2: Polyhedral structures of different POM clusters **a)** Lindqvist structure $[M_6O_{19}]^{n-}$ with six $[MO_6]$ units combined with edge-sharing. **b)** Keggin structure $[XM_{12}O_{40}]^{n-}$ with three $[MO_6]$ units combined with edge-sharing. **d)** Dawson structure $[X_2M_{18}O_{62}]^{n-}$ (X is anions from a tetrahedral group e.g. $[PO_4]^{3-}$). **d)** Anderson structure $[XM_6O_{24}]^{n-}$ Colour scheme: red: oxygen, green: octahedra $[MO_6]$ and center addenda atom, templating metal X: orange, oxygen: yellow

On the other hand, heteropolyoxometalates, as their name implies, include additional heteroatoms X, leading to a general chemical formula of $[X_aM_xO_y]^{n-}$ (where a is less than or equal to x). This structure can provide enhanced structural stability by incorporating these heteroatoms. The anions from tetrahedral groups, such as $[PO_4]^{3-}$, $[SO_4]^{2-}$, and $[SiO_4]^{4-}$, are known as heteroatoms. They often serve as models for stable complex structures. The chosen template in the POM material has the potential to alter the structural, redox, and photoactive characteristics significantly. **Figure 2** shows a collection of widely recognized POM structures.

The structures of the initial POMs $[PMo_{12}O_{40}]^{3-}$ and $[AsMo_{12}O_{40}]^{3-}$, synthesized by Berzelius, remained unknown until 1933, when Keggin introduced the exact structure with the help of powder X-ray diffractometry technique.[18] These clusters are classified as Keggin-type clusters. During the following decades, several different POM material structures were reported, including additional heteroatoms into the framework. This resulted in the emergence of a new family of POM clusters, including structures such as Anderson, Lindqvist, and Dawson types (see **Figure 2(b-d)**).[17,19,20]

This remarkable structural flexibility set a new benchmark in the quest for high-performance supramolecular POM clusters, allowing for significant molecular adjustments and structural modifications. This unique feature of POM's structures enables the incorporation of heteroatoms (such as P, S, and Si) and alkali earth metals (such as Na, K, and Mg) into their metal oxide building blocks, facilitating the construction of a novel cluster framework.[21] Therefore, this systematic approach of combining various alkali earth metals and heteroatoms with transition metals leads to changes in their physicochemical properties.

Nevertheless, this structure alteration often results in intricacy during the initial stages of synthesizing the starting precursor. The limited number of synthesis stages increases the challenge of controlling the complex mixture during synthesis, and even a small adjustment to the reaction conditions results in the formation of different cluster frameworks. [22]

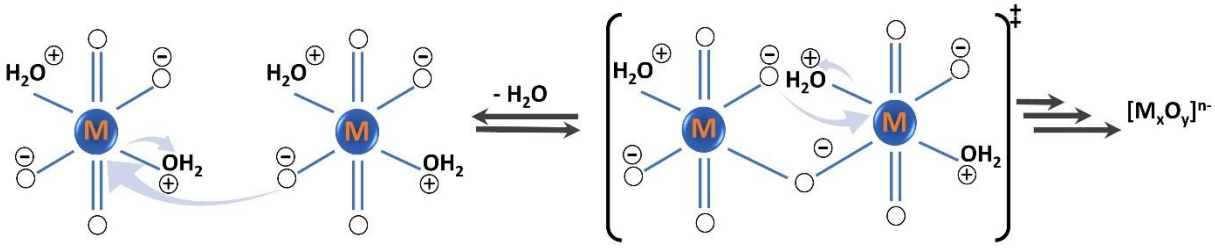

Figure 3: schematic representation of the synthesis mechanism of large polynuclear POM anion $[M_xO_y]^{n-}$ (where M: V, Mo, and W) by the condensation reaction between two small $[MO_6]$ octahedral units.

The synthesis mechanism of POM typically involves the development of complex structures of polyanion, which is achieved by carefully controlling various chemical conditions such as concentration, acidity, temperature, and type of solvent. POM synthesis is a systematic procedure of cross-linking small oxometalate $[MO_z]$ units in the solution through self-assembly. Because fewer synthesis steps are involved, this procedure is commonly called a *one-pot-synthesis* method. The self-assembly reaction mostly takes place in an aqueous solution with a controlled pH value, following a few simple stages. Within the specific pH range, the aqueous

solution containing metal oxides becomes more acidic. This acidity leads to the nuclearity of metal oxide anions by a condensation mechanism as shown in **Figure 3**.[21] This method is normally employed for the isopolyanions class of POM (V, W, Mo) structure, which occasionally necessitates a significant amount of time to achieve equilibrium, particularly for tungsten-based POM.[21] The concentration of heteroatoms in heteropolyanions is a crucial factor that enhances the stability of big cluster assemblies.[23]

1.2 Vanadium-based polyoxometalates

As previously mentioned, POM clusters have emerged as a promising composite material for several important applications, such as energy storage and conversion systems.[24] However, in addition to the POM cluster based on the molybdenum and tungsten, significant focus has been directed on the polyoxometalates based on vanadium (known as polyoxovanadate: POV). As the lightest transition metal in group 5, stands in contrast to other transition metals with higher molecular weights, such as Molybdenum and tungsten. It exhibits distinctive characteristics of reversible multi-oxidation states, most often transitioning from V^{5+} to V^{4+} and V^{4+} to V^{3+}. It maintains stable chemical properties in both aqueous and non-aqueous solutions.[25,26] The material property of the vanadium surge is a suitable element for the synthesis of polyoxovanadate.[27]

1.2.1 Classification and detailed molecular structural properties

The structural stability of the POV cluster is assessed by a complex symmetrical arrangement of clusters that start from different small units such as tetrahedral, pyramidal, and octahedral configurations. This is in contrast to the other two classes of POM, which start with [MoO_6] and [WO_6] units.[6] However, the synthesis mechanism of the POV cluster also follows the same self-assembly methods in aqueous conditions. The pH of the solution plays a vital role in defining the coordination environments of the resultant clusters.[28]

The variation in the arrangement of vanadium oxide units results from the different oxidation states of vanadium, which are affected by the pH level. At highly acidic conditions (pH < 2) the vanadium compounds are in their most unstable state and presented as $[VO_2]^{2+}$ and can be

oxidized strongly. As the pH increases from strongly acidic to neutral condition (2 < pH > 6), vanadium primarily exists in the form of protonated decavanadate $[V_{10}O_{28}]^{6-}$, which can then undergo additional oxidation to result in vanadium pentoxide (V_2O_5). At highly alkaline conditions, a stable deprotonated form of vanadium oxide species known as orthovanadate $[VO_4]^{3-}$ dominant. The condensation process occurring within this pH range leads to the formation of different vanadium oxide species, including monovanadates to metavanadate $[V_nO_{3n}]^{n-}$ (where n= 3 and 4). Therefore, the most usable oxidation state of vanadium compounds is possible, ranging from V^{3+} to V^{5+}.[29] However, attaining a stable cluster design is still challenging in the absence of external conditions including the hydrothermal method, which necessitates elevated temperature and pressure.[30]

A novel and efficient approach has been lately developed, incorporating a self-assembly technique to synthesize solid-state functionalized cluster structure.[31] This method not only opens new possibilities for the functionalization of vanadium oxide clusters in a more controlled way but also tunes their electrochemical properties by inserting redox-active transition metal. The method entails the process of self-assembly synthesis using an organic solvent such as acetonitrile (MeCN), N, N-dimethylformamide (DMF), and N-methly-2-pyrorrolidone (NMP) or dimethyl sulfoxide (DMSO).

1.2.2 Overview of the {V_{12}} and {V_{18}} POVs structures

Dodecavanadate Cluster: $(n\text{-}Bu_4N)_3(Me_2NH_2)_2[V_{12}O_{32}Cl]$ = ***{V_{12}}***

As described above, Kastner et al. provided a concise explanation of the self-assembly process of larger dodecavanadate clusters of $[V_{12}O_{32}Cl]$ from smaller $\{VO_5\}$ units.[31] **Figure 4** shows how three-square pyramids with edge-sharing $[VO_5]$ produce a unit known as $\{V_3\}$. The two $\{V_3\}$ units are joined in a corner-sharing manner, forming a ring-shaped $\{V_6\}$ structure. Further, the obtained two $\{V_6\}$ rings connected with a torsion angle of 30°, surrounding a chloride template, resulting in the formation of the $\{V_{12}\}$ end product. Notably, the chloride at the center of the cluster design is characterized as a template and plays a crucial role in the self-assembly process, but does not contribute to the structural tuning of the cluster. The formed $\{V_6\}$ hexagonal ring at the top and bottom of the cluster, consists of four μ^2-oxo ligands which are essential for the metal functionalization. Upon further investigation, it has been shown that the metal bonding involving μ^2-oxo ligands has a negative partial charge. This chemical property is advantageous for the formation of the strong transition metal-functionalized (TM=Fe, Co,

and Cu) bonds with the {V_{12}} cluster. During the synthesis of {V_{12}}, the metal bonding sites are blocked by the one dimethyl ammonium (Me_2NH^+) cation with μ^2-oxo ligands by a weak hydrogen bond. The process of transition metal functionalization involves stepwise replacing the weakly bonded organic cations placeholder with TM cations within the cluster framework. This results in the formation of a cluster with the molecular entity of [$(ML_x)_aV_{12}O_{32}Cl$] (where a = 1, 2, 3; M = metal cation; and L = ligand such as MeCN).[31,32] This placeholder exchange with the transition metal approach opens new possibilities for fine-tuning the molecular, structural, and catalytic properties of the POV cluster. Hence, this modification to the POV structure has been demonstrated in several applications, including catalysis and energy storage.[33,34]

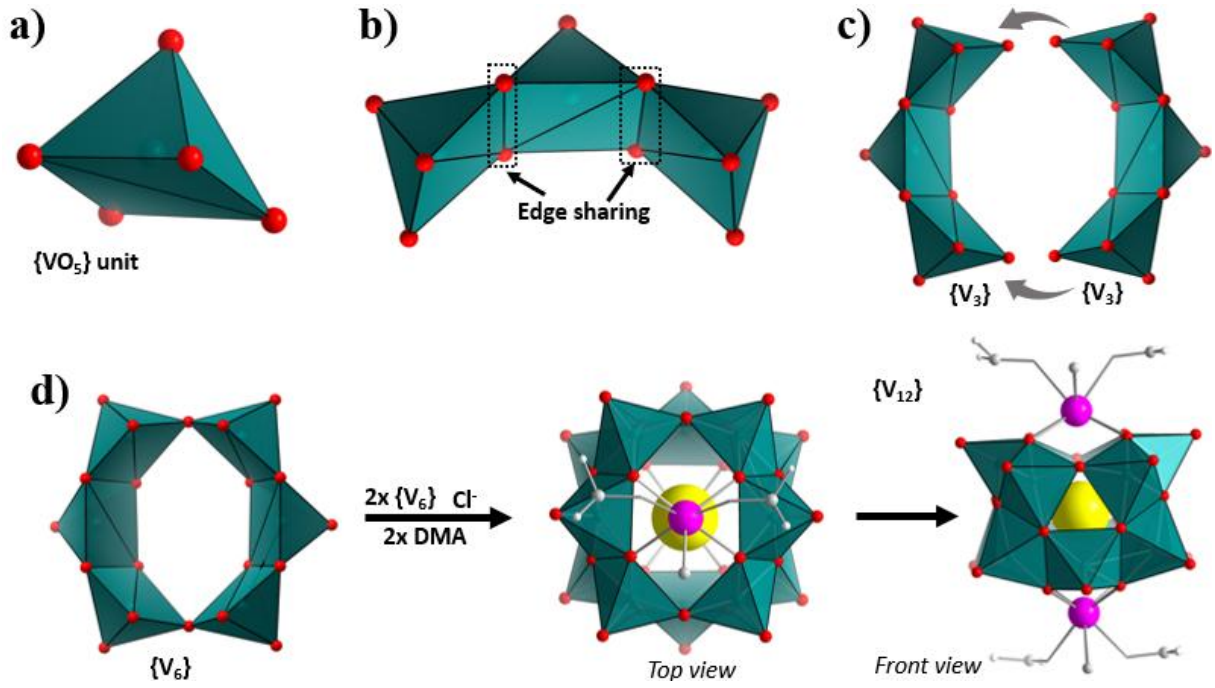

Figure 4: Self-assembly process involved during **{V_{12}}** synthesis **(a)** a single polyhedral {VO_5} unit containing five oxygen and vanadium centers. **(b)** Three edge-shared polyhedral units {VO_5} to form {V_3} **(c)** Two nearest {V_3} units connected to form cyclic{V_6} ring. **(b)** Two {V_6} rings are placed on top and bottom of the chloride templates to form **{V_{12}},** (color code: polyhedra {VO_5}: green, oxygen: red, chloride: yellow, nitrogen: pink, carbon: light gray, hydrogen: white.

Later, it was determined that replacing the suitable solvent with the {V_{12}} cluster enabled the strontium-functionalized cluster to exhibit sufficient stability, facilitating controlled 1D supramolecular infinite chain polymerization.[35] The detailed investigation suggested that replacing the DMSO ligands with DMF or NMP resulted in the formation of three coordinative bonds between Sr^{+2} ions and NMP ligands, linking the nearby Sr-functionalized vanadate cluster with four μ^2-bridging NMP ligands. Nevertheless, achieving a stable supramolecular

structure composed of solid-state clusters in this solvent-based cluster framework remained a challenging task.

*The three-dimensional supramolecular assembly of solid-state potassium vanadate cluster;(K-POV, $[K_{10}(V_{12}O_{32}Cl)_2]$. 4.5 CH_3CN (= **$K_5\{V_{12}\}$**))*

These findings provide new opportunities to investigate the synthesis of 3D nanostructured metal functionalized vanadate clusters with precise coordinative flexibilities. Recently, Streb et.al. reported a study where they demonstrated the insertion of potassium cations into the polyoxovanadate cluster $\{V_{12}\}$ framework. This resulted in the formation of a three-dimensional structured network with precise metal binding sites.[36] This method enables the retrieval of both the placeholder sites for the adjacent K^+ cation functionalized $\{V_{12}\}$ cluster, facilitated by the acetonitrile ligands. The resulting structure comprises five K^+ ions per vanadate framework, as shown in **Figure 5.** As an intermediate stage, two dissolved units of $\{V_{12}\}$ are crosslinked with six K^+ ions, with an extra K^+ ion providing support to produce an asymmetric structure of the cluster unit (see **Figure 5b**). In addition, the acetonitrile ligands formed asymmetric linkages with each vanadate cluster unit, resulting in the manifestation of a tortuous long-chain chirality (see **Figure 5c**).[36,37] The presence of potassium enables the interaction between each cluster unit, allowing the asymmetric propagation of the units in a 3D hierarchical network. Another significant observation is that introducing K^+ ions does not reduce the vanadium center atoms, indicating that the center atoms of the dodecavanadate cluster remain in a fully oxidized state (V^{5+}).[36,38] The results demonstrated that the synthesized $K_5\{V_{12}\}$ cluster successfully incorporated K^+ into the $\{V_{12}\}$, which leads to the formation of a complex 3D cluster framework. The polyoxovanadate structures, which are formed by the incorporation of potassium, have enhanced structural flexibility. These nanostructured supramolecular assemblies have the potential to be investigated for use in a multi-electron transfer energy storage system.

*Octadecavanadate cluster $(nBu_4N)_5[V_{18}O_{46}(NO_3)]$=**$\{V_{18}\}$***

Another substantial synthetic route to synthesize a large functional polyoxovanadate cluster like $(nBu_4N)_5[V_{18}O_{46}(NO_3)]$=**$\{V_{18}\}$,** involves the thermal treatment of a decavanadate precursor $(^nBu_4N)_3[H_3V_{10}O_{28}]$=**$\{V_{10}\}$**. The $\{V_{10}\}$ decavanadate cluster was produced from the self-assembly method following the dissolution of vanadium pentoxide in an acidic aqueous condition. In the aqueous medium with a certain pH, the distinct protonation cluster species are

isolated and precipitated as solid substances in the presence of a suitable courter cation such as tetrabutylammonium.

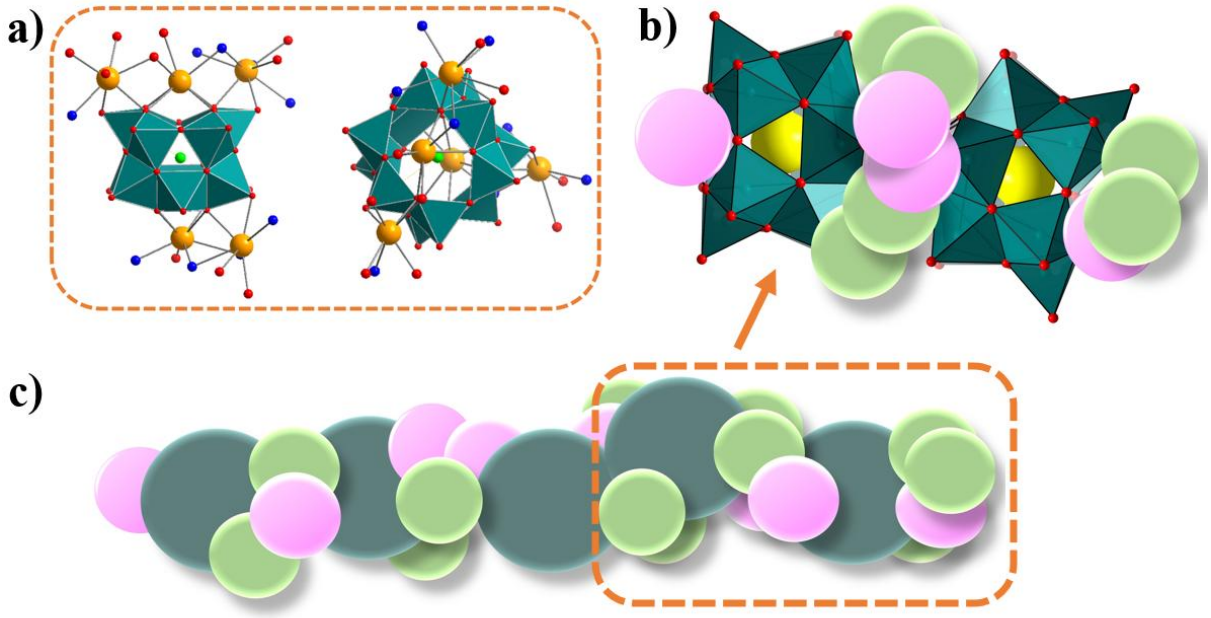

Figure 5: a) Schematic representation of a $\{V_{12}\}$ polyoxovanadate cluster incorporating shared potassium ions in both lacunary binding sites (here K^+ ions are depicted in yellow) **b)** Formation of a single asymmetric unit consisting of two$\{V_{12}\}$ clusters, facilitating the coordination of 10 potassium ions (potassium ions at the lacunary binding sites are shown in light green color). **c)** A molecular chain growth from the several asymmetric units. (MeCN is omitted for clarity) Color scheme: V, $[VO_5]$ polyhedral and $\{V_{12}\}$ spheres: dark green; O: red; N: light purple; Cl: yellow; K within placeholder sites: light green. Schematic figure in 5 (a, b, c) is reproduced with permission copyrights from CrystEngComm (2021)[36]

After the crystallization process, the pure $(nBu_4N)_3[H_3V_{10}O_{28}]$ decavanadate compound was obtained. The structural analysis of this $\{V_{10}\}$ cluster reveals that ten octahedral $[VO_6]$ units are linked together *via* edge-sharing. Out of these ten units, six octahedral units are arranged in the equatorial plane in two rows as shown in **Figure 6a**. The two octahedral units are positioned vertically, with one unit exactly above and the other unit exactly below the equatorial plane. The three distinct vanadium centers and four oxygen atoms are classed according to the unique cluster topology. The oxygen atoms exhibit varying vanadium bridge sharing as they change from terminal oxygen atoms to central oxygen atoms. The decavanadate cluster enhances both thermal and structural stability, making it particularly valuable for metal functionalization and the development of alternative redox-active cluster structures.

Anjass et. al. recently conducted a thorough investigation of the $\{V_{10}\}$ cluster, which functions as a stable vanadate precursor in both solid-state and solution. The aim was to develop highly reactive larger polyoxovanadate cluster compounds.[39]

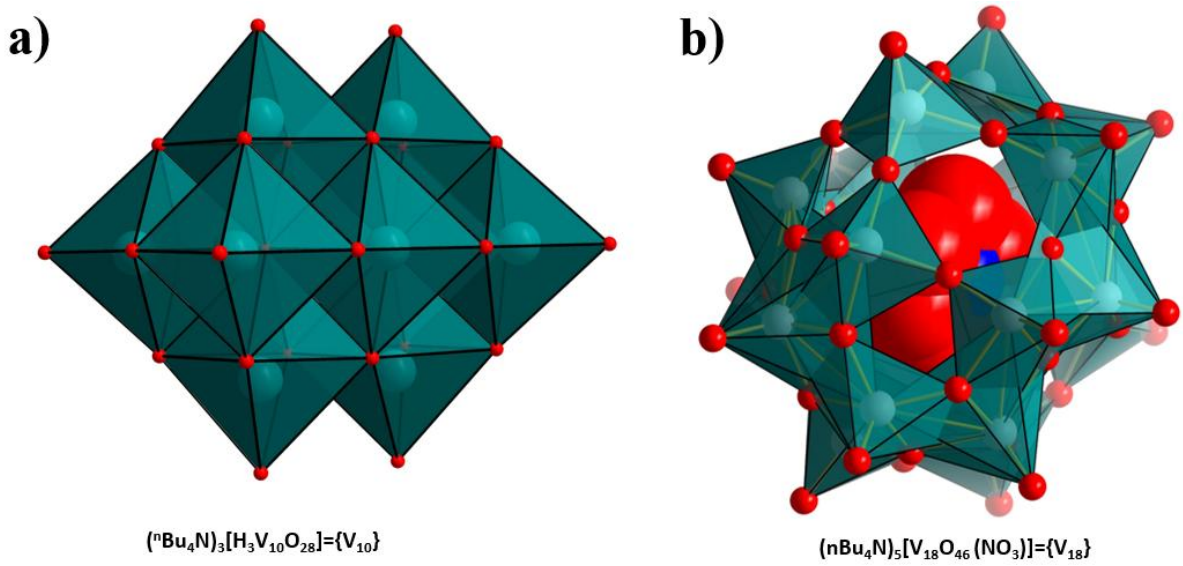

Figure 6: a) Schematic representation of the polyhedral $[VO_6]$ assembly in dodecavanadate cluster. **b)** polyhedral presentation of nitrate template supported **$\{V_{18}\}$** motifs, color scheme: V, $[VO_5]$ polyhedral: green, oxygen: red.

This work established a new standard for synthesizing vanadium-rich high-performance clusters, such as $(nBu_4N)_5[V_{18}O_{46}(NO_3)]$=**$\{V_{18}\}$,** $(nBu_4N)_4[Cu_6V_{30}O_{82}(NO_3)_2(CH_3CN)_6]$=**$(Cu_6\{V_{30}\})$**, and $(nBu_4N)_3[Ca_2(C_4H_8O_2)_6V_{18}O_{48}(NO_3)]$=**$(Ca_2\{V_{18}\})$**, which all drive from the initial $\{V_{10}\}$ decavanadate precursor. As a first step in the synthesis process, the $\{V_{10}\}$ sample was heat-treated at 195°C and subsequently cooled down to obtain the dark brown powder. Interestingly, this resultant product retains the characteristic material properties of the POV cluster. However, most of the POV structures exhibit thermal sensitivity and undergo decomposition at temperatures above 150 °C, resulting in the formation of solid-state vanadium oxide species.[40] The heat-treated $\{V_{10}\}$ substance exhibited good solubility in a non-aqueous solvent, such as acetonitrile. This indicates a strong reactivity and provides new opportunities to utilize it as a precursor in the synthesis of the new POV cluster's structure. So far, the heat-treated $\{V_{10}\}$ precursor uses a nitrate-based anionic template to achieve a high nuclearity POV profile during the synthesis. To achieve this the heat-treated $\{V_{10}\}$ precursor dissolved and stir overnight in the acetonitrile with $(nBu_4N)(NO_3)$. The ethyl acetate (EtOAc) was added to the prepared reaction mixture to obtain nitrate template induced $(nBu_4N)_5[V_{18}O_{46}(NO_3)]$=**$\{V_{18}\}$** cluster as shown in **Figure 6b**. Due to these distinguished structural properties, the $\{V_{18}\}$ cluster showed high redox activity during the electrochemical measurements.[40] The substantial redox

activity observed during the electrochemical testing, combined with multiple fully reversible redox events, indicates that excellent structural tunning is achievable through controlled reduction of the vanadium centers. Therefore, this large cluster is worth exploring for further electrochemical tunning to show some functional applications in the energy storage field.

1.3 Immobilization of polyoxometalates into conductive substrates

This recent progress in the POM cluster, specifically polyoxovanadates, resulted in extensive research into their potential uses in various fields such as catalysis, battery electrodes, materials science, photocatalysis, electrocatalysis, and functional molecular structures for diverse applications. [24,41–47] Polyoxovanadates have been intensively studied for their use in energy storage due to their excellent electrochemical activity, versatile molecular structure, and ability to transport multiple electrons.[48–50] However, the significant challenges hinder their functionality in these applications, primarily due to their high solubility and structural deformation in both aqueous and non-aqueous electrolytes (or solvents).[51] These issues arise because POV clusters have a tendency to easily oxidize even under atmospheric conditions, a consequence of the sensitivity of presented vanadium atoms. Moreover, the structural manipulation of POV at the molecular level often leads to complex nanostructures, which makes it difficult to comprehend their molecular interactions, topology, and material characteristics. To overcome these challenges and achieve maximum performance, several approaches have been explored such as redox active metal insertion into POV framework, encapsulation of POV, electrochemical deposition of redox-active POV structure, electrochemical tunning, and polymer or conductive additives incorporated POV nanostructure.[52–57]

The above-stated techniques offer effective methods for immobilizing the POV-based composites on a functional substrate. However, further exploration is needed to attain promising deposition of redox-active solid-state polyoxovanadate. A closer look at these approaches clarifies the mechanism used for the POM (or POV) deposition.

Functionalization with of reactive heteroatoms: This prevailing method entails the integration of reactive metals into the polyoxometalate (POM) structure by heteroatom functionalization. Heteroatom functionalization, commonly reported for molybdenum or tungsten-based POM clusters, typically results in Keggin or Dawson-type structure. Jie and co-authors successfully reported the integration of three-dimensional organic-inorganic hybrid heterometal incorporation in tungsten-based Keggin-type POM structure through a hydrothermal reaction. [58] However, such lacunary clusters are only limited to molybdenum or tungsten oxides-based structures. A recently proposed placeholder technique for functionalizing POV clusters with the desired transition metals is a significant advancement. The synthesis mechanism is explained in section 1.2.2.[31] This method allows for a controlled and precise step-by-step metal

incorporation, enabling fine-tuning of the physical and electrochemical properties of these vanadate clusters.

Another method, known as *encapsulation of POM*, involves immobilizing the POM by utilizing polymer or sol-gel molecules to preserve its structure. This technique employs the direct mixing of the POM with a very stable molecular framework, followed by immobilization on a solid-state electrode-like substrate for important practical uses.[59]

In addition to the aforementioned techniques, *electrodeposition* offers a straightforward approach for transitioning soluble POM species into functional solid-state material, resulting in immobilized POM with slightly altered physical and electronic properties. Recent reports highlighted the use of electrodeposition for achieving typical tungsten and molybdenum-based POM nanocrystal growth or stable molecular film on different substrates.[60–62] However, this method is largely unexplored for restructuring and tunning the POV structures.

This thesis primarily focused on the synthesis of high-performance, excellent redox-active immobilized nanostructured complexes, and similar composites, specifically targeting the polyoxovanadate clusters by electrochemical deposition method.

1.3.1 Electrodeposition

The electrodeposition technique is a long-standing process used for producing a thin coating of redox-active material on conductive surfaces. Electrodeposition is widely used in industry because it is a highly adaptable technology for creating a protective layer on different substrates. The electrochemical deposition can be carried out in an electrochemical cell setup using either a galvanostatic mode, where a DC power supply is used to maintain a constant current or a more advanced mode known as potentiostatic deposition, where the potential is controlled to study the relevant electrochemical reactions during the deposition. Before moving to the electrochemical deposition mechanism in detail, it is important to comprehend the important tools needed for this method. The potentiostatic electrodeposition method is performed in a typical three-electrode electrochemical cell that is connected to an external electrochemical workstation. The electrochemical cell combined a configuration consisting of three different electrodes: working electrode (WE), reference electrode (RE), and counter electrode (CE). The working electrode is a key component of a constructed electrochemical cell and provides the specific controlled potential to study the electrochemical reaction occurring on its surface. The

working electrodes possess chemical inertness and exhibit superior electron transmission capability.

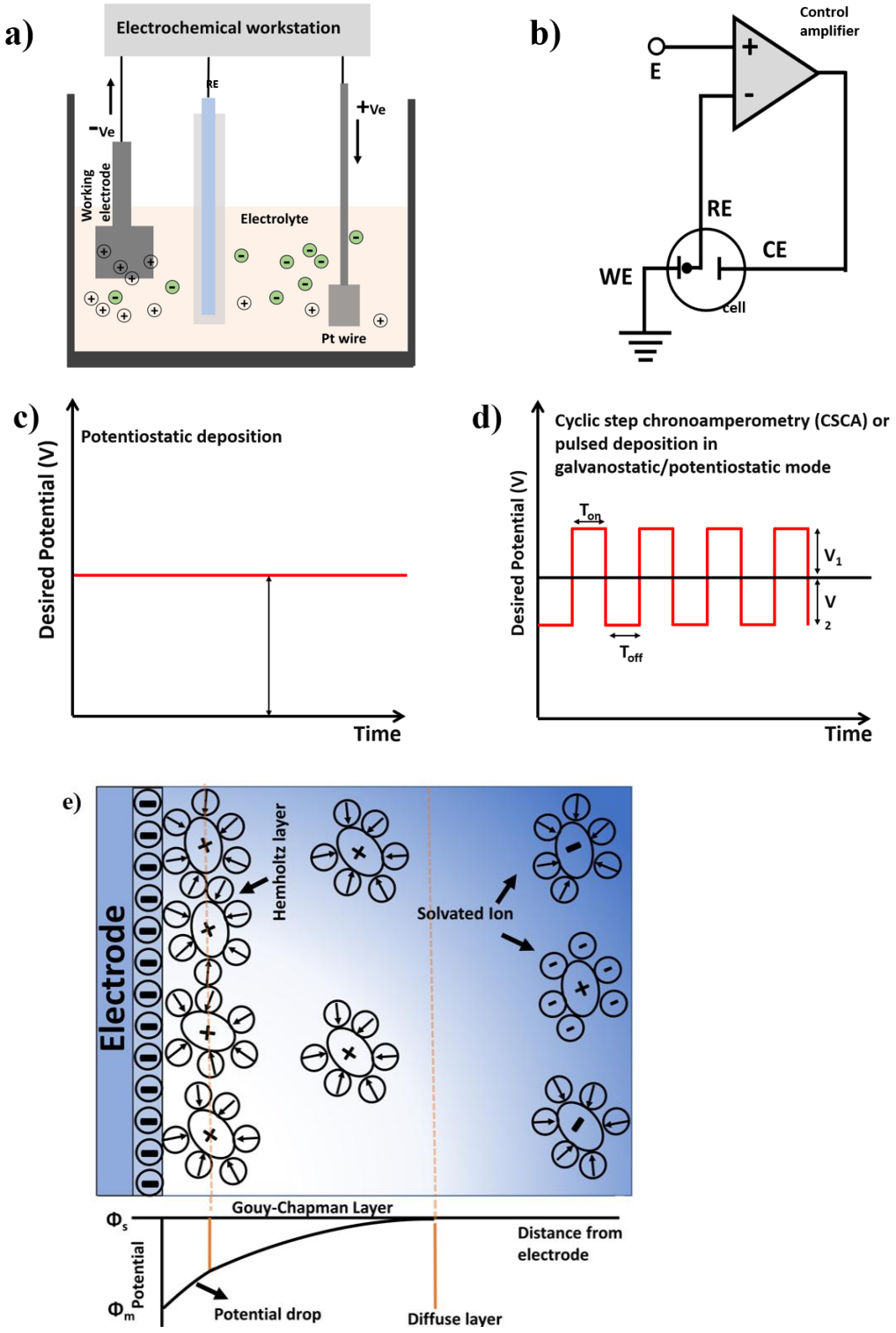

Figure 7: a) Schematic representation of a three-electrode cell configuration with an ionic electrolyte connected to the potentiostat workstation **b)** A circuit diagram of simplified potentiostatic operation **c), d)** Schematic representation of the operating mechanism of potentiostatic pulsed electrodeposition **e)** The graphic illustration of the electric double layer formation near the negatively charged electrode surface by absorbed solvated ions (top), and the corresponding potential drop due to the formation of the EDL near electrode surface (bottom).[63]

Common examples of materials used as working electrodes include glassy carbon, gold, and platinum. However, the electric potential drops caused by the transition from ions to reduced species in the vicinity of the charged region on the WE surface are quantified using a standard reference electrode. The RE possesses a well-defined standard potential value, which is utilized to quantify the potential of the working electrode relative to this standard potential. The most common reference electrodes are silver/silver chloride (Ag/AgCl) and the calomel electrode (Hg/Hg_2Cl_2). Similarly, the counter electrode was employed to quantify the current generated by the working electrode during the electrochemical process. A conventional CE is composed of chemically inert materials, such as platinum and graphite which are not involved in the electrochemical process. **Figure 7a** illustrates the general schematic of a three-electrode cell assembly, in which all three electrodes are connected to an electrochemical workstation normally known as a potentiostat. A potentiostat device is used to maintain and sustain the required potential between the WE and RE. The functionality of the potentiostat can be elucidated by a simplified potentiostat circuit diagram as seen in **Figure 7b**. The control amplifier unit (CA) regulates the voltage between the reference and working electrode to the specified input voltage E. The potentiostat unit is an invaluable instrument in the field of electrochemistry for studying various electrochemical data, including cyclic voltammetry (CV), square wave voltammetry (SWV), and galvanostatic charge-discharged (GCD) reaction, and more. Potentiostatic deposition is an electrodeposition process in which a constant potential is delivered to the electrochemical cell for a certain duration, and the resulting cell output current is observed, as seen in **Figure 7c**. On the other hand, a technique in which the deposition is carried out at a certain current value and the cell potential is monitored is referred to as galvanostatic mode. Cyclic step chronoamperometry (CSCA) is the most often employed technique for material deposition. In CSCA, the reaction taking place on the surface of the working electrode is controlled by applying a constant voltage for a certain time. The CSCA approach quantifies the output cell current response concerning the time at a certain potential. When two distinct operating potentials are delivered to measure the corresponding cell currents, this is referred to as a step or pulse, as seen in **Figure 7d**. Additionally, the process of material electrodeposition can be accomplished using a straightforward cyclic voltammetry scan. This approach enables better insight into the fundamental cathodic or anodic response while performing the deposition.

The electrodeposition process is dependent on the interaction between electrolyte species in the solution and the electrically charged surface of the electrode. The mobility of the dissolved

electrolyte species towards the working electrode is essential for their reaction and for the attainment of uniform deposited mass. The rate of reaction between the electrolyte species and electrode is primarily determined by three crucial phenomena inside the system: diffusion, migration, and convection. The mass diffusion took place as a result of variations in the concentration of the dissolved species between two points in the electrolyte, referred to as the concentration gradient. Whereas in migration, the movement of the dissolved electrolytic species was reliant upon a localized electric field. Mass transportation is referred to as convection when the movement of the dissolved species is affected by an external force such as mechanical stirring.

At the surface of the working electrode, electrolyte ions with the opposite charge accumulate as a result of charge separation. The charge separation is dominant at the electrode-electrolyte interface. The process of charge separation results in the formation of an electrochemical double layer (EDL) on the surface of the electrode as shown in **Figure 7e**. The main component of this double layer comprised of the Helmholtz layer, which arises from the separation of ions in a monolayer, and the Gouy-Chapman layer, where the concentration gradient of charged ions is significantly affected by the distance between the electrode surface and the bulk electrolyte.[63] The graphic illustrates the formation of a layer of solvated positively charged ions on the surface of the electrode, resulting from the electrostatic force. This layer, known as the EDL, leads to an effective potential drop near the electrode surface. During the electrodeposition process, these solvated ions penetrate the diffusion layer and are absorbed into the electrode surface by accepting or donating the additional electrons. The initial growth of deposited species is ascribed to the spontaneous formation of nuclei at the surface of the electrode. When the electrodeposition process is diffusion-limited, the concentration gradient at the electrode-electrolyte interfaces increases and the diffusion layer decreases, resulting in an improved overall current response. The current at the working electrode is developed either by a faradic response or a non-faradic response. A faradic reaction occurs when charged ions pass through the barrier between a liquid-solid boundary and exchange electrons. On the other hand, a non-faradic reaction occurs when charged ions are absorbed and desorbed without affecting the interface between the solid-electrolyte interface.

1.3.2 Mechanism of electrochemical immobilization of POVs

There is currently limited research on the immobilization technique of vanadium-based POM clusters using the electrochemical method. Although the POV clusters have impressive redox chemistry, there is currently no systematic and direct method to synthesize supramolecular

nanostructured growth on a functional substrate employing the electrodeposition method. The recent advancement in the vanadium oxide cluster $(nBu_4N)_3(Me_2NH_2)_2[V_{12}O_{32}Cl]=\{V_{12}\}$ to enable straightforward heterometals functionalization through an effective placeholder route,

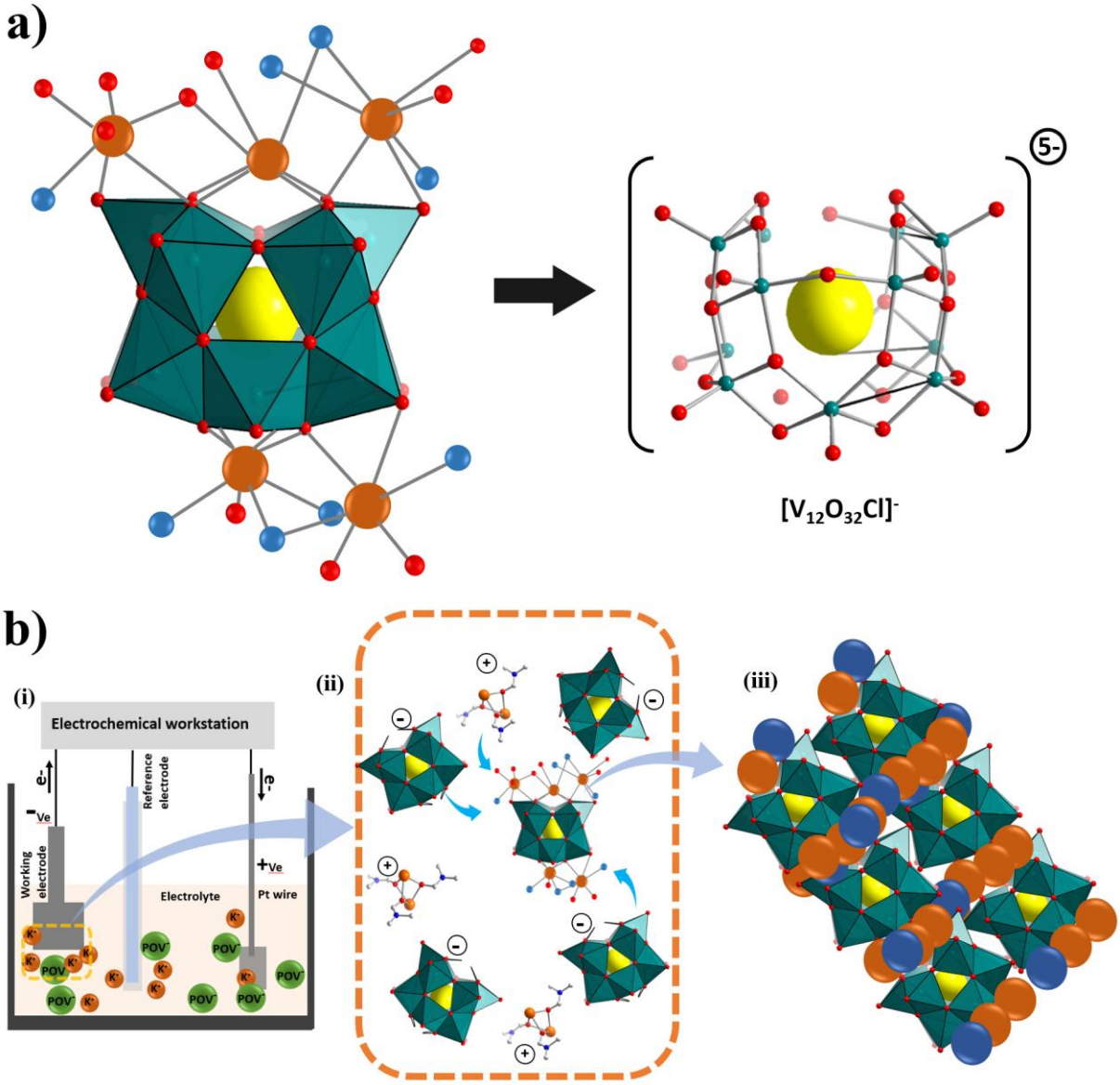

Figure 8: a) schematic representation of the polymeric fragmentation process of the $K_5\{V_{12}\}$ cluster upon dissolving in acetonitrile, leading to the formation of the $[V_{12}O_{32}Cl]^-$ anionic species. **b)** Graphical illustration of the electrochemical mechanism detailing the interaction between POV anions and K^+ cations in solution, followed by the depositing on the working electrode as a complex supramolecular chain. (Conditions: acetonitrile solvent containing 0.1 M $(nBu_4N)PF_6$ as electrolyte salt and $K_5\{V_{12}\}$ = 0.5 mM, RE: a silver wire in a glass frit, containing electrolyte solution, CE: Pt wire) Color scheme: V, $[VO_5]$ polyhedral and $\{V_{12}\}$ spheres: dark green; O: red; N: blue; Cl: yellow; K within placeholder sites: orange. Schematic figure in 8 (a) is reproduced with permission copyrights from chemistry A European Journal (2014)[31]

providing an additional possibility to modify their molecular structure using an electrochemical process directly. The parent dodecavanadate $\{V_{12}\}$ cluster exhibited exceptional solubility in organic solvents such as MeCN and DMA and transformed into an anionic solution. This $\{V_{12}\}$

cluster's anionic species has reversible redox activity within a certain potential range. This behavior is ascribed to the reversible reduction of the vanadium canter under atmospheric circumstances.[64] This significant redox behavior of the dodecavanadate cluster was subsequently expanded for potassium functionalized $K_5\{V_{12}\}$ POV cluster which is synthesized from a predetermined placeholder exchange method (refer to section 1.2.2). A detailed analysis of the charge balance and bond valence sum calculation of $K_5\{V_{12}\}$ in solution demonstrates that all the vanadium centers in the structure exist in a completely oxidized V^{+5} oxidation state. In addition, when the cluster is dissolved in the acetonitrile, the $K_5\{V_{12}\}$ undergoes protonated fragmentation, resulting in the formation of a stable anionic form: $[V_{12}O_{32}Cl]^-$ as seen in **Figure 8a.**[36] The unique characteristic of $K_5\{V_{12}\}$ enables further cluster architecture rearrangement by exerting an external electrostatic force and immobilizing itself to the surface of the working electrode. An electrodeposition approach was introduced to develop a film with superior redox active based on $K_5\{V_{12}\}$ on a conductive substrate (i.e., working electrode). This was achieved by including reduction of the cluster framework. Thus, an in-depth investigation was conducted on an electrochemical deposition technique for the synthesis of a novel $K_5\{V_{12}\}$ cluster. The deposition was carried out in a water-free and de-aerated acetonitrile solution, with the addition of 0.1 M $(nBu_4N)PF_6$ as the electrolyte salt. The presence of this supporting electrolyte does not influence the redox process, but it does enhance the ionic conductivity and ion-diffusivity. Electrodeposition was conducted using a three-electrode electrochemical cell configuration as shown in **Figure 8b**, to ensure precise control over the electrochemical reaction conditions. The electrodeposition mechanism of $K_5\{V_{12}\}$ facilitates the electrochemical reaction at the working electrode to proceed in response to the applied potential. At an optimally negatively charged working electrode surface, the dissolved protonated species $[V_{12}O_{32}Cl]^-$and solvated K^+ ions diffuse towards the working electrode surface. At first, the electrode surface absorbs these charged cluster ions and forms an EDL, resulting in the recognition of a capacitive current caused by the variation in potential at the electrode surface. The concentration of redox-active cluster species decreases with respect to distance from the electrode surface and mass transport towards the working electrode is diffusion-limited. At the electrode-electrolyte interphase, it is possible that localized $[V_{12}O_{32}Cl]^-$ species were reduced by the electrode surface. This caused a change in the oxidation state of some vanadium centers from V^{5+} to V^{4+}. To compensate for the charge balance, additional acetonitrile-supported K^+ cations interacted spontaneously with the reduced POV species as illustrated in **schematic 8b**. Simultaneously, this process results in a significant surge in the Faradic current. However, with time, the observed current response steadily diminishes, indicating the presence of mass transport limitation. This cation (K^+) and

anion (reduced $\{V_{12}\}$ interaction structural rearrangement occurring in the solution likely enhances their high insolubility and develops as a nucleus for the formation of a stable film on the electrode surface. This process may continue to evolve as the formation of a 3D hierarchical nanostructured film on the surface after the incorporation of a neighboring dissolve POV unit with the deposited species through the bridging of K^+ cations. The presence of K^+ bridging is crucial for stabilizing the cluster structure. However, because of their relatively high ionic radius, the K^+ ions are unable to break into the POVs cluster shell and cause any deformation. This could be an efficient method to immobilize a potassium-reduced POV film with uniform redox activity onto an electrode surface and allow for its utilization as a multi-electron storage system.

1.3.3 In-situ electrodeposition of potassium assisted reduced $\{V_{12}\}$ and $\{V_{18}\}$ film on a conductive surface

The described phenomena were also observed when a non-functionalized dodecavanadate cluster $\{V_{12}\}$ performed an electrochemical reaction with a potassium salt-based electrolyte. Evaluating the stability of this POV cluster in solution is a key feature for further functionalization and application. The solid-state $\{V_{12}\}$ POV structure is characterized by two metal-binding sites that are blocked by two dimethylammonium (DMA) cations by weak hydrogen bonding, as shown in **Figure 9a**. This metal binding site is supported by four μ^2-oxo ligands and may eventually replace one or both DMA cations with the first transition series ions, such as TM: Co^{2+}, Cu^{2+}, Fe^{3+}.[31] The self-assembly approach of transition metal functionalization of $\{V_{12}\}$, causes the cluster to dissolve in acetonitrile as a protonated form. As a result, the negatively charged POV separates from DMA cations, as shown in **Figure 9 (b, c)**. In order to render the potassium functionalized stable film growth, the metal binding sites that are exposed to K^+ ions are utilized to immobilize the dissolved $\{V_{12}\}$ cluster. The reduction of several vanadium centers within a specified potential range can lead to the formation of a potassium-bridged POV-stable film. This film allows for the interaction of more than two K^+ ions.

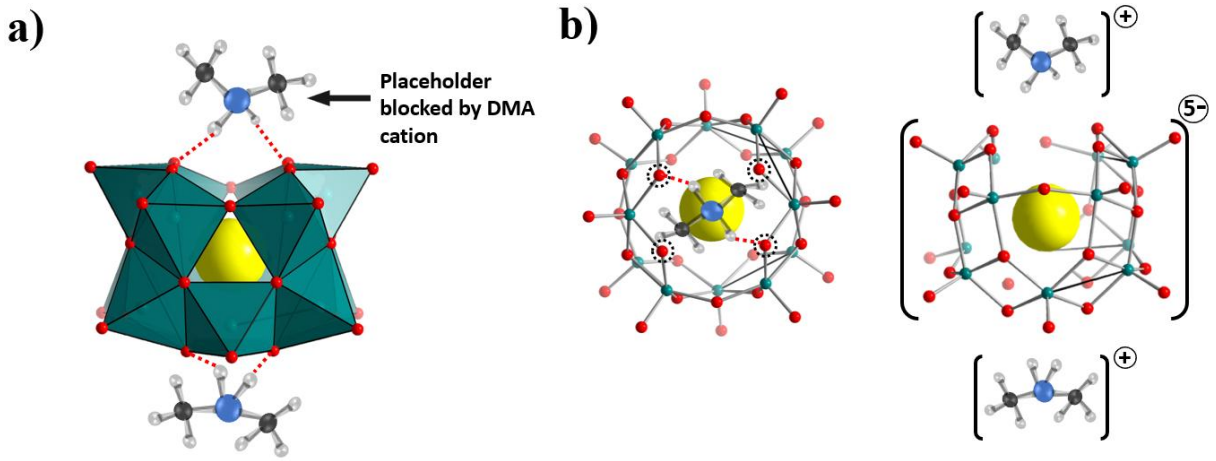

Figure 9: a) Polyhedral view of the $((DMA)_2[V_{12}O_{32}Cl]^{3-})$={$V_{12}$} cluster, where two DMA cations are connected by hydrogen bonding to metal binding sites **b)** Ball-and-stick illustration of the{V_{12}} framework, with four μ^2-oxo ligands highlighted by the circle (left), and a non-functionalized {V_{12}} polymeric view in acetonitrile (right). Color scheme: V, [VO_5] polyhedral and {V_{12}} spheres: dark green; O: red; N: blue; Cl: yellow; C: black; H: light grey. Schematic figure 9 (a, b) is reproduced with permission copyrights from chemistry A European Journal (2014)[31]

This research explored a novel electrodeposition approach that might facilitate the creation of a redox-active metal functionalized film of POV on the electrode surface, allowing for multiple electron transfers. This method was then employed on a large POV structure known as octadecavanadate {= V_{18}} (refer to section 1.2.2). Recent research has shown that this structure was synthesized under simple atmospheric conditions by introducing a nitrate-template NO_3. This octadecavanadate cluster comprises three {V_6} units and is connected to the adjacent {V_6} units by four shared oxygen corner atoms. The preliminary investigation of the redox properties of the {V_{18}} cluster reveals the presence of multiple reversible redox waves during a simple cyclic voltammetry scan.[39] The strong reversible redox activity is attributed to the cluster's exceptional reactivity while in a solution state. The reversible redox peaks of the POV-based cluster have been previously studied within a specific potential range. These peaks are associated with the partial reduction of the vanadium center and subsequent highly reactive insertion of K^+ cations into the {V_{18}} structure. Consequently, the synthesized {V_{18}} cluster was also utilized as a precursor for electrodeposition to develop a high redox active film on the electrode surface, with K^+ integrated into the {V_{18}} nanostructured.

1.4 POM-based redox active thin films and composites for energy storage

1.4.1 Lithium-ion batteries/post-lithium-ion batteries

The first mechanism for ion intercalation in solid-state compounds was introduced by Robert Huggins and Carl Wagner in 1960.[65] During the 1970s, there were notable breakthroughs in the field of ion intercalation, with a particular focus on reversible ion intercalation processes. After a few years, Armand pioneered the first conceptual framework for Li-ions batteries, and the first solid-state battery was introduced using inorganic and transition metal oxides as an electrode component.[66] The first commercially viable rechargeable lithium-ion battery was developed by Sony in 1991, which attracted significant attention for its potential use in portable electronics such as mobile phones.

Component, function, and working of Li-ion batteries

Figure 10 illustrates the schematic of a typical lithium-ion (Li-ion) cell. A Li-ion cell primarily comprises two electrodes: the cathode and the anode. An ion-conductive separator separates these electrodes to prevent direct electrical contact. An electrolyte solution, which acts as an ionic conductive medium, is situated between two electrodes. This electrolyte typically contains a lithium-based salt dissolved in a non-aqueous solvent, ensuring an electrically insulating environment while providing excellent ion mobility between the electrodes. To enhance the battery's longevity and safety, the electrolyte must meet several crucial requirements such as electrochemical stability, ionic conductivity, redox inactive, thermal stability, and cell safety.

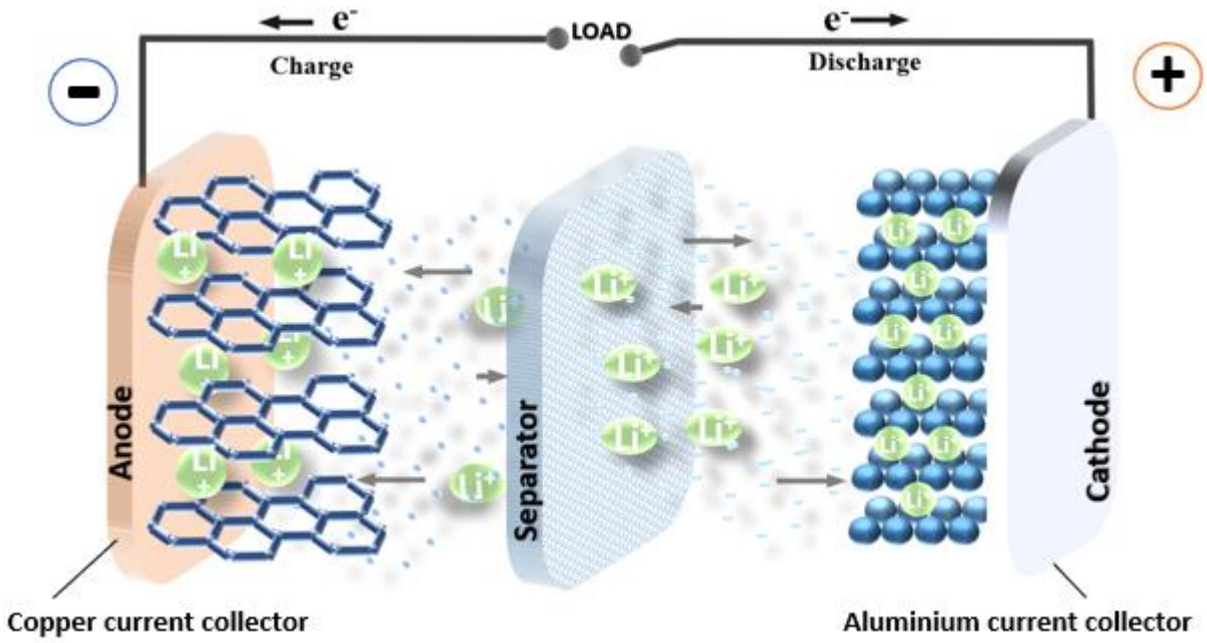

Figure 10: Schematic representation of the working principle of the lithium-ion battery cell.

To fulfill these requirements, a lithium-based electrolyte salt, such as $LiPF_6$ is normally dissolved in a mixture of cyclic carbonates (e.g., ethylene carbonate: EC) and linear carbonate

(e.g., diethyl carbonate: DEC, and di-methyl carbonate: DMC). This solvent composition significantly influences the electrolyte's physico- and electrochemical properties.[67] The most commonly employed electrolyte in Li-ion batteries is a 1 M $LiPF_6$ in EC/DEC mixture at a 50/50 volume ratio. The dissolved lithium ions move between the negative and positive electrode (i.e., anode and cathode) as part of charge-discharge cycles. The anode material is responsible for the absorbance and hosts the Li^+ during the electrochemical process. To date, carbon-based materials such as graphite are the optimal anode materials for secondary Li-ion batteries.[68,69] Also, the anode material is attributed to forming a stable solid-electrolyte interphase (SEI) on the surface which is essential for reversible cycling. Consequently, the choice of anode electrode significantly influences the rate capability and overall cell performance.[70] On the other hand, the cathode material is a pivotal component that significantly impacts LIB's performance, determining the overall energy density and operational voltage range. Around half of the production cost of LIBs is allocated to the active cathode material, which has led to substantial research effort in finding the optimal materials for cathode synthesis.[71] The layered structured transition metal oxides such as $LiCoO_2$, $LiNiO_2$, and $LiNi_{1-x}Co_xO_2$ have proven successful as cathode materials due to their high energy density and electrochemical stability.[72–74] In LIBs, these materials maintain their crystal structure during the Li^+ intercalation and de-intercalation, despite the valance state changes and potential phase transitions. In recent years, there has been research and investigation into different cathode materials such as spinel oxides (e.g., $LiMnO_4$), polyanionic material (e.g., $LiFePO_4$, $LiMnO_4$), and conversion-type (e.g., transition metals halides and LiS_2). These materials have shown various advantages such as improved structural stability, low cost, and enhanced safety features.[75] The $LiCoO_2$-based cathode has an applicable capacity of 140 mAh g^{-1}. However, by integrating various transition metals including Mn, Ni, Cr, and Fe, it is possible to attain a practical capacity of 200 mAh g^{-1} and higher operating voltage of up to 4.5 V. Nevertheless, these enhanced cathodes often suffer from capacity decay due to active material dissolution or cation mixing (e.g., Li^+ and Ni^+).[76–78]

The vanadium oxides, particularly those with layered structures, have demonstrated excellent specific capacities, reaching up to 215 mAh g^{-1} with good cycling performance. For instance, hydrothermally pre-lithiated vanadium pentoxide (V_2O_5) structures (e.g., $Li_{0.0625}V_2O_5$) have shown promising results.[79] Although NMC ($Li_{x+1}M_{1-x}O_2$) based cathodes have been widely used in battery production for many years, significant research continues to address persistent challenges associated with these cathode materials. The major challenges included the phase

transition, safety concerns, high material cost, gas formation, and scarcity of raw materials. To mitigate these problems, various strategies have been reported, such as cation doping, coating, and surface modification. In addition to these approaches, the research efforts have increasingly diverted from conventional LIBs to alternative low-cost post-lithium metal ion batteries including sodium-ion, potassium-ion, and magnesium-ion batteries. These new-generation batteries offer several advantages, such as low material cost, enhanced safety, ecological compatibility, and improved performance.

1.4.2 The mechanism of charge storage in POM-based electrodes

In the past decade, polyoxometalates have garnered considerable interest in the energy storage field. Their inherent molecular structure provides exceptional electron storage capabilities, facilitated by controlled structural modifications and redox tuning.[80] Kawasaki *et al.* reported successfully incorporating Keggin-type $(nBu_4N)_3[PMo_{12}O_{40}]$ POM structures into the SWCNTs to produce a nano-hybridized cathode for Li-ion batteries.[81] Similarly, a hybrid nanofiber composed of polyaniline and $[PMo_{12}O_{40}]^{3-}$ demonstrated the 1D polymerized chain defined an impressive rate capability and a specific charge storage capacity of 183.4 mAh g^{-1}, which is approximately 40% higher than that of pristine polyaniline (PANI) nanostructured cathodes.[82] The reversible charge storage mechanism in the PANI/PMo_{12} structure is explained by an "electron sponge" characteristic, wherein the reduced $[PMo_{12}O_{40}]^{27-}$ cluster can accommodate up to 24 Li^+ during the redox process.[82] These methods suggest that the POM material enables a straightforward synthesis with conductive polymers (or materials), retaining their molecular properties while significantly enhancing their electrical conductivity.

To expand upon these findings and investigate the use of POM in battery technology, polyoxovanadate has recently demonstrated significant potential as an electrode material. This is primarily due to its high energy density, cost-effectiveness, and abundant raw materials.[27] The reversible redox reaction of the POV-based cathode in LIBs resembles that of previously reported molybdenum and tungsten-based POM structures. The molecular POV clusters offer the essential ability to reversibly change into the various valance states of the vanadium centers, ranging from V^{5+} to V^{4+}, and in rare cases from V^{4+} to V^{3+}. This characteristic optimizes the electrode material in metal-ion batteries, resulting in a high specific capacity.[83,84] The charge storage mechanism in POV material involves the subsequent reversible reduction of partial (or full) vanadium centers at specific operating potential, facilitating the electrochemical

interaction of Li^+ ions without decomposing the initial molecular structure of POV, as shown in **Figure 11**.

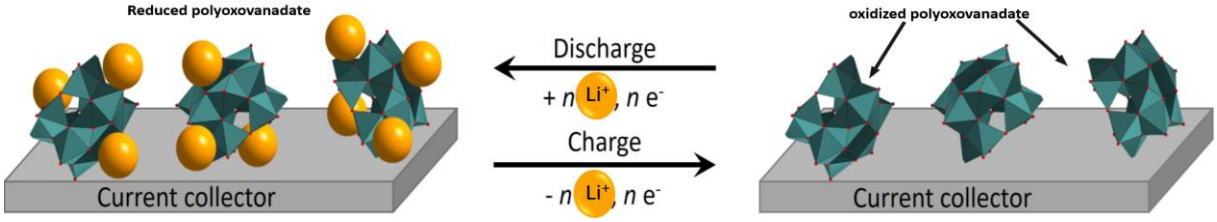

Figure 11: Schematic representation of the charge-discharge mechanism in polyoxovanadate molecular nanostructure-based cathode material in lithium-ion batteries.[27]

However, the utilization of POV clusters in battery technology is still limited. Recent studies have identified the decavanadate cluster $X_6[V_{10}O_{28}] \times xH_2O$ (where X can be Li or Na, x=9-16) as a promising cathode material in LIBs. Thermally treated $Li_6[V_{10}O_{28}]$ demonstrated the maximum discharge capacity of 400 mAh g^{-1} but suffered from low cyclic stability, indicating an irreversible redox reaction during battery cycling.[85] Further investigation revealed that the initial structure of decavanadate $Li_6[V_{10}O_{28}].16H_2O$, which consists of the $[V_{10}O_{28}]^{6-}$ anionic form with 10 edge-shared $[VO_6]$ units, transforms into two solid-state oxides, LiV_3O_8 and $LiVO_3$, upon heat treatment.[86] This structural rearrangement is detrimental for battery electrodes based on POV, as it causes the decomposition of the POV nanostructure, adversely affecting cyclic stability. Therefore, it is important to investigate the recent developments in POV nanoclusters, specifically the use of heterometal functionalization (e.g., K, Ca, Zn) and the integration of large decavanadate-derived frameworks (e.g., $\{V_{18}\}$) into redox-active electrodeposited thin film in a non-aqueous medium. Such research should be explored to achieve more structural stability and highly redox active POV composites for energy storage. This thesis presents innovative approaches for effectively immobilizing high-performance POV nanostructures, aiming to prevent the dissolution or transformation of POV nanostructure into non-redox active composites during energy storage applications.

1.4.3 Electrochemical double-layer supercapacitors (EDLSCs) and pseudocapacitors

High-performance supercapacitors (SCs) are among the most researched energy storage systems due to their exceptional power density, electrochemical stability, and remarkable charge-discharge cycle performance. The working principle of SCs is categorized into two distinct charge storage processes: electric double layer (EDL) and pseudocapacitive charge

storage

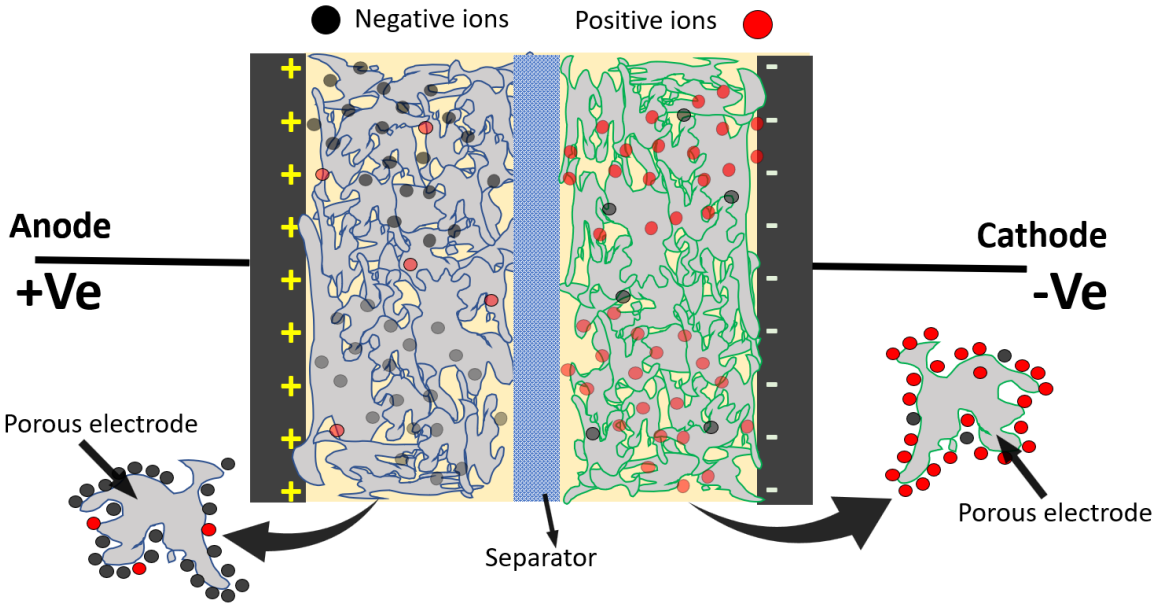

Figure 12: Schematic view of a symmetric supercapacitor at a charged state.

mechanism. In an electric double-layer supercapacitor (EDLSC) device, electrical energy storage is achieved through electrostatic charge separation through the formation of an electrochemical double-layer at the interface between the porous electrode and electrolyte.[87] On the other hand, pseudocapacitance occurs as a result of Faradic redox reactions that take place between the surface of the electrode and electrolyte species.[88,89] The surging demand for smaller and more compact energy storage devices has positioned high-performance EDLSCs as an ideal choice, considering their high-power density, enhanced electrochemical stability, and outstanding cyclic performance.

As depicted in **Figure 12**, the important components of EDLSC include a high electron/ion conductive porous carbon electrode and electrolyte ions, with charge storage accomplished by the non-faradaic fast adsorption/desorption of oppositely charged ions on the electrode surface. However, active carbon electrodes exhibit low theoretical capacitance and limited energy density due to intrinsic structural modification or electronic deterioration in the presence of strong electrolytes.[90] The electrode's specific surface area is essential to the overall performance of EDLSCs. A large specific surface area and good porosity allow for the diffusion of oppositely charged electrolyte ions into the electrode microstructure at high concentrations, enhancing the charge accumulation on the electrode surface and resulting in a high charge storage capacity.[91] Nevertheless, the low energy density of EDLSCs remains a challenge that restricts their use in various applications. Extensive research has been conducted to develop a

new class of electrode materials aimed at enhancing the electronic properties, charge storage capacity, and energy density of EDLSCs. The most effective electrode materials introduced to date include high surface area carbon, metal oxides, and conductive polymers.[92] For high-specific surface area carbon materials, several types, such as graphene-based electrodes, and carbon nanotubes (CNTs), have demonstrated exceptional performance.[93] Similarly, metal oxide-based materials like MnO_2 and RuO_2 exhibited good electrode conductivity and improved capacitive performance as EDLSC electrodes.[94] Conductive polymers such as polyaniline (PANI), polypyrrole (PPy), and polythiophene offer comparatively lower internal resistance and stable electrochemical performance.[95] Current research is increasingly focusing on developing hybrid electrodes that combine the advantageous properties of these materials while maintaining low costs. The integration of high-specific surface area carbon materials with electrochemically active metal oxides presents a promising hybrid material for supercapacitor electrode materials.

1.4.4 POM Composites for high-performance supercapacitor electrodes

Polyoxometalates bridge the gap between the high specific surface area material and metal-oxides-based electrode materials for supercapacitors, offering good electrochemical stability, flexible structural modifications, and significant heterometal functionalization. Several techniques have been reported to integrate redox-active polyoxometalate composites into the porous microstructure of carbon materials.[96] Skunik et. al. demonstrated that adsorption of Keggin-type polyoxometalates on MWCNT substrate effectively doubled the overall capacitance and specific energy density, attributed to the significant combination of EDL and pseudocapacitance, resulting in multi-electron transfer.[97] Similarly, the P_2Mo_{18} incorporated activated carbon (AC) electrode enhanced capacitance by 51% compared to pristine AC electrode, also exhibiting outstanding cyclic stability.[98] These approaches indicate that the integration of POMs into the carbon matrix not only enhances capacity but also provides more stable cyclic performance and improved operating voltage, contributing to higher energy density. POM-modified electrodes typically exhibit a combination of EDL with pseudocapacitance, thanks to their exceptional ability to undergo fast and reversible redox reactions at the interface between the electrode and the electrolyte.[99] Several other methods, such as chemisorption and electrodeposition, have been reported to significantly incorporate POM materials into versatile carbon substrates to improve performance.[100] Although numerous studies have focused on Keggin-type Mo and W-based POM materials, vanadium-

based POMs have not been explored extensively, despite their rich redox activity and multi-valance properties. Recent studies in polyoxovanadate chemistry have demonstrated significant potential for these nanocomposites as supercapacitor electrode material.

In this study, we have demonstrated a simple and cost-effective strategy to enhance the capacitive charge storage performance of a highly porous LIG graphene nanostructured surface by embedding $K_5\{V_{12}\}$ nanocluster. This potassium-enriched POV nanocluster deposition enhanced the number of pseudocapacitive active sites of the graphene surface, facilitating a reversible redox process for rapid charge storage. During the electrochemical cycling, the $K_5\{V_{12}\}$ modified electrode exhibited stable vanadium complexes that effectively prevented the LIG substrate from restacking and degrading into an amorphous carbon structure during charge-discharge cycles.

2. Objective

Vanadium-based POM materials gained significant attention in energy storage applications due to their structural versatility and unique redox properties. The POV structures, composed of $[VO_5]$ or $[VO_6]$ polyhedral units, exhibit stable molecular frameworks with mixed valance vanadium centers (V^{5+}/V^{4+}). This multivalent nature of POVs confers excellent electrochemical stability, enabling reversible multi-electron transfer without compromising the structural integrity of the cluster. Nevertheless, solid-state POVs encounter critical challenges in energy storage systems, primarily due to their instability in solid form and high solubility in electrolytes.

We recently reported a 1D dodecavanadate chain cluster. The dodecavanadate cluster derived from the $(DMA)_2[V_{12}O_{32}Cl]_3(=(H_2NMe_2)_2$**{V12}**) precursor molecular structure where (H_2NMe_2) placeholder can be replaced with s-, d- or f-block. This method allowed a systematic way to introduce metallic cations to improve their electrochemical properties and molecular stability.

In this study, we report the direct immobilization and electrodeposition of reduced POV-based thin film on a conductive substrate, aiming to enhance their redox activity and electronic structure for reversible multi-electron storage.

The following key areas are described in detail in this thesis work:

1) Reversible electrodeposition of potassium-enabled POV film on the conductive surface:

This methodology was further expanded by incorporating K^+ ions into the POV framework, resulting in the formation of a complex three-dimensional structure through the coordination of K^+ ions within and adjacent to the specific binding site. This coordination allowed for the stabilization of more than two K^+ ions, yielding a cluster with the sum formula of $K_5(CH_3CN)_3[V_{12}O_{32}Cl]$ (denoted as $K_5\{V_{12}\}$). Unlike previously reported di-metal functionalized clusters, this approach enables a reduction step for the introduction of additional heterometallic cations. In this study, we investigated the possible derived reduction of $K_5\{V_{12}\}$, hypothesizing that this reduction could enhance the interaction between the negatively charged POV cluster and the charge-compensating K^+ cations, thereby facilitating electrodeposition. The reduction-induced deposition of POV-based thin films was systematically studied in the

presence of alkali cations. Our detailed electrochemical analysis reveals that the process involves a multi-electron reduction of the cluster. This investigation was supplemented by a thorough characterization of the deposited films, focusing on their morphology and thickness.

2) Electronic and electrochemical tunning of porous LIG substrate *via* polyoxovanadate nanocluster deposition:

In this work, a sustainable approach was employed to tune the electronic and electrochemical properties of hierarchically porous LIG substrates. The previously established electrodeposition technique was applied, utilizing the redox-active $K_5\{V_{12}\}$ polyoxovanadate cluster on the highly porous, graphene-like LIG structure. Comprehensive characterization was conducted using micro-Raman spectroscopy and in-depth XPS analysis to elucidate both the deposition mechanism and electronic characteristics of the synthesized electrode. Detailed electrochemical measurement provided an in-depth understanding of the physicochemical properties, structural tunning, and redox behavior of the electrochemically deposited $K_5\{V_{12}\}$. The $K_5\{V_{12}\}$-modified LIG electrode exhibited enhanced redox activity, increasing the number of pseudocapacitive active sites and facilitating reversible redox reactions, which led to a significant improvement in the rapid charge storage capacity.

During the electrodeposition process, the reduction-induced growth of potassium-enriched $K_x\{V_{12}\}$ complexes was observed on the conductive surface, promoting the formation of mixed-valence vanadium centers (V^{5+}/ V^{4+}). This multivalent property of the POV clusters, combined with their incorporation of transition metals, has proven advantageous in various electrocatalytic applications.[101] The deposition of the reduced $K_5\{V_{12}\}$ on the LIG surface further enhanced the electrocatalytic activity of the electrode, leading to the formation of vanadium-based oxosulphato/hydroxysulphato complexes with electrolyte anions. These complexes effectively prevented the restacking of the LIG graphene substrate, which could degrade into an amorphous, soot-like carbon structure during repeated charge-discharge cycles. As a result, the $K_5\{V_{12}\}$ modified electrode maintained high redox activity, contributing to a significant enhancement in the specific charge storage capacity.

3) Direct immobilization and electrochemical performance of reduced potassium-assisted polyoxovanadate thin films on commercial carbon-coated current collector Al foil (C-Al):

To investigate the potential of POVs as an electrode material in battery applications, we focused on in-situ functionalization of a large vanadium-based cluster (such as $\{V_{18}\}$) with potassium cations via electrodeposition at different potentials, aiming to optimize its structural stability. The synthesized $K_x\{V_{18}\}$ film demonstrated significant structural and electrochemical enhancement, attributed to the electrodeposition process. A thin $K_x\{V_{18}\}$ film was successfully deposited directly onto commercially available C-Al foil without the need for additional carbon additives or binders. This potassium-bridged POV film exhibited the partial reduction of the vanadium center from V^{5+} to V^{4+}, and in some cases, from V^{5+} to V^{3+}, facilitating reversible multiple electron storage while maintaining structural integrity.

Preliminary electrochemical testing revealed that the $K_x\{V_{18}\}$ thin film achieved a high specific capacity of 240 mAh/g at a current density of 50 mA/g. Additionally, the film's structural integrity was evaluated over 1000 GCD cycles at 100 mA/g, demonstrating nearly 50% capacity retention, equivalent to 64 mAh/g. This indicates decent redox reversibility and sustained electrochemical performance. These findings define the potential of $K_x\{V_{18}\}$ film for application as stable and high-performance cathode materials in lithium-ion batteries.

3. Results and Discussion

3.1 Reversible electrodeposition of $K_5\{V_{12}\}$ for multi-electron storage (NA1)

In this approach the molecular tunning of a novel potassium-bridged decavanadate cluster $[K_{10}(V_{12}O_{32}Cl)_2].4.5\ CH_3CN = K_5\{V_{12}\}$, was accomplished *via* an electrodeposition method. This process enabled the formation of supramolecular nanostructured film growth on the conductive substrate in a non-aqueous medium. This method involved the re-introduction of the K^+ ions into the polyanionic POV clusters by generating electrostatic force at the surface of the working electrode. This approach resulted in a homogeneous film growth *via* the subsequent reduction of the $K_5\{V_{12}\}$ framework, which facilitated additional K^+ interactions within the modified POV cluster framework. Previous studies have reported the incorporation of di-metal ions within the decavanadate cluster without cluster reduction.[38] This study presents the first instance of reduction-induced $K_5\{V_{12}\}$ deposition, utilizing applied potential as the driving force.

3.1.1 Electrochemical characterization of the K_5V_{12} reduction

A comprehensive electrochemical analysis was conducted using a three-electrode cell configuration to characterize the reduction behavior of the synthesized $K_5\{V_{12}\}$ cluster. The cluster was dissolved in a non-aqueous, de-oxygenated supporting electrolyte solution prepared by dissolving 0.1 M $(nBu_4N)PF_6$ in acetonitrile solvent. The three-electrode cell setup consisted of a glassy carbon electrode as the working electrode, a Pt wire as a counter electrode, and a polished silver wire in a glass frit containing the supporting electrolyte solution as a quasi-reference electrode. The CV response was measured across three distinct potential windows to investigate the influence of the applied potential on the dissolved $K_5\{V_{12}\}$ cluster.

When the potential of the working electrode was swept from -250 to 500 mV vs. Ag^+/Ag, a notable reduction process was commenced at -100 mV vs. Ag^+/Ag, as depicted in **Figure 13a**. at this potential, the deposition of the reduced $K_5\{V_{12}\}$ on the working electrode surface was observed. Previously, the $\{V_{12}\}$ decavanadate precursor demonstrated electrochemical activity within the potential range of -500 to 500 mV vs. Ag^+/Ag, indicating a reversible reduction of the vanadium centers (V^{+5}/V^{+4}).[64] During the electrodeposition of $K_5\{V_{12}\}$, the successive reduction of the cluster facilitated the reduction of a few vanadium centers, along with the

strong interactions between K^+ ions and the reduced cluster species, leading to the formation of a complex supramolecular chain structure.

Further CV analysis revealed a prominent oxidation peak at -50 mV during the anodic sweep, suggesting strong oxidation and stripping of the deposited film. A comparable CV response was obtained at a slightly broader potential window of -500 to 500 mV vs. Ag^+/Ag, with higher peak intensities, confirming a higher concentration of the reduced species. Extending the potential range to -900 to 500 mV vs. Ag^+/Ag induced an additional reduction process, as indicated by a broad reduction peak at -500 mV. This suggests a further reduction of the deposited species, indicating structural modifications of the vanadate cluster. The distinct shift in the anodic peak potential indicates strong irreversibility of the deposited cluster species.

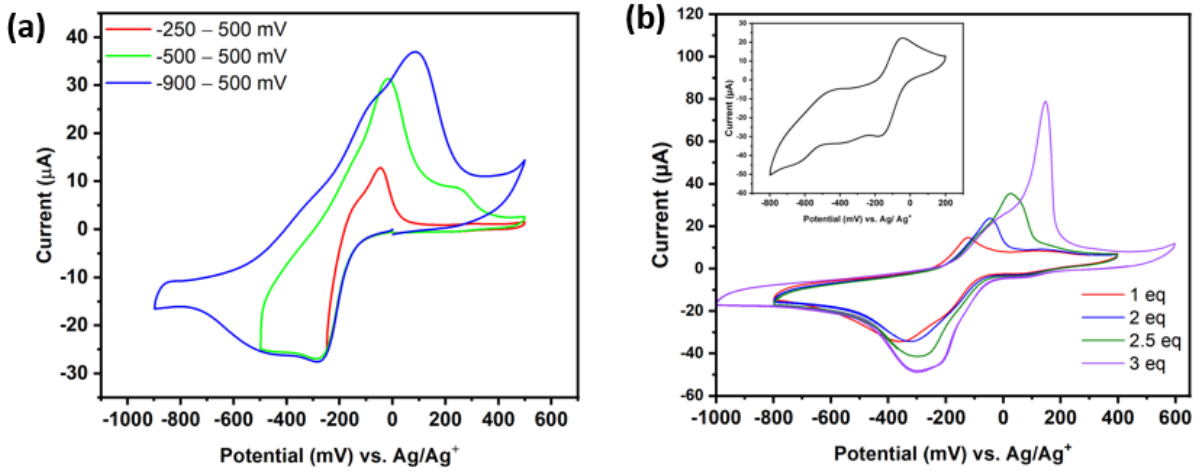

Figure 13: (a) CVs of $K_5\{V_{12}\}$ at different cathodic switching potentials in anhydrous, de-oxygenated acetonitrile containing 0.1 M (nBu$_4$N)PF$_6$ as supporting electrolyte salt, [$K_5\{V_{12}\}$]=0.5 mM **(b)** CVs of $\{V_{12}\}$; $((DMA)_2[V_{12}O_{32}Cl])^{3-}$ (containing 0.1 M (nBu4N)PF$_6$ as electrolyte salt) with different concentrations of KPF$_6$; scan rate: 100 mV/s; inset: CV of $\{V_{12}\}$; $((H_2NMe_2)_2[V_{12}O_{32}Cl])^{3-}$ in acetonitrile in absence of K^+ ions. Schematic figure 13 (a, b) is reproduced with permission copyrights from Wiley Library (2023)[102]

The presence of K^+ ions exerts a significant effect on the electrodeposition process of the vanadate cluster. To elucidate this effect, a series of CV measurements were conducted at varying concentrations of the K^+ in the electrolyte solution. Initially, the CV response for a non-functionalized $\{V_{12}\}$ cluster was recorded in a 0.1 M (nBu$_4$N)PF$_6$ electrolyte solution, revealing a quasi-reversible redox process at $E_{1/2}$= -150 mV vs. Ag^+/Ag, without any signs of deposition on the working electrode, as illustrated in **Figure 13b**. Subsequently, KPF$_6$ salt was incrementally added to the 0.1 M (nBu$_4$N)PF$_6$ electrolyte solution, and the CV response was recorded for each concentration, as shown in **Figure 13b**. A prominent broad peak emerged at -350 mV vs. Ag^+/Ag, corresponding to the successive interaction between potassium cations

and the vanadate cluster. Additionally, a strong oxidative peak appeared around E_{peak}= -123 mV vs. Ag^+/Ag during the anodic sweep, indicative of the reversible interaction between the cluster and K^+ ions. As the concentration of the K^+ increased from equation 1 to 2.5, the cathodic peak also increased, along with the broadening of the peak. This behavior suggests the occurrence of an electrodeposition process involving multiple electron transfers. The observed anodic peak shift following each addition of KPF_6 indicates that a higher concentration of K^+ results in a much stronger interaction with the reduced vanadate cluster.

3.1.2 Structural and elemental composition of reduced $K_5\{V_{12}\}$

To confirm the reversible electrodeposition and corresponding mass change on the working electrode surface as a function of the applied potential range, a detailed electrochemical quartz crystal microbalance (EQCM) measurement was performed. When the reduction of the $K_5\{V_{12}\}$ cluster was conducted up to the cathodic potential limit of -250 mV vs. Ag^+/Ag, a fully reversible mass deposition on the electrode surface was observed, as presented in **Figure 14.** Similarly, when the cathodic potential was extended to -500 mV vs. Ag^+/Ag, cluster deposition followed by stripping was detected. However, at this high negative potential, the deposited mass was nearly doubled compared to that at the lower negative potential of -250 mV, demonstrating that the applied potential has a significant influence on the deposited mass.

During the anodic sweep, the deposited film is entirely stripped from the electrode surface as the potential moves toward the anodic range. This is supported by the nearly identical electrochemical responses observed between the first and fifth CV cycles, indicating an electrochemical equilibrium process characterized by reversible deposition and stripping within the potential range of -500 to 500 mV vs. Ag^+/Ag. However, when the electrode potential is extended to a more negative value of -900 mV vs. Ag^+/Ag, a distinctly irreversible mass deposition occurs on the electrode surface, which cannot be reversibly extracted during the subsequent anodic sweep up to 500 mV vs. Ag^+/Ag. This suggests that the reduction of the cluster at more negative potentials leads to structural modifications that hinder oxidation and reversible stripping.

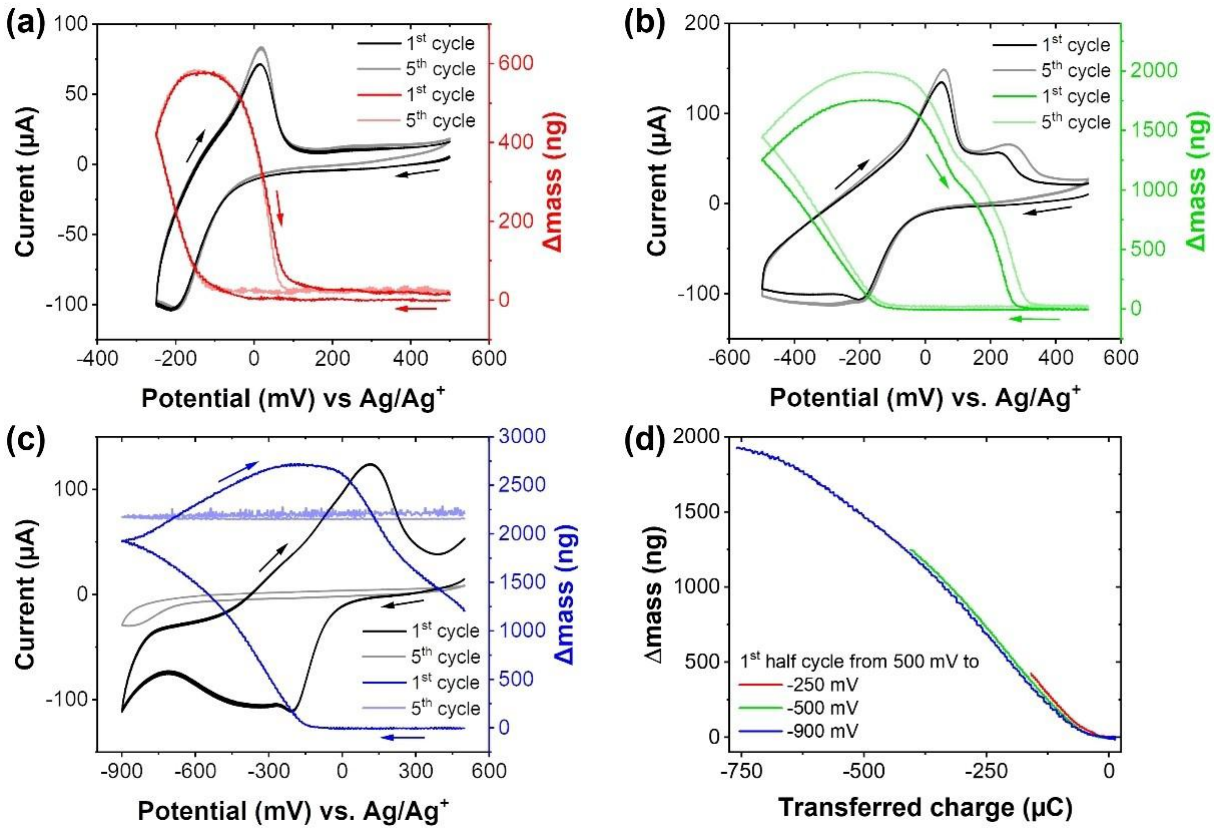

Figure 14: EQCM measurement of $K_5\{V_{12}\}$ (0.5 mM in acetonitrile containing 0.1 M $(nBu_4N)PF_6$ while using cyclic voltammetry (scan rate=100 mV/s) in the potential ranges of **(a)** 500 mV to -250 mV, **(b)** 500 mV to -500 mV, and **(c)** 500 mV to -900 mV vs. Ag^+/Ag with the corresponding mass changes for the first and fifth cycle, respectively. **(d)** Deposited mass vs. transferred charge during the first half cycle for the three potential ranges shown in a), b), and c). Schematic figure 14 is reproduced with permission copyrights from Wiley Library (2023)[102]

Furthermore, the charge transfer behavior during the electrodeposition process was analyzed, as illustrated in **Figure 14d** shows the interconnection between deposited mass and charge transferred. When the cluster was reduced up to -500 mV vs. Ag^+/Ag, a minor deviation in the curve was observed, indicating a net electron transfer of 4.9 e^-. This is attributed to charge compensation due to the possible interaction of additional K^+ ions with the reduced POV framework. In contrast, the maximum electron transfer of 6.32 e^- was recorded when the cluster reduced at -900 mV vs. Ag^+/Ag, suggesting the highest degree of interaction between K^+ and the reduced cluster structure, which potentially leads to structural deterioration.

To investigate the elemental composition and the oxidation state of the reduced cluster film at different cathodic potentials, X-ray photoelectron spectroscopy (XPS) was employed. For the pristine $K_5\{V_{12}\}$ cluster, all vanadium centers are identified to be in the V^{5+} oxidation state, and potassium incorporation occurred without reducing these vanadium centers, as shown in **Figure 15a**. The detailed elemental spectra reveal that the $V2p_{3/2}$ peak at a binding energy of 517 eV

deconvolutes into two peaks: a major peak at ~517 eV, confirming the presence of V^{5+} oxidation state, and a small signal at ~516 eV, corresponding to the V^{4+} oxidation state for the electrodeposited film at -250 mV vs. Ag^+/Ag. Additionally, a well-defined $K2p_{3/2}$ peak confirms the integration of potassium following film deposition.

From the XPS data, the V: K atomic ratio was calculated to be 1: 0.72 for the deposited film at -250 vs. Ag^+/Ag, indicating that each $\{V_{12}\}$ cluster interacted, on average, with approximately 8.6 K^+ ions. This suggests that the reduction of each $\{V_{12}\}$ cluster framework is adjusted with the additional of around 3.6 K^+ ions, enabling an approximate transfer of 3.6 electrons compared to the native $K_5\{V_{12}\}$ cluster. The peak fitting data estimated a V^{4+}/ V^{5+} ratio of approximately 0.3:1, clearly indicating that each additional K^+ interaction is associated with subsequent reduction of the vanadium center within the $\{V_{12}\}$ cluster.

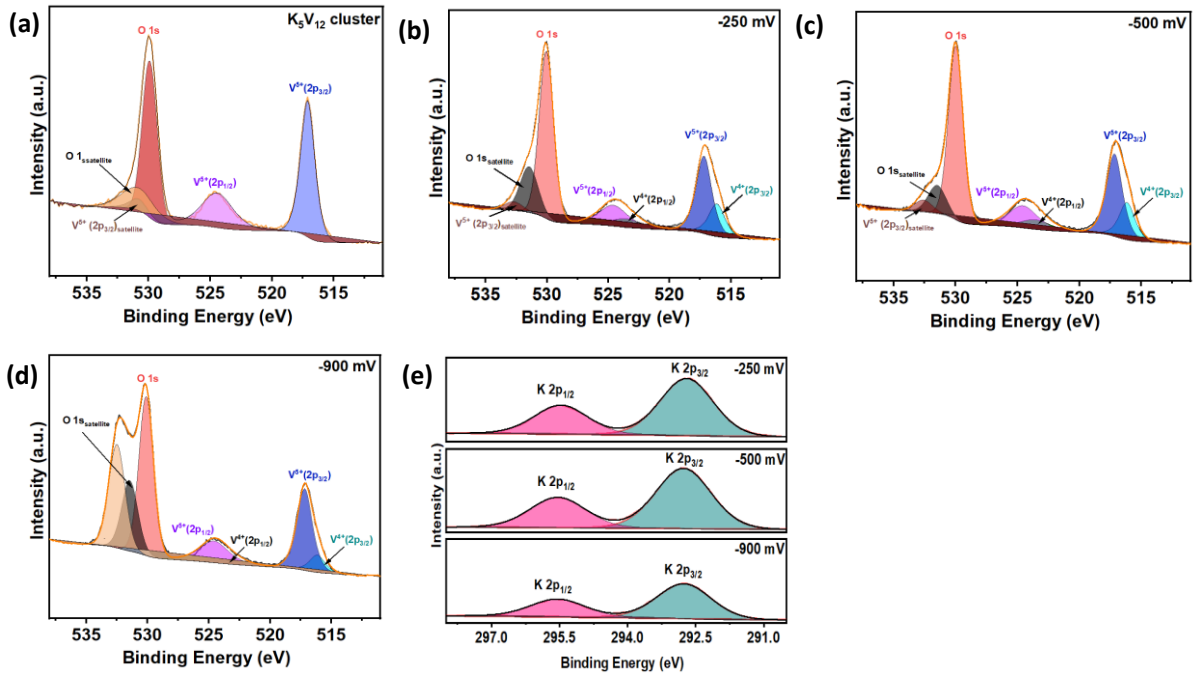

Figure 15: High-resolution XPS spectra of **(a)** $K_5\{V_{12}\}$ cluster and reduced $K_5\{V_{12}\}$ films at reduction potential **(b)** -250 mV, **(c)** -500 mV, and **(d)** -900 mV vs. Ag/Ag+, and **(e)** the K 2p XPS spectrum of the deposited films. Schematic figure 15 is reproduced with permission copyrights from Wiley Library (2023)[102]

For the film deposited at -500 vs. Ag^+/Ag, a similar electrochemical response was observed, with the calculated V: K atomic ratio of 1: 0.78, slightly higher than at -250 mV. This ratio indicates that approximately 9.4 K^+ ions are incorporated per $\{V_{12}\}$ cluster unit, corresponding to an estimated transfer of about 4.4 electrons. The V^{4+}/ V^{5+} ratio was determined to be approximately 0.4: 1, suggesting that reduction of $\{V_{12}\}$ at this potential facilitates nearly 4.8 electrons of transfer. By combining these quantitative XPS elemental analysis results with the

EQCM findings, the possible chemical formulas of the deposited films were deducted as $K_{8.64}[V_{12}O_{32}Cl]$ for the deposition at -250 mV vs. Ag^+/Ag and $K_{9.36}[V_{12}O_{32}Cl]$ for deposition at -500 mV vs. Ag^+/Ag.

At a more negative potential of -900 mV vs. Ag^+/Ag, the film exhibited strong irreversible deposition, and electrochemical measurements indicated an additional reduction phenomenon at this potential. The high-resolution XPS spectra of $V2p_{3/2}$ revealed a V^{4+}/V^{5+} ratio of 0.18: 1, indicating a maximum interaction of 11.6 K^+ ions per $\{V_{12}\}$ cluster. This high concentration of potassium within the reduced film suggests a significant irreversible structural arrangement, contributing to a strongly electrochemically deposited nanostructured film.

Morphological characterization of deposited films

The morphology of the deposited films was examined using SEM, EDX, and AFM analysis. SEM images confirm the uniform deposition of the reduced $K_5\{V_{12}\}$ film at all three different potentials -250 mV, -500 mV, and -900 mV vs. Ag^+/Ag (see **Figure 16(a-c))**. The chemical composition of the deposited film, as obtained from the EDX mapping, showed that the major components originated from the native $K_5\{V_{12}\}$ cluster.

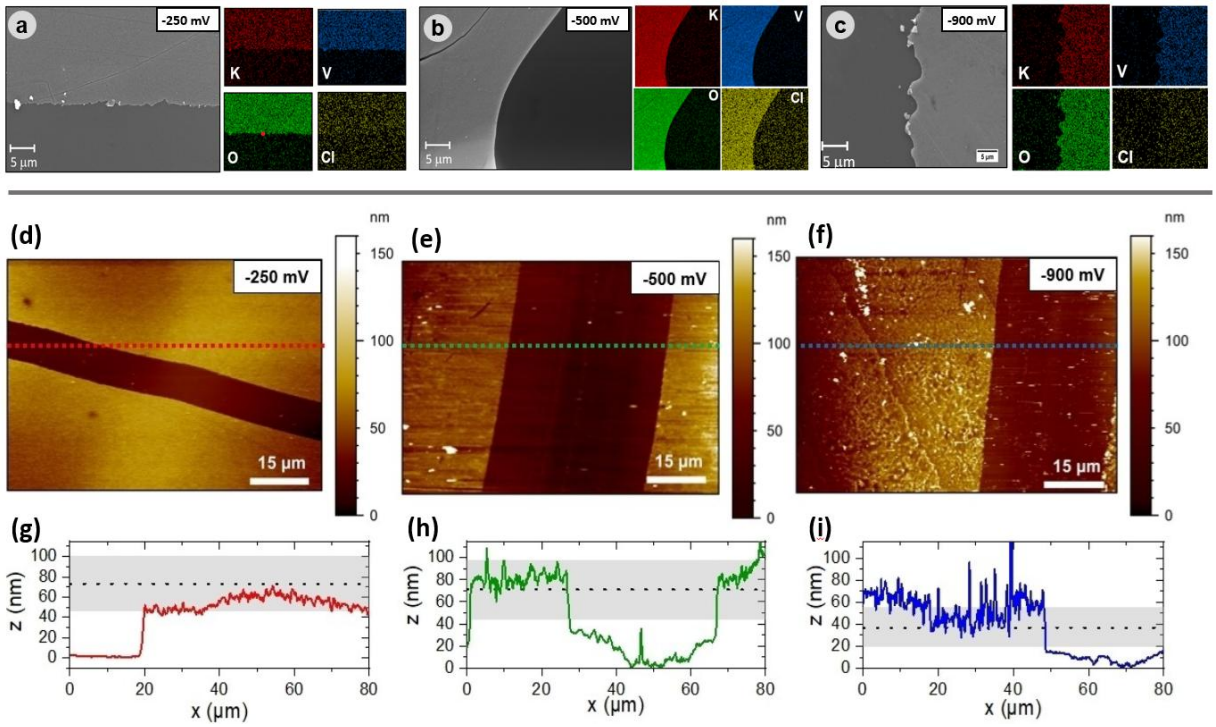

Figure 16: EDX elemental mapping of the $K_5\{V_{12}\}$ based film deposited at **(a)** -250 mV, **(b)** -500 mV, and **(c)** -900 mV vs. Ag^+/Ag. AFM topography images of $K_5\{V_{12}\}$ films deposited on glassy carbon at **d)** -250 mV, **e)** -500 mV, and **f)** -900 mV vs. Ag^+/Ag: images were recorded in contact mode in acetonitrile. Corresponding line scans **(g-i)** extracted from the topography images at the position marked by the dotted lines; dotted black lines represent average film thicknesses with standard deviations

depicted as gray areas (*n*=30 profiles). Schematic figure 16 is reproduced with permission copyrights from Wiley Library (2023)[102]

To further understand the influence of the applied potential on the thickness and uniformity of the deposited films, AFM measurements were employed. **Figure 16 (d-f)** shows the topography images of films deposited at three different potentials. At -250 mV vs. Ag^+/Ag, the film exhibited a uniform morphology with surface roughness (S*a*) = 9 ± 2 nm (n = 5, area = 625 μm^2). However, film deposited at more negative potentials of -500 and -900 mV vs. Ag^+/Ag showed less uniformity with roughness values of S*a* = 45 ± 13 nm (n = 4) and S*a* = 32 ± 19 nm, (n = 5), respectively, for the same areas of 625 μm^2. Also, the line profiles obtained from topography images defined the thick film deposition of 73 ± 27 nm occurred at a starting negative potential of -250 mV vs. Ag/Ag^+, while 71 ± 27 nm and 37 ± 18 nm film deposited at -500 mV and -900 mV vs. Ag^+/Ag respectively, as shown in **Figure 16 (g-i)**.

3.1.3 Formation of a highly redox active thin film of K_5V_{12}

In this study, we present the first demonstration of the reversible electrodeposition of a novel molecular potassium-functionalized vanadium oxide cluster. Comprehensive electrochemical and material characterization reveals that a highly stable potassium-incorporated dodecavanadate ($K_5\{V_{12}\}$) thin film can be achieved through systematic electrochemical deposition. The deposition is significantly influenced by the selected potential window, showing strong reversibility at a potential range below -500 mV vs. Ag^+/Ag, which is advantageous for multi-electron storage systems. The controlled mass deposition as a uniform film on a current collector presents promising potential for sustainable battery electrode application.

We employed a cyclic step chronoamperometry (CSCA) pulsed deposition method to precisely control mass deposition at the specific potential of -250 mV, -500 mV, and -900 mV vs. Ag^+/Ag onto a carbon-coated aluminum foil (C-Al) foil. We used stepwise cyclic deposition where the deposition potential was applied for 120 seconds followed by a 60-second rest at 0 V vs. Ag^+/Ag to mitigate diffusion limitation during electrodeposition. **Figure 17** illustrates the pulsed profiles for each potential (-250 mV, -500 mV, and -900 mV vs. Ag^+/Ag). Initially, for deposition, ten consecutive pulses were applied for each deposition potential, and as the reduction potential increased from -250 mV to -900 mV vs. Ag^+/Ag, the corresponding reduction current response was notably affected across the three deposition potentials.

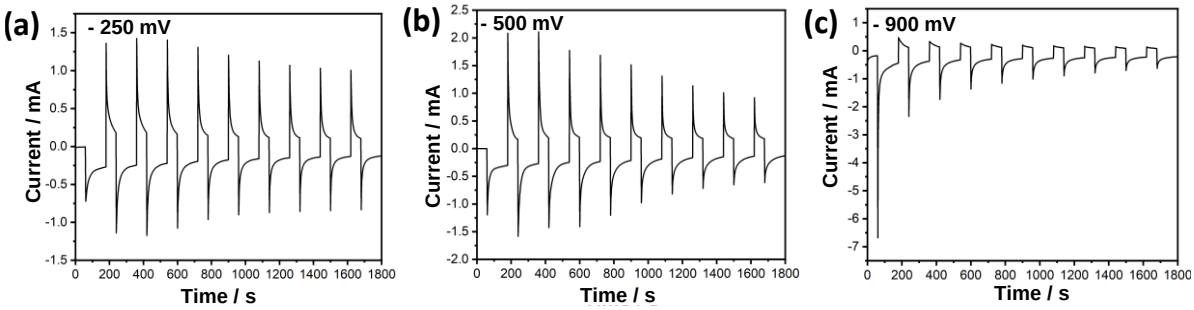

Figure 17: pulsed electrodeposition profile of $K_5\{V_{12}\}$ at three different reduction potentials **a)** -250 mV, **b)** -500 mV, and **c)** -900 mV vs. Ag^+/Ag, (conditions: dry, deoxygenated acetonitrile containing 0.1 M $(nBu_4N)PF_6$ as electrolyte salt and $[K_5\{V_{12}\}] = 0.5$ mM)

We systematically examined the effect of applied potentials and the number of deposition pulses on the thickness of the deposited $K_5\{V_{12}\}$ film. As shown in **Figure 18**, the film deposited at -250 mV vs. Ag^+/Ag exhibited an average thickness of approximately 600 nm, which progressively increased to around 920 nm as the applied potential became more negative, reaching -900 mV vs. Ag^+/Ag. A similar trend was observed with an increase in the number of deposition pulses, as the pulse count rose from 3 to 30, a significant increase in film thickness was observed, indicating enhanced mass loading with extended deposition duration.

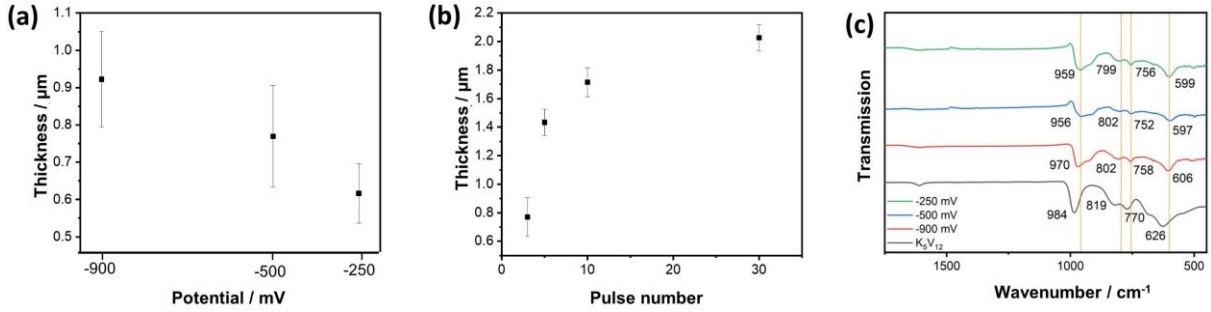

Figure 18: a) average thickness of the deposited film vs deposition potential, **b)** average thickness of the deposited film vs number of CSCA pulses, and **c)** FTIR spectra of the pristine $K_5\{V_{12}\}$ cluster as well as the deposited $K_5\{V_{12}\}$ film at -250 mV, -500 mV, and -900 mV vs. Ag^+/Ag.

The structural rearrangement of the deposited films was analyzed using FTIR spectroscopy, as shown in **Figure 18c**. The characteristic peak at 984 cm^{-1} corresponds to the V=O stretching vibration in the $K_5\{V_{12}\}$ cluster, while the bands at 626 cm^{-1} and 819 cm^{-1} are attributed to the V-O-V stretching mode.[103] However, the FTIR spectra of the deposited films revealed a noticeable shift of these peaks towards the lower wavenumber, indicating a change of the oxidation state of V, which is also confirmed by the splitting and broadening of the peak at around 1000 cm^{-1} after deposition.

These results were published in "Reversible electrodeposition of potassium-bridged molecular vanadium oxides: a new approach towards multi-electron storage." *Angewandte Chemie International Edition* 62, no. 35 (2023): e202306170.

For more detailed information see *Chapter 6.1*

3.2 Reduce K_5V_{12} nanocomposites on porous graphene for supercapacitor (NA2)

Laser-induced graphene is widely recognized as a promising electrode material for flexible supercapacitors (SCs) due to its exceptional physiochemical properties, including high electrical, porous micro/nanostructure, and favorable thermal and mechanical stability. LIG's effectiveness as a flexible electrode material for SCs and micro-SCs applications is attributed to the enhanced electrolyte ion diffusion through its porous surface. This work demonstrated a simple and effective method to improve capacitive charge storage performance by embedding vanadium oxide nanoclusters on a hierarchical porous LIG surface. Expanding on previous studies, we immobilized a high redox active $K_5\{V_{12}\}$ cluster onto the porous LIG nanostructured. The cyclic voltammetry (CV) technique was employed to achieve the successive deposition of reduced $K_5\{V_{12}\}$ cluster, synthesizing modified LIG electrodes with increased pseudocapacitive active sites, enhanced redox activity, and improved charge storage capacity.

3.2.1 Electrodeposition of $K_5\{V_{12}\}$ on nanoporous LIG surface

The schematic in **Figure 19** illustrates the key steps for synthesizing $K_5\{V_{12}\}$-modified LIG electrodes *via* electrodeposition. The electrochemical deposition process and subsequent supramolecular aggregation of $K_5\{V_{12}\}$ onto the porous LIG surface were initiated by dissolving the $K_5\{V_{12}\}$ in a potassium hexafluorophosphate (KPF_6)-based supporting electrolyte, enabling effective deposition onto the LIG surface.

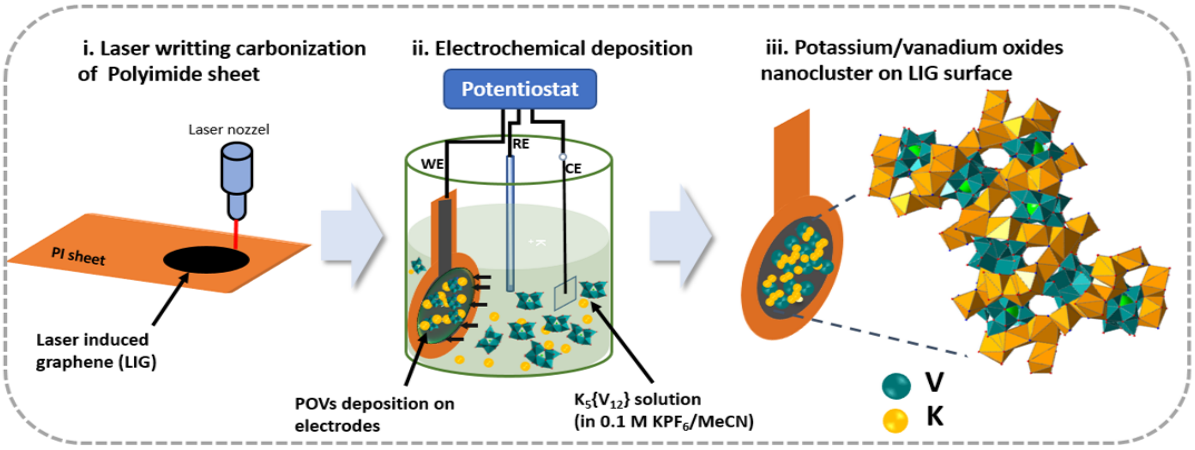

Figure 19: Schematic representation of LIG electrode fabrication and electrochemical immobilization of $K_5\{V_{12}\}$. Schematic Figure 19 is reproduced with permission copyrights from Wiley Library (2024)[104]

As previously discussed, a strongly electropositive cation, such as K^+, in the solvent enables controlled crosslinking with the vanadium oxide framework, resulting in a uniform deposition on the conductive electrode surface. In this study, the controlled electrodeposition of $K_5\{V_{12}\}$ within the nanoporous graphene network was accomplished by CV scans across the three different potential ranges: -250 – 250 mV, -500 – 500 mV, and -750 – 750 mV vs. Ag^+/Ag, at a scan rate of 100 mV/s. The experiments were conducted using a conventional three-electrode cell configuration using a non-aqueous ionic electrolyte solution (1 mM $K_5\{V_{12}\}$ in 0.1 M KPF_6 in MeCN).

The pristine LIG electrode initially rested at 0 mV vs. Ag^+/Ag, cycled towards the upper oxidative potential limit during the first sweep, and then reduced to the reduction potential limit. All the CVs that were measured showed a broad anodic peak at approximately 220 mV vs. Ag^+/Ag during the scan from the initial resting potential to the oxidative potential limit as shown in **Figure 20a**. This is in line with the solute $\{V_{12}\}$ cluster's characteristic reversible oxidation behavior. Similarly, during the cathodic sweep to -500 mV vs. Ag^+/Ag, a reduction process started at around 100 mV vs. Ag^+/Ag. This was caused by the partial reduction of the vanadium centers from V^{+5} to V^{+4} oxidation state **(Figure 20b).** This reduction process facilitates stronger interaction between the reduced anionic cluster framework $\{V_{12}\}$ and dissolved K^+ ions, which enhanced the cluster's insolubility and resulted in the electrodeposition of the POVs on the LIG surface. Increasing the potential window from -500 to -750 mV vs. Ag^+/Ag leads to an additional reduction feature in the CV at about -550 mV vs. Ag^+/Ag, possibly representing a further reduction of the already deposited cluster species.

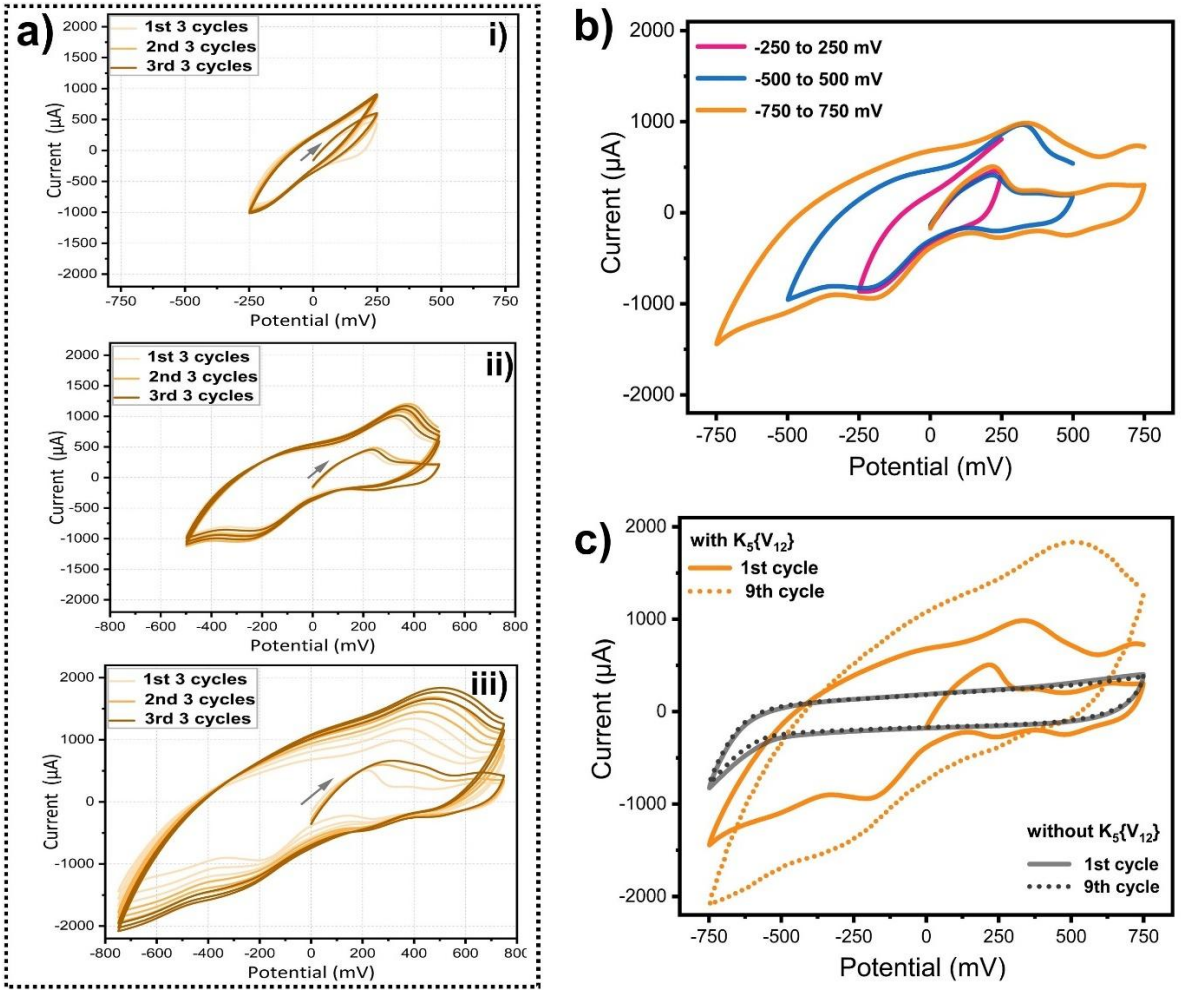

Figure 20: (a) cyclic voltammetry response during $K_5\{V_{12}\}$ deposition on LIG for three different potential windows: **(i)** -250 to 250 mV, **(ii)** -500 to 500 mV, and **(iii)** -750 to 750 mV (all potentials vs. Ag^+/Ag) (conditions: electrolyte: non-aqueous 1 mM $K_5\{V_{12}\}$/0.1 M KPF_6/MeCN, WE: LIG with 1 cm^2 surface area, RE: silver wire in 0.1 M KPF_6/MeCN, CE: Pt wire). **(b)** First cyclic voltammetry response at each given potential range of -250 to 250 mV, -500 to 500 mV, and -750 to 750 mV vs. Ag^+/Ag. **(c)** Comparison of first and ninth CV response of pristine LIG and K-POV-750 electrodes. Schematic figure 20 is reproduced with permission copyrights from Wiley Library (2024)[104]

This leads to an enhanced cathodic current observed for -750 mV vs. Ag^+/Ag potential range. In addition, the following cycles observe a significant shift of the anodic peak (from 220 to 340 mV vs. Ag^+/Ag), confirming that the charge compensating K^+ cations stabilized the reduced cluster, making its reoxidation more difficult. This aligns with earlier findings detailed in *Chapter 3.1*. The deposition of the cluster at a potential range of -750 to 750 mV vs. Ag^+/Ag shows multiple redox peaks during the first CV cycle. This confirms that the $K_5\{V_{12}\}$ cluster has distinct redox-active properties in a higher potential range. To investigate the influence of the deposition of the $K_5\{V_{12}\}$ cluster on the LIG electrode, a blank CV measurement was performed on a fresh LIG electrode under similar conditions but without the $K_5\{V_{12}\}$ in the

supporting electrolyte (only 0.1 M KPF_6/MeCN). More experimental details can be found in the supporting information. **Figure 20c** displays the comparison between the CV responses measured with and without $K_5\{V_{12}\}$ in the potential window of -750 to 750 mV vs. Ag^+/Ag. In the absence of $K_5\{V_{12}\}$, the measured CV response exhibits a charge storage behavior that is completely non-faradaic and without any redox features. This confirms that there are no redox-active species in the electrolyte. As a result, after nine consecutive cycles, no obvious changes were visible in the LIG electrode's CVs. In contrast, in the presence of $K_5\{V_{12}\}$ in the supporting electrolyte, the first cycles showed multiple redox peaks due to cluster reduction on the LIG surface. Notably, the LIG electrode with dissolved $K_5\{V_{12}\}$ exhibited two broad peaks after nine CV cycles at a reduction potential (E_1) of -300 and an oxidation potential (E_2) of 600 mV vs. Ag^+/Ag, confirming quasi-reversible charge storage. Consequently, the substantial increase in the area under the CV curve signifies a noteworthy alteration in the electrochemical performance of the LIG electrode due to $K_5\{V_{12}\}$ deposition at a higher overpotential within the range of -750 to 750 mV vs. Ag^+/Ag.

3.2.2 Material characterization of the POVs modified LIG electrode

The synthesized $K_5\{V_{12}\}$ modified LIG electrodes at the different CV potential ranges of -250, -500, and -750 mV are referred to as K-POV-250, K-POV-500, and K-POV-750. **Figure 21(a, b)** shows the scanning electron microscopy (SEM) images of a highly porous morphology of the pristine LIG substrate which is essential for the diffusion and deposition of the $K_5\{V_{12}\}$ cluster into the nanostructure of the surface upon application of cathodic potential. **Figure 21(c-f)** shows the morphology of the LIG surface after electrodeposition at different potentials, revealing no significant influence on the porous nanostructure of the LIG. These microstructural properties are preserved even after $K_5\{V_{12}\}$ deposition, hence the important mechanical properties are well preserved such as electronic conductivity and a microporous architecture that facilitates enhanced electron mobility and ionic conductivity. Furthermore, the elemental composition and confirm the homogeneous deposition of $K_5\{V_{12}\}$ on the LIG carbon nanostructure, energy dispersive X-ray (EDX) spectroscopy analysis was performed for all three synthesized electrodes. The detailed EDX mapping suggests the presence of primary cluster components, vanadium (V) and potassium (K), for all synthesized electrodes, also a slight variation to the K: V ratio, due to the different applied potential ranges **(Table 1)**.

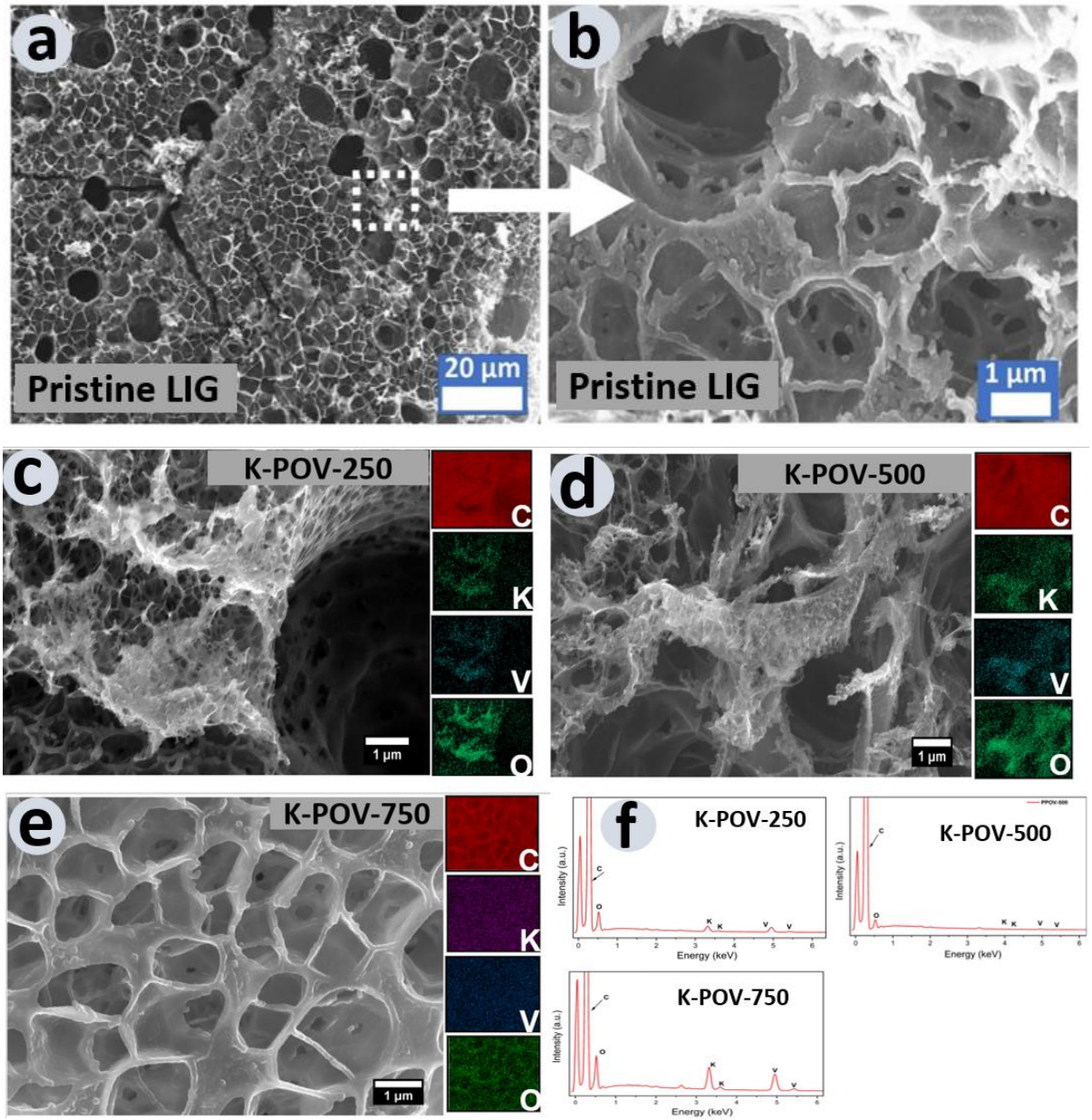

Figure 21: (a-b) SEM images of pristine LIG electrode, **(c)** SEM & EDX elemental mapping of K-POV-250, **(d)** K-POV-500 and **(e)** K-POV-750, and **(f)** EDX elemental spectra of all three synthesized electrodes. Schematic figure 21 is reproduced with permission copyrights from Wiley Library (2024)[104]

Table 1. Results of EDX analysis of synthesized K-POV electrodes.

Sample	K: V (Atomic %)
K-POV-250	0.45:1
K-POV-500	0.50:1
K-POV-750	0.52:1

Raman spectroscopic measurement was employed to study the possible structural and electronic changes in the LIG substrate after $K_5\{V_{12}\}$ deposition. The pristine LIG micro-Raman spectrum is shown in **Figure 22a**. The pristine LIG revealed three prominent Raman bands at ~1350 cm^{-1}, 1586 cm^{-1}, and 2695 cm^{-1}, assigned to the D, G, and 2D bands respectively, which are frequent in graphitic lattices.[105] The D band is caused by defects in the sp^2-carbon lattice, the G band by symmetric stretching, and the 2D band by second-order zone-boundary phonons. The D' band at 1620 cm^{-1}, is a defect-related vibrational mode and is observed as a shoulder band to the G band. Conventionally, the ratio of peak intensities I_D/I_G measures graphite layer disorder, and the measured value of 0.72 for LIG supports a nanocrystalline graphitic lattice.[106]

Additionally, graphitic material's electrical conductivity and ion mobility depend on sp^2 lattice structural properties. Hence it is crucial to quantify changes in the number of defects during electrochemical deposition of $K_5\{V_{12}\}$ and evaluate LIG electrode crystallinity after cycling. The quantification of defects in the graphitic lattice involves examining I_D/I_D' and D bandwidth concerning the G-band-width.[107,108]

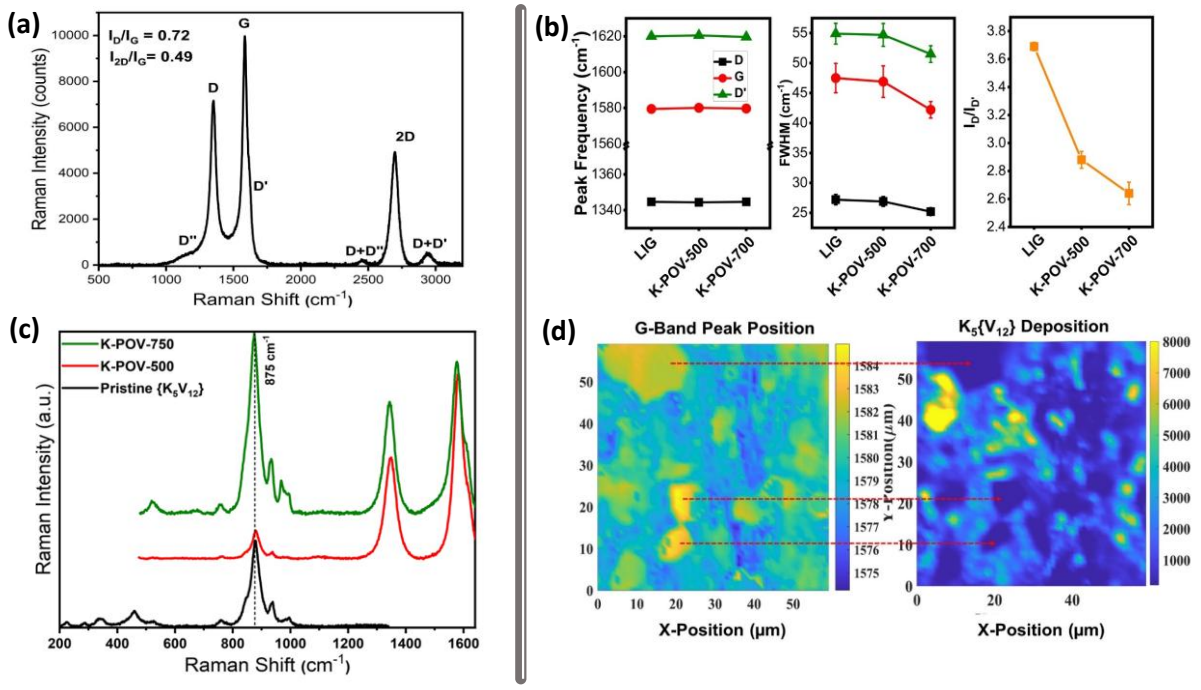

Figure 22: (a) micro-Raman spectrum of LIG electrode **(b)** comparison of Raman band parameters of unmodified LIG with K-POV-500 and K-POV-750 electrodes. **(c)** Raman spectra of pristine $K_5\{V_{12}\}$ cluster and K-POV-500 and K-POV-750 electrodes **(d)** Raman mapping of G band peak position and $K_5\{V_{12}\}$ deposition (from the intensity of the V-O stretch vibration at 875 cm^{-1}) for the synthesized K-POV-750 electrode, illustrating preferential deposition in the regions of low crystallinity region. Schematic figure 22 is reproduced with permission copyrights from Wiley Library (2024)[104]

A 60x60 mm^2 Raman imaging study was conducted to better understand the defect distribution in the graphitic lattice of the pristine LIG surface. The D, G, and D' bands' peak intensities,

locations, and widths (FWHM) were mapped and put in the histogram. The G and D bands were in the range of 1568–1586 cm^{-1} and 1335–1348 cm^{-1}, respectively.

The pristine LIG had an I_D/I_D' ratio of 3.69, indicating that grain boundary-type defects significantly affect LIG's nano-graphitic structure.[106,107] **Figure 22b** shows the evolution of Raman spectra peak positions (D, G, and D' band), FWHM, and I_D/I_D' peak intensity ratio for pristine LIG, K-POV-500, and K-POV-750 electrodes. These values were calculated by averaging Raman maps. Although the average peak frequency of all bands remains constant, $K_5\{V_{12}\}$ deposition displays a decreasing trend in FWHM and I_D/I_D' values with increasing deposition potentials. The I_D/I_D' ratio decreased from 3.69 (pristine LIG) to 2.88 and 2.66 for K-POV-500 and K-POV-750 electrodes, indicating the elimination of grain boundary defects in the nano-graphite lattice, likely improving LIG's electrochemical properties. The absence of sp^3-like defects or vacancies in LIG suggests that electrochemical deposition of $K_5\{V_{12}\}$ nanocluster was strongly physisorption in nature. Hence, the deposition and reduced $K_5\{V_{12}\}$ do not form direct covalent or ionic bonds with the graphitic lattice.

To explain deposited vanadate species, **Figure 22c** shows Raman spectra of the $K_5\{V_{12}\}$ cluster and compared with the synthesized K-POV-500 and K-POV-750 electrodes. The intense band at 875 cm^{-1}, together with weaker bands at ~938 cm^{-1} and 995 cm^{-1}, represents the stretching vibration of VO_6/VO_5 units in polyoxovanadates.[109] Similarly, the low-frequency bands of 400-600 cm^{-1} are associated with terminal V-O linkage stretching vibrations, while 200-400 cm^{-1} are associated with V-O-V bending modes. Firstly, the K-POV-500 and K-POV-750 electrodes represent a strong intense band at 875 cm^{-1}, indicating the presence of $K_5\{V_{12}\}$ nanocluster into the carbon surface. The K-POV-500 electrode's peak mapping also shows a heterogeneous spatial distribution of $K_5\{V_{12}\}$ on the surface. A comparison of the mapping result and G-band peak position indicates that $K_5\{V_{12}\}$ is located in locations with higher G-band peak frequencies, which correlate with higher graphitic lattice crystallinity. However, it can be said that the deposition started at the boundary between low- and high-crystalline regions, therefore the electrochemical deposition of $K_5\{V_{12}\}$ favors the less crystalline regions of the LIG surface. K-POV-750 mapping results **(Figure 22d)** show a similar tendency, with $K_5\{V_{12}\}$ deposition preference in low crystallinity locations. Preferential deposition reveals the produced LIG's physiochemical composition. In LIG, pristine crystalline segments exhibit high electrical and ionic mobility, while $K_5\{V_{12}\}$-deposited sections in K-POV-750 and K-POV-500 alter the chemical inertness of the sp^2 lattice.

X-ray photoelectron spectroscopy (XPS) characterization was utilized to investigate the surface layer's elemental composition and chemical condition. **Figure 23a** shows pristine samples (LIG and K-POV-750) recorded before electrochemical cycling. The obtained survey spectra of pristine LIG predominated the carbon (C1s peak at ~285 eV) and oxygen (O1s peak at ~532 eV) signals, as shown in **Figure 23a**. The $K_5\{V_{12}\}$ modified electrodes resulted in new characteristics survey spectrum, attributed to potassium (K2p peak at ~293 eV) and vanadium ($V2p_{3/2}$ peak at ~517 eV). In the C1s region, pristine LIG exhibits graphitic characteristics, with a dominant sp^2-C peak at 284.5 eV and a π-π* satellite at 290.9 eV **(Figure 23b)**. The LIG surface contributed large amounts of C-C/C-H, C-O, and C=O species, as shown by prominent peaks at 285.1, 286.6, and 288.3 eV, respectively.

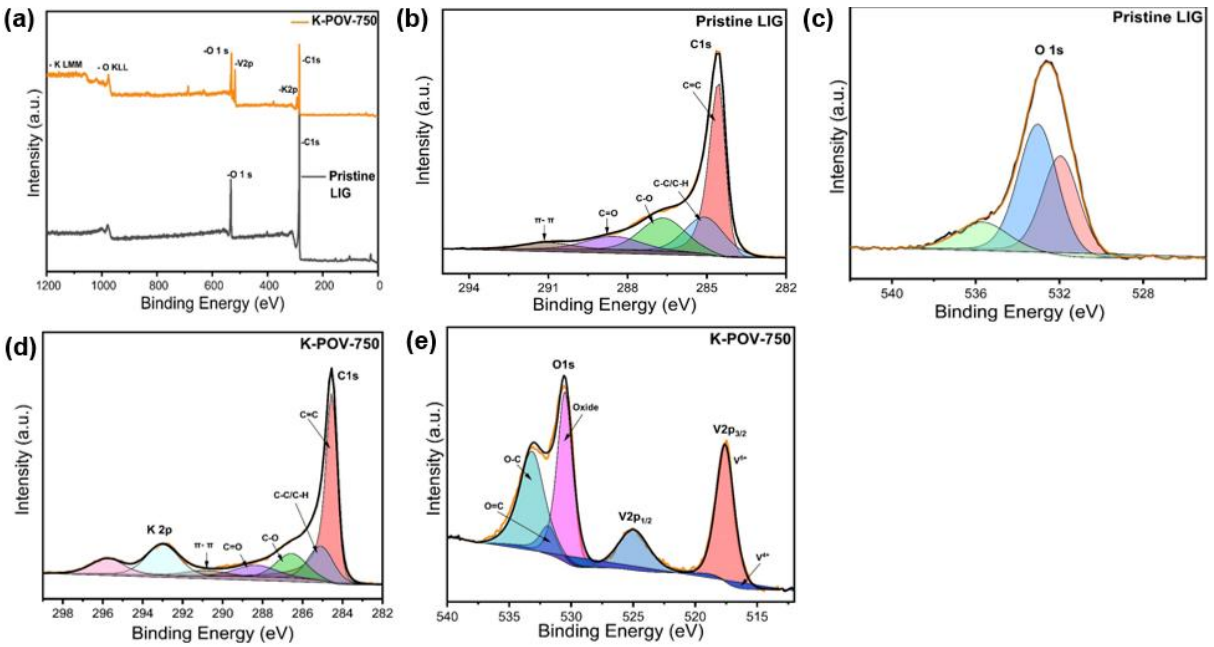

Figure 23: (a) XPS survey spectra of pristine LIG and K-POV-750 electrode, **(b, c)** detail spectra in the C1s and O1s region of pristine LIG and **(d, e)** K-POV-750 electrodes. Schematic figure 23 is reproduced with permission copyrights from Wiley Library (2024)[104]

Similar to the C1s region, the primary peaks in the O1s spectrum **(Figure 23c)** are attributed to C=O (531.9 eV) and C-O (533.1 eV) functional groups. K-POV-750's C1s detail spectrum **(Figure 23d)** features a similar C species as pristine LIG. The stronger reduction of the intensities of the C-C/C-H, C-O, and C=O contributions compared to the sp^2-C signal corroborates the preferential deposition of $K_5\{V_{12}\}$ clusters on defect sites. The C1s spectrum includes the K2p peak doublet of the K-POV cluster with the $K2p_{3/2}$ peak component at 293.3 eV. The binding energy of O1s and V2p peaks of K-POV-750 is shown in **Figure 23e**. In the peak fit, most vanadium is in oxidation state V^{5+} ($V2p_{3/2}$ peak at 517.6 eV), with a lesser

contribution from V^{4+} ($V2p_{3/2}$ peak at 516.3 eV). The obtained peak at 530.3 eV defines the strong contribution of oxygen atoms. **Table 2** presents pristine LIG and three $K_5\{V_{12}\}$-modified electrode quantitative analysis results. A study of $K_5\{V_{12}\}$ modified electrodes reveals that K-POV-750 has the highest V concentration, making $K_5\{V_{12}\}$ nanocluster deposition most promising when deposited at a large potential window.

Table 2. Results of quantitative XPS analysis for the expected elements in LIG and K-POV electrodes.

Sample	**C1s (%)**							**O1s (%)**			**V2p (%)**			**K2p (%)**
	C=C	C-C/C-H	C-O	O-C=O	Pi-Pi*	**sum**	C=O	C-O	oxide	**sum**	V^{5+}	V^{4+}	**sum**	
LIG	40.53	18.42	11.69	9.66	4.66	**84.96**	4.95	6.80	0	**11.75**	-	-	-	-
K-POV-750	33.83	10.63	9.09	5.77	2.81	**62.13**	2.06	10.5	11.44	**24.09**	7.64	0.16	**7.8**	**3.66**
K-POV-500	62.85	8.40	2.58	4.21	3.59	**81.63**	3.33	7.94	1.34	**12.61**	1.19	0.14	**1.3**	**1.16**
K-POV-250	50.41	12.52	3.74	5.42	3.07	**75.16**	5.47	7.50	3.42	**16.39**	2.55	0.37	**2.9**	**2.03**

3.2.3 Mechanism of charge storage of POVs modified LIG electrode

To obtain a comprehensive understanding of the charge storage mechanism, the kinetics of charge storage in the synthesized electrodes were systematically investigated through cyclic voltammetry sweeps. The CV measurements were conducted in a conventional three-electrode cell configuration, employing a standard Ag/AgCl electrode in an aqueous environment, a Pt wire as the counter electrode, and 1 M H_2SO_4 as the electrolyte. The optimized operating potential window was maintained between -300 to 1000 mV (vs. Ag^+/Ag). The quantitative analysis of the specific capacitance identified two distinct charge storage processes: the electric double-layer capacitance (EDLC), characterized by a non-faradaic current response associated with the capacitive behavior, and a diffusion-controlled current indicative of faradic intercalation and deintercalation of the electrolyte ions, as determined via Dunn's analysis.[110] The current response (I) at a given potential (V) was attributed to these two mechanisms and is described by the equation:

$$I(V) = k_1 v + k_2 v^{1/2} \quad (1)$$

Where v is the scan rate, k_1v defines the non-faradaic process and $k_2v^{1/2}$ represents the diffusion-controlled (faradic) contribution.[111,112] **Figure 24a** illustrates the voltage profile of the synthesized K-POV-750 electrode at a scan rate of 10 mV s^{-1}, highlighting the magnitude of the two-charge storage mechanism. At this scan rate, 95.5% of the total current response is attributed to the diffusion-controlled mechanism, indicating significantly enhanced ion diffusivity within the carbon matrix, while only a minor current response is due to EDLC-related capacitive behavior. A comparative analysis with the other synthesized electrodes (K-POV-250 and K-POV-500) reveals that the capacitive contribution to the charge storage becomes more prominent at increasing scan rates (**Figure 24 b-d**).

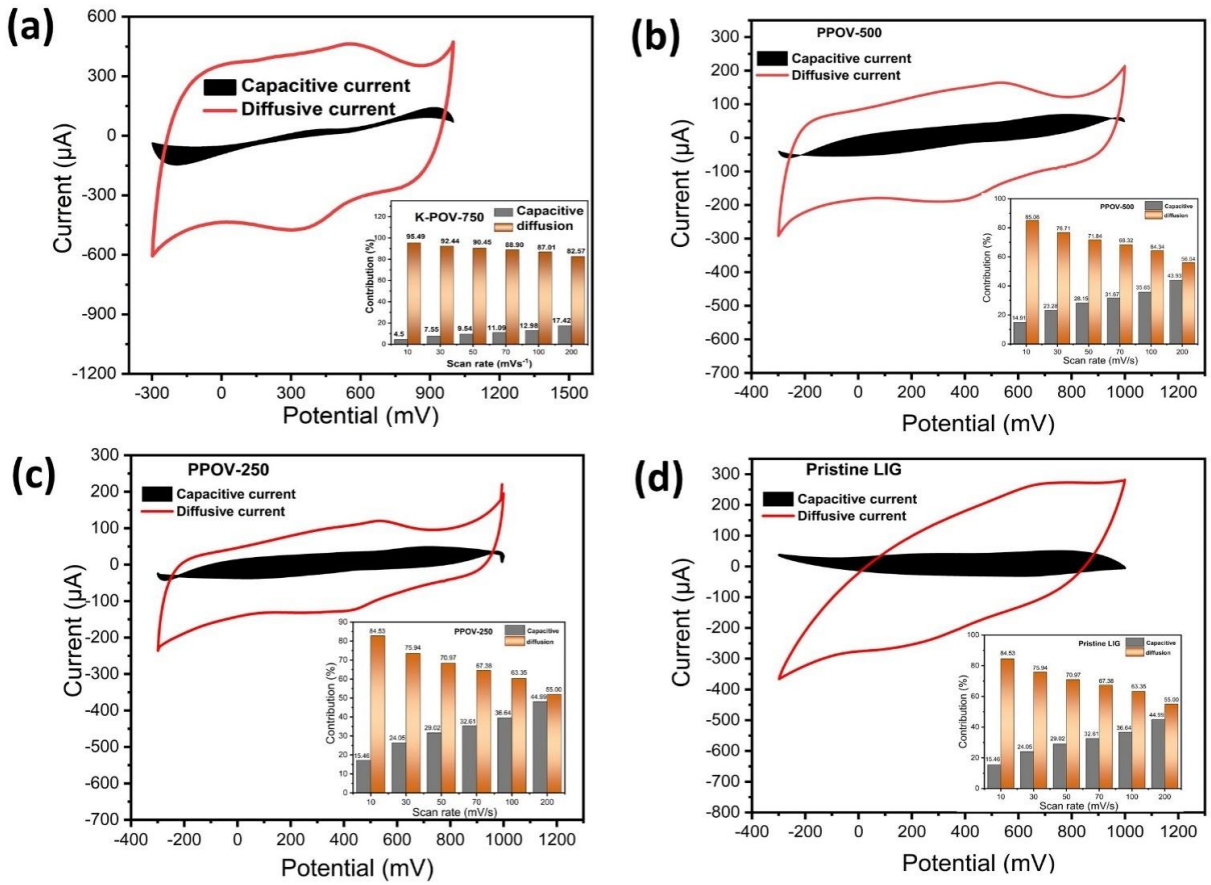

Figure 24: quantitative analysis of charge storage mechanism at 10 mV s^{-1} of **(a)** K-POV-700, **(b)** K-POV-500, and **(c)** pristine LIG electrode, and **(d)** K-POV-250, (inset: diffusion and capacitive controlled current response at different scan rates). Schematic figure 24 is reproduced with permission copyrights from Wiley Library (2024)[104]

These results are published in "Tuning the Electronic and Electrochemical Properties of 3D Porous Laser-Induced Graphene by Electrochemically Induced Deposition of Polyoxovanadate Nanoclusters for Flexible Supercapacitors." *Advanced Functional Materials* (2024): 2410943.

For more detailed information see *Chapter 6.2*

3.3 In-situ alkali metal functionalization of POVs nanocluster

3.3.1 In-situ alkali metal functionalization of {V_{12}}

As detailed in *Chapters 3.1 and 3.2*, the dodecavanadate cluster $K_5\{V_{12}\}$ showed excellent electrochemical performance within a specific reduction potential range, allowing for the formation of a highly redox-active thin film on a conductive surface. Previous studies used $K_5\{V_{12}\}$ as the active material to achieve a stable film deposition. However, the detailed electrochemical study revealed that the deposition occurs when the $\{V_{12}\}$ clusters dissolve into an ionic solution involving strong cations in the electrolyte. It was found that the $K_5\{V_{12}\}$ cluster dissolves as a polyanionic $\{V_{12}\}$ framework alongside K^+ cations. Electrodeposition of $K_5\{V_{12}\}$ occurs when sufficient electrostatic force is generated near the working electrode, including spontaneous reduction of the polyanionic $\{V_{12}\}$ cluster. This subsequent reduction of vanadium is facilitated by electrochemical interactions with K^+ cations, which enable the rearrangement of the clusters and promote its strong insolubility on the electrode surface.

Building on this observation, we further explored the in-situ potassium functionalization of $\{V_{12}\}$ dodecavanadate nanocluster using a similar electrochemical deposition method while ensuring infinite K^+ cations access. This time, the $\{V_{12}\}$ cluster was dissolved in a 0.1 M KPF_6/MeCN supporting electrolyte. The deposition was carried out with 3 consecutive CSCA pulses on the C-Al foil current collector. The pulsed deposition was performed at -250 mV, -500 mV, and -900 mV (vs. Ag^+/Ag), which were other experimental conditions as before. The

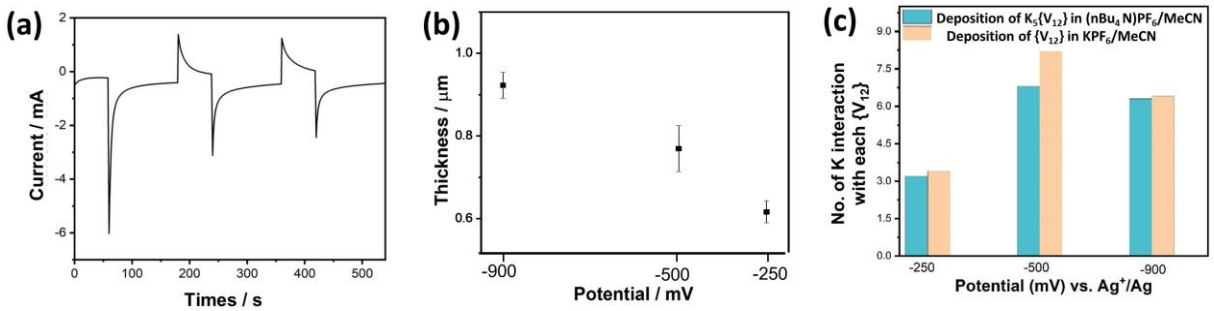

Figure 25: (a) pulsed electrodeposition profile of the $\{V_{12}\}$ cluster in a 0.1 M KPF_6/MeCN electrolyte solution, with three consecutive CSCA pulses at -900 mV vs. Ag^+/Ag, **(b)** average thickness of the deposited film as a function of the applied deposition potential, and **(c)** comparative analysis of the number of K interacting with each $\{V_{12}\}$ unit after pulsed deposition of $K_5\{V_{12}\}$ cluster in a 0.1 M $(nBu_4N)PF_6$/MeCN and $\{V_{12}\}$ cluster deposition in 0.1 M KPF_6/MeCN supporting electrolyte (conditions: area of the C-Al foil (WE) = 15x15 mm^2)

Figure 25a shows the measured reduction current when the film was deposited at -900 mV vs. Ag^+/Ag, this current response was almost similar to the $K_5\{V_{12}\}$ deposition in 0.1 M $(nBu_4N)PF_6$/MeCN. This result confirms that the reduction and subsequent deposition of $\{V_{12}\}$ is possible in similar conditions. The film thickness and stochiometric ratio of K: V remain consistent during functionalization of $\{V_{12}\}$ in the presence of KPF_6 as shown in **Figure 25 (b, c).**

Figure 26a illustrates the film morphology analyzed *via* SEM, showing a smooth surface at the lower negative potentials and crack-induced surface features at higher negative potentials. **Figure 26b** displays the Raman spectra for the $\{V_{12}\}$ cluster and synthesized films deposited at the three different potentials. The native $\{V_{12}\}$ cluster exhibits a characteristic Raman band at ~1007 cm^{-1}, corresponding to the VO_6/VO_5 units within the $\{V_{12}\}$ structure.[113] A shoulder at 984 cm^{-1} reflects monomeric behavior with significant potassium cation doping. The deposited films show a distinct peak at ~882 cm^{-1}, and a shift of the primary band from 1007 cm^{-1} to ~996 cm^{-1}, indicative of V=O bond elongation during the reduction. This confirms structural modifications similar to those seen in the functionalized $K_5\{V_{12}\}$ cluster after deposition.

XPS analysis of the film deposited at -500 mV vs. Ag^+/Ag shows the vanadium centers in a comparable oxidation state to those observed with $K_5\{V_{12}\}$, with approximately three reduced vanadium atoms per 12 vanadium centers. Quantitative XPS analysis reveals a K: V of 1: 0.78, indicating the presence of two additional K^+ as compared to $K_5\{V_{12}\}$ reduction at -500 vs. Ag^+/Ag under similar conditions (see *Chapter 3.1.2*).

3.3.2 In-situ nanostructured PEDOT/{V_{12}} complexes

In the preceding chapters, we detailed a straightforward electrochemical process that facilitates homogeneous growth of $K_5\{V_{12}\}$ and $\{V_{12}\}$ based POV film. We demonstrated that the $K_5\{V_{12}\}$ nanocluster can be immobilized on different substrates, such as smooth glassy carbon, C-Al foil, and highly porous LIG electrodes. Furthermore, we showed how the film's mass loading and thickness can be precisely controlled by adjusting the electrochemical parameters. However, for battery applications, it is crucial to synthesize a highly stable and redox-active film on a commercially viable current collector. To achieve this, we introduced a conductive polymer network

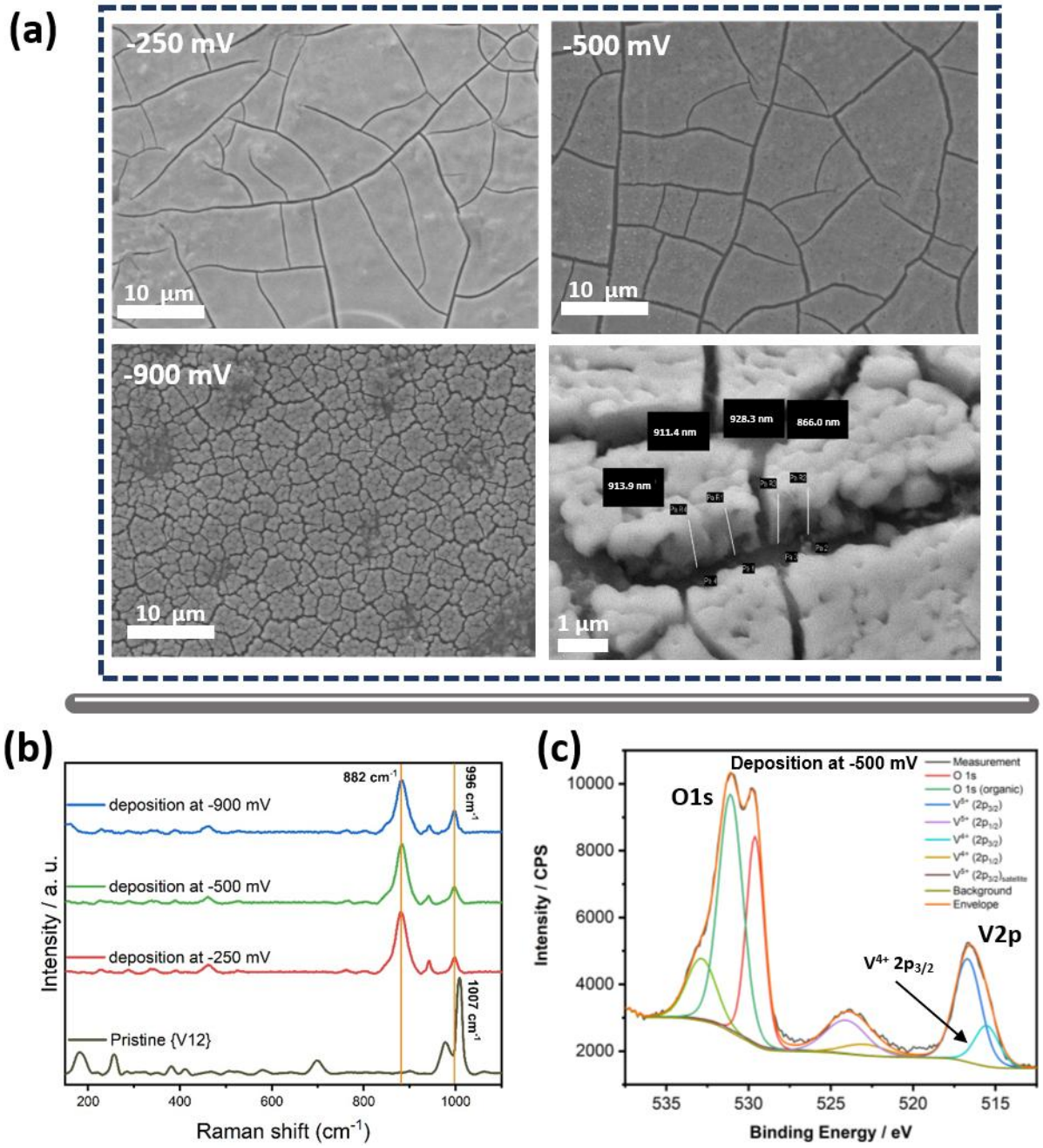

Figure 26: (a) surface morphology of $\{V_{12}\}/KPF_6$ deposited film at three different reduction potentials: -250 mV, -500 mV, and -900 mV vs. Ag^+/Ag, **(b)** Raman spectra of pristine $\{V_{12}\}$ cluster and deposited film at three different reduction potentials, **(c)** detail XPS spectra in the V2p and O1s region of film deposited at -500 mV vs. Ag^+/Ag**.** (Conditions: area of C-Al foil (WE) for deposition = 15x 15 mm^2)

during the electrodeposition of the $K_5\{V_{12}\}$ nanocluster, a complex polymer/POV composite is formed, demonstrating the remarkable flexibility of the dodecavanadate cluster. The native $\{V_{12}\}$ cluster can easily functionalize, transforming into a solid-state redox-active supramolecular film. To further enhance the composite, 3,4-Ethylenedioxythiophene (EDOT) was introduced during polyoxovanadate electrodeposition, leveraging its superior mechanical stability, reversible electrochemical properties, and high surface area.[114,115] EDOT is

responsive to the applied potential ranges and forms a stable polymerized EDOT coating known as PEDOT.

This method allows the formation of a K-POV/PEDOT complex thin layer on a commercial current collector, combining the redox-active POV within the conductive PEDOT polymer matrix. To synthesize a stable PEDOT/ $K_5\{V_{12}\}$ composite, a precursor solution of 20 mM EDOT was added to the prepared 0.5 mM $K_5\{V_{12}\}/(nBu_4N)PF_6$/MeCN electrolyte. The polymerization of EDOT and deposition of $K_5\{V_{12}\}$ were achieved by alternating two CSCA pulses at -500 vs. Ag^+/Ag for $K_5\{V_{12}\}$ deposition, followed by the two CV cycles from 0 to 1.6 V vs. Ag^+/Ag to polymerize EDOT. This process was repeated twice to confirm high mass loading and effective deposition of POV clusters within the polymer matrix.

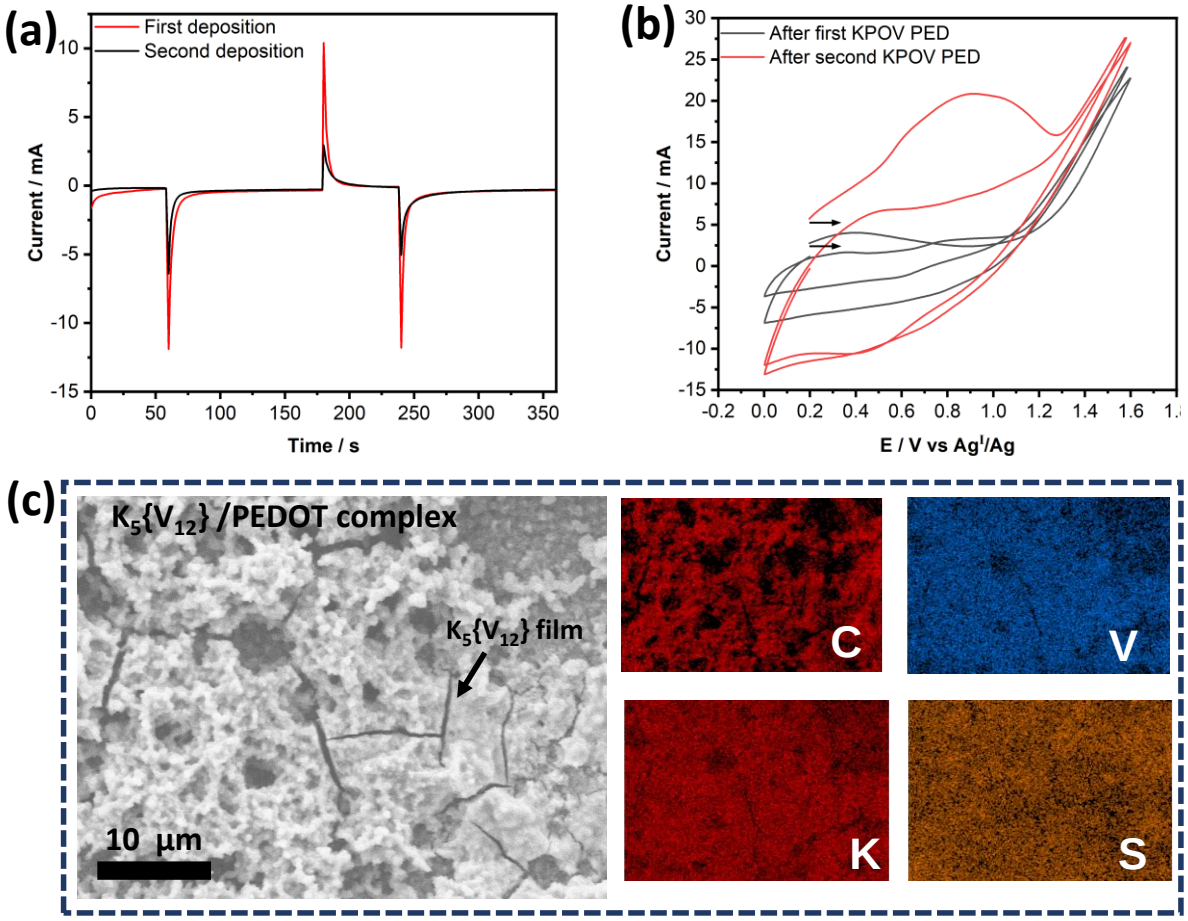

Figure 27: (a) CSCA pulsed deposition profile for $K_5\{V_{12}\}$ at -500 mV vs. Ag^+/Ag before and after EDOT polymerization, **(b)** measured CV response during EDOT polymerization on $K_5\{V_{12}\}$ film modified C-Al foil, and **(c)** surface morphology of PEDOT/ $K_5\{V_{12}\}$ composite deposited on the C-Al foil after two CSCA and two CV cycles, and respective EDX mapping of the PEDOT/ $K_5\{V_{12}\}$. (Conditions: are of C-Al foil (WE) for deposition = 15x 15 mm^2)

The reduction current observed during the first CSCA confirmed the successful deposition of $K_5\{V_{12}\}$. Additionally, a sharp oxidation peak at 1.2 V vs. Ag^+/Ag during the CV sweep

indicated the characteristic polymerization of EDOT following $K_5\{V_{12}\}$ deposition. In the second CSCA cycle, a significant decrease in the reduction current was recorded, due to the modification of the WE surface after PEDOT coating, similarly, the CV response revealed a large surface area under the curve, attributed to the high double-layer charge storage capacity provided by the PEDOT deposition, as shown in **Figure 27 (a, b)**.[116]

The SEM/EDX characterization confirmed the successful incorporation of the reduced $K_5\{V_{12}\}$ film within the high surface area 3D PEDOT matrix, as shown in **Figure 27c**. EDX mapping revealed strong signals for V, S, and K, indicating a homogeneous deposition of $K_5\{V_{12}\}$ alongside polymerized EDOT.

Further investigation of the chemical composition of the PEDOT/KPOV composite was conducted using XPS analysis. The XPS analysis showed a broad S2p doublet appeared at the binding energy of ~ 164 eV and deconvoluted as S $2p_{3/2}$ peak at ~163 eV and oxidized sulfur (S_{ox} $2p_{3/2}$) at ~164.5 eV (**Figure 28a)**. The presence of a mixed oxidation state of sulfur indicates subsequent polymerization of the EDOT during the electrochemical sweep.

Similarly, the high-resolution XPS spectra for vanadium identified a small peak at ~515.5 eV, corresponding to the $V2p_{3/2}$ signal. Quantitative analysis revealed that approximately 11% of the vanadium was present in the reduced V^{4+} oxidation state, confirming the structural tunning of the synthesized PEDOT/KPOV composite.

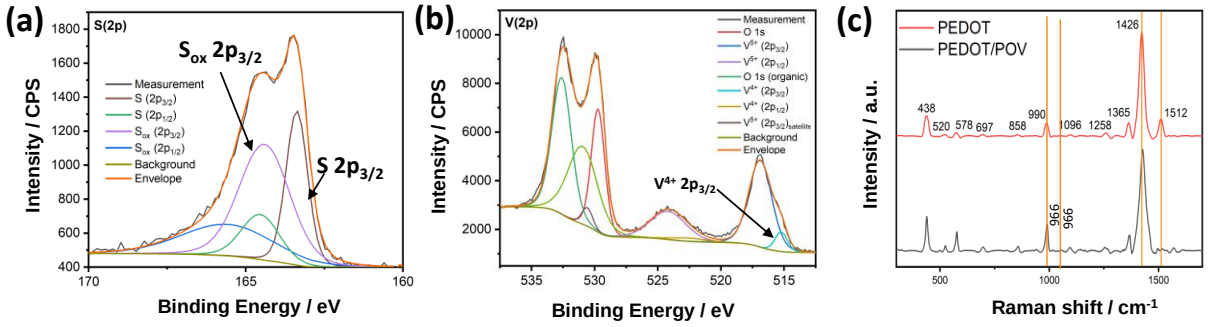

Figure 28: (a) detail XPS spectra in the S2p region deposited PEDOT/ $K_5\{V_{12}\}$ composite**. (b)** detail XPS spectra in the V2p and O1s region of the film deposited PEDOT/ $K_5\{V_{12}\}$ composite **(c)** Raman spectra of pristine PEDOT film and synthesized PEDOT/ $K_5\{V_{12}\}$ composite, (Conditions: area of C-Al foil (WE) for deposition = 15x 15 mm^2)

Raman measurement of the PEDOT/KPOV composite revealed distinctive peaks for both PEDOT and $K_5\{V_{12}\}$. The PEDOT/KPOV complex exhibited a strong Raman band at 1423 cm^{-1}, corresponding to the C_α-C_β stretching. Additionally, the band at 1365 cm^{-1} and 1512 cm^{-1} confirmed the typical C_β-C_β stretching and C_α-C_β asymmetrical stretching, respectively. The

reduced $K_5\{V_{12}\}$ film is generally displayed at peaks at 882 cm^{-1} and 996 cm^{-1}, which overlapped with the PEDOT band at 858 cm^{-1} and 990 cm^{-1}. Notably, the 1512 cm^{-1} Raman band for PEDOT disappeared after $K_5\{V_{12}\}$ deposition, suggesting an interaction between polymeric EDOT and $K_5\{V_{12}\}$ cluster.

These findings demonstrate that the in-situ deposition of the $K_5\{V_{12}\}$ alongside EDOT polymerization can be achieved through the electrochemical method, forming a polymer/POV complex directly on the current collector.

3.3.3 In-situ alkali metal functionalization of $\{V_{18}\}$

The structural tunning of the nitrate-template-enabled octadecavanadate $\{V_{18}\}$ cluster was explored, revealing a similar in-situ potassium functionalization and deposition mechanism as observed for the dodecavanadate $K_5\{V_{12}\}$ and $\{V_{12}\}$ clusters. The $\{V_{18}\}$ cluster consists of $[VO_5]$ units, linked together *via* edge-sharing, which are crucial for cluster reduction and K^+ ion interaction. This large POV cluster can undergo reduction at several vanadium centers, enabling reversible multi-electron transfer and formation of a stable potassium-functionalized reduced $K_x\{V_{18}\}$ thin film.

To obtain a $\{V_{18}\}$ based redox-active thin film, the $\{V_{18}\}$ cluster dissolved in a 0.1 M KPF_6/MeCN supporting electrolyte to create a 0.5 mM $\{V_{18}\}/KPF_6$/MeCN, similar to the $K_5\{V_{12}\}$ deposition process. The deposition was carried out with 10 CSCA pulses on a C-Al foil current collector, with potential values identical to those used for the $K_5\{V_{12}\}$ cluster (-250 mV, -500 mV, and -900 mV vs. Ag^+/Ag), while maintaining the same experimental conditions.

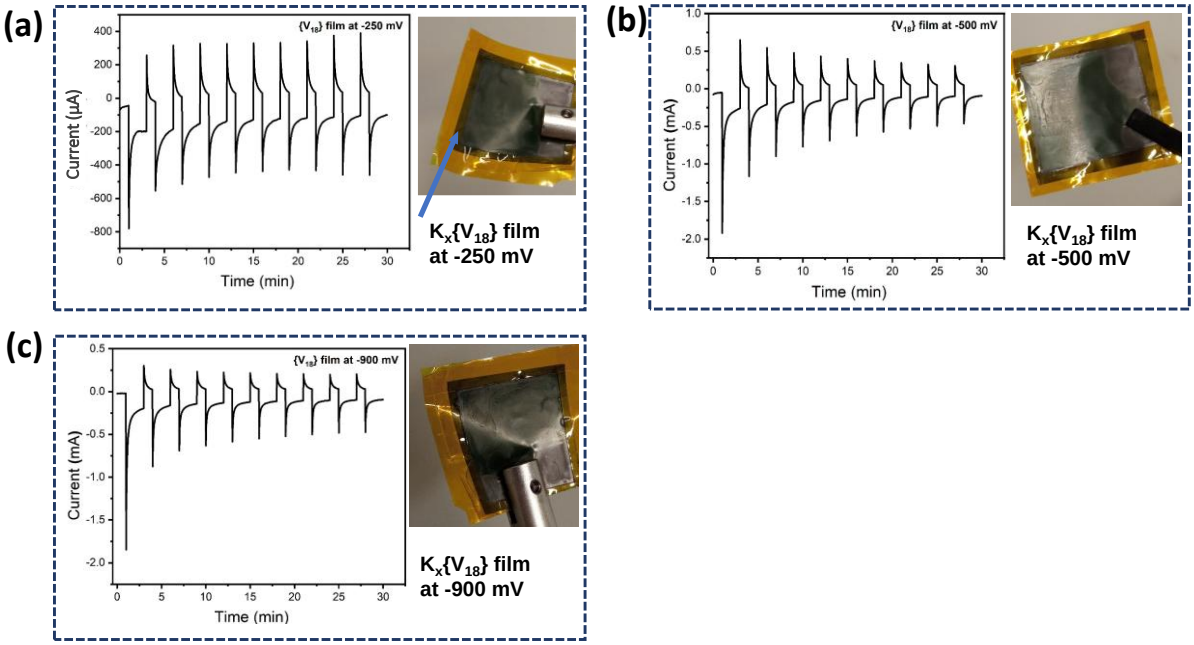

Figure 29: (a) CSCA profile of the $\{V_{18}\}$ cluster electrodeposition in 0.1 M KPF_6/MeCN electrolyte solution, with ten consecutive pulses at -250 mV vs. Ag^+/Ag, **(b)** -500 mV vs. Ag^+/Ag, and **(b)** -900 mV vs. Ag^+/Ag (inset: deposition of stable $K_x\{V_{18}\}$ film at different cathodic potentials on C-Al foil) (Conditions: area of C-Al foil (WE) for deposition = 15x 15 mm^2)

The reduction current response measured during the deposition of the $\{V_{18}\}$ cluster was significantly lower compared to the $\{V_{12}\}$ cluster, as shown in **Figure 29**. The reduction current for the first CSCA pulse at -900 mV vs. Ag^+/Ag during $\{V_{18}\}$ deposition was around 1.7 mA, nearly five times less than of $\{V_{12}\}$ deposition. Consequently, the $\{V_{18}\}$ cluster exhibited diminished efficacy in reducing vanadium centers from V^{5+} to V^{4+} under the given conditions. A similar reduction current response was observed at -250 mV and -500 mV vs. Ag^+/Ag, further indicating a weaker reduction current for $\{V_{18}\}$ compared to $\{V_{12}\}$.

Despite this, the deposited $\{V_{18}\}$ films exhibited a much stronger coating and adhered more firmly to the C-Al foil, even after being immersed in MeCN for washing the remaining electrolyte salt. SEM images of the $K_x\{V_{18}\}$ films obtained at -500 and -900 mV vs. Ag^+/Ag (**Figure 30a-b)** revealed a similar morphology to the $\{V_{12}\}$-based film but with a more pronounced crack-oriented surface. EDX mapping confirmed that the main components of the deposited films were V and K, as shown in **Figure 29c-d.** The deposited $\{V_{18}\}$ film suggested an interaction of 0.45 K^+ per vanadium center at -500 mV and 0.42 K^+ per vanadium center at -900 mV vs. Ag^+/Ag.

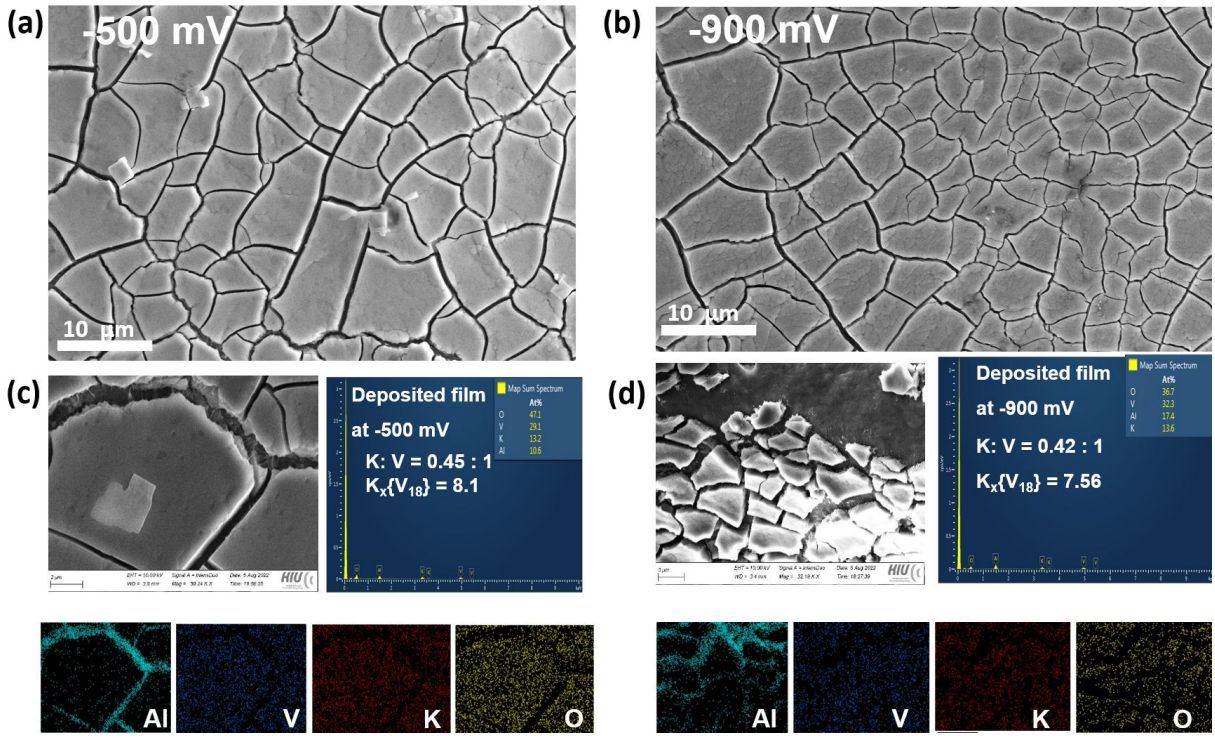

Figure 30: (a) SEM characterization of $K_x\{V_{18}\}$ deposited films at -500 mV and -900 mV vs. Ag^+/Ag on the C-Al foil after ten CSCA pulses, and **(b)** EDX elemental analysis of the obtained films (Conditions: area of C-Al foil (WE) for deposition = 15x 15 mm^2)

At higher negative potentials, the reduced $K_x\{V_{18}\}$ film demonstrated better stability and insolubility, so a thin film was deposited at -850 mV vs. Ag^+/Ag with only three CSCA pulses. This thinner film was synthesized to test the possible implementation of these binder/carbon additives-free electrodes as cathode material for Li-ion battery applications.

To further enhance the film insolubility in a non-aqueous solvent, the PEDOT/$\{V_{18}\}$ composites were immobilized by performing the 3 consecutive CV sweeps from 0 to 1.6 vs. Ag^+/Ag, similar to the process used for $\{V_{12}\}$/PEDOT composites. Different concentrations of EDOT were dissolved in the prepared $\{V_{18}\}$-based supporting electrolytes (0.1 M $(nBu_4N)PF_6$/MeCN) to control the vanadium-to-sulfur (V:S) ratio in the resulting thin films, as shown in **Table 3**. This method allowed for directly incorporating the native $\{V_{18}\}$ cluster into the polymerized PEDOT matrix without cluster reduction or altering the structure.

Table 3: Elemental composition of the deposited film from 3 CV cycles in different concentration ratios of $\{V_{18}\}$: EDOT.

$\{V_{18}\}$: EDOT Ratio (mM)	**V (%)**	**S (%)**	**V:S (atomic ratio)**	**AM loading (mg) 12 mm electrode**
1:10	10.3	8	1.28: 1	0.57
1:25	11.1	10	1.11: 1	1.17
1:50	8	7.8	1.03: 1	0.52

As shown in **Figure 31**, three different $\{V_{18}\}$/PEDOT composites were formed on the C-Al foil with initial $\{V_{18}\}$/EDOT ratio of 1:10, 1:25, and 1:50. All three complexes suggested exhibited a dominated PEDOT microstructure with no significant visible traces of $\{V_{18}\}$ cluster deposition. However, EDX analysis confirmed that each complex contained a significant amount of vanadium, which decreased as the concentration of EDOT in the electrolyte increased, as shown in **Figure 31a-b**.

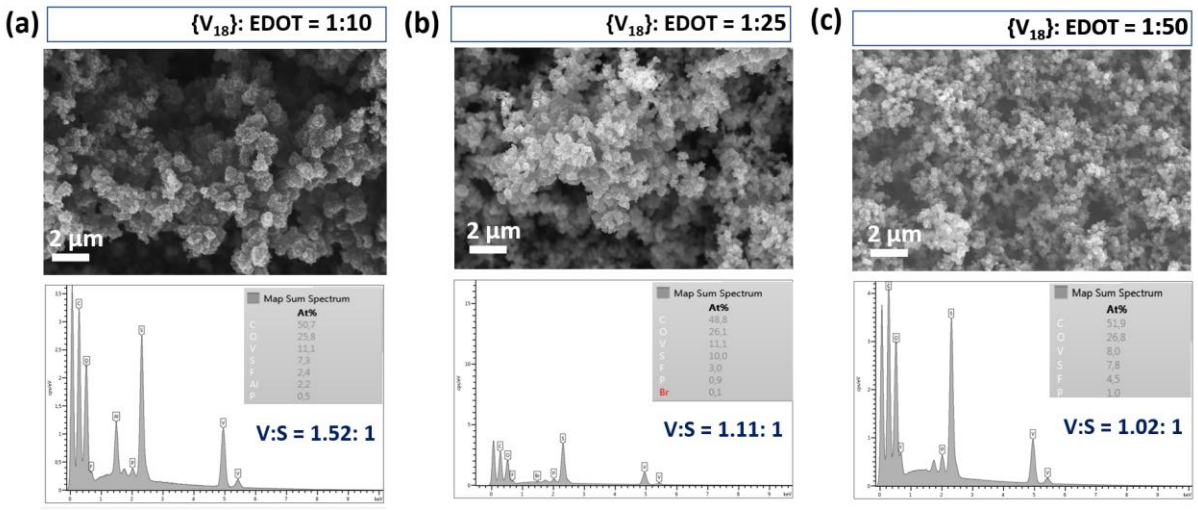

Figure 31: SEM and EDX analysis of $\{V_{18}\}$/ PEDOT complex derived at different concentration ratios of $\{V_{18}\}$: PEDOT **(a)** 1:10, **(b)** 1:125, and **(a)** 1:50 on a C-Al foil (Conditions: area of C-Al foil (WE) for deposition = 15x 15 mm^2)

To analyze the oxidation state and chemical composition of the vanadium and sulfur in the synthesized $\{V_{18}\}$/PEDOT complexes, high-resolution XPS spectra were examined, as shown in **Figure 32**. The S2p spectra, corresponding to sulfur atoms in the PEDOT chain, were deconvoluted into two distinct peaks at binding energies of 163.8 and 164.8 eV. These peaks represent the spin-split components $S2p_{1/2}$ and $S2p_{3/2}$, with a peak separation of ~1 eV, which is comparable to the α-α' bonding typically observed with the separation of ~1.2 eV.

In addition, the high-resolution V2p spectra confirmed that vanadium was deposited within the PEDOT matrix for all three synthesized $\{V_{18}\}$/PEDOT composites, as shown in **Figure 32**. The vanadium atom in the deposited films primarily existed in the V^{5+} oxidation state, with a small concertation of V^{4+}. This indicates that the $\{V_{18}\}$ cluster was successfully integrated into the PEDOT matrix without substantial reduction. The V^{4+}: V^{5+} ratio in the deposited $\{V_{18}\}$/PEDOT complexes across different concentrations was consistent with that of the native $\{V_{18}\}$ cluster, maintaining a V^{4+}: V^{5+} ratio of approximately 2.1: 15.9.

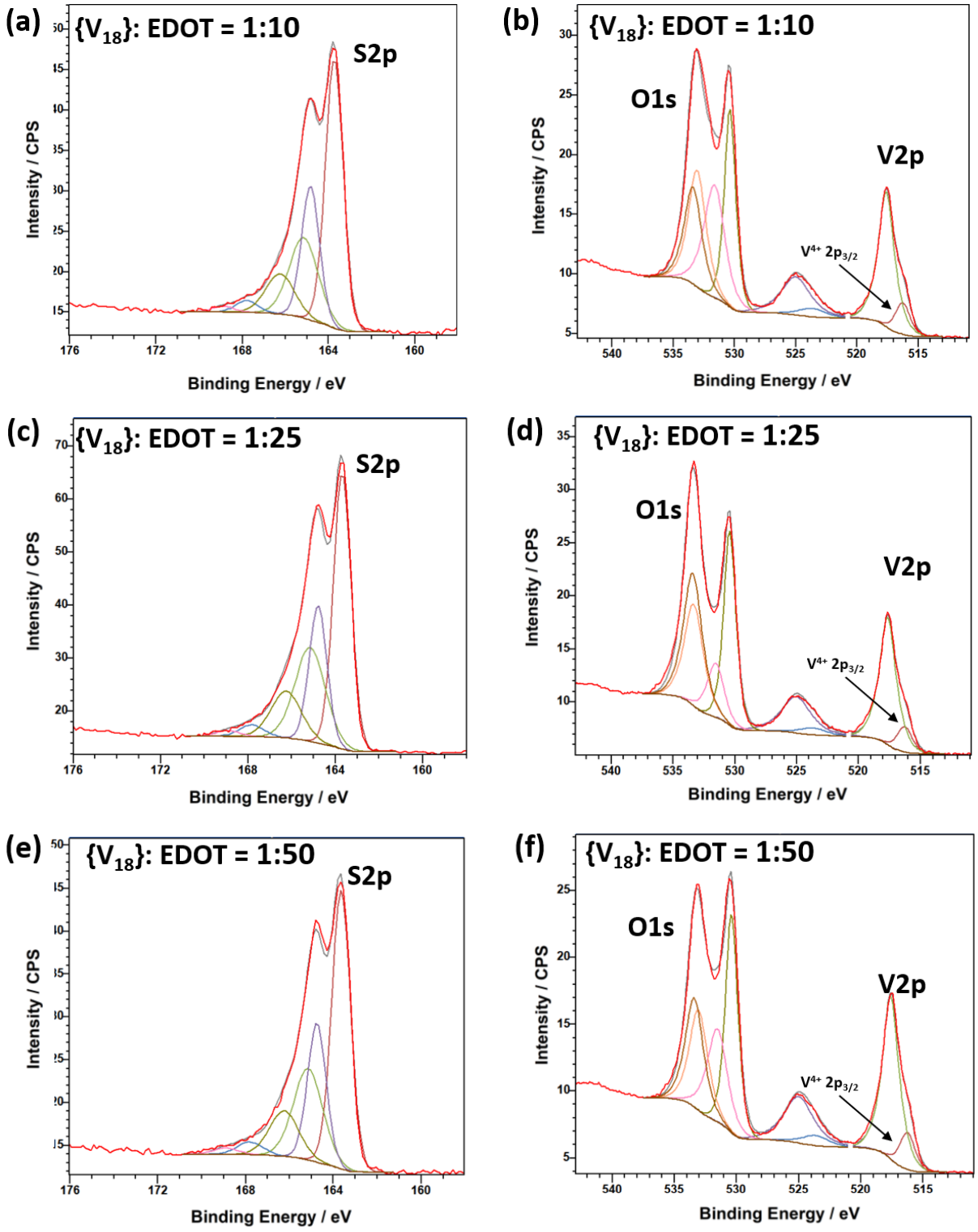

Figure 32: detail XPS spectra in the S2p, V2p, and O1s region of $\{V_{18}\}$/ PEDOT composite derived at different concentration ratios of $\{V_{18}\}$: PEDOT **(a)** 1:10, **(b)** 1:125, and **(a)** 1:50

3.4 Electrochemical performance of different POV-based thin supramolecular films as an electrode material in battery and supercapacitor

3.4.1 $K_5\{V_{12}\}$-based redox active thin film for (post-) lithium-ion batteries

The electrochemical charge storage capacity of $K_5\{V_{12}\}$ films were evaluated as active cathode materials in a prototype potassium-ion battery (PIB). Films were electrodeposited at -250 mV, -500 mV, and -900 mV vs. Ag^+/Ag using 3 CSCA pulses on C-Al foil substrates. These films were subjected to CV response and GCD cycles, within a voltage window of 1.5 - 3.8 V vs. K^+/K at a current density of 50 mA/g and a scan rate of 0.05 mV/s.

Battery cell testing of these synthesized films was conducted using Swagelok-type cells, without carbon additives or binder. A thin foil of potassium metal was used as an anode, with 1 M KFSI in DME as the electrolyte. The $K_5\{V_{12}\}$ deposited C-Al was cut into a 12 mm electrode and dried at 60°C overnight under vacuum. Assembled cells were allowed to rest at OCV for 3 hours before recording the measurements.

The CV measurements were performed for all 3 synthesized electrodes at -250 mV, -500 mV, and -900 mV. The CV response during charging discharge is shown in **Figure 33a-c**. The electrode derived from the film deposited -500 mV mainly consists of two broad peaks at ~2.5 V vs. K^+/K during charging and at ~2.2 V vs. K^+/K during discharging. These redox peaks likely represent electrochemical interactions between deposited $K_5\{V_{12}\}$ cluster and K^+ cations within this voltage range. A small shift towards the lower voltage values was observed in the reduction peak after a few charge-discharge cycles, indicating possible structural modification and causing a capacity fading.

Film at -250 mV represents a weak redox peak at ~2.25 V vs. K^+/K and ~2.6 V vs. K^+/K, along with several small oxidative peaks above ~3 V vs. K^+/K. These features are attributed to the film remaining in an oxidized state at lower potentials, resulting in distinct reduction and oxidation peaks during electrochemical cycling. Similarly, synthesized film at -900 mV defined a strong irreversible cathodic peak at ~1.9 V vs. K^+/K in the first cycle, corresponding to the reduction of the active material. However, a prominent reversible redox process was not observed for the film deposited at this higher reduction potential.

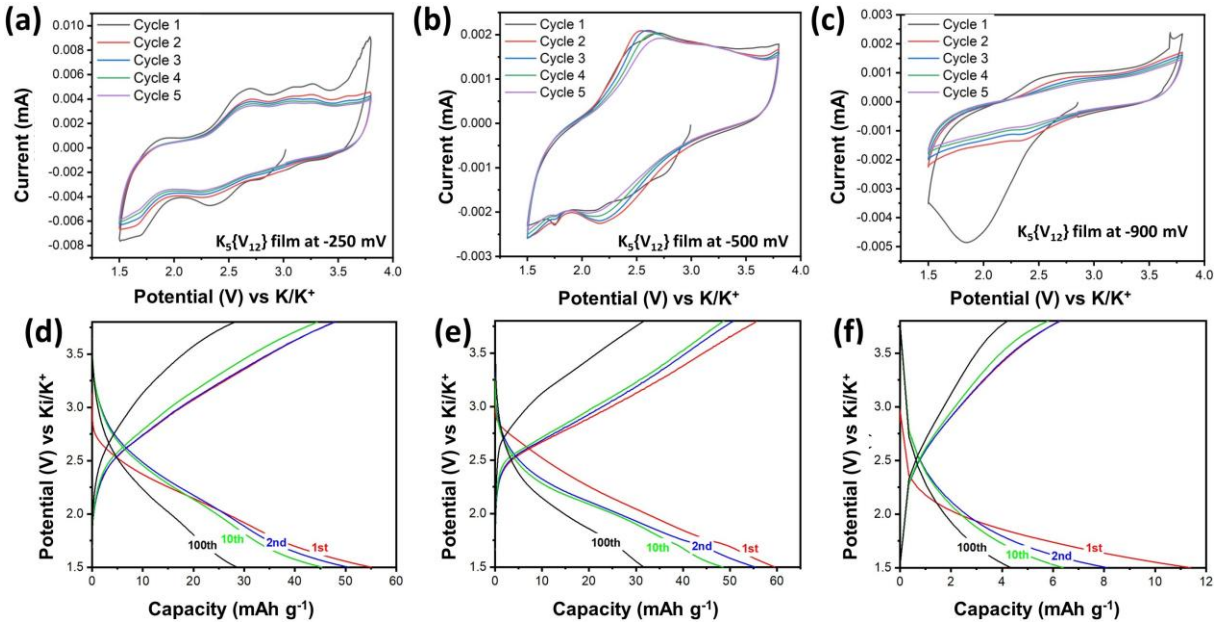

Figure 33: CV performance of the synthesized $K_5\{V_{12}\}$ film at **(a)** -250 mV, **(b)** -500 mV, and **(c)** -900 mV Ag^+/Ag, and voltage capacity profile for the synthesized films at **(d)** -250 mV, **(e)** -500 mV, and **(f)** -900 mV Ag^+/Ag (conditions: cathode= 12 mm $K_5\{V_{12}\}$ film at C-Al foil, anode material= K metal foil, CV scanned at 0.05 mV/s and GCD measured at current density of 50 mA/g, 1 M KFSI in DME as an electrolyte)

The discharge capacity of each synthesized electrode was evaluated by performing 100 GCD cycles, as shown in **Figure 33d-f**. The film deposited at -250 mV exhibited an initial discharge capacity of 55 mAh/g, corresponding to the insertion of 3.06 electrons per $K_{8.64}[V_{12}O_{32}Cl]$ unit (all empirical formulas determined via XPS analysis, refer *chapter 3.1.1*). The theoretical capacity (Q) can be calculated as:

$$Q = \frac{nF}{3.6\ M_W} = \frac{(n.26800)}{M_W} \quad (1)$$

Where Q represents the reversible charge/discharge capacity, n is the number of electrons transferred, M_W is the molecular weight, and F is the Faraday constant.

Similarly, the electrode synthesized at -500 mV showed the highest capacity of 59 mAh/g, corresponding to the transfer of approximately 3.37 electrons. This result suggests that the film deposited at -500 mV provides optimal conditions for efficient charge storage and electron transfer. Whereas, the film derived at a higher negative potential of -900 mV defined only 0.68 electrons transferred. This poor charge storage capacity can be attributed to irreversible structural changes and reduced electrochemical performance at higher negative potentials. All three synthesized electrodes exhibited notable capacity fading during the 100 GCD cycles. This

fading is likely due to the partial dissolution of the deposited film in the battery electrolyte or irreversible structural modification occurring during the cycling process.

In-situ potassium functionalized {V_{12}} reduced film K_x{V_{12}} performance as a cathode material in LIBs

The performance of reduced $K_x\{V_{12}\}$ film as a cathode material in lithium-ion battery (half-cell). Two different films were electrodeposited by electrodeposition, at negative potentials of -450 mV and -850 mV vs. Ag^+/Ag, both using 3 CSCA pulses on C-Al foil. The electrochemical performance of these films was assessed in a voltage window of 1.2 - 4 V vs. Li^+/Li, with a current density of 50 mA/g and a scan rate of 0.05 mV/s. A thin lithium metal foil was used as the anode, and 1 M $LiPF_6$ in EC/DEC (1:1 *v/ v*) served as the electrolyte. Other experimental conditions remained consistent with those used in the PIB battery testing.

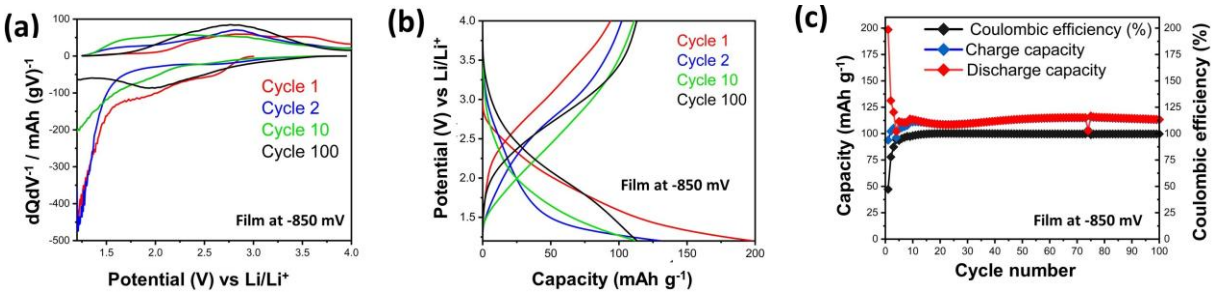

Figure 34: (a) differential capacity vs voltage (dQ/dV) curve for assembled LIBs half cell **(b)** voltage capacity profile of synthesized film **(c)** cycling performance of the cell at 50 mA/g (conditions: cathode= 12 mm electrode cut from $K_5\{V_{12}\}$ film synthesized at -850 mV with 3 CSCA, anode material= Li metal foil, GCD measured at current density of 50 mA/g)

First, we measured the differential capacity (dQ/dV) as a function of voltage (V) at different cycles as shown in **Figure 34a**. The initial two cycles displayed a strong irreversible discharge peak at 1.2 V vs. Li^+/Li, likely due to the activation of the electrode material. After the 10th cycle, the peak at 1.2 V gradually decreased and a new broad discharge peak emerged at ~1.7 V vs. Li^+/Li. After 100 cycles, prominent reversible redox peaks were observed at ~1.7 V and ~2.7 V vs. Li^+/Li, indicating a stable phase of the deposited film.

The charge-discharge curves suggested the presence of a plateau after the first cycle, confirming some interactions between the deposited film and Li^+ ions during the insertion and extraction process. Additionally, the film exhibited significant cyclic stability during 100 GCD cycles at 50 mA/g and maintained its performance after the initial few cycles.

The preliminary findings suggest that synthesized $K_x\{V_{12}\}$ thin films exhibit promising potential as a redox-active material in energy storage applications, without requiring the use of binder or carbon additives. The electron storage capacity of this POV cluster is governed by the number of vanadium centers, which are reduced during the charge and discharge process. This observation was further extended by evaluating the charge storage performance of potassium-functionalized $\{V_{18}\}$ POV cluster films, with similar assessments performed for their applicability in LIBs.

3.4.2 Potassium-functionalized reduced {V_{18}} thin film for Li-ion battery

An electrode comprising $K_x\{V_{18}\}$ films was synthesized and tested at deposition and reduction potentials of -250 mV, -500 mV, and -900 mV vs. Ag^+/Ag films (refer to *section 3.4.3)* to optimize their performance in LIBs. The assembly of LIB cells followed identical experimental protocols as outlined in the previous section. The films synthesized using the 10 CSCA pulses were initially evaluated over 50 GCD cycles at 50 mA/g **(Figure 35)**. Notably, the $K_x\{V_{18}\}$ films synthesized at -900 mV demonstrated the highest electrochemical performance, closely reassembling the behavior of $\{V_{12}\}$ based films reduced at -850 mV in LIB testing. The film deposited at -900 mV exhibited the maximum discharge capacity of 34 mAh/g and retained approximately 54 % of its capacity after 50 cycles, outperforming the other synthesized film. These initial results indicate that further optimization of the reduction potential could enhance the redox activity and conductivity of the film.

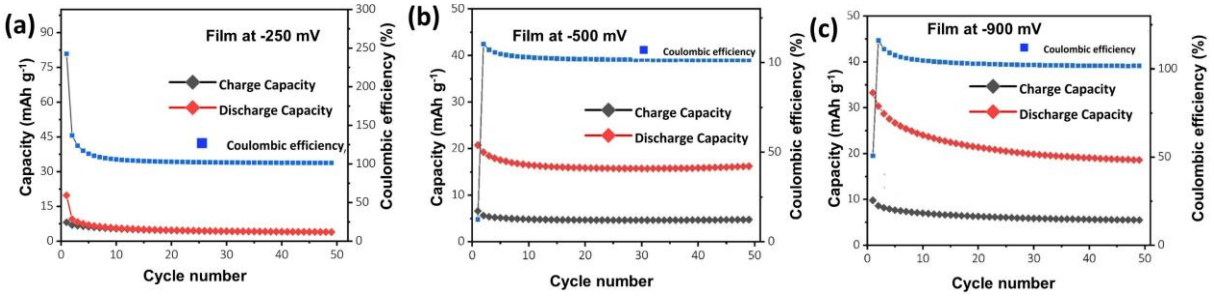

Figure 35: (a) electrochemical performance of the synthesized $K_x\{V_{18}\}$ films measured in a LIBs half-cell at 50 mA/g (conditions: cathode= 12 mm electrode cut from as-synthesized $K_x\{V_{18}\}$ films with 10 CSCA pulses, anode material= Li metal foil, GCD measured at the current density of 50 mA/g)

In the next approach, the electrochemically reduced $\{V_{18}\}$ film was further optimized by refining the electrodeposition parameter to synthesize potassium-supported, redox-active $K_x\{V_{18}\}$ thin film. The film was synthesized under the same experimental conditions previously described (see *Chapter 3.4.3*) at -850 mV vs. Ag^+/Ag and applying only 3 CSCA pulses. This

method resulted in the formation of a reduced $K_x\{V_{18}\}$ thin film with enhanced conductivity, structural stability, and improved charge transfer during the battery cycling.

The electrochemical characterization of the film, deposited at -850 mV with 3 pulses, was conducted within an operating voltage range of 1.5 - 4 V vs. Li^+/Li (**Figure 36)**. The CV at a scan rate of 0.05 mV/s for the first five cycles revealed two broad redox peaks at 2.8 V and 3.0 V vs Li^+/Li, corresponding to the reduction of the deposited $K_x\{V_{18}\}$ film during discharge and oxidation during charge. However, the intensity of these peaks diminishes after two CV cycles, indicating irreversible structural modification in the cluster. Notably, after two CV cycles, a distinct reduction process emerged below 2 V vs Li^+/Li, suggesting an incomplete reduction of the active material.

Similarly, the first two GCD curves exhibited a plateau during the charging and discharge processes, which stabilized over the subsequent 100 GCD cycles, with minimal variation observed in the GCD profiles **(Figure 36b)**. After the initial 20 GCD cycles, the cluster structure appeared to stabilize, resulting in only ~15% capacity fading over the remaining 80 GCD cycles **(Figure 36c)**.

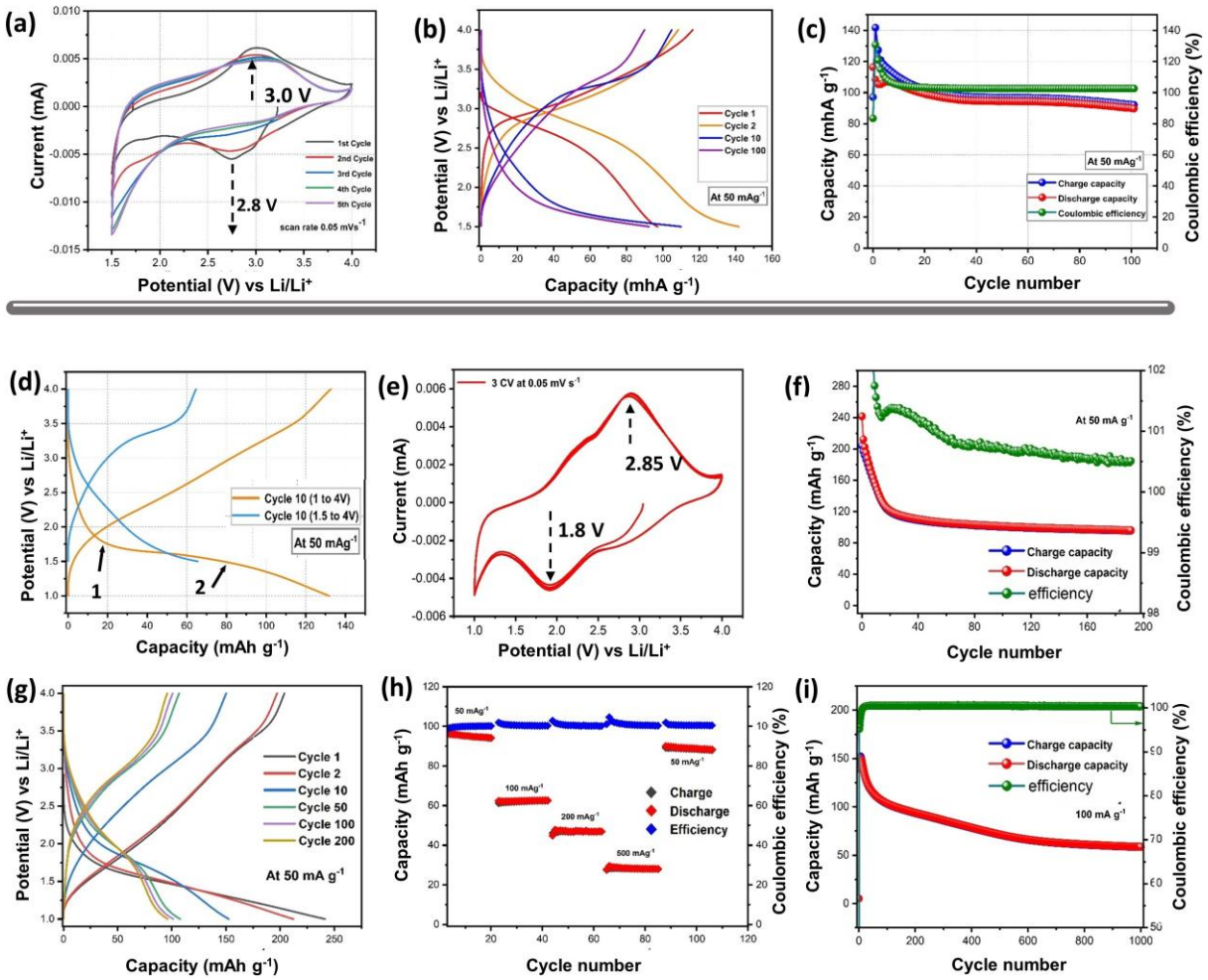

Figure 36: (a) CV, **(b)** voltage capacity profile, and **(c)** cyclic stability performance of the synthesized $K_x\{V_{18}\}$ based cathode in a half-cell LIBs (at operating voltage range 1.5 to 4 V vs Li^+/Li) **(d)** GCD curves obtained at two different operating voltage range, **(e)** CV measurement, **(f)** cyclic stability performance, **(g)** voltage capacity profile, **(h)** rate capability test, and **(i)** cyclic stability up 1000 GCD cycles ((d-i) all measurement at operating voltage range 1 to 4 V vs Li^+/Li) (conditions: cathode= 12 mm $K_x\{V_{18}\}$ film deposited at C-Al foil, anode material= Li metal foil, CVs scanned at 0.05 mV/s)

Following the 100 GCD cycles, the discharge cut-off voltage of the same cell was extended from 1.5 to 1 V vs Li^+/Li to further investigate the possible redox processes during the electrochemical cycling. After the 10 cycles, the GCD curves were compared for both voltage ranges, as illustrated in **Figurec36d**. The results confirmed the initiation of an additional reduction process, evidenced by a notable increase in discharge capacity upon lowering the discharge cut-off voltage. To verify the stability of this redox process across the broader operating voltage range, three CVs were performed post-GCD cycling **(Figure 36e).** The CV profiles showed nearly identical responses with no significant peak shift, indicating a structurally stable $K_x\{V_{18}\}$ film. The broad, reversible redox peak suggests the fully reversible electrochemical interaction between Li^+ and the deposited $K_x\{V_{18}\}$ cluster framework, enabled by the stable reduction and oxidation of the film.

The charge storage mechanism within the POV structure involves the reduction of vanadium atoms to a lower valance state during discharge, which facilitates Li^+ ion intercalation, and re-oxidation to a higher valance state during charging, completing the reversible charge storage cycle. The observed redox peak at ~1.8 V vs Li^+/Li during the discharge corresponds to a reduction of the deposited $K_x\{V_{18}\}$ film, while the oxidized peak at ~2.85 V vs Li^+/Li during charging confirms reoxidation. This multi-step reversible redox process, attributed to multiple electron transfers, results in a high specific capacity.

To confirm the structural stability and reversibility of this redox process, an additional 200 GCD cycles were conducted at the extended voltage window. Initial results indicated a sharp capacity loss within the first 20 cycles, likely due to the loss/dissolution of the active material of the $K_x\{V_{18}\}$ film. However, over the subsequent 180 GCD cycles, the capacity loss was limited to only 14% **(Figure 36f-g)**. Furthermore, rate capability tests, as shown in **Figure 36h,** demonstrated excellent structural stability at varying current densities (50, 100, 200, and 500 mA/g). Long-term cycling stability was assessed over 1000 GCD cycles at 100 mA/g, revealing a decent capacity retention of ~50%.

This study demonstrates that the reduction of $\{V_{18}\}$ in the presence of potassium cations results in the formation of a highly redox-active thin film, capable of undergoing reversible redox processes with minimal structural deformation. The successful reduction and immobilization of $K_x\{V_{18}\}$ film on the commercial current collector, without the use of carbon additives or binders, has been achieved, with preliminary charge storage capacity demonstrated through testing in half-cell LIB.

3.4.3 Reduced K_5V_{12} nanocluster deposition for flexible supercapacitors (NA2)

The electrochemical performance of pristine LIG and $K_5\{V_{12}\}$ deposited electrodes are shown in **Figure 37**, we conducted CV measurements in a typical three-electrode cell setup at a set operating potential referenced to the standard Ag/AgCl electrode (aqueous reference), using a Pt wire as counter electrode and aqueous 1 M H_2SO_4 as electrolyte. The operating potential window for the measurement ranged from -300 to 1000 mV (vs. aq. Ag^+/Ag). The CV curves in **Figure 37a** indicate that all K-POV electrodes exhibit significantly improved cyclic voltammetry responses compared to pristine LIG electrode, thus enhancing charge storage capacity. The $K_5\{V_{12}\}$ cluster deposition preferentially takes place at regions of low

crystallinity on the LIG electrode, which seems to contribute to the improved electronic and electrochemical properties of the graphitic structure. Next, to confirm the enhanced electrochemical efficacy of the K-POV-750 electrode, the GCD response was recorded at various current densities ranging from 0.1 to 2 mA cm^{-2} as illustrated in **Figure 37b**. The GCD curves display a quasi-linear charge-discharge profile, affirming the excellent reversible supercapacitive behavior at different current densities. The K-POV-750 electrode exhibited the highest areal capacitance of 125 mF cm^{-2} at a current density of 0.1 mA cm^{-2}, a significant improvement compared to the pristine LIG electrode, which achieved a maximum areal capacitance of 25 mF cm^{-2}, i.e., only one-fifth of the K-POV-750 electrode, as depicted in **Figure 37c**. This outcome implies superior capacitive performance when the $K_5\{V_{12}\}$ molecular nanocluster was deposited on the LIG surface within a comparatively wide potential range, significantly influencing the overall electrochemical performance of the synthesized electrode. Presumably, the electrochemical deposition of the $K_5\{V_{12}\}$ within this enhanced potential window delineated the structural and chemical modification of the LIG, favoring the fast reversible Faradic response between the electrolyte and $K_5\{V_{12}\}$ modified LIG nanostructure.[117] This structural modification on the LIG surface promotes a vanadium oxide framework complex, facilitating reversible interaction/de-insertion of electrolyte ions during charging and discharging. Additionally, the poor electrochemical performance at higher current density is in agreement with the high internal resistance, i.e., equivalent series resistance (ESR), which can be directly measured from the voltage drop V_{ESR} during the GCD cycles.[118] At a current density of 1 mA cm^{-2}, the calculated V_{ESR} for the K-POV-750 electrode is 260 mV, whereas the pristine LIG electrode exhibits a significantly higher V_{ESR} value of 1204 mV **Figure 37d**.

The concept's validity was ultimately shown by assembling a flexible solid-state supercapacitor (SSC-KPOV-750) using two symmetrical K-POV-750 electrodes with PVA-H_2SO_4 gel electrolyte and laboratory-grade micropores tissue paper as a separator, as illustrated in **Figure 37e**. The performance of SSC-KPOV-750 was compared with a similar SSC-LIG device based on pristine LIG electrodes. The fabricated device has better pseudocapacitive performance compared to SSC-LIG, as indicated by a quasi-reversible CV within the potential range from -300 to 1000 mV. The two pronounced broad peaks at approximately 200 and 550 mV vs. Ag^+/Ag (at 30 mV s^{-1}) represent the reversible faradic reaction, contributing to excellent charge storage behavior even at a higher scan rate. Additionally, the CV of pristine SSC-LIG at 100 mV s^{-1}, when compared with SSC-KPOV-750, demonstrates significantly inferior charge

storage behavior **Figure 37f**. The total areal capacitance for SSC-KPOV-750 is 24.92 mF cm^{-2} at a current density of 0.1 mA cm^{-2}, approximately 11 times higher than that of the pristine LIG-based SSC **Figure 37g**.

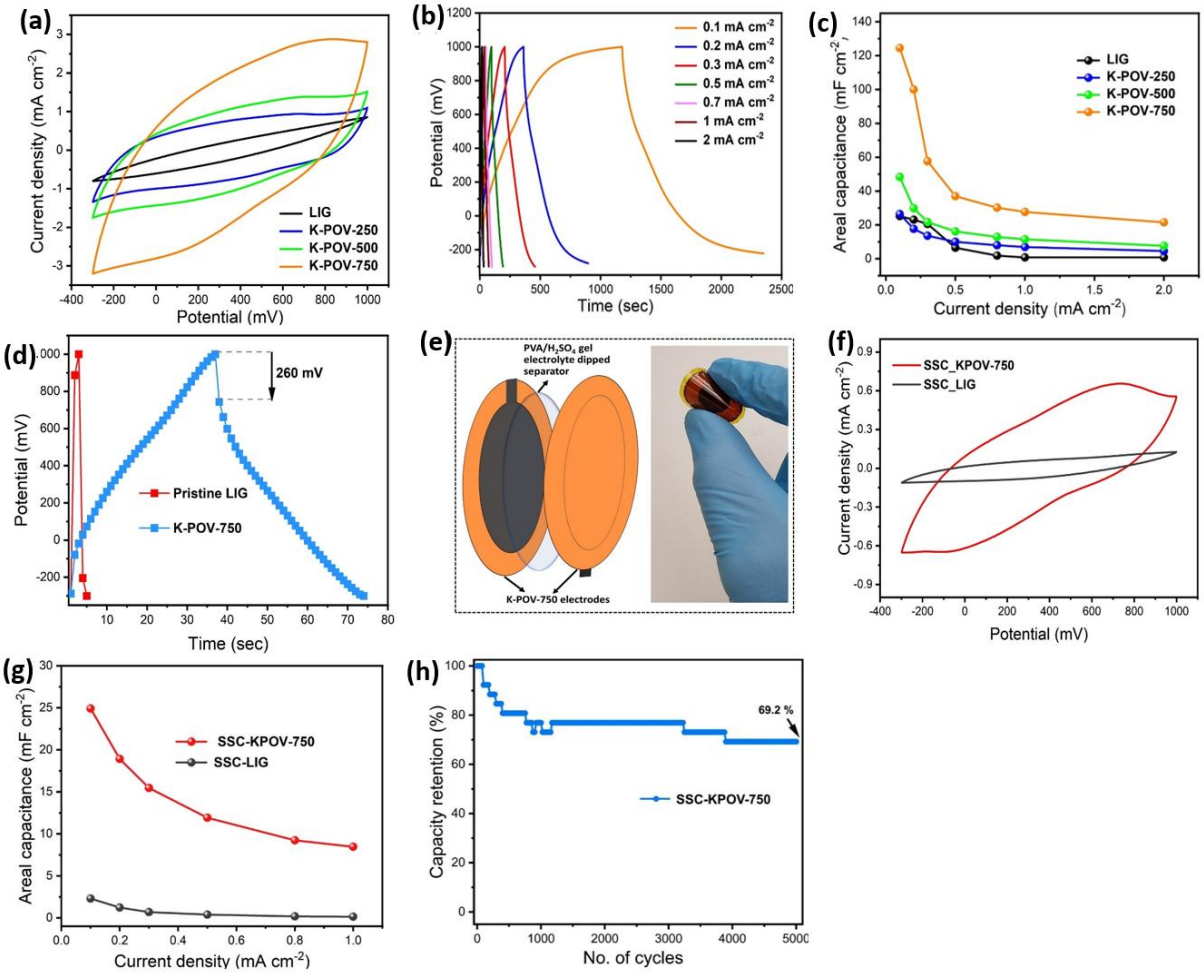

Figure 37: (a) Cyclic voltammograms of K-POV-250, K-POV-500, and K-POV-750 electrodes compared with pristine LIG electrode, **(b)** GCD profiles of K-POV-750 electrode at various current densities from 0.1 to 2 mA cm^{-2} **(c)** areal capacitance (C_A) of the synthesized electrodes at different current densities, **(d)** voltage drop V_{ESR} profile of K-POV-750 and pristine LIG electrode at 1 mA cm^{-2} and **(e)** schematic illustration of fabricated SSC-KPOV-750, inset: image of real flexible supercapacitor device, **(f)** comparison of the CV curve at 100 mV s^{-1} for SSC-KPOV-750 and SSC-LIG, **(g)** specific areal capacitance of SSC-KPOV-750 and SSC-LIG at various current densities, and **(h)** cycling performance of SSC-KPOV-750 device during 5000 cycles at 0.8 mA cm^{-2} Schematic figure 38 is reproduced with permission copyrights from Wiley Library (2024)[104]

Similarly, at the higher current density of 1 mA cm^{-2}, the SSC-KPOV-750 sustains a decent performance of C_A ~ 8.5 mF cm^{-2}, whereas the SSC-LIG exhibits instability after 0.5 mA cm^{-2} (C_A<< 1 mF cm^{-2}) due to a high internal resistance. These results confirm the better rate capability of the SSC-KPOV-750. Furthermore, the cycling stability of the SSC-KPOV-750

device was evaluated through 5000 consecutive charge-discharge cycles performed at 0.8 mA cm^{-2}, as depicted in **Figure 37h**.

This study demonstrates the effective electrochemical immobilization of $K_5\{V_{12}\}$ on a highly porous graphene-like LIG substrate through a straightforward CV method. The electrochemical deposition of the nanoclusters within different potential ranges corresponds to distinct electronic and electrochemical changes in the LIG electrodes. The optimum POV deposition was achieved for electrodeposition in a potential range of -750 to 750 mV vs. Ag^{+}/Ag, which leads to the presence of a highly redox-active and stable reduced cluster species on the LIG surface. This process also fine-tunes the electrochemical active sites on the graphene surface. At the same time, detailed Raman analysis on the modified K-POV-750 electrode reveals the oxidation of surface sp^2 carbon centers. The deposited $K_5\{V_{12}\}$ clusters also transformed to dimeric V^{5+} or monomeric V^{4+} polyoxovanadate centers on the modified electrode surface. The performance of the modified K-POV-750 electrode was evaluated in a symmetrical real supercapacitor device assembled with PVA/H_2SO_4-based gel electrolyte. The flexible symmetrical supercapacitor with K-POV-750 sustains excellent electrochemical response and good capacity retention. The SSC-KPOV-750 device delivers an energy density of 5.68 mWh cm^{-2} and a power density of 0.063 mW cm^{-2}. In summary, this work presents a sustainable approach for introducing a highly redox-active potassium-bridged polyoxovanadate nanocluster into a graphene-like LIG framework, enhancing structural stability and improving electrochemical performance. The findings hold promise for applications in micro-flexible smart devices, particularly in the fabrication of flexible micro-supercapacitors, without binders or current collectors.

For more detailed information refer to *Chapter 6.2 (NA2)*

3.5 Enhancing Si-dominant anodes: impact of polyacrylic acid neutralization degree on low-cost micron-sized silicon anodes for high-energy Li-ion full cells (NA3)

This work focuses on optimizing silicon (Si)-dominant anodes for lithium-ion batteries using micron-sized silicon particles (SiMPs) and polyacrylic acid (PAA) as a binder. We investigated how the neutralization degree of PAA impacts electrode performance, structural integrity, and cycle life, particularly in full-cell configurations. The optimized PAA composition with a 70% neutralization degree ($Li_{0.7}PAA$) achieved the best results. It enhanced electrode properties, first cycle efficiency (FCE) (up to 78.1% at C/3), and capacity retention (85.4% after 150 cycles at 1C). However, over-neutralization (e.g., 80%) caused a performance decline due to slurry instability and excessive gassing. Higher neutralization degrees improved binder distribution and adhesion. Uniform binder coverage around silicon particles reduced degradation and supported stable solid electrolyte interphase (SEI) formation.

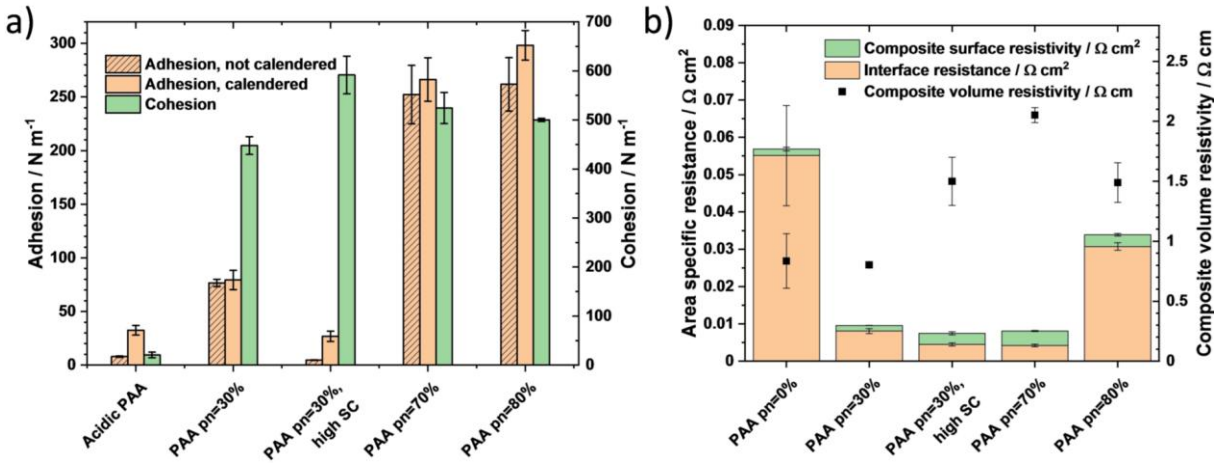

Figure 38: a) Adhesion of non-calendered (shaded orange) and calendered (orange) electrodes with varying PAA neutralization degrees and cohesion (green) were measured using 90° peel tests. **b)** Measured resistances of calendered electrodes with different PAA neutralization degrees are shown: composite surface resistivity (green) and interface resistance (orange) as bars, and composite volume resistivity (black) as dots. Schematic figure 39 is reproduced with permission copyrights from "Batteries & Supercaps" (2024)[119]

We investigated the physical properties of the fabricated electrodes as shown in **Figure 38**. The adhesion of pure silicon anode slurry increases with higher partial neutralization of PAA due to stretched polymer chains enhancing surface interactions. Higher pH from neutralization also promotes more chemical bonding. However, $Li_{0.3}PAA$ with high SC showed low adhesion despite high cohesion as shown in **Figure 38a**. Overall, cohesion is more critical than adhesion for electrode performance, with both neutralization degree and mixing protocols playing key roles. Furthermore, the electronic resistivity at room temperature on multiple spots of electrodes

to ensure reproducibility as shown in **Figure 38b**. The Interface resistance of the $Li_{0.3}$PAA (0.0081 Ω cm²) and $Li_{0.7}$PAA (0.0042 Ωcm²) had low values, comparable to standard mixing methods, whereas Li_0PAA had the highest (0.055 Ω cm²). $Li_{0.8}$PAA fell in between at 0.031 Ω cm². The lowest resistivity was observed in Li_0PAA (0.835 Ω cm) and $Li_{0.3}$PAA (0.802 Ω cm), while $Li_{0.3}$PAA with high SC (1.499 Ω cm) and $Li_{0.7}$PAA (2.052 Ω cm) exhibited the highest values. Whereas, the synthesized $Li_{0.8}$PAA electrode had an intermediate value (1.489 Ω cm). Partially neutralized PAA (e.g., $Li_{0.3}$PAA) provided significant improvements in interface resistance compared to non-neutralized PAA (Li_0PAA). $Li_{0.3}$PAA emerged as the optimal material, balancing low interface and composite volume resistivity.

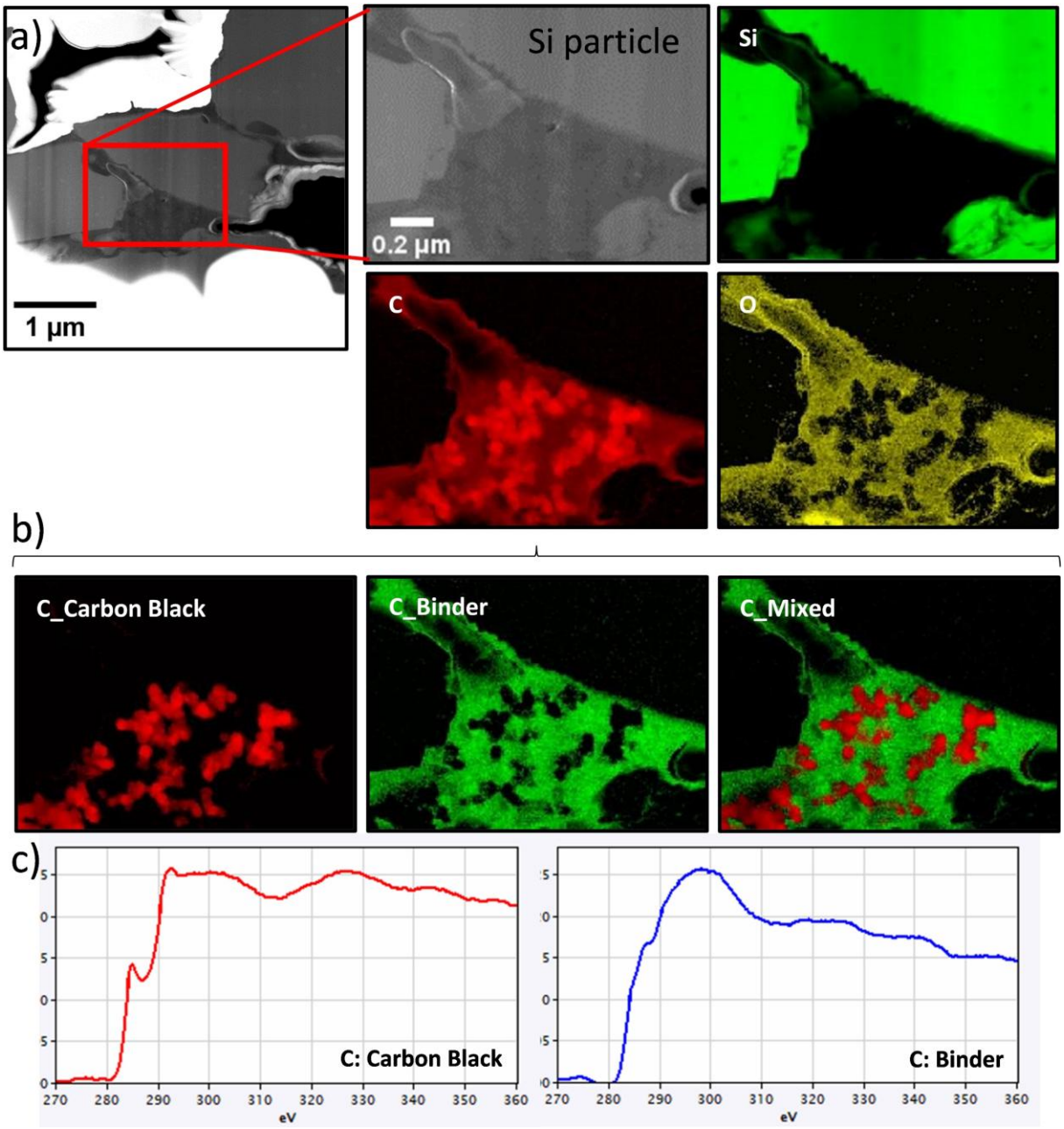

Figure 39: cross-section TEM image of the $Li_{0.7}$PAA electrode show Si particles surrounded by a binder/conductive additive mixture, with elemental mapping for silicon (green), carbon (red), and oxygen (yellow). EELS analysis differentiates carbon states, highlighting carbon black (red) and binder (green), with corresponding spectra confirming the assignments. Schematic figure 40 is reproduced with permission copyrights from "Batteries & Supercaps" (2024)[119]

The transmission electron microscopy (TEM)/ focused ion beam (FIB) cross-section images were used to examine the surface morphology of silicon electrodes with varying degrees of binder partial neutralization as shown in **Figure 39**. The partial neutralization of the $Li_{0.7}$PAA ensures homogeneous binder distribution around silicon, embedding carbon black to form efficient conductive paths, though with higher resistivity. Therefore, partial neutralization improves binder distribution and silicon connectivity while reducing carbon black agglomeration. The detailed XPS measurement was utilized to analyze the electrodes, providing insights into their elemental composition and differentiating between various oxygen states as shown in **Figure 40**. The Si 2p spectra of Li_0PAA, $Li_{0.3}$PAA, and $Li_{0.7}$PAA electrodes show three distinct features corresponding to elemental Si^0 ($Si\ 2p_{3/2}$ at a binding energy of 99.0 eV), intermediate SiO_x (100.5 eV), and SiO_2 (103.1 eV) as shown in **Figure 40 (left Column)**. The intensity of these peaks decreases significantly for $Li_{0.3}$PAA and $Li_{0.7}$PAA compared to Li_0PAA, attributed to a more homogeneous binder coverage. Partially neutralized samples show a higher SiO_x/SiO_2 ratio due to increased slurry pH during fabrication. In the C 1s spectra, contributions include conductive carbon (284.4 eV), C–C/C–H (285.0 eV), C–O (286.3 eV), and O=C–O (288.8 eV) **Figure 40 (middle Column)**. With increased neutralization, the C–O signal intensifies while the O=C–O signal remains constant. Additionally, the dominant C signal shifts from C–C/C–H to conductive carbon, likely due to altered interactions between the neutralized binder and conductive carbon. The O 1s spectra align with findings in the Si 2p and C 1s regions, showing reduced SiO_2 intensity for partially neutralized samples and an increase in the O–C peak intensity with higher neutralization levels **Figure 40 (middle Column)**.

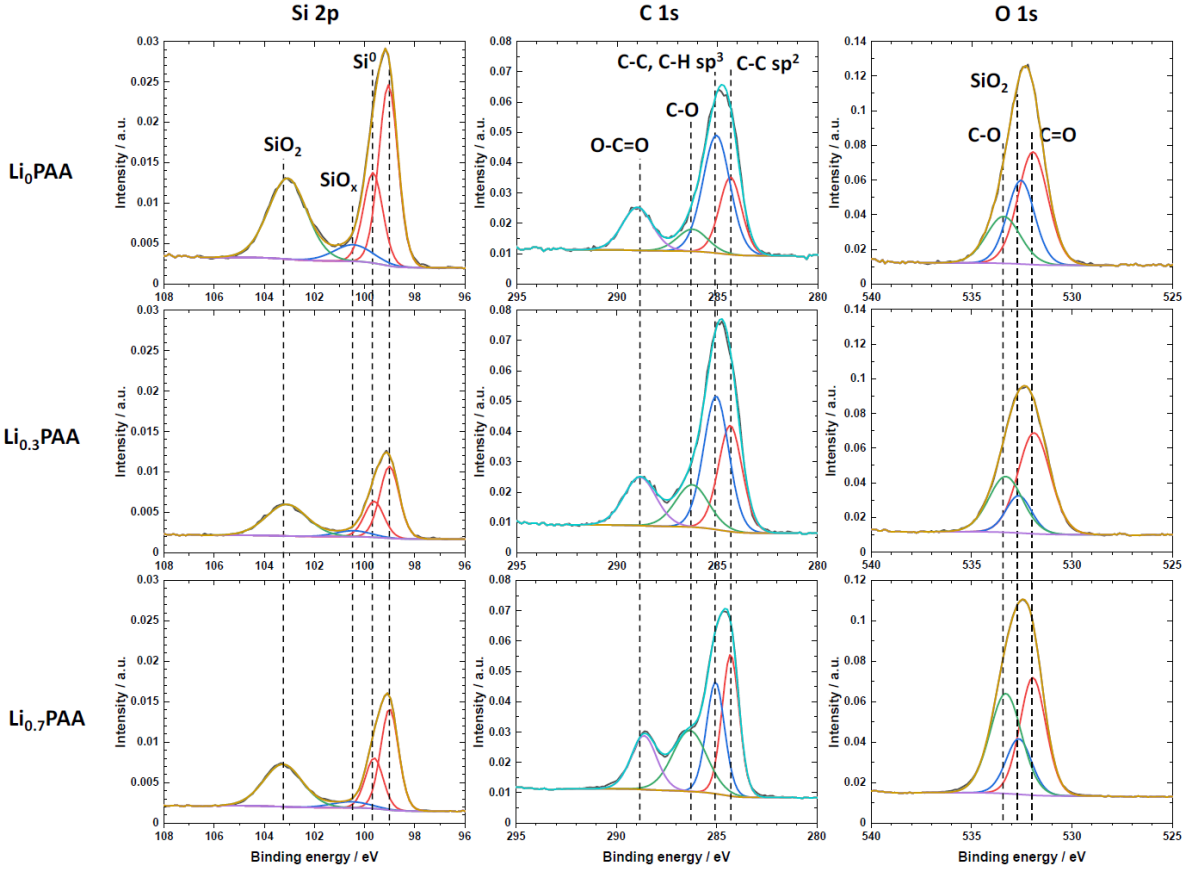

Figure 40: XPS detail measurements in the Si 2p, C 1s, and O 1s regions from pristine electrodes containing PAA binder with different neutralization degrees: Li0PAA (top row), Li0.3PAA (middle row) and Li0.7PAA (bottom row). Schematic figure 41 is reproduced with permission copyrights from "Batteries & Supercaps" (2024)[119]

The cycle life test at 1C with C/3 check-up cycles shows that partial neutralization significantly improves capacity retention as shown in **Figure 41**. The Li_0PAA electrode reaches SOH=80% after 100 cycles, while $Li_{0.3}$PAA and $Li_{0.8}$PAA last 150 cycles, and $Li_{0.7}$PAA extends to 200 cycles before rapid degradation begins. Furthermore, the C-rate tests reveal better performance in discharge and charge with higher neutralization degrees **Figure 41b**. The optimized $Li_{0.7}$PAA electrode performs best, while $Li_{0.8}$PAA shows slightly lower performance due to higher resistivity and worse adhesion. Despite lower resistivity, $Li_{0.3}$PAA's carbon black agglomeration creates an inefficient conductive network, leading to poorer performance than $Li_{0.8}$PAA. The C/3 capacity retention after the C-rate test highlights $Li_{0.7}$PAA's superior durability, maintaining near-initial capacity, while Li_0PAA shows rapid degradation.

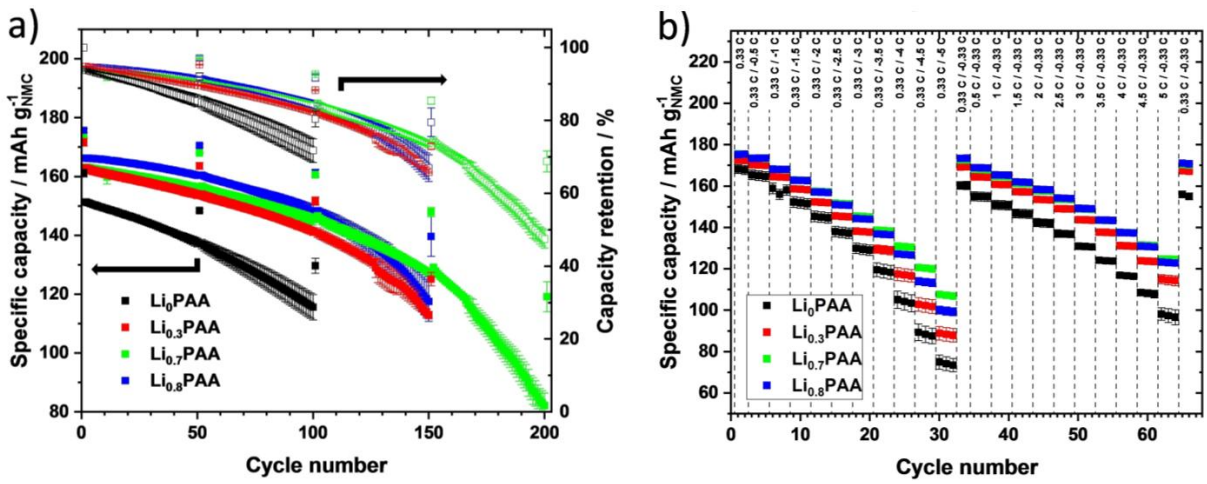

Figure 41: a) The cycling performance at 1C, with C/3 check-up cycles every 50th cycle, shows specific cathode capacity on the left y-axis and capacity retention on the right y-axis. The threshold of SOH=80% is used as the endpoint criterion. **b)** The C-rate performance of different binder variations (Li_0PAA, $Li_{0.3}$PAA, and $Li_{0.7}$PAA) is shown, with the discharge rate varying in the first half of the cycles and the charge rate in the second half. The charge and discharge rates were kept constant at C/3 during the remaining cycles. The test ends with C/3 cycles to evaluate how well the initial capacity is maintained. Schematic figure 42 is reproduced with permission copyrights from "Batteries & Supercaps" (2024)[119]

In summary, partial neutralization of PAA improves the processability and electrochemical properties of pure silicon-based anodes, enhancing their performance. However, excessive neutralization (above 70%) reduces cycle life and causes slurry gassing, making it essential to find an optimal balance. Higher specific conductivity (SC) during mixing also improves cycle life, but its interaction with neutralization degree requires further investigation. TEM-EELS and XPS analyses revealed the interaction between Si particles and the binder, as well as binder distribution. This work highlights the performance of Si-dominant anodes, with better stability in the SEI and less degradation at the electrode and particle level. Future efforts will focus on binder modifications, particularly with crosslinkers and multivalent cations, to improve self-healing properties. Ongoing experiments are exploring the impact of lower cutoff voltage on SiMP-based anodes.

These results were published in "Enabling Si-dominant Anodes: Influence of Neutralization Degree of Polyacrylic Acid on Low-Cost Micron-Sized Silicon Anode in High-Energy Li-Ion Full Cell." *Batteries & Supercaps*: e202400330.

For more detailed information see *Chapter 6.3*

3.6 Enhancing Mg deposition and dissolution from ionic liquids: the impact of additives on Mg-ion battery applications (NA4)

In this work we explored the optimization of ionic liquid (IL)-based electrolytes for magnesium-ion batteries (MgBs) by addressing challenges such as high deposition overpotential and electrolyte decomposition. We investigated the impact of various additives, including glyme-based co-solvents and $Mg(BH_4)_2$, on the electrochemical performance of $Mg(TFSI)_2$ dissolved in MPPip-TFSI ionic liquid. Glyme co-solvents significantly improved Mg deposition and dissolution kinetics compared to other additives.

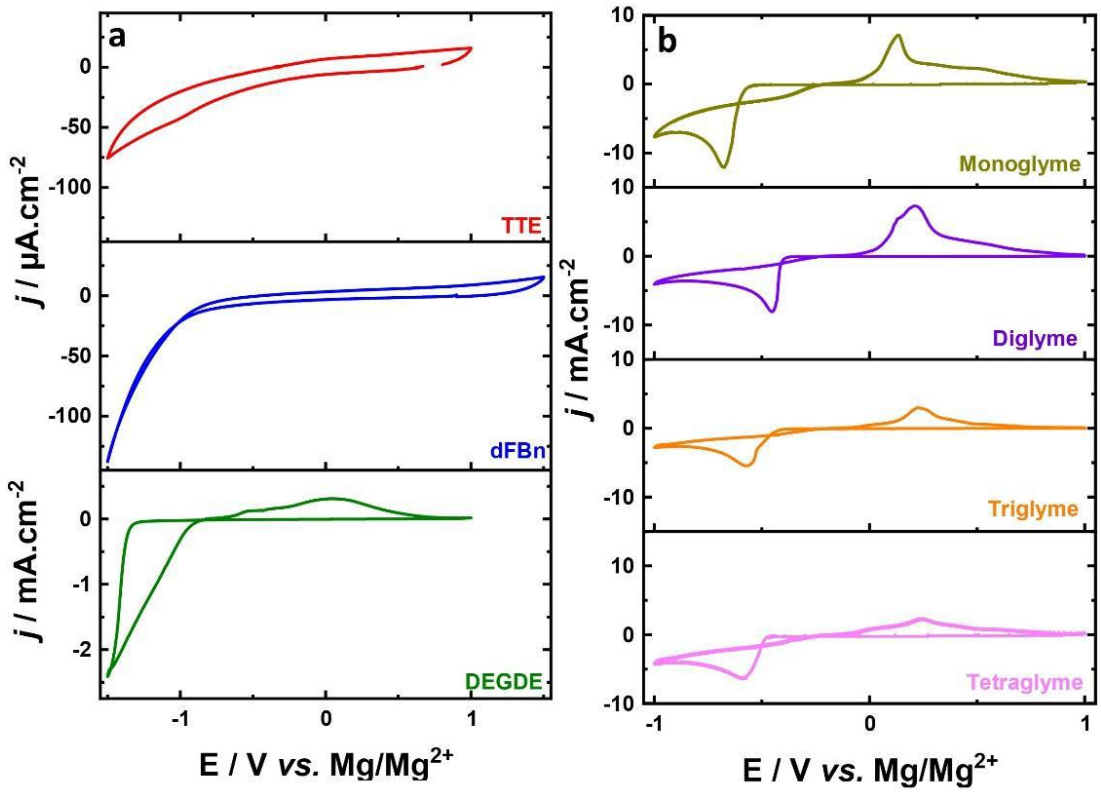

Figure 42: Cyclic voltammograms showing Mg deposition on a Pt working electrode using 0.1 M $Mg(TFSI)_2$ + 0.01 M $Mg(BH_4)_2$ in MPPip-TFSI ionic liquid with different co-solvents (1:1 ratio): **a)** Tetrafluoroethyl tetrafluoropropyl ether (TTE), difluorobenzene (dFBn), and diethylene glycol diethyl ether (DEGDE). **b)** Monoglyme, diglyme, triglyme, and tetraglyme. Scan rate: 50 mV/s vs. Mg/Mg^{2+}. Schematic figure 43 is reproduced with permission copyrights from "papers.ssrn.com" (2024)[120]

The study systematically evaluated the impact of various co-solvents on Mg deposition and dissolution in MPPip-TFSI-based electrolytes as shown in **Figure 42**. Monoglyme, added in a 1:1 ratio with 0.1 M $Mg(TFSI)_2$, exhibited negligible effects on electrochemical performance. However, the inclusion of 10 mM $Mg(BH_4)_2$ significantly facilitated Mg deposition at –0.5 V vs. Mg/Mg^{2+} and dissolution at 0.2 V vs. Mg/Mg^{2+}. Co-solvents such as dFBn and DEGDE displayed distinct behaviors: dFBn supported Mg deposition at –1.0 V vs. Mg/Mg^{2+} without

detectable dissolution, while DEGDE enabled reversible Mg deposition at –1.5 V vs. Mg/Mg^{2+} and dissolution near 0.0 V vs. Mg/Mg^{2+}. DEGDE's ability to form moderately stable Mg-ion complexes enhanced the deposition/dissolution processes, although its efficiency was inferior to glyme-based systems. Glymes demonstrated superior performance by forming optimally stable Mg complexes, achieving deposition at –0.5 V vs. Mg/Mg^{2+} and dissolution at 0.1 V vs. Mg/Mg^{2+}. These findings underscore the critical role of glyme co-solvents in facilitating efficient Mg-ion transport, with further investigations into DEGDE and dFBn planned for future studies.

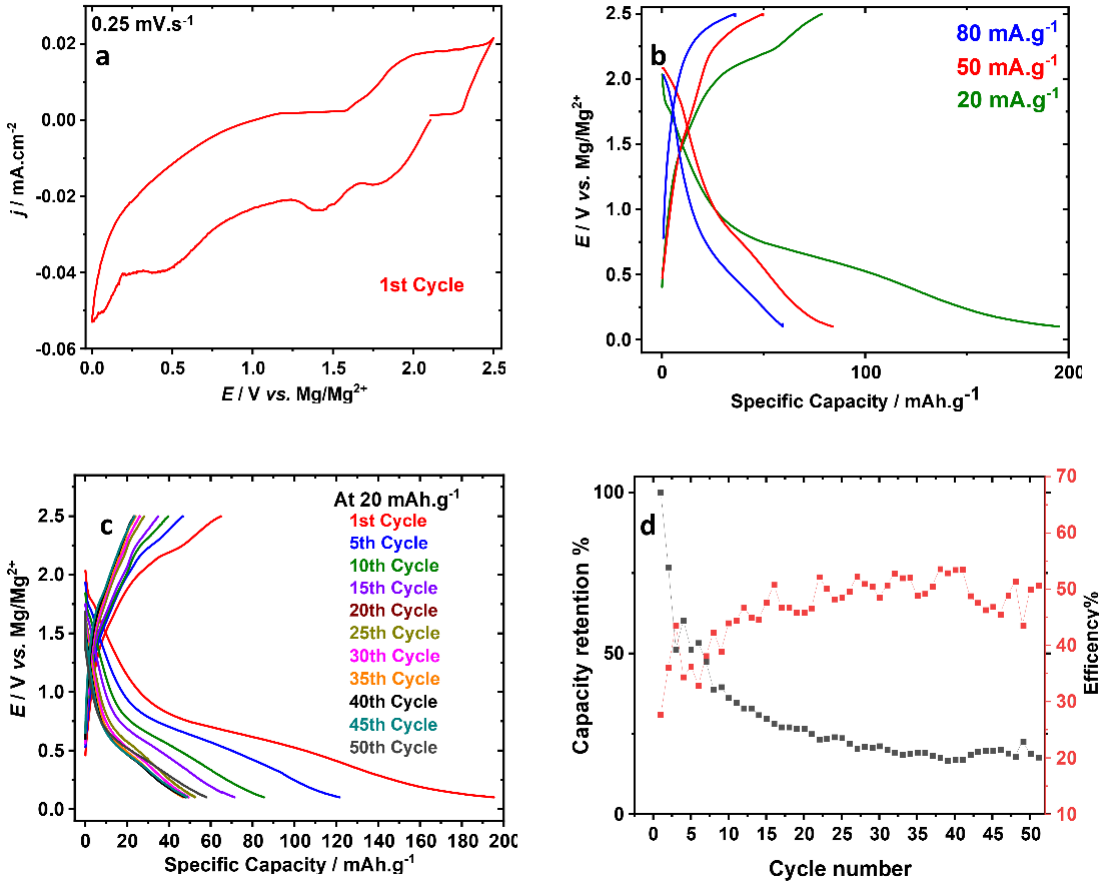

Figure 43: a) CV of WS_2/PANI-40 | 0.1 M $Mg(TFSI)_2$ + 0.01 M $Mg(BH_4)_2$ in MPPip-TFSI IL with G2 (1:3) | Mg, at a scan rate of 0.25 mV/s. **b)** Charge–discharge profiles of WS_2/PANI-40 at varying current densities. **c)** Stability of the WS_2/PANI-40 electrode over 50 cycles at 20 mA/g. **d)** Capacity retention and coulombic efficiency as a function of the number of cycles. Schematic figure 44 is reproduced with permission copyrights from "papers.ssrn.com" (2024)[120]

As a proof of concept, the optimized electrolyte was tested in a Mg full cell using WS_2/PANI composites as the cathode. Polyaniline (PANI) improved ionic conductivity and mitigated restacking and agglomeration. SEM and XRD analyses confirmed the successful formation and purity of the WS_2/PANI composite. Asymmetric WS_2/PANI | optimized electrolyte | Mg cells were assembled and rested at 1.9 V (OCV) overnight. Cyclic voltammetry revealed

intercalation and deintercalation peaks at 0.5 V and 2.0 V vs. Mg/Mg^{2+}, respectively, with additional cathodic peaks at 1.5 V and 2.0 V vs. Mg/Mg^{2+} attributed to PANI reduction as shown in **Figure 43a**. The first cycle capacities for WS_2/PANI-40 were 84, 60, and 195 mAh/g at 80, 50, and 20 mA/g, respectively, with the 20 mA/g capacity being 2.5 times higher than WS_2/graphene in MAAC (magnesium-aluminum chloride complex) electrolytes as shown in **Figure 43b**. After 50 cycles at 20 mA/g, ~25% of the initial capacity was retained, while coulombic efficiency improved to 50%. The low-capacity retention was attributed to partial PANI degradation during cycling. To address this, WS_2/PANI was dried at 70 °C (WS_2/PANI-70) for further investigation.

The optimized electrolyte system demonstrated improved ionic conductivity, lower viscosity, and enhanced electrochemical stability. Galvanostatic cycling in symmetric Mg cells confirmed the electrolyte's stability over 125 hours. The electrolyte was validated using a WS_2/PANI composite cathode in Mg full cells. The composite achieved a specific capacity of 197 mAh/g at 20 mA/g. However, significant capacity fading (75% after 50 cycles) was attributed to the electrode material degradation during cycling.

This study addresses the challenges of Mg deposition from pure MPPip-TFSI, hindered by electrolyte decomposition and high overpotential. An optimized electrolyte system was developed using Mg salt additives and glyme-based co-solvents, with a 1:3 MPPip-TFSI-to-G2 ratio achieving the best performance. The addition of $Mg(BH_4)_2$ further lowered deposition overpotential by 68.42% and supported higher current densities. When tested in a Mg metal battery with WS_2/PANI as the cathode, the optimized system achieved a high initial capacity of 197 mAh/g at 20 mA/g, 2.5 times higher than previous WS_2/graphene systems. However, capacity faded by 75% after 50 cycles, attributed to PANI cross-linking and degradation during cycling.

These results were published in "Boosting Mg Deposition and Dissolution from Ionic Liquids – the Role of Different Additives for Applications in Mg-Ion Batteries." Available at SSRN: https://ssrn.com/abstract=4948315 or doi.org/10.2139/ssrn.4948315

For more detailed information see *Chapter 6.4 (NA4)*

4. Summary and Outlook

The research presented in this thesis provides a comprehensive analysis of the molecular structural properties of solid-state polyoxovanadate clusters. The electrochemical deposition, recognized for its versatility, was employed to synthesize highly stable, solid-state, redox-active POV nanostructured. This method was extensively investigated to bridge the gap between the tunability of POV clusters and the development of high-performance POV-based active materials for energy storage applications. The electrochemical deposition approach not only offers a systematic pathway for the tuning of POV materials but also facilitates the in-situ reduction of the POV framework, allowing for heterometallic functionalization. This strategy enables straightforward and reproducible structural and electrochemical modifications of the POV framework, optimizing it for energy storage performance.

4.1 High-performance reversible electrodeposited potassium-bridged molecular vanadium cluster for energy storage

We have reported, for the first time, the fully reversible reduction and electrodeposition of a novel molecular nanocluster, $K_5\{V_{12}\}$, under non-aqueous conditions. This method was systematically explored as a successive approach to achieve multi-electron storage with structural stability. A high-performance homogeneous film was synthesized by incorporating potassium cations and subsequently reducing the $\{V_{12}\}$ cluster onto a conductive electrode surface under controlled conditions. The influence of various electrodeposition parameters was investigated to optimize the reduced $K_5\{V_{12}\}$ film. Within a specific potential range, the electrodeposition process demonstrated complete reversibility. This electrochemical tunning of the synthesized film enables a design of devices capable of multi-electron storage and release. Detailed mechanistic and structural studies revealed that deposition of $K_5\{V_{12}\}$ in the potential range of -500 to 500 mV vs Ag^+/Ag results in a fully reversible deposition of the $K_5\{V_{12}\}$ cluster. However, at an increasingly negative potential, from -900 mV to 500 mV vs Ag^+/Ag, significant structural changes in the film occur, affecting the reversibility of the deposition process. Initial investigations into the electron storage capacity of the deposited films suggested promising potential active cathode materials in PIBs, encouraging further exploration of this material class for electrochemical energy storage systems.

4.2 Highly porous Laser-induced graphene surface modification by the reduced polyoxovanadate ($K_5\{V_{12}\}$) nanocluster and shown the improved supercapacitive performance

In this work, we demonstrated the effective electrochemical immobilization of the $K_5\{V_{12}\}$ nanocluster on a highly porous graphene-like LIG substrate through a straightforward cyclic voltammetry technique. The electrochemical deposition of the nanocluster within different potential ranges corresponds to distinct electronic and electrochemical changes in the LIG electrodes. The optimum POV deposition was achieved for electrodeposition in the potential range of -750 to 750 mV vs Ag^+/Ag, which leads to the presence of a highly redox-active and stable reduced cluster species on the LIG surface. This process also fine-tunes the electrochemical active sites on the graphene surface. The resulting K-POV-750 electrode exhibits a superior areal capacity of 125 mF/cm^2 at a current density of 0.1 mA/cm^2. As a comparison, the unmodified LIG electrode delivers an areal capacity of 25 mF/cm^2 at 0.1 mA/cm^2. Detailed Raman measurements and XPS analysis provide insights into the deposition of POV clusters at different potential ranges and possible structural and material modifications of the LIG surface. Raman mapping reveals preferential deposition of $K_5\{V_{12}\}$ cluster in low crystallinity regions, enabling high electronic conductivity of LIG after deposition. At the same time, detailed Raman analysis on the modified K-POV-750 electrode reveals the oxidation of surface sp^2 carbon centers. The deposited $K_5\{V_{12}\}$ clusters also transformed to dimeric V^{5+} or monomeric V^{4+} polyoxovanadate centers on the modified electrode surface. Furthermore, the performance of the modified K-POV-750 electrode was evaluated in a symmetrical real supercapacitor device assembled with PVA/H_2SO_4-based gel electrolyte. The flexible symmetrical supercapacitor (SSC) with K-POV-750 sustains excellent electrochemical response with an areal capacitance of 24.92 mF/cm^2 at 0.1 mA/cm^2 and good capacity retention of 69% for up to 5000 charge-discharge cycles. The SSC-KPOV-750 device delivers an energy density of 5.68 mWh/cm^2 and a power density of 0.063 mW/cm^2. This work presents a sustainable approach for introducing a highly redox-active potassium-bridged polyoxovanadate nanocluster into a graphene-like LIG framework, enhancing structural stability and improving electrochemical performance. The findings hold promise for applications in micro-flexible smart devices, particularly in fabricating flexible micro-supercapacitors, without binders or current collectors.

4.3 Challenges and approaches for integrating carbon-additive and binder-free potassium-stabilized vanadium oxides thin film as cathode materials in LIBs and (Post-) lithium-ion batteries

The integration of molecular POV structures into the field of energy storage faces significant challenges, primarily related to maintaining their structural stability in solid-state form. Battery electrode materials require a high degree of structural integrity to sustain redox processes at high voltage ranges. Previous studies have demonstrated the potential of molecular polyoxovanadates as a promising active material for electrode fabrication in LIBs. For instance, $Li_7[V_{15}O_{36}(CO_3)]$ has shown an excellent reversible redox process at a high discharge rate of 2 A/g, achieving a capacity of 170 mAh/g.[121] Similarly, a hydrothermally synthesized Mn_3V_{19}-HIL/RGO-1 cathode material exhibited a discharge capacity of 121 mAh/g at 5 A/g, indicating outstanding cycling stability. The superior performance of these POV-based electrodes relies on the multiple valance state of vanadium, which easily transitions from V^{5+} to V^{4+}, or even from V^{5+} to V^{3+}, involving multiple electron transfer processes. However, altering the oxidation state can lead to the decomposition of their molecular structure, resulting in rapid capacity fading. To address this issue, the incorporation of heterometals into the POV structure has set a new benchmark for stabilizing the molecular framework and preventing irreversible deformation.

In this study, we demonstrate the electrochemical heterometallic functionalization of $\{V_{12}\}$, $K_5\{V_{12}\}$, and $\{V_{18}\}$ clusters to obtain potassium cation-supported supramolecular films on conductive surfaces. We thoroughly investigated the reduced POV cluster frameworks enabled by potassium to mitigate cluster dissolution in both aqueous and non-aqueous electrolytes. Due to the strong electrochemical interaction between the POV framework and K^+, the growth of a highly stable and homogeneous film was achieved. Notably, this cluster reduction and film deposition method represents a promising approach to modifying the material and electrochemical properties by adjusting the electrodeposition parameters. We demonstrated that the synthesized $K_5\{V_{12}\}$ cluster could be restructured to accommodate more than five potassium cations per cluster unit after optimizing the reduction potential range. Similarly, the mass loading and thickness of the film could be precisely controlled by varying the deposition potentials and duration. We also investigated the in-situ reduction and K^+ interaction of the large octadecavanadate $=\{V_{18}\}$ cluster to synthesize high-performance, stable $K_x\{V_{18}\}$ thin films directly on the commercial current collectors.

The initial findings confirmed that these potassium-supported POV films exhibit strong reversible redox activity and show promising charge storage capacity when used as cathode materials in half-cell LIBs and PIBs. The $K_x\{V_{12}\}$ derived from $K_5\{V_{12}\}$ nanocluster undergoes fast, reversible reductions involving multiple electron redox processes when tested as cathode materials in PIBs. The optimized film achieved a discharge capacity of 59 mAh/g at a discharge rate of 50 mA/g. Similarly, in-situ functionalized $\{V_{12}\}$ with K^+ tested as a cathode material in half-cell LIBs exhibited a high initial discharge capacity of ~200 mAh/g at 50 mA/g for the first few cycles, stabilizing at 120 mAh/g for the next 80 cycles. These results indicate that the electrochemically deposited $\{V_{12}\}$-based films undergo reversible stabilization during electrochemical cycling with multiple electron transfer.

Furthermore, the film synthesized with large $\{V_{18}\}$ nanoclusters showed a similar electrochemical response, with electrodeposition occurring alongside slightly higher cations incorporation. The optimized thin film, when tested as a cathode material for half-cell LIBs, resulted in a discharge capacity of 156 mAh/g at the current density of 50 mA/g and demonstrated excellent cycling stability, maintaining 80 mAh/g for up to 1000 cycles.

4.4 Preliminary results of Mg^{2+} and Na^+ cation interactions with $\{V_{18}\}$ nanocluster *via* electrochemical deposition

To expand upon these findings, we further explored in-situ functionalization of $\{V_{18}\}$ molecular structure beyond K^+ cations, incorporating different alkali earth metal cations such as Na^+, Mg^{2+}, and Li^+.

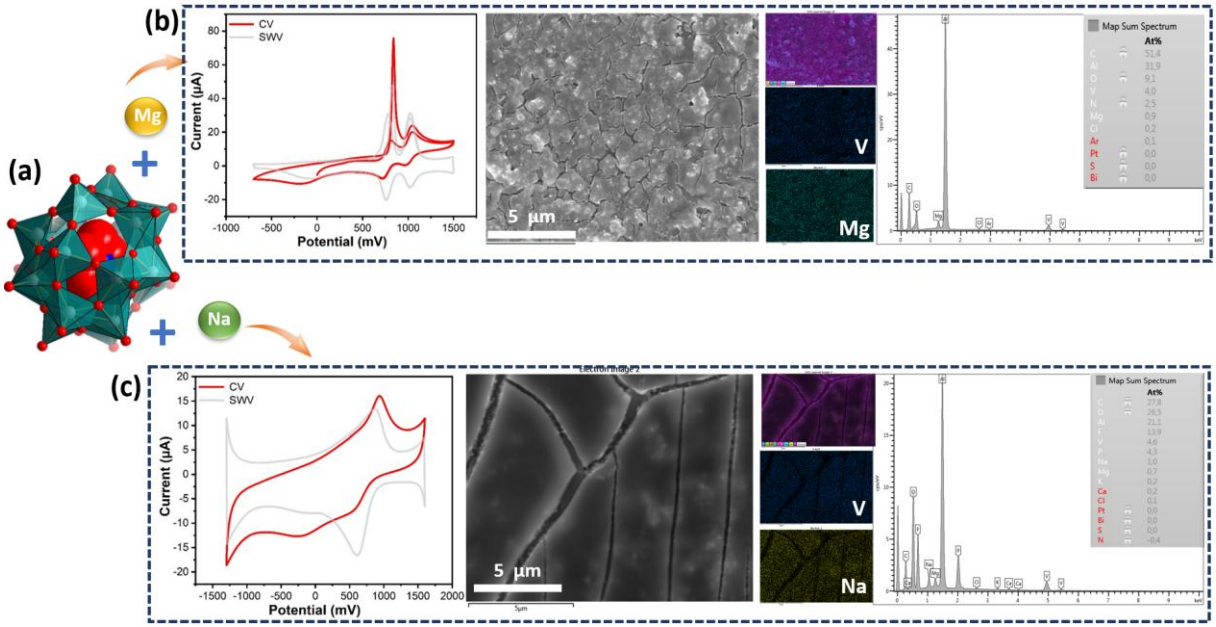

Figure 44: (a) unit molecular $\{V_{18}\}$ cluster structure, **(b)** electrochemical study and material properties of the obtained $Mg_x\{V_{18}\}$ film, and **(c)** electrochemical study and material properties of the obtained $Na_x\{V_{18}\}$ film, (condition: CV and SWV measurement performed in three electrodes setup with Ag^+/Ag reference electrode, Pt wire as a counter electrode, electrolyte prepared by mixing Mg and Na based electrolyte salt (e.g. $Mg(ClO_4)_2$ and $NaPF_6$) in MeCN and then dissolved $\{V_{18}\}$ cluster to obtain 0.5 mM electrolyte solution)

Figure 44 presents the preliminary results of the interaction between Mg^{2+} and Na^+ cation and $\{V_{18}\}$ nanocluster using the electrochemical deposition method. Interestingly, both Mg^{2+} and Na^+ cations exhibit similar deposition behaviors to the previously observed K^+ cations. This electrochemical interaction between $\{V_{18}\}$ and alkali cations was achieved by dissolving the $\{V_{18}\}$ nanocluster in Mg- and Na-based supporting electrolytes. The electrochemical measurement confirmed the successful interaction between these cations and the $\{V_{18}\}$ cluster, resulting in mass deposition on the electrode surface through an electrochemical process. Further studies are needed to explore the detailed material properties of Mg- and Na-functionalized $\{V_{18}\}$ film, which could serve as promising binder- and carbon-additives-free cathode materials for (post-) lithium-ion battery applications.

5. References

[1] R. Jung, M. Metzger, F. Maglia, C. Stinner, H. A. Gasteiger, *J Electrochem Soc* **2017**, *164*, A1361–A1377.

[2] E. A. Olivetti, G. Ceder, G. G. Gaustad, X. Fu, *Joule* **2017**, *1*, 229–243.

[3] Y. Zhang, J. Liu, S. L. Li, Z. M. Su, Y. Q. Lan, *EnergyChem* **2019**, *1*, 100021.

[4] M. Anjass, G. A. Lowe, C. Streb, *Angewandte Chemie International Edition* **2021**, *60*, 7522–7532.

[5] M. T. Pope, A. Müller, *Angewandte Chemie International Edition in English* **1991**, *30*, 34–48.

[6] M. T. Pope, A. Müller, *Angewandte Chemie International Edition in English* **1991**, *30*, 34–48.

[7] S. S. Wang, G. Y. Yang, *Chem Rev* **2015**, *115*, 4893–4962.

[8] B. Keita, L. Nadjo, *J Mol Catal A Chem* **2007**, *262*, 190–215.

[9] A. Proust, R. Thouvenot, P. Gouzerh, *Chemical Communications* **2008**, 1837–1852.

[10] J. T. Rhule, C. L. Hill, D. A. Judd, R. F. Schinazi, *Polyoxometalates in Medicine*, **1998**.

[11] J. Wang, Z. Tao, T. Tian, J. Qiu, H. Qian, Z. Zha, Z. Miao, Y. Ma, H. Wang, *Chemical Engineering Journal* **2021**, *416*, 129137.

[12] M. B. Čolović, M. Lacković, J. Lalatović, A. S. Mougharbel, U. Kortz, D. Z. Krstić, *Curr Med Chem* **2020**, *27*, 362–379.

[13] S. Herrmann, N. Aydemir, F. Nägele, D. Fantauzzi, T. Jacob, J. Travas-Sejdic, C. Streb, *Adv Funct Mater* **2017**, *27*, DOI 10.1002/adfm.201700881.

[14] Y. Zhang, J. Liu, S.-L. Li, Z.-M. Su, Y.-Q. Lan, *EnergyChem* **2019**, *1*, 100021.

[15] Y. Ji, L. Huang, J. Hu, C. Streb, Y.-F. Song, *Energy Environ Sci* **2015**, *8*, 776–789.

[16] D. Long, R. Tsunashima, L. Cronin, *Angewandte Chemie International Edition* **2010**, *49*, 1736–1758.

[17] I. Lindqvist, *Acta Crystallogr* **1952**, *5*, 667–670.

[18] *Proceedings of the Royal Society of London. Series A, Containing Papers of a Mathematical and Physical Character* **1934**, *144*, 75–100.

[19] B. Dawson, *Acta Crystallogr* **1953**, *6*, 113–126.

[20] J. S. ANDERSON, *Nature* **1937**, *140*, 850.

[21] Y. J. M. F. MT Pope, **n.d.**

[22] L. and L. C. Vilà-Nadal, *Nature Reviews Materials 2* **2017**.

[23] K. Wassermann, M. H. Dickman, M. T. Pope, *Angewandte Chemie International Edition in English* **1997**, *36*, 1445–1448.

[24] T. Zhou, L.-L. Xie, Y. Niu, H.-R. Xiao, Y.-J. Li, Q. Han, X.-J. Qiu, X.-L. Yang, X.-Y. Wu, L.-M. Zhu, H. Pang, X.-Y. Cao, *Rare Metals* **2023**, *42*, 1431–1445.

[25] S. Surnev, M. G. Ramsey, F. P. Netzer, *Prog Surf Sci* **2003**, *73*, 117–165.

[26] L. E. VanGelder, T. R. Cook, E. M. Matson, *Comments on Inorganic Chemistry* **2019**, *39*, 51–89.

[27] M. Anjass, G. A. Lowe, C. Streb, *Angewandte Chemie International Edition* **2021**, *60*, 7522–7532.

[28] G. Ladwig, *Z Anorg Allg Chem* **1967**, *353*, 311–319.

[29] H. Michibata, T. Ueki, *Biomol Concepts* **2010**, *1*, 97–107.

[30] D. Hou, K. S. Hagen, C. L. Hill, *J. Chem. Soc., Chem. Commun.* **1993**, *0*, 426–428.

[31] K. Kastner, J. T. Margraf, T. Clark, C. Streb, *Chemistry – A European Journal* **2014**, *20*, 12269–12273.

[32] K. Kastner, J. Forster, H. Ida, G. N. Newton, H. Oshio, C. Streb, *Chemistry – A European Journal* **2015**, *21*, 7686–7689.

[33] Y. Ji, J. Hu, J. Biskupek, U. Kaiser, Y. Song, C. Streb, *Chemistry – A European Journal* **2017**, *23*, 16637–16643.

[34] K. Kastner, M. Lechner, S. Weber, C. Streb, *ChemistrySelect* **2017**, *2*, 5542–5544.

[35] B. Schwarz, M. Dürr, K. Kastner, N. Heber, I. Ivanović-Burmazović, C. Streb, *Inorg Chem* **2019**, *58*, 11684–11688.

[36] S. Greiner, M. Anjass, C. Streb, *CrystEngComm* **2021**, *23*, 3946–3950.

[37] Q. C. R. C. H. J. Z. A. C. J. O. VICTORIA SOGHOMONIAN, **1993**, *259*.

[38] K. Kastner, J. Forster, H. Ida, G. N. Newton, H. Oshio, C. Streb, *Chemistry – A European Journal* **2015**, *21*, 7686–7689.

[39] S. Greiner, J. Hettig, A. Laws, K. Baumgärtner, J. Bustos, A. Pöppler, A. H. Clark, M. Nyman, C. Streb, M. Anjass, *Angewandte Chemie* **2022**, *134*, DOI 10.1002/ange.202114548.

[40] M. H. Anjass, M. Deisböck, S. Greiner, M. Fichtner, C. Streb, *ChemElectroChem* **2019**, *6*, 398–403.

[41] K. Wang, Y. Niu, D. Zhao, Y. Zhao, P. Ma, D. Zhang, J. Wang, J. Niu, *Inorg Chem* **2017**, *56*, 14053–14059.

[42] T.-Y. Dang, R.-H. Li, H.-R. Tian, Q. Wang, Y. Lu, S.-X. Liu, *Inorg Chem Front* **2021**, *8*, 4367–4375.

[43] J.-K. Li, X.-Q. Huang, S. Yang, H.-W. Ma, Y.-N. Chi, C.-W. Hu, *Inorg Chem* **2015**, *54*, 1454–1461.

[44] L. E. VanGelder, A. M. Kosswattaarachchi, P. L. Forrestel, T. R. Cook, E. M. Matson, *Chem Sci* **2018**, *9*, 1692–1699.

[45] C.-D. Zhang, S.-X. Liu, B. Gao, C.-Y. Sun, L.-H. Xie, M. Yu, J. Peng, *Polyhedron* **2007**, *26*, 1514–1522.

[46] T. Rom, R. Biswas, K. K. Haldar, U. Saha, S. Rayaprol, A. K. Paul, *Cryst Growth Des* **2022**, *22*, 4666–4672.

[47] L. Qiao, M. Song, A. Geng, S. Yao, *Chinese Chemical Letters* **2019**, *30*, 1273–1276.

[48] H. Chen, G. Wee, R. Al-Oweini, J. Friedl, K. S. Tan, Y. Wang, C. L. Wong, U. Kortz, U. Stimming, M. Srinivasan, *ChemPhysChem* **2014**, *15*, 2162–2169.

[49] J. L. Gunjakar, A. I. Inamdar, B. Hou, S. Cha, S. M. Pawar, A. A. Abu Talha, H. S. Chavan, J. Kim, S. Cho, S. Lee, Y. Jo, H. Kim, H. Im, *Nanoscale* **2018**, *10*, 8953–8961.

[50] H. Hu, L. Lian, X. Ji, W.-L. Zhao, H. Li, W. Chen, H. N. Miras, Y.-F. Song, *Coord Chem Rev* **2024**, *503*, 215640.

[51] S. Greiner, B. Schwarz, M. Ringenberg, M. Dürr, I. Ivanovic-Burmazovic, M. Fichtner, M. Anjass, C. Streb, *Chem Sci* **2020**, *11*, 4450–4455.

[52] Q. Zhang, J. Ondus, K. Sheriff, J. Mills, A. Bahadori, J. Smith, S.-J. Hwu, *Polyhedron* **2021**, *209*, 115459.

[53] M. Wendt, U. Warzok, C. Näther, J. van Leusen, P. Kögerler, C. A. Schalley, W. Bensch, *Chem Sci* **2016**, *7*, 2684–2694.

[54] S. Mulkapuri, S. K. Kurapati, S. K. Das, *Dalton Transactions* **2019**, *48*, 8773–8781.

[55] S. Repp, M. Steiner, M. Anjass, D. Sorsche, C. Streb, *Chemical Communications* **2022**, *58*, 13397–13400.

[56] A. Mahmoud, B. Keita, L. Nadjo, O. Oung, R. Contant, S. Brown, Y. de Kouchkovsky, *Journal of Electroanalytical Chemistry* **1999**, *463*, 129–145.

[57] G. Bidan, E. M. Genies, M. Lapkowski, *J Electroanal Chem Interfacial Electrochem* **1988**, *251*, 297–306.

[58] J. Luo, C. Leng, L. Chen, J. Yuan, H. Li, J. Zhao, *Synth Met* **2012**, *162*, 1558–1565.

[59] Z.-H. Li, Z.-Y. Yao, X.-L. Xie, S. Wang, Y. Zou, H.-J. Yu, X.-M. Ren, *ACS Applied Engineering Materials* **2023**, *1*, 350–358.

[60] Z. Sun, M. Zhao, F. Li, T. Wang, L. Xu, *Mater Res Bull* **2014**, *60*, 524–529.

[61] D. M. Fernandes, S. M. N. Simões, H. M. Carapuça, A. M. V. Cavaleiro, *Electrochim Acta* **2008**, *53*, 6580–6588.

[62] A. Dolbecq, J. Compain, P. Mialane, J. Marrot, F. Sécheresse, B. Keita, L. R. B. Holzle, F. Miserque, L. Nadjo, *Chemistry – A European Journal* **2009**, *15*, 733–741.

[63] M. Endo, T. Takeda, Y. Kim, K. Koshiba, K. Ishii, *Carbon letters* **2001**, *1*.

[64] M. H. Anjass, K. Kastner, F. Nägele, M. Ringenberg, J. F. Boas, J. Zhang, A. M. Bond, T. Jacob, C. Streb, *Angewandte Chemie International Edition* **2017**, *56*, 14749–14752.

[65] S. Fletcher, *Bottled Lightning: Superbatteries, Electric Cars, and the New Lithium Economy*, Hill And Wang, 2012, **n.d.**

[66] Armand M, in *Fast Ion Transport in Solids: Solid State Batteries and Devices* (Ed.: van Gool W), Amsterdam, **1973**, pp. 665–673.

[67] J. Kalhoff, G. G. Eshetu, D. Bresser, S. Passerini, *ChemSusChem* **2015**, *8*, 2154–2175.

[68] Md. A. Rahman, Y. C. Wong, G. Song, C. Wen, *Journal of Porous Materials* **2015**, *22*, 1313–1343.

[69] J. Yamaura, Y. Ozaki, A. Morita, A. Ohta, *J Power Sources* **1993**, *43*, 233–239.

[70] H. Adenusi, G. A. Chass, S. Passerini, K. V. Tian, G. Chen, *Adv Energy Mater* **2023**, *13*, DOI 10.1002/aenm.202203307.

[71] P. Nelson, S. Ahmed, K. Gallagher, D. Dees, *Modeling the Performance and Cost of Lithium-Ion Batteries for Electric-Drive Vehicles, Third Edition*, Argonne, IL (United States), **2019**.

[72] P. Suresh, S. Rodrigues, A. K. Shukla, S. A. Shivashankar, N. Munichandraiah, *J Power Sources* **2002**, *112*, 665–670.

[73] W. LI, J. REIMERS, J. DAHN, *Solid State Ion* **1993**, *67*, 123–130.

[74] J. N. Reimers, J. R. Dahn, U. von Sacken, *J Electrochem Soc* **1993**, *140*, 2752–2754.

[75] M. Kotal, S. Jakhar, S. Roy, H. K. Sharma, *J Energy Storage* **2022**, *47*, 103534.

[76] M. Gu, I. Belharouak, J. Zheng, H. Wu, J. Xiao, A. Genc, K. Amine, S. Thevuthasan, D. R. Baer, J.-G. Zhang, N. D. Browning, J. Liu, C. Wang, *ACS Nano* **2013**, *7*, 760–767.

[77] A. Rougier, P. Gravereau, C. Delmas, *J Electrochem Soc* **1996**, *143*, 1168–1175.

[78] T. Ohzuku, Y. Makimura, *Chem Lett* **2001**, *30*, 744–745.

[79] W. Zhong, J. Huang, S. Liang, J. Liu, Y. Li, G. Cai, Y. Jiang, J. Liu, *ACS Energy Lett* **2020**, *5*, 31–38.

[80] Y. Ji, L. Huang, J. Hu, C. Streb, Y.-F. Song, *Energy Environ Sci* **2015**, *8*, 776–789.

[81] N. Kawasaki, H. Wang, R. Nakanishi, S. Hamanaka, R. Kitaura, H. Shinohara, T. Yokoyama, H. Yoshikawa, K. Awaga, *Angewandte Chemie* **2011**, *123*, 3533–3536.

[82] H. Yang, T. Song, L. Liu, A. Devadoss, F. Xia, H. Han, H. Park, W. Sigmund, K. Kwon, U. Paik, *The Journal of Physical Chemistry C* **2013**, *117*, 17376–17381.

[83] A. Xie, C.-A. Ma, L. Wang, Y. Chu, *Electrochim Acta* **2007**, *52*, 2945–2949.

[84] L. E. VanGelder, T. R. Cook, E. M. Matson, *Comments on Inorganic Chemistry* **2019**, *39*, 51–89.

[85] H. Liu, J. Wang, *Ionics (Kiel)* **2010**, *16*, 379–383.

[86] M. H. Anjass, M. Deisböck, S. Greiner, M. Fichtner, C. Streb, *ChemElectroChem* **2019**, *6*, 398–403.

[87] S. Shiraishi, in *Carbon Alloys*, Elsevier, **2003**, pp. 447–457.

[88] N. R. Chodankar, H. D. Pham, A. K. Nanjundan, J. F. S. Fernando, K. Jayaramulu, D. Golberg, Y. Han, D. P. Dubal, *Small* **2020**, *16*, DOI 10.1002/smll.202002806.

[89] D. P. Dubal, N. R. Chodankar, P. Gomez-Romero, D.-H. Kim, in *Metal Oxides in Supercapacitors*, Elsevier, **2017**, pp. 79–98.

[90] J. Gamby, P. L. Taberna, P. Simon, J. F. Fauvarque, M. Chesneau, *J Power Sources* **2001**, *101*, 109–116.

[91] W.-J. Liu, K. Tian, Y.-R. He, H. Jiang, H.-Q. Yu, *Environ Sci Technol* **2014**, *48*, 13951–13959.

[92] Z. S. Iro, C. Subramani, S. S. Dash, *Int J Electrochem Sci* **2016**, *11*, 10628–10643.

[93] H. Choi, H. Yoon, *Nanomaterials* **2015**, *5*, 906–936.

[94] M. Zhi, C. Xiang, J. Li, M. Li, N. Wu, *Nanoscale* **2013**, *5*, 72–88.

[95] M. G. Tadesse, A. S. Ahmmed, J. F. Lübben, *Journal of Composites Science* **2024**, *8*, 53.

[96] M. Genovese, K. Lian, *Curr Opin Solid State Mater Sci* **2015**, *19*, 126–137.

[97] M. Skunik, M. Chojak, I. A. Rutkowska, P. J. Kulesza, *Electrochim Acta* **2008**, *53*, 3862–3869.

[98] J. Wang, X. Wang, D. Gu, C. Liu, L. Shen, *Ceram Int* **2018**, *44*, 17492–17498.

[99] T. Zhao, L. Cui, K. Yu, J. Lv, Y. Ma, A. Yang, B. Zhou, *ACS Appl Mater Interfaces* **2022**, *14*, 30099–30111.

[100] Y. Liu, W. Yao, H. Gan, C. Sun, Z. Su, X. Wang, *Chemistry – A European Journal* **2019**, *25*, 16617–16624.

[101] H. Lv, Y. V. Geletii, C. Zhao, J. W. Vickers, G. Zhu, Z. Luo, J. Song, T. Lian, D. G. Musaev, C. L. Hill, *Chem Soc Rev* **2012**, *41*, 7572.

[102] N. Arya, T. Philipp, S. Greiner, M. Steiner, C. Kranz, M. Anjass, *Angewandte Chemie International Edition* **2023**, *62*, DOI 10.1002/anie.202306170.

[103] T. Kobayashi, S. Kuwajima, T. Kurata, Y. Hayashi, *Inorganica Chim Acta* **2014**, *420*, 69–74.

[104] N. Arya, S. Dinda, T. Diemant, K. Wang, M. Fichtner, M. Anjass, *Adv Funct Mater* **2024**, DOI 10.1002/adfm.202410943.

[105] M. A. Pimenta, G. Dresselhaus, M. S. Dresselhaus, L. G. Cançado, A. Jorio, R. Saito, *Phys. Chem. Chem. Phys.* **2007**, *9*, 1276–1290.

[106] A. C. Ferrari, J. Robertson, *Phys Rev B* **2000**, *61*, 14095–14107.

[107] A. Eckmann, A. Felten, A. Mishchenko, L. Britnell, R. Krupke, K. S. Novoselov, C. Casiraghi, *Nano Lett* **2012**, *12*, 3925–3930.

[108] S. Dinda, T. Braun, F. D. Pammer, J. Choi, S. Fleischmann, M. Fichtner, *Carbon N Y* **2024**, *218*, 118753.

[109] R. Baddour-Hadjean, A. Boudaoud, S. Bach, N. Emery, J.-P. Pereira-Ramos, *Inorg Chem* **2014**, *53*, 1764–1772.

[110] J. Wang, J. Polleux, J. Lim, B. Dunn, *The Journal of Physical Chemistry C* **2007**, *111*, 14925–14931.

[111] T. Brezesinski, J. Wang, S. H. Tolbert, B. Dunn, *Nat Mater* **2010**, *9*, 146–151.

[112] N. Kumar, M. Singh, A. Kumar, T. Y. Tseng, Y. Sharma, *ACS Appl Energy Mater* **2020**, *3*, 2450–2464.

[113] R. Baddour-Hadjean, A. Boudaoud, S. Bach, N. Emery, J.-P. Pereira-Ramos, *Inorg Chem* **2014**, *53*, 1764–1772.

[114] I. M. Taylor, E. M. Robbins, K. A. Catt, P. A. Cody, C. L. Happe, X. T. Cui, *Biosens Bioelectron* **2017**, *89*, 400–410.

[115] Y. Luo, M. S. Shoichet, *Biomacromolecules* **2004**, *5*, 2315–2323.

[116] Q. Zhao, G. Wang, K. Yan, J. Yan, J. Wang, *J Appl Polym Sci* **2015**, *132*, DOI 10.1002/app.42549.

[117] S. Boukhalfa, K. Evanoff, G. Yushin, *Energy Environ Sci* **2012**, *5*, 6872.

[118] L. Köps, P. Zaccagnini, C. F. Pirri, A. Balducci, *Journal of Power Sources Advances* **2022**, *16*, 100098.

[119] G. Kloker, D. Vrankovic, N. Arya, T. Diemant, M. Anjass, *Batter Supercaps* **2024**, DOI 10.1002/batt.202400330.

[120] O. W. Elkhafif, H. K. Hassan, M. Hashmi, N. Arya, M. Anjass, T. Jacob, **2024**, DOI 10.2139/ssrn.4948315.

[121] J. Chen, M. D. Symes, S. Fan, M. Zheng, H. N. Miras, Q. Dong, L. Cronin, *Advanced Materials* **2015**, *27*, 4649–4654.

6. Publications

Parts of this dissertation have been published in the following journal articles. Reprint of the publications are presented in chapter this section and were made with permission of the respective journals.

6.1 (NA1): Reversible Electrodeposition of Potassium-bridged Molecular Vanadium Oxides: A New Approach Towards Multi-Electron Storage

Nikhil Arya[+], Tom Philipp[+], Simon Greiner, Michael Steiner, Christine Kranz, and Montaha Anjass[*]

[+]Authors contributed equally to this manuscript, *corresponding author

Published in: Angewandte Chemie International Edition 62, no. 35 (2023): e202306170

Copyright: Arya, Nikhil, Tom Philipp, Simon Greiner, Michael Steiner, Christine Kranz, and Montaha Anjass. "Reversible electrodeposition of potassium-bridged molecular vanadium oxides: a new approach towards multi-electron storage." *Angewandte Chemie International Edition* 62, no. 35 (2023): e202306170

DOI: https://doi.org/10.1002/anie.202306170

Licence: CC BY 4.0 (https://creativecommons.org/licenses/by/4.0/)

Author contribution:

N. Arya: Material synthesis and characterization, electrochemical characterization, data analysis, writing and revision of the manuscript

T. Philipp: Performed EQCM, AFM and FTIR-ATR measurements and analysis, writing the and writing and revision of the Manuscript

M. Steiner: Material synthesis and characterization, electrochemical characterization, data analysis

C. Kranz: Discussion and revision of the manuscript

M. Anjass: Result discussion, writing, and revision of the manuscript

GDCh Research Articles Angewandte Chemie International Edition www.angewandte.org
Check for updates
How to cite: Angew. Chem. Int. Ed. 2023, 62, e202306170
doi.org/10.1002/anie.202306170

Polyoxometalates

Reversible Electrodeposition of Potassium-bridged Molecular Vanadium Oxides: A New Approach Towards Multi-Electron Storage

*Nikhil Arya[+], Tom Philipp[+], Simon Greiner, Michael Steiner, Christine Kranz, and Montaha Anjass**

Abstract: Molecular metal oxides, so-called polyoxometalates (POMs), have shown outstanding performance as catalysts and lately attracted interest as materials in energy conversion and storage systems due to their capability of storing and exchanging multiple electrons. Here, we report the first example of redox-driven reversible electrodeposition of molecular vanadium oxide clusters, leading to the formation of thin films. The detailed investigation of the deposition mechanism reveals that the reversibility is dependent on the reduction potential. Correlating electrochemical quartz microbalance studies with X-ray photoelectron spectroscopy (XPS) data gave insight into the redox chemistry and oxidation states of vanadium in the deposited films in dependence on the potential window. A multi-electron reduction of the polyoxovanadate cluster, which facilitates the potassium (K^+) cation-assisted reversible formation of potassium vanadium oxide thin films was confirmed. At anodic potentials, re-oxidation of the polyoxovanadate and complete stripping of the thin film is observed for films deposited at potentials more positive than −500 mV vs. Ag/Ag^+, while electrodeposition at more negative cathodic potential reduces the electrochemical reversibility of the process and increases the stripping overpotential. As proof of principle, we demonstrate the electrochemical performance of the deposited films for potential use in potassium-ion batteries.

Introduction

The steadily growing demand for electrochemical energy storage systems in mobile applications, grid storage, and electric vehicles is driving the need to design novel materials for effective and energy-dense electrochemical energy storage.[1] Metal oxides are chemically suitable and economically viable materials class for energy technologies including batteries,[2] fuel cells,[3] and water electrolysis.[4]

Molecular metal oxides, so-called polyoxometalates (POMs) combine physicochemical similarity to solid-state metal oxides with molecularly well-defined structures (Figure 1).[5] POMs are anionic metal oxo clusters of high-valent, early transition metals (often molybdenum (Mo), tungsten (W), and vanadium (V)), which form spontaneously in

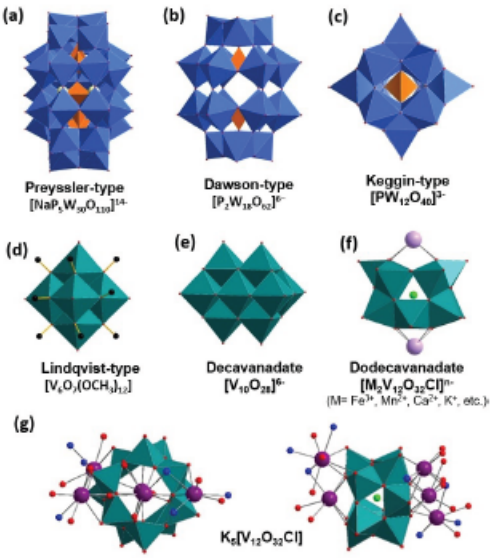

Figure 1. Polyhedral illustration of POM anions, used so far for cation—POM interaction studies. (a) Preyssler polyoxoanion, $[NaP_5W_{30}O_{110}]^{14-}$; (b) Dawson anion $[P_2M_{18}O_{62}]^{6-}$; (c) Keggin anion $[PM_{12}O_{40}]^{3-}$; (d) Lindqvist alkoxide cluster $[V_6O_7(OCH_3)_{12}]$; (e) Decavanadate anion $[V_{10}O_{28}]^{6-}$; (f) Dodecavanadate anion $[V_{12}O_{32}Cl]^{n-}$; (g) top and side view of $K_5\{V_{12}\}$. Colour Scheme: W (blue); O (red), V (teal), C (clack), P (orange), Cl (green), metal coordination (pink), K (plum).

[*] N. Arya,[+] Dr. S. Greiner, M. Steiner, Dr. M. Anjass
Institute of Inorganic Chemistry I, Ulm University
Albert-Einstein-Allee 11, 89081 Ulm (Germany)
and
Helmholtz Institute Ulm (HIU)
Helmholtzstraße 11, 89081 Ulm (Germany)
E-mail: montaha.anjass@uni-ulm.de
T. Philipp,[+] Prof. Dr. C. Kranz
Institute of Analytical and Bioanalytical Chemistry, Ulm University
Albert-Einstein-Allee 11, 89081 Ulm (Germany)
[+] These authors contributed equally to this work.

© 2023 The Authors. Angewandte Chemie International Edition published by Wiley-VCH GmbH. This is an open access article under the terms of the Creative Commons Attribution License, which permits use, distribution and reproduction in any medium, provided the original work is properly cited.

© 2023 The Authors. Angewandte Chemie International Edition published by Wiley-VCH GmbH

15213773, 2023, 35, Downloaded from https://onlinelibrary.wiley.com/doi/10.1002/anie.202306170 by RUB der Universitäts Uibn, Wiley Online Library on [18/09/2023]. See the Terms and Conditions (https://onlinelibrary.wiley.com/terms-and-conditions) on Wiley Online Library for rules of use; OA articles are governed by the applicable Creative Commons License

solution by self-assembly.[5b] Particularly, Mo- and W-based POMs have attracted widespread attention in catalysis and sensing,[6] energy conversion and storage,[7] and increasingly as building blocks for supramolecular assemblies and nanostructured materials.[8] In contrast, molecular vanadium oxides (polyoxovanadates, POVs) have only recently gained substantial attention due to their rich electrochemistry.[9] Additionally, the targeted synthesis of heterometal-functionalized POVs has enabled systematic studies on the controlled structural[10] and electrochemical tuning[11] of POVs, which led to the application of POVs in (post-) Li-ion batteries,[12] water oxidation catalysis,[13] and as metal-oxide surface models.[14]

Recently, the interaction between alkali cations and POMs has been studied, and how these interactions can affect the structure and influence the electrochemical behavavior of POMs, especially POVs.[15] Matson and coworkers investigated the interaction of a Lindqvist-type POV alkoxide cluster ($[V_6O_7(OCH_3)_{12}]$, Figure 1d) with different hard and soft cations. Hard ions (e.g., Li^+) exhibit specific binding and strong interaction with POVs clusters, whereas softer cations (e.g., nBu_4N^+ or K^+), show nonspecific binding and weaker interactions. Further, they showed that the identity and concentration of the charge compensating cations modulate the redox behavior of ($[V_6O_7(OCH_3)_{12}]$) in solution.[15a] In this context, Schimpf and co-workers demonstrated, how the concentration of charge compensating K^+ ions influences the phase of a polyoxotungstate-based coordination network using a Preyssler-type polyoxoanion, $[NaP_5W_{30}O_{110}]^{14-}$ (Figure 1a) cluster.[16] Also, the cation-controlled reversible storage of up to 18 electrons of Dawson-type polyoxotungstates (Figure 1b) in solution has recently been reported.[17]

As a final step for the deployment of POMs in technological applications, the transition from soluble species to solid materials and the immobilization on functional substrates remains a challenge. While most strategies so far focus on encapsulation or electrostatic interaction, the growth of supramolecular films enables a bottom-up approach towards functional (nano-) materials.[18] Additionally, electrochemical deposition enables controllable film growth. For example, the Keggin-type $[H_3PW_{12}O_{40}]$ (Figure 1c) was deposited on TiO_2 nanotube arrays via electrodeposition, and the deposited films were used for photocatalytic degradation of nitrobenzene.[19] Recently, Hwu and co-workers reported the electrochemical crystal growth of decavanadate-based organic-inorganic hybrids (Figure 1e).[20] The applied potential was used as the driving force for the phase nucleation and thus enabled the deposition of a polyoxometalate-organic framework (POMOF).

In recent studies, we reported the polymerization and formation of 1D chains of dodecavanadate clusters (Figure 1f) bridged with alkaline earth metal ions.[11d,21] Dodecavanadate clusters are derived from $(H_2NMe_2)_2[V_{12}O_{32}Cl]^{3-}$ (= $(H_2NMe_2)_2$**[V$_{12}$]**), where two open binding sites are occupied by organic $(H_2NMe_2)^+$ cations. One or both placeholders can be replaced by s-,[21] d-,[22] or f-block[23] metal cations. Thereby, the magnetic, redox, catalytic, and photocatalytic properties can be tuned.

This approach was subsequently expanded by introducing K^+ ions,[21] leading to a complex 3D framework by coordination of K^+ ions inside and next to the predetermined binding site. Thereby, coordination of more than two K^+ ions was achieved leading to a cluster with the sum formula $K_5(CH_3CN)_3[V_{12}O_{32}Cl]$ (= **K$_5$[V$_{12}$]**, Figure 1g). In contrast to earlier di-metal functionalized clusters, no reduction was required to introduce a second heterometal cation. In this current study, we investigated a possible reduction of $K_5[V_{12}]$ that may lead to an increased interaction between the negatively charged POM and the charge compensating K^+ cations enabling electrodeposition.

Consequently, we report here reduction-induced electrodeposition of POV-derived thin films directed by the inclusion of alkali cations. Our detailed electrochemical investigations of the underlying processes indicate a multiple electron reduction of the cluster. The electrochemical studies are accompanied by the characterization of the obtained films regarding their morphology and thickness of the deposited films.

Results and Discussion

Electrochemical characterization

Comparing $K_5[V_{12}]$ with related di-functionalized $\{V_{12}\}$-analogues, the fully oxidized vanadium centers as well as the complex 3D structure of $K_5[V_{12}]$ are the most striking differences.[21] We hypothesized that reduction of the cluster framework could increase the electrostatic attraction between the K^+ ions and the vanadate cluster. This may decrease the solubility and induce the deposition of thin films. Therefore, we investigated the electrochemical behavior of $K_5[V_{12}]$ in water-free, de-aerated acetonitrile (containing 0.1 M $(nBu_4N)PF_6$ as electrolyte salt, which has been used as a standard electrolyte in our previous studies.[11d] For most of the presented studies, glassy-carbon electrodes (Ø: 3 mm) have been used in a three-electrode cell configuration (with a Pt wire counter electrode and a silver wire in a glass frit, containing electrolyte solution as quasi-reference electrode). The cyclic voltammogram (CV) of $K_5[V_{12}]$ in a potential range of −250–500 mV vs. Ag/Ag^+ (Figure 2a) shows a reduction process that starts at −120 mV vs. Ag/Ag^+, which appears to be the reminiscence of plating behavior. Indeed, a deposited film becomes visible at the working electrode. Additionally, a sharp oxidation peak at $E_{peak} = -50$ mV vs. Ag/Ag^+ is observed suggesting stripping of the deposited material. Further reduction of the cluster is observed upon decreasing the cathodic potential to −500 mV vs. Ag/Ag^+. Moreover, a second convoluted reduction process can be identified as a shoulder, which might be related to further reduction of the already deposited film. The oxidation is shifted anodically by ~30 mV, and a new oxidative peak appears at $E_{peak} =$ 220 mV vs. Ag/Ag^+ indicating that the second reduction step decreases the reversibility and slightly increases the

© 2023 The Authors. Angewandte Chemie International Edition published by Wiley-VCH GmbH

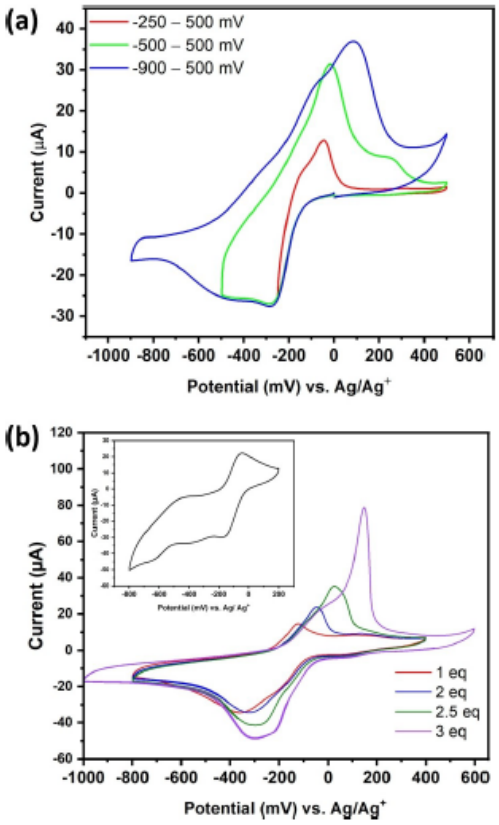

Figure 2. a) CVs of $K_5\{V_{12}\}$ at different cathodic switching potentials in anhydrous, de-aerated acetonitrile containing 0.1 M $(nBu_4N)PF_6$ as supporting electrolyte salt, $[K_5\{V_{12}\}] = 0.5$ mM. b) CVs of $\{V_{12}\}$; $(H_2NMe_2)_2[V_{12}O_{32}Cl]^{3-}$ (containing 0.1 M $(nBu_4N)PF_6$ as electrolyte salt) with different concentrations of KPF_6; scan rate: 100 mV s^{-1}; inset: CV of $\{V_{12}\}$; $(H_2NMe_2)_2[V_{12}O_{32}Cl]^{3-}$ in acetonitrile in absence of K^+ ions.

overpotential of the stripping process. This behavior is consistent with the reduction of the cluster and associated charge compensation as the electron transfer is coupled with cation transfer, where the reduced cluster has a higher affinity for K^+ cations and is therefore more difficult to re-oxidize.

A further extension of the cathodic potential window to −900 mV vs. Ag/Ag^+ resulted in an anodic shift of the oxidation potential by 130 mV and an incomplete stripping of the deposited film. We hypothesize that at a potential lower than −500 mV vs. Ag/Ag^+, successive reduction occurs across the deposited film resulting in structural changes of the vanadate clusters stabilizing the film and affecting its stripping reversibility.

Interestingly, the CV of the non-functionalized $\{V_{12}\}$ in $(nBu_4N)PF_6$ containing electrolyte shows a quasi-reversible redox process at $E_{1/2} = -150$ mV vs. Ag/Ag^+ but no electrodeposition of a film,[11d] indicating that the presence of K^+ is crucial for the electrodeposition process. These observations prompted further investigation of the electrochemical behavior of $\{V_{12}\}$ at different K^+ concentrations. The CV of the non-functionalized $\{V_{12}\}$; $(H_2NMe_2)_2[V_{12}O_{32}Cl]^{3-}$ in acetonitrile (containing 0.1 M $(nBu_4N)PF_6$ as electrolyte salt) shows a quasi-reversible redox process at $E_{1/2} = -150$ mV vs. Ag/Ag^+ (Figure 2b, inset) and additional irreversible reduction processes were observed at lower potentials, indicating cluster decomposition upon further reduction. The CV changed by the addition of 1 eq KPF_6 salt, revealing a broad reduction peak centered at −350 mV vs. Ag/Ag^+ with a shoulder at ~−170 mV vs. Ag/Ag^+ and one oxidation wave at $E_{peak} = -123$ mV vs. Ag/Ag^+ (Figure 2b). Notably, the absence of irreversible reduction peaks at lower potential indicates that the presence of K^+ in solution stabilized the reduced clusters and prevented their decomposition. With addition of 2 eq K^+, a peak shift towards less cathodic potentials was observed; the subsequent additions were then resulting in an increase of the cathodic current. This indicates that the presence of more K^+ ions in solution facilitates the electrodeposition process during the reductive cycle. Further, this increase in current is also associated with a peak broadening, which may result from an overlap of multiple reduction steps of the cluster in a narrow potential range.[15a] Additionally, a shift of the oxidation peak to higher anodic potentials, in addition to an increase of anodic current is observed after each addition of KPF_6. This positive shift might be attributed to the stronger interaction between the reduced form of the cluster and K^+ ions, which reduces the electrochemical reversibility of the oxidation process.

Film electrodeposition

To further investigate the electrodeposition behavior of the $K_5\{V_{12}\}$ upon reduction as observed in the CV, bulk electrolysis (BE) was performed in a 0.5 mM acetonitrile solution of $K_5\{V_{12}\}$ (containing 0.1 M $(nBu_4N)PF_6$) at −250 mV vs. Ag/Ag^+. After electrolysis (~6 h), UV/Vis spectroscopy of the bulk solution (Supporting Information, Figure S1) shows no intervalence charge transfer (IVCT) absorbance in the Vis-to-near-IR region, indicating that no detectable amounts of reduced vanadates (i.e., V^{IV}-containing) are present in the solution. At the same time, film formation was observed on the glassy carbon electrode. This provides further evidence that the reduction of $K_5\{V_{12}\}$ leads to film formation, while no reduced species are detected in the electrolyte solution, given the limit of detection (LOD) of the method.

The electrodeposition behavior and reversibility of the process were further investigated via electrochemical quartz microbalance (EQCM) analysis to determine the relation between deposited mass and transferred charge at three different potentials, i.e., −250 mV, −500 mV and −900 mV

© 2023 The Authors. Angewandte Chemie International Edition published by Wiley-VCH GmbH

15213773, 2023, 35, Downloaded from https://onlinelibrary.wiley.com/doi/10.1002/anie.202306170 by KIT-Bibliothek, Wiley Online Library on [18/09/2023]. See the Terms and Conditions (https://onlinelibrary.wiley.com/terms-and-conditions) on Wiley Online Library for rules of use; OA articles are governed by the applicable Creative Commons License

vs. Ag/Ag$^+$. Applying a constant potential of −250 mV vs. Ag/Ag$^+$ resulted in a linear increase of deposited mass per transferred charge (Supporting Information, Figure S2). The slope of the deposited mass-to-charge ratio suggests deposition of approximately one $K_{8.64}[V_{12}O_{32}Cl]$ per 3.46 e$^-$ (sum formula derived from XPS data).

In the next step, CVs at three different cathodic switching potentials in combination with EQCM (Figure 3a–c) were recorded. The CVs with a potential limit of −250 mV vs. Ag/Ag$^+$ show full reversibility with the expected plating and stripping behavior visible by the increase and decrease of the observed mass change. However, when the cathodic potential was changed to −500 mV vs. Ag/Ag$^+$, a deviation from the linear behavior of the transferred charge versus deposited mass was observed (Figure 3d), indicating that the deposited film was further reduced as noted by an apparent higher electron count per deposited cluster (4.9 e$^-$ per $K_{9.36}[V_{12}O_{32}Cl]$, sum formula derived from XPS data). It should be noted that up to a lower switching potential of −500 mV vs. Ag/Ag$^+$ during cycling the potential, the plated films can still be completely stripped (visible in the massogram). An additional oxidative peak becomes visible, which is in line with the initial CV measurements. In case, the potential was cycled to a cathodic switching potential of −900 mV vs. Ag/Ag$^+$, the deposited mass per charge curve shows a significant flattening which indicates that the deposited film undergoes a further reduction as the dominant electrochemical process (6.32 e$^-$ per $K_{11.64}[V_{12}O_{32}Cl]$, sum formula derived from XPS data). Additionally, the deposited mass was no longer fully stripped (re-oxidized) when the potential was swept anodically (to 500 mV vs. Ag/Ag$^+$), suggesting irreversible electrodeposition, possibly due to structural changes during further reduction. At the fifth cycle, a strong decrease in current was observed, which is in line with the absence of a frequency change, i.e., indicating that the electrode surface of the quartz sensor was blocked by an insulating film.

In the next step, pulsed electrochemical depositions (PEDs) were performed at three different potentials −250 mV, −500 mV and −900 mV vs. Ag/Ag$^+$, respectively, to study the influence of the reduction potential on film formation in more detail. All pulsed electrodeposition experiments were carried out in two distinct steps, the potential of 0 mV vs. Ag/Ag$^+$ was applied to the working electrode for 60 seconds known as relaxing period (t_{off}) to establish the bulk concentration of the dissolved cluster ions near the electrode surface. Then the desired reduction potential e.g., −250 mV vs. Ag/Ag$^+$ was applied for a period

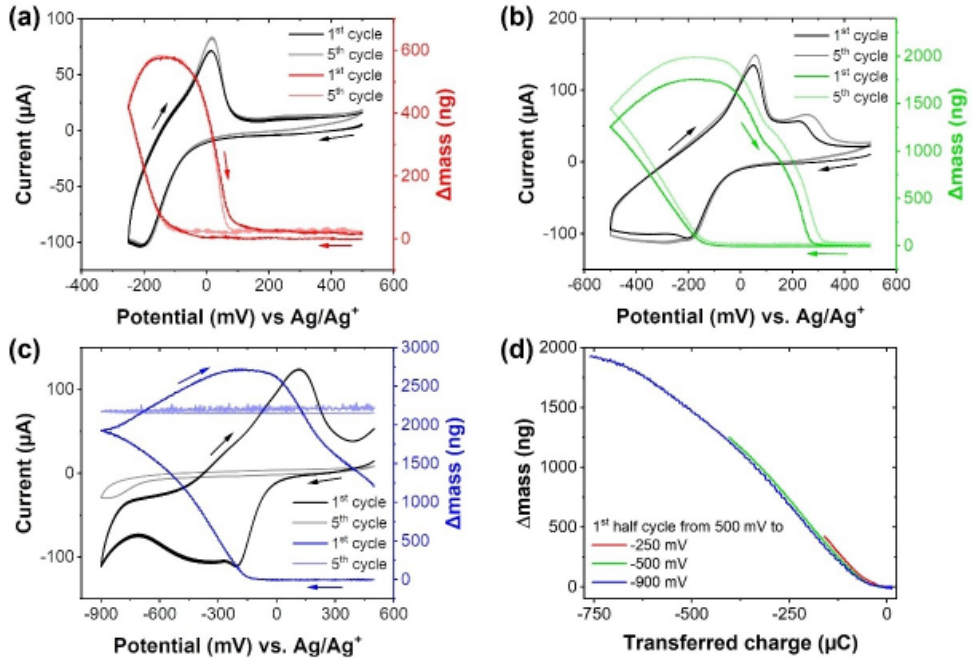

Figure 3. EQCM measurement of $K_8\{V_{12}\}$ (0.5 mM in acetonitrile containing 0.1 M $(nBu_4N)PF_6$ while using cyclic voltammetry (scan rate = 100 mV s^{-1}) in the potential ranges of **a)** 500 mV to −250 mV, **b)** 500 mV to −500 mV, and **c)** 500 mV to −900 mV vs. Ag/Ag$^+$ with the corresponding mass changes for the first and fifth cycle, respectively. **d)** Deposited mass vs. transferred charge during the first half cycle for the three potential ranges shown in **a)**, **b)**, and **c)**.

© 2023 The Authors. Angewandte Chemie International Edition published by Wiley-VCH GmbH

15213773, 2023, 34, Downloaded from https://onlinelibrary.wiley.com/doi/10.1002/anie.202306170 by KIT der Universitaet Ulm, Wiley Online Library on [18/08/2023]. See the Terms and Conditions (https://onlinelibrary.wiley.com/terms-and-conditions) on Wiley Online Library for rules of use; OA articles are governed by the applicable Creative Commons License

of 120 seconds known as deposition period (t_{on}) to induce the reduction of the clusters. The deposition period (t_{on}) and the relaxing potential (t_{off}) were repeated alternately to accomplish 10 successive reduction pulses.

The potentiostatic pulse profile at −250 mV vs. Ag/Ag^+ resulted in a gradually decreasing current response over 10 reduction pulse cycles (see Supporting Information, Figure S3), which may be associated with film formation and associated with that limited electron transfer for further reduction of the clusters. The pulse sequence with a cathodic potential of −500 mV vs. Ag/Ag^+ shows a higher reduction current, which is most likely due to the deposition of more $K_5[V_{12}]$ clusters and possibly additional reduction of the plated material.

Upon further decreasing the cathodic potential to −900 mV vs. Ag/Ag^+, the potentiostatic pulse profile reveals a fast decay in current response, which is assigned to a reduced electrical conductivity of the film at this potential. At the same time, a comparatively small oxidative current response shows that the deposition has become mostly irreversible, and the deposited film could not be completely re-oxidized (stripped). These findings are consistent with our EQCM results, which show irreversible POM electrodeposition when the applied potential is more negative than −500 mV vs. Ag/Ag^+. In sum, fully reversible electrodeposition of $K_5[V_{12}]$ is possible up to a cathodic potential of −500 mV vs. Ag/Ag^+, while irreversible electrodeposition occurs when more negative cathodic potentials are used. We hypothesized that this change of behavior could be due to chemical and/or structural changes of the deposited films at sufficiently low potentials. Thus, the thin films were characterized via scanning electron microscopy (SEM), energy dispersive X-ray spectroscopy (EDX) element mapping, Fourier transform infrared-attenuated total reflection spectroscopy (FTIR-ATR), and X-ray photoelectron spectroscopy (XPS) to elucidate the key differences of films which were pulse-deposited at the different reduction potentials (−250 mV, −500 mV and −900 mV vs. Ag/Ag^+).

Characterization of the electrodeposited thin films

SEM images of the three films deposited at −250 mV, −500 mV and −900 mV vs. Ag/Ag^+ show that uniform films with similar morphologies are formed (Supporting Information, Figure S4b–d). EDX element analyses (Supporting Information, Figure S5) reveal the presence of vanadium, potassium, oxygen, and chlorine as expected from the $K_5[V_{12}]$ clusters, which appear to be homogeneously distributed (Supporting Information, Figure S4b–d). To determine the film thickness and roughness (arithmetic mean height, *Sa*), atomic force microscopy (AFM) measurements were performed in acetonitrile for the three pulse-deposited films (at −250 mV, −500 mV and −900 mV vs. Ag/Ag^+). Figure 4a–c shows the topography images of the films, where defined areas of the films were partially removed to determine the film height. Especially, the deposition at −250 mV vs. Ag/Ag^+ resulted in uniform coatings with roughness values (*Sa*) of 9 ± 2 nm (n = 5, areas of 625 µm² were evaluated), whereas films deposited at more negative potentials (−500 and −900 mV vs. Ag/Ag^+) appear less uniform (*Sa* = 45 ± 13 nm and 32 ± 19 nm; n = 4 and 5, respectively, areas of 625 µm² were evaluated). Extracted line profiles (Figure 4d–f) obtained from the topography images (marked with dotted lines in Figure 4a–c) show film thicknesses of 73 ± 27 nm (−250 mV vs. Ag/Ag^+), 71 ± 27 nm (−500 mV vs. Ag/Ag^+) and 37 ± 18 nm (−900 mV vs. Ag/Ag^+) (n = 30, profiles from three different areas were evaluated, respectively).

The reduced thickness of the film deposited at −900 mV vs. Ag/Ag^+ might be attributed to the formation of a film that effectively blocks electron transfer and with that further

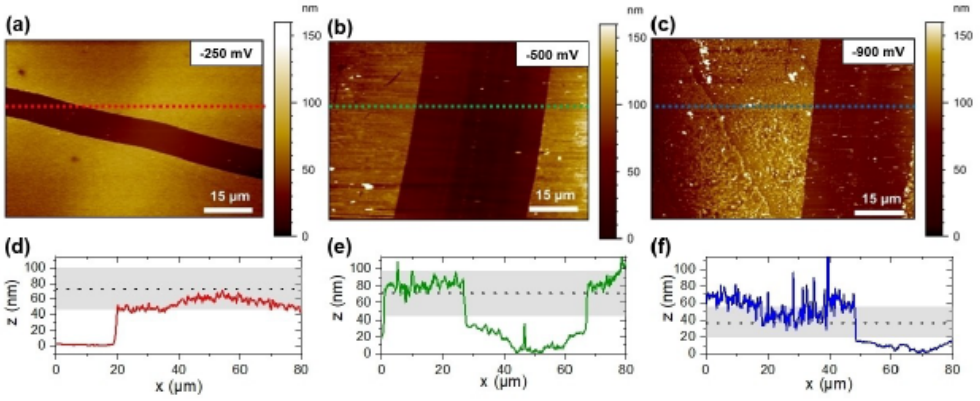

Figure 4. AFM topography images of $K_5[V_{12}]$ films deposited on glassy carbon via PED at **a)** −250 mV, **b)** −500 mV and **c)** −900 mV vs. Ag/Ag^+; images were recorded in contact mode in acetonitrile. Corresponding line scans **(d–f)** extracted from the topography images at the position marked by the dotted lines; dotted black lines represent average film thicknesses with standard deviations depicted as gray area (n = 30 profiles).

© 2023 The Authors. Angewandte Chemie International Edition published by Wiley-VCH GmbH

15213773, 2023, 35, Downloaded from https://onlinelibrary.wiley.com/doi/10.1002/anie.202306170 by RWTH der Universitätsbibliothek, Wiley Online Library on [18/09/2023]. See the Terms and Conditions (https://onlinelibrary.wiley.com/terms-and-conditions) on Wiley Online Library for rules of use; OA articles are governed by the applicable Creative Commons License

deposition which is in line with the EQCM measurements. In addition, this deviating behavior compared to the other films implies a structural change of the film, which may attribute to changes in film morphology.

We also conducted FTIR-ATR spectroscopy studies to get further insights into structural integrity and possible structural changes of the $K_5[V_{12}]$-based films. For the films deposited at −250 mV and −500 mV vs. Ag/Ag^+, a shift of the characteristic V–O–V (820 cm^{-1}, 767 cm^{-1}, 686 cm^{-1} and 633 cm^{-1})[24] and V=O (988 cm^{-1})[24b] bands towards lower wavenumbers (by ~20 cm^{-1}) and a slight shoulder, which may originate from a peak splitting due to the further reduction of the film was observed when compared with the non-reduced, native $K_5[V_{12}]$ cluster (Supporting Information, Figure S6). The presence of only minor changes suggests that the $[V_{12}]$ molecular structure is retained, while the cluster environment (i.e., K^+ ions bound to the cluster) might be arranged in a different fashion compared to the native compound. The IR spectra of the film deposited at −900 mV vs. Ag/Ag^+ show minute differences compared to the films deposited at more positive potentials; peak shifting is less pronounced (~10 cm^{-1} towards lower wave numbers), while the splitting of the 988 cm^{-1} band still occurs. Also, new bands at 1033 cm^{-1} and 736 cm^{-1} were observed, the one at 736 cm^{-1} might indicate further structural changes of the deposited species, while the one at 1033 cm^{-1} might indicate deposition of new vanadium oxide species that could be one reason for the observed irreversibility of the electrodeposition.

Additionally, UV/Vis spectroscopy was used to probe spectral changes before and after deposition of $K_5[V_{12}]$. To this end, a film deposited on a glassy carbon electrode at −250 mV vs. Ag/Ag^+ was transferred to a fresh electrolyte containing 0.1 M KPF_6 (to avoid cation exchange with nBu_4N^+). The film was stripped using a pulsed potential of 500 mV vs. Ag/Ag^+ (applied for a period of total 20 minutes) resulting in re-oxidation and dissolution of the film. UV/Vis spectroscopy of the electrolyte with the stripped sample (Supporting Information, Figure S7) shows that the characteristic absorption signals of the native $K_5[V_{12}]$ are present in solution. This indicates that the structural integrity of $K_5[V_{12}]$ is retained during deposition and subsequent stripping. Also, no intervalence charge transfer bands in the Vis region were observed, indicating the complete re-oxidation of the cluster to all V^V species.[11d,21]

We further studied the films by using XPS to gain insights into the elemental composition and metal oxidation states in the deposited $K_5[V_{12}]$ films. Survey XPS spectra of the films deposited at −250 mV, −500 mV and −900 mV vs. Ag/Ag^+ show peaks corresponding to V, K, O, Cl, C as major components (see Supporting Information, Figure S8a). Moreover, small peaks corresponding to N and F present in the spectra originate from residual electrolyte and solvent from the electrodeposition process. XPS data for the native $K_5[V_{12}]$ cluster revealed the exclusive presence of V^V centers (see Supporting Information, Figure S8b). In contrast, the films electrodeposited at −250 mV and −500 mV vs. Ag/Ag^+ showed a sharp signal in the $V2p_{3/2}$ region at binding energies of ~517 eV (assigned to V^{5+}),[25] as well as weak signals at ~516 eV (indicative of V^{4+}),[26] which confirms the reduction of the cluster during the electrodeposition (Supporting Information, Figure S8c–e). For the films deposited at −250 mV vs. Ag/Ag^+, the V:K atomic ratio is 1:0.72, indicating that each $[V_{12}]$ cluster interacts on average with ca. 8.6 K^+ cations and resulting in an average reduction degree of 3.6 electrons per $[V_{12}]$ (as the native compound features five K^+ per $[V_{12}]$). The estimated V^{4+}:V^{5+} ratio from the curve data fitting of the $V2p_{3/2}$ is 0.3:1 indicating that the $[V_{12}]$ cluster is reduced on average by 3.6 electrons. The film deposited at −500 mV vs. Ag/Ag^+ showed a slightly higher V:K atomic ratio (1:0.78), corresponding to 9.4 K^+ ion per $[V_{12}]$, and a reduction degree of 4.4 electrons per $[V_{12}]$) and V^{4+}:V^{5+} ratio (0.4:1), which corresponds to a reduction degree of 4.8 electrons per $[V_{12}]$. These data are in excellent agreement with the EQCM results, which show that the film is further reduced following electrodeposition. The XPS data for the film deposited at −900 mV vs. Ag/Ag^+ shows the largest K^+ content (V:K, 1:0.97, corresponding to 11.6 K^+ per $[V_{12}]$, and a reduction degree of 6.6 electrons per $[V_{12}]$), which is also in line with our EQCM results, indicating further reduction processes at this potential. Surprisingly, the film deposited at −900 mV vs. Ag/Ag^+ shows the lowest V^{4+} to V^{5+} ratio (0.18:1). While current work focuses on the reversible plating and stripping of the molecular vanadium oxides, future research will also continue to study the structure of the irreversibly deposited films.

Proof-of-concept: $K_5[V_{12}]$ films as potential battery electrode material

To assess the storage capacity of the deposited $K_5[V_{12}]$ films as active cathode material in a prototype potassium-ion battery (PIB), the films deposited at −250 mV, −500 mV and −900 mV vs. Ag/Ag^+ on carbon-coated Al-foil substrates were tested via galvanostatic charge/discharge cycling in a voltage range between 1.5–3.8 V vs. K/K^+ at 50 mA g^{-1}. The film deposited at −250 mV vs. Ag/Ag^+ delivered an initial discharge capacity of 55 mAh g^{-1} (Figure 5a) which corresponds to the storage of 3.06 e^- per $K_{8.64}[V_{12}O_{32}Cl]$ (all sum formulas are derived from XPS data) according to the following equation:

$$Q = (nF)/(3.6\ M_W) = (n \cdot 26{,}800)/M_W$$

where Q is the reversible charge/discharge capacity, n is the number of electrons transferred, M_w is the molecular weight and F is the Faraday constant.

The film deposited at −500 mV vs. Ag/Ag^+ shows a slightly higher capacity of 59 mAh g^{-1}, which corresponds to the storage of 3.37 e^- per $K_{9.36}[V_{12}O_{32}Cl]$. While the film deposited at −900 mV vs. Ag/Ag^+ shows a significantly lower capacity of ~11 mAh g^{-1} (see Figure S10), which corresponds to the storage of only 0.68 e^- per $K_{11.64}[V_{12}O_{32}Cl]$. This low storage capacity of the film deposited at −900 mV vs. Ag/Ag^+ might be due to the more insulating nature of the film, which effectively hinders electron trans-

© 2023 The Authors. Angewandte Chemie International Edition published by Wiley-VCH GmbH

15213773, 2023, 35, Downloaded from https://onlinelibrary.wiley.com/doi/10.1002/anie.202306170 by KIT-Bibliothek, Wiley Online Library on [18/09/2023]. See the Terms and Conditions (https://onlinelibrary.wiley.com/terms-and-conditions) on Wiley Online Library for rules of use; OA articles are governed by the applicable Creative Commons License

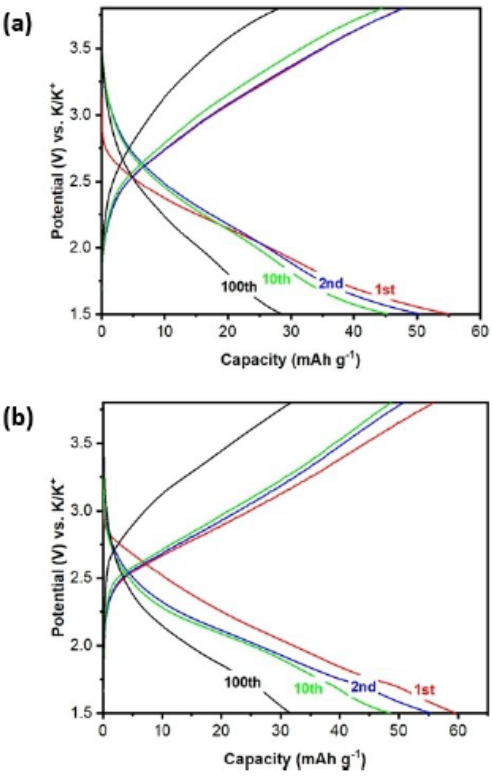

Figure 5. Selected cycles of galvanostatic cycling of the film deposited on carbon-coated Al-foil substrates at **a)** −250 mV and **b)** −500 mV vs. Ag/Ag^+ via PED; in the range of 1.5–3.8 V vs. K^+/K at 50 mA g^{-1}.

fer; again this behavior is in line with our EQCM measurements. Similarly, Pyo and co-workers previously reported the potassium-vanadium-based composite (KVP_2O_7) for high voltage cathode for PIBs and achieved the maximum discharge capacity of 60 mAh g^{-1}.[27]

All deposited films reveal a capacity fading during cycling, which might be attributed to partial dissolution of $K_5[V_{12}]$ into the battery electrolyte or structural rearrangements due to the intercalation/deintercalation of K^+ ions in the electrode material. Therefore, future work will focus on advanced deposition processes, targeting stable and homogeneous thin films with tunable morphology and thickness to enhance the overall capacity and address the observed capacity fading.

Conclusion

We report here the first example of reversible electrodeposition of molecular vanadium oxide clusters as a new approach towards multi-electron storage. We demonstrate that uniform films based on potassium-stabilized, reduced $[V_{12}]$ clusters can be formed on electrode surfaces. Within a given potential range, the deposition of the film is fully reversible, so that an electrochemical electron storage and release device can be envisaged. Mechanistic structural studies indicated that at increasingly negative deposition potentials (e.g., as shown here −900 mV vs. Ag/Ag^+), structural changes of the film occur, which affects the reversibility of the deposition process. Initial investigations of the electron storage capacity of the deposited films as future active cathode material in PIBs show promising results and will hopefully foster further investigations of this material class for electrochemical energy storage systems.

Acknowledgements

This work contributes to the research performed at CELEST (the Center for Electrochemical Energy Storage Ulm-Karlsruhe) and was funded by the Deutsche Forschungsgemeinschaft (DFG, German Research Foundation) under Germany's Excellence Strategy—EXC 2154—Project number 390874152 (POLiS Cluster of Excellence) and the TRR234 "CataLight" (project no: 364549901). Financial support by Ulm University, the Helmholtz-Gemeinschaft (HGF) is gratefully acknowledged. M. A. acknowledges the State of Baden-Württemberg for a Margarete-von-Wrangell fellowship and the Baden Württemberg Stiftung (Elite programme for Postdocs). S. G. gratefully acknowledges financial support through a Ph.D. fellowship by the Fonds der Chemischen Industrie (FCI). Dr. Thomas Diemant is acknowledged for XPS measurements. Open Access funding enabled and organized by Projekt DEAL.

Conflict of Interest

The authors declare no conflict of interest.

Data Availability Statement

The data that support the findings of this study are available from the corresponding author upon reasonable request.

Keywords: Electrochemical Quartz Microbalance · Multi-Electron Reduction · Polyoxovanadates · Pulse Electrodeposition

[1] S. Chu, A. Majumdar, *Nature* **2012**, *488*, 294–303.
[2] P. G. Bruce, B. Scrosati, J.-M. Tarascon, *Angew. Chem. Int. Ed.* **2008**, *47*, 2930–2946.
[3] F. S. da Silva, T. M. de Souza, *Int. J. Hydrogen Energy* **2017**, *42*, 26020–26036.
[4] D. G. Nocera, *Acc. Chem. Res.* **2012**, *45*, 767–776.

© 2023 The Authors. Angewandte Chemie International Edition published by Wiley-VCH GmbH

15213773, 2023, 33, Downloaded from https://onlinelibrary.wiley.com/doi/10.1002/anie.202306170 by KIZ der Universität Ulm, Wiley Online Library on [18/08/2023]. See the Terms and Conditions (https://onlinelibrary.wiley.com/terms-and-conditions) on Wiley Online Library for rules of use; OA articles are governed by the applicable Creative Commons License

[5] a) A. Müller, S. Roy, *Coord. Chem. Rev.* **2003**, *245*, 153–166; b) D. L. Long, R. Tsunashima, L. Cronin, *Angew. Chem. Int. Ed.* **2010**, *49*, 1736–1758.

[6] a) H. Lv, Y. V. Geletii, C. Zhao, J. W. Vickers, G. Zhu, Z. Luo, J. Song, T. Lian, D. G. Musaev, C. L. Hill, *Chem. Soc. Rev.* **2012**, *41*, 7572–7589; b) C. Streb, *Dalton Trans.* **2012**, *41*, 1651; c) A. Sartorel, M. Carraro, F. M. Toma, M. Prato, M. Bonchio, *Energy Environ. Sci.* **2012**, *5*, 5592–5603; d) Q. Yin, J. M. Tan, C. Besson, Y. V. Geletii, D. G. Musaev, A. E. Kuznetsov, Z. Luo, K. I. Hardcastle, C. L. Hill, *Science* **2010**, *328*, 342–346.

[7] a) T. Ueda, *ChemElectroChem* **2018**, *5*, 823–838; b) Y. C. Ji, L. J. Huang, J. Hu, C. Streb, Y. F. Song, *Energy Environ. Sci.* **2015**, *8*, 776–789; c) N. Kawasaki, H. Wang, R. Nakanishi, S. Hamanaka, R. Kitaura, H. Shinohara, T. Yokoyama, H. Yoshikawa, K. Awaga, *Angew. Chem. Int. Ed.* **2011**, *50*, 3471–3474.

[8] a) M. Stuckart, K. Y. Monakhov, *Chem. Sci.* **2019**, *10*, 4364–4376; b) H. N. Miras, L. Vilà-Nadal, L. Cronin, *Chem. Soc. Rev.* **2014**, *43*, 5679–5699.

[9] M. Anjass, G. A. Lowe, C. Streb, *Angew. Chem. Int. Ed.* **2021**, *60*, 7522–7532.

[10] a) S. Greiner, M. H. Anjass, M. Fichtner, C. Streb, *Inorg. Chem. Front.* **2020**, *7*, 134–139; b) L. E. VanGelder, B. E. Petel, O. Nachtigall, G. Martinez, W. W. Brennessel, E. M. Matson, *ChemSusChem* **2018**, *11*, 4139–4149; c) K. Kastner, J. T. Margraf, T. Clark, C. Streb, *Chem. Eur. J.* **2014**, *20*, 12269–12273; d) F. Li, L. E. Vangelder, W. W. Brennessel, E. M. Matson, *Inorg. Chem.* **2016**, *55*, 7332–7334.

[11] a) F. Li, S. H. Carpenter, R. F. Higgins, M. G. Hitt, W. W. Brennessel, M. G. Ferrier, S. K. Cary, J. S. Lezama-Pacheco, J. T. Wright, B. W. Stein, M. P. Shores, M. L. Neidig, S. A. Kozimor, E. M. Matson, *Inorg. Chem.* **2017**, *56*, 7065–7080; b) R. L. Meyer, M. H. Anjass, B. E. Petel, W. W. Brennessel, C. Streb, E. M. Matson, *Chem. Eur. J.* **2020**, *26*, 9905–9914; c) L. E. VanGelder, A. M. Kosswattaarachchi, P. L. Forrestel, T. R. Cook, E. M. Matson, *Chem. Sci.* **2018**, *9*, 1692–1699; d) S. Greiner, B. Schwarz, M. Ringenberg, M. Dürr, I. Ivanovic-Burmazovic, M. Fichtner, M. Anjass, C. Streb, *Chem. Sci.* **2020**, *11*, 4450–4455.

[12] a) J. J. Chen, J. C. Ye, X. G. Zhang, M. D. Symes, S. C. Fan, D. L. Long, M. Sen Zheng, D. Y. Wu, L. Cronin, Q. F. Dong, *Adv. Energy Mater.* **2018**, *8*,1701021; b) S. Hartung, N. Bucher, H. Chen, R. Al-oweini, S. Sreejith, P. Borah, Z. Yanli, U. Kortz, U. Stimming, H. E. Hoster, M. Srinivasan, *J. Power Sources* **2015**, *288*, 270–277; c) Y. Ji, J. Hu, J. Biskupek, U. Kaiser, Y.-F. Song, C. Streb, *Chem. Eur. J.* **2017**, *23*, 16637–16643.

[13] a) B. Schwarz, J. Forster, M. K. Goetz, D. Yücel, C. Berger, T. Jacob, C. Streb, *Angew. Chem. Int. Ed.* **2016**, *55*, 6329–6333; b) B. Schwarz, J. Forster, M. H. Anjass, S. Daboss, C. Kranz, C. Streb, *Chem. Commun.* **2017**, *53*, 11576–11579.

[14] a) B. E. Petel, R. L. Meyer, M. L. Maiola, W. W. Brennessel, A. M. Müller, E. M. Matson, *J. Am. Chem. Soc.* **2020**, *142*, 1049–1056; b) E. Schreiber, B. E. Petel, E. M. Matson, *J. Am. Chem. Soc.* **2020**, *142*, 9915–9919.

[15] a) E. Schreiber, N. A. Hartley, W. W. Brennessel, T. R. Cook, J. R. McKone, E. M. Matson, *ACS Appl. Energ. Mater.* **2019**, *2*, 8985–8993; b) J. J. Chen, M. A. Barteau, *Ind. Eng. Chem. Res.* **2016**, *55*, 9857–9864; c) T. Konishi, K. Kodani, T. Hasegawa, S. Ogo, S. X. Guo, J. F. Boas, J. Zhang, A. M. Bond, T. Ueda, *Inorg. Chem.* **2020**, *59*, 10522–10531.

[16] L. Chen, M. J. Turo, M. Gembicky, R. A. Reinicke, A. M. Schimpf, *Angew. Chem. Int. Ed.* **2020**, *59*, 16609–16615.

[17] a) J. J. Chen, M. D. Symes, L. Cronin, *Nat. Chem.* **2018**, *10*, 1042–1047; b) J. J. Chen, L. Vilà-Nadal, A. Solé-Daura, G. Chisholm, T. Minato, C. Busche, T. Zhao, B. Kandasamy, A. Y. Ganin, R. M. Smith, I. Colliard, J. J. Carbó, J. M. Poblet, M. Nyman, L. Cronin, *J. Am. Chem. Soc.* **2022**, *144*, 8951–8960.

[18] A. S. Cherevan, S. P. Nandan, I. Roger, R. Liu, C. Streb, D. Eder, *Adv. Sci.* **2020**, *7*, 1903511.

[19] Z. Sun, M. Zhao, F. Li, T. Wang, L. Xu, *Mater. Res. Bull.* **2014**, *60*, 524–529.

[20] Q. Zhang, J. Ondus, J. Mills, A. Bahadori, J. Smith, T. Jordan, H. Xu, S. J. Hwu, *J. Solid State Chem.* **2020**, *287*, 121368.

[21] S. Greiner, M. Anjass, C. Streb, *CrystEngComm* **2021**, *23*, 3946–3950.

[22] a) M. H. Anjass, K. Kastner, F. Nägele, M. Ringenberg, J. F. Boas, J. Zhang, A. M. Bond, T. Jacob, C. Streb, *Angew. Chem. Int. Ed.* **2017**, *56*, 14749–14752; b) K. Kastner, M. Lechner, S. Weber, C. Streb, *ChemistrySelect* **2017**, *2*, 5542–5544; c) K. Kastner, J. Forster, H. Ida, G. N. Newton, H. Oshio, C. Streb, *Chem. Eur. J.* **2015**, *21*, 7686–7689.

[23] A. Seliverstov, C. Streb, *Chem. Eur. J.* **2014**, *20*, 9733–9738.

[24] a) H. Zhang, X. Xiao, X. Lu, G. Chai, Y. Sun, Y. Zhan, G. Xu, *J. Alloys Compd.* **2015**, *636*, 106–112; b) J. K. Li, J. Dong, C. P. Wei, S. Yang, Y. N. Chi, Y. Q. Xu, C. W. Hu, *Inorg. Chem.* **2017**, *56*, 5748–5756.

[25] E. Hryha, E. Rutqvist, L. Nyborg, *Surf. Interface Anal.* **2012**, *44*, 1022–1025.

[26] G. Silversmit, D. Depla, H. Poelman, G. B. Marin, R. De Gryse, *J. Electron Spectrosc. Relat. Phenom.* **2004**, *135*, 167–175.

[27] P. W. Bae, S. Ch. Han, Ch. Park, S. U. Hong, U. Han, S. P. Singh, Y. H. Jung, D. Ahn, K.-S. Sohn, M. Pyo, *Adv. Energy Mater.* **2017**, *8*, 1703099.

Manuscript received: May 3, 2023
Accepted manuscript online: May 22, 2023
Version of record online: July 18, 2023

© 2023 The Authors. Angewandte Chemie International Edition published by Wiley-VCH GmbH

15213773, 2023, 35, Downloaded from https://onlinelibrary.wiley.com/doi/10.1002/anie.202306170 by KIZ der Universität Ulm, Wiley Online Library on [18/06/2024]. See the Terms and Conditions (https://onlinelibrary.wiley.com/terms-and-conditions) on Wiley Online Library for rules of use; OA articles are governed by the applicable Creative Commons License

Angewandte Chemie
Eine Zeitschrift der Gesellschaft Deutscher Chemiker

Supporting Information

Reversible Electrodeposition of Potassium-bridged Molecular Vanadium Oxides: A New Approach Towards Multi-Electron Storage

*N. Arya, T. Philipp, S. Greiner, M. Steiner, C. Kranz, M. Anjass**

WILEY-VCH

SUPPORTING INFORMATION

Table of Contents

Experimental Procedures S2
Results and Discussion S3
1. UV Vis spectroscopy of $K_5\{V_{12}\}$ S3
2. Electrochemical quartz crystal microbalance (EQCM) S4
3. Pulsed electrodeposition of $K_5\{V_{12}\}$ S4
4. Scanning Electron Microscopy (SEM) and Energy-dispersive X-ray spectroscopy S5
5. Infrared spectroscopy (FTIR-ATR) S6
6. UV-Vis spectroscopy of the striped film S6
7. X-ray photoelectron spectroscopy S7
8. Galvanostatic cycling S8
References S8
Author Contributions S8

Experimental Procedures

Chemicals: Acetonitrile (≥99.8% for the HPLC), tetrabutylammonium hexafluorophosphate ($(n\text{Bu}_4\text{N})\text{PF}_6$), potassium thiocyanate (KSCN, reagent Plus ≥99.0%), dimethylamine hydrochloride (DMA-HCl), indium (III) chloride (99.99%) and diethyl ether (ACS, ISO) were purchased from Sigma Aldrich and VWR. Glassy carbon plates (25x25 mm), carbon coated aluminum foil sheet (A= 50 mm²) and standard glassy carbon disk electrode (OD: 3 mm) were purchased from Alfa Aesar and Pine research respectively. All chemicals were of reagent grade and used without further purification unless stated otherwise.

Synthesis: Synthesis of $K_5(CH_3CN)_3[V_{12}O_{32}Cl]$ (= $K_5\{V_{12}\}$): $K_5\{V_{12}\}$ was synthesized according to a procedure reported elsewhere;[1] $(n\text{Bu}_4\text{N})_3[(C_2H_8N)_2V_{12}O_{32}Cl] \cdot CH_3CN$ (240 mg, 0.12 mmol, 1 eq) and KSCN (94 mg, 0.96 mmol, 8 eq) were dissolved in acetonitrile (20 ml) and stirred at room temperature for 5 h. Diffusion crystallization of diethyl ether yielded fine, needle-shaped, yellow-greenish crystals.
Characteristic IR bands (in cm^{-1}): 3527 (b), 1947 (w), 1614 (m), 1462 (w), 1396 (w), 1363 (w), 986 (vs), 819 (s), 767 (s), 685 (s), 630 (vs).

Characterization: Fourier transform infrared-attenuated total reflection spectroscopy (FTIR-ATR) was performed using a Bruker Vertex 70 Fourier transform infrared (FTIR) spectrometer (Bruker Optics, Ettlingen, Germany) equipped with a single-bounce ATR cell (GladiATR™, PIKE Technologies, Wisconsin, USA) and a liquid nitrogen cooled mercury cadmium telluride (MCT) detector. All spectra were recorded at room temperature in a spectral range from 4000 cm^{-1} to 400 cm^{-1} with a spectral resolution of 1 cm^{-1} averaging 64 scans. Shown spectra are baseline corrected using OPUS 8.1 (Bruker Optics, Ettlingen, Germany).

X-ray photoelectron spectroscopy (XPS) was performed on Physical Electronics PHI 5800 spectrometer with monochromatized $Al_{K\alpha}$ (1486.6 eV) radiation. Films deposited at -250 mV, -500 mV and -900 mV vs. Ag/Ag^+ were dipped in acetonitrile to remove residual electrolyte solution and air dried overnight before further investigations. The samples were handled under ambient condition. The measurements were performed with a detection angle of 45°, using pass energies at the analyzer of 93.9 and 29.35 eV for survey and detail spectra, respectively. The samples were neutralized with electrons from a flood gun (current 3 µA) to compensate for charging effects at the surface.

Scanning electron microscopy (SEM) and energy-dispersive X-ray spectroscopy (EDX) were performed on a Zeiss Gemini Leo 1550 VP equipped with a Silicon Drift Detector (OXFORD Instruments) using a 10 keV electron beam. The deposited films were dipped in acetonitrile to remove residual electrolyte solution and air dried overnight before further investigations.

UV-Vis spectroscopy was performed on a Varian Cary 50 spectrophotometer in a standard cuvette (d = 10.0 mm).

Electrochemical characterization: Cyclic voltammetry (CV) and bulk electrolysis (BE) were carried out using a Pine Research WaveDriver 200 electrochemical workstation applying IR-compensation at 95%. Uncompensated resistance was determined by impedance using the EIS-RU tool included in the AfterMath software. All experiments were performed in dry acetonitrile using $n\text{Bu}_4\text{NPF}_6$ (0.1 M) as a supporting electrolyte. The solutions were purged with argon for at least 15 min to remove O_2 and kept under a slight positive Ar pressure during the experiments. Cyclic voltammetry was performed in a standard three-electrode arrangement using a glassy carbon disc as the working electrode, a platinum wire as a counter electrode and a silver wire in a glass frit, containing electrolyte solution, as a quasi-reference electrode. Bulk electrolysis was performed using a glassy carbon plate working electrode, which was placed in a two-compartment cell separated from the Pt wire by a frit. The Ag reference electrode was placed in a glass tube with a porous frit close to the working electrode. During BE, the working electrode was kept at a constant potential -250 mV vs. Ag/Ag^+ and the solution was stirred carefully.

WILEY-VCH

SUPPORTING INFORMATION

Pulsed electrodeposition of $K_6\{V_{12}\}$: Pulsed electrodeposition (PED) was performed using the Pine WaveDriver 200 Potentiostat with the cyclic step chronoamperometry (CSCA) module. The experimental conditions including the electrolyte concentration (0.5 mM $K_6\{V_{12}\}$ in 0.1 M (nBu_4N) PF_6)/acetonitrile), platinum wire as a counter electrode and a silver wire in a glass frit, containing electrolyte solution as a quasi-reference electrode are the same as used in bulk electrolysis experiments. The $K_6\{V_{12}\}$ based thin films were deposited on the glassy carbon electrode or carbon-coated aluminum foil in an unstirred cell by employing the specific reduction potentials. The CSCA experiment was carried out in two distinct steps, first a potential of 0 mV vs. Ag/Ag^+ was applied to the working electrode for 60 seconds known as relaxing period (t_{off}), then the desired reduction potential of e.g. -250 mV vs. Ag/Ag^+ was applied for a period of 120 seconds known as deposition period (t_{on}). These two steps were repeated alternately to accomplish 10 successive pulse cycles. The experiments were performed at different deposition potentials -250, -500 and -900 mV vs. Ag/Ag^+.

Electrochemical characterization of the deposited films in a prototype potassium-ion battery half-cell: Electrochemical tests were carried out in Swagelok-type using Whatman glass fiber as separator and metallic potassium as the counter and reference electode. A solution of 1 M KFSI in dimethoxyethane (DME) was used as electrolyte. Working electrodes were prepared by pulsed electrodeposition of $K_6\{V_{12}\}$ on carbon-coated aluminum foil at three different deposition potentials -250, -500 and -900 mV vs. Ag/Ag^+ as described above. After deposition, the samples were carefully washed with acetonitrile to remove the access electrolyte from the electrode surface, dried at 40 °C for 12 h under vacuum and cut into 12 mm (diam.) working electrodes with average total mass loading of ca. 0.40 mg. The galvanostatic charge-discharge (GCD) measurement was conducted using the Bio-Logic VMP-3 potentiostat. The GCD cycling of the deposited films was performed in the voltage range of 1.5 – 3.8 V vs. K/K^+ at a current density of 50 mA g^{-1}.

Electrochemical quartz crystal microbalance: EQCM experiments were performed with a CHI440 electrochemical quartz crystal microbalance (CH Instruments, TX, USA) using 8 MHz quartz crystal sensors coated with Au (CH Instruments, TX, USA) in a three-electrode set-up: Au coated quartz crystal (area = 0.205 cm^2) as working electrode, a silver wire as reference electrode and a platinum wire as counter electrode. All experiments were performed in 0.5 mM $K_6\{V_{12}\}$ in 0.1 M (nBu_4N)PF_6/acetonitrile. The solutions were purged with Ar for at least 15 min to remove O_2. During bulk electrolysis (BE) the working electrode was kept at a constant potential of -250 mV vs. Ag/Ag^+ and cyclic voltammetry (CV) was performed using potential ranges of 500 mV to -250 mV, -500 mV and -900 mV vs. Ag/Ag^+, respectively, using a scan rate of 100 mV s^{-1}.

Atomic force microscopy: AFM measurements were performed with a 5500 AFM/SPM microscope (Keysight Technologies, Arizona, USA) in contact mode. Films deposited at -250 mV, -500mV and -900 mV vs. Ag/Ag^+ were recorded in acetonitrile to avoid cracking and curling of the film due to drying. All images were recorded with silicon nitride probes (Model: ORC8-10, Bruker AFM Probes, USA) with a scan speed of 0.40 ln s^{-1}. Topography images were line by line leveled and corrected for better depiction. For data evaluation, only a slope correction was applied using the software MountainsSPIP® Academic (Digital Surf, France). Values for the arithmetic mean height (*Sa*) and film thickness are reported as mean value ± standard deviation (*Sa*: n = 5 areas of 25 x 25 μm^2 for the films deposited at -250 mV and -900 mV vs. Ag/Ag^+, n = 4 areas of 25 x 25 μm^2 for the film deposited at -500 mV vs. Ag/Ag^+ film thickness: n = 30 profiles from three different areas distributed over the sample, respectively).

Results and Discussion

1. UV-Vis spectroscopy of $K_6\{V_{12}\}$

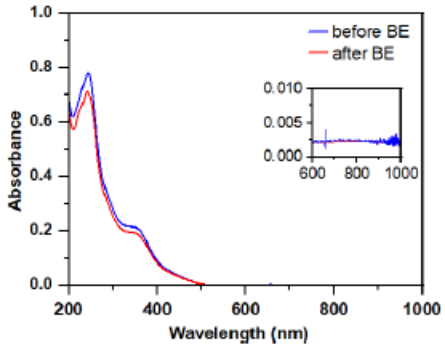

Figure S1: UV-Vis spectrum of $K_6\{V_{12}\}$ in acetonitrile (c = 4.5 x 10^{-6} M) before and after the bulk electrolysis.

2. Electrochemical quartz crystal microbalance (EQCM)

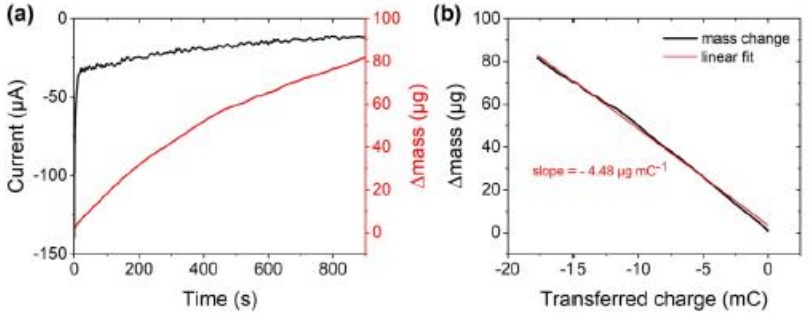

Figure S2: a) *I-t* curve (black) of the deposition in $K_6\{V_{12}\}$ (0.5 mM; 0.1 M $(nBu_4N)PF_6$)/ acetonitrile as supporting electrolyte) at a constant potential of -250 mV vs. Ag/Ag^+ with corresponding mass change (red) related to the film deposition (8 MHz quartz sensor); **b)** deposited mass versus transferred charge during the deposition showing the linear fit.

3. Pulsed electrodeposition of $K_6\{V_{12}\}$

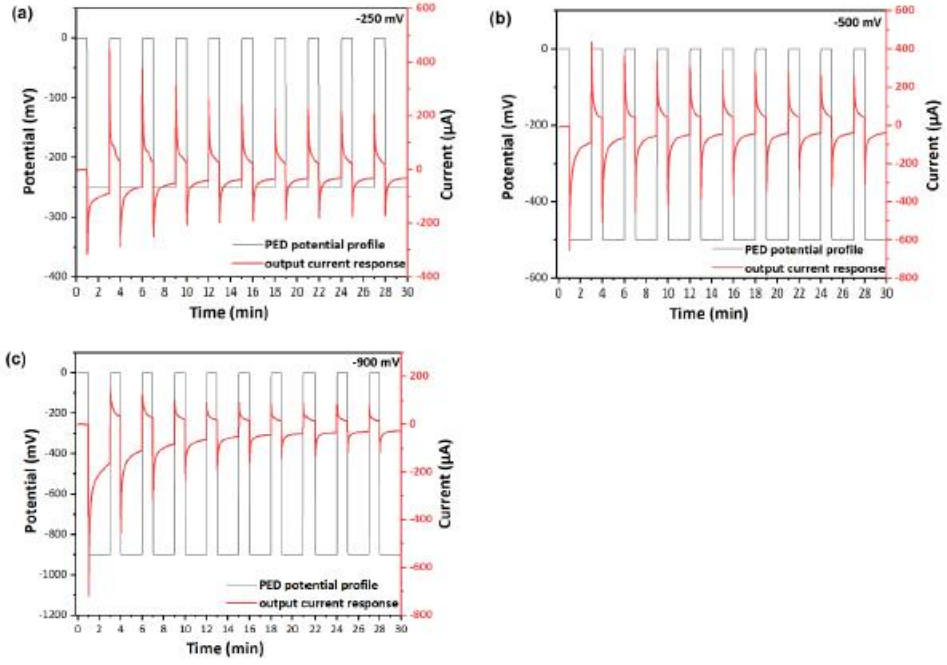

Figure S3: Pulsed electrodeposition profile of $K_6\{V_{12}\}$ at three different reduction potentials **a)** -250 mV, **b)** -500 mV and **c)** -900 mV vs. Ag/Ag^+, Conditions: dry, de-aerated acetonitrile containing 0.1 M $(nBu_4N)PF_6$ as electrolyte salt and $[K_6\{V_{12}\}]$ = 0.5 mM.

4. Scanning electron microscopy (SEM) and energy-dispersive X-ray spectroscopy (EDX) maps

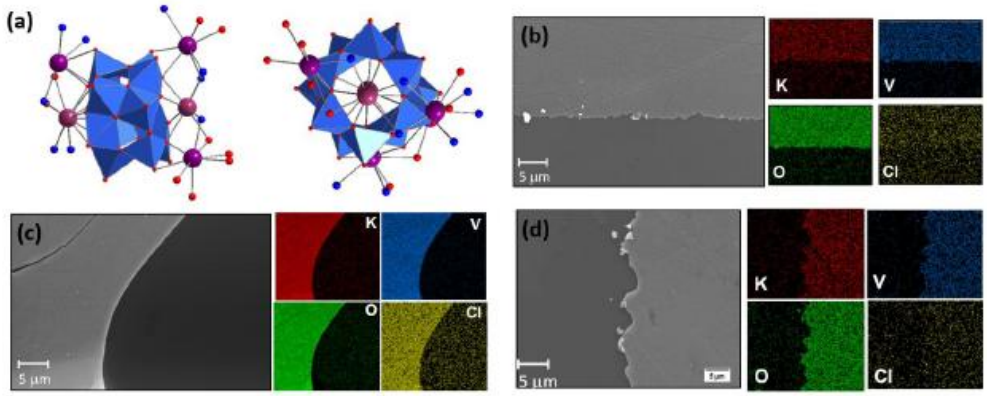

Figure S4: **a)** Scheme of side and top view of $K_6\{V_{12}\}^{Cl}$ Colour scheme: V, $[VO_5]$ polyhedral: blue; O: red; N: dark blue; Cl: green; K: plum. SEM image (left) and EDX elemental mapping (right) of the $K_6\{V_{12}\}$ based film deposited at **b)** -250 mV, **c)** -500 mV, and **d)** -900 mV vs. Ag/Ag^+.

5. EDX spectra

EDX analysis of the deposited films in dependence of the deposition potential.

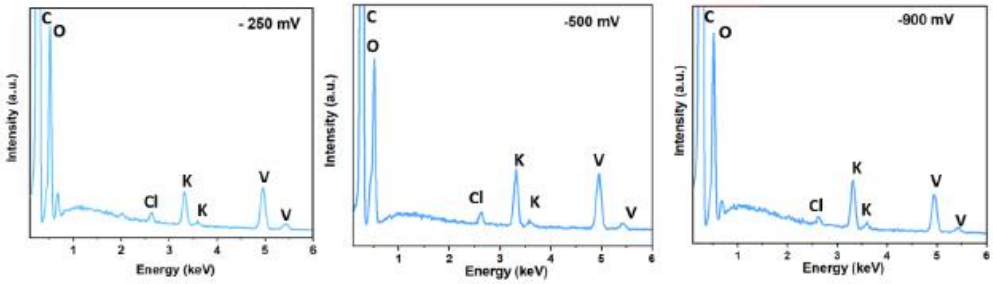

Figure S5: EDX spectra of $K_6\{V_{12}\}$ films deposited at **a)** -250 mV, **b)** -500 mV, and **c)** -900 mV vs. Ag/Ag^+.

6. Fourier transform infrared-attenuated total reflection spectroscopy (FTIR-ATR)

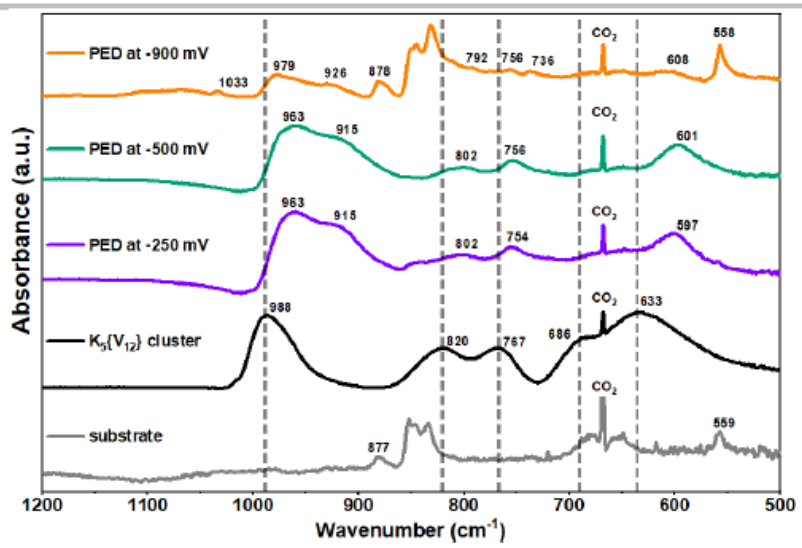

Figure S6: FTIR-ATR spectra in the spectral range from 1200 cm^{-1} to 500 cm^{-1} of the $K_5\{V_{12}\}$ cluster as well as the substrate and deposited $K_5\{V_{12}\}$ film deposited at -250 mV, -500 mV and -900 mV vs. Ag/Ag^+. The distinct bands visible at 878 cm^{-1} and 558 cm^{-1} as well as in the range of 825 cm^{-1} to 860 cm^{-1} can be attributed to the carbon substrate. Those bands are hardly visible in the films deposited at -250 mV and -500 mV vs. Ag/Ag^+ due to the increased thickness, which likely leads to a superposition of the signals.

7. UV-Vis spectroscopy of the solution after stripping the film

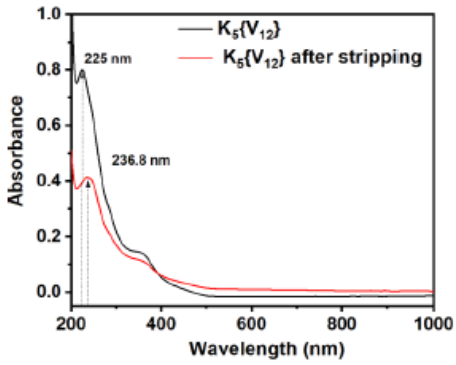

Figure S7: UV-Vis spectra of $K_5\{V_{12}\}$ in acetonitrile before electrodeposition (black) and $K_5\{V_{12}\}$ after stripping of the film into fresh electrolyte.

8. X-ray photoelectron spectroscopy (XPS)

The high-resolution XPS spectra were fitted using CasaXPS software. The presented XPS data were calibrated with the carbon C 1s peak at 284.8 eV as the reference. Also, all spectra were fitted with the Shirley background type and included the O 1s peak at the binding energy ~530.2 eV to determine the region underneath the V 2p. The ratio between both oxidation states can be calculated by correlating the area under the curves for V^{5+} $2p_{3/2}$ and V^{4+} $2p_{3/2}$ using the equation given below: [3]

$$\text{Ratio}_{\text{Species 2}} = ((B/f_2)/(A/f1 + B/f2))$$

The V 2p spectrum of the pure $K_5\{V_{12}\}$ shows the $2p_{3/2}$ peak that confirms the presence of +5 oxidation states as a prominent oxidation state of vanadium centers.

SUPPORTING INFORMATION

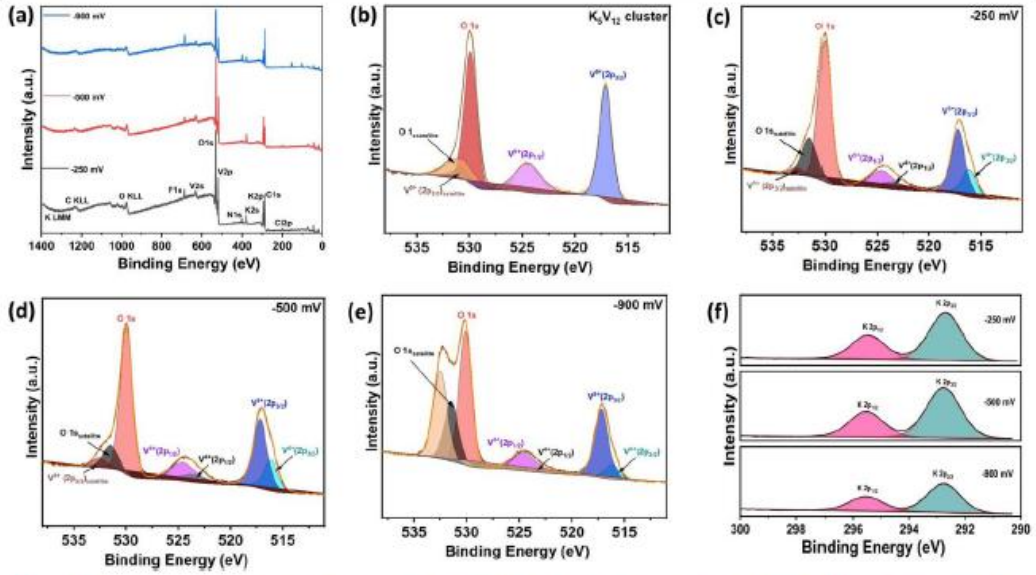

Figure S8: **a)** Survey XPS spectra of the deposited $K_5\{V_{12}\}$ films at different potentials, high-resolution XPS spectra of **b)** $K_5\{V_{12}\}$ cluster and reduced $K_5\{V_{12}\}$ films at reduction potential **c)** -250 mV, **d)** -500 mV, and **e)** -900 mV vs. Ag/Ag^+, and **f)** the K 2p XPS spectrum of the deposited films.

X-ray photoelectron spectroscopy of K_5V_{12} film deposited at -900 mV vs. Ag/Ag^+ in inert condition

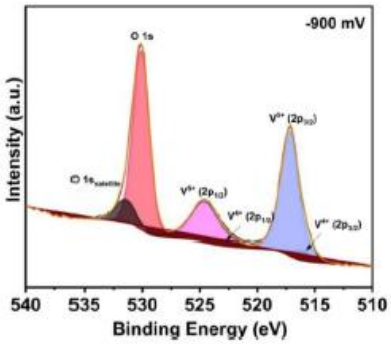

Figure S9: High-resolution XPS spectra of the reduced $K_5\{V_{12}\}$ films at -900 mV *vs.* Ag/Ag^+ measured in inert condition

9. Galvanostatic cycling

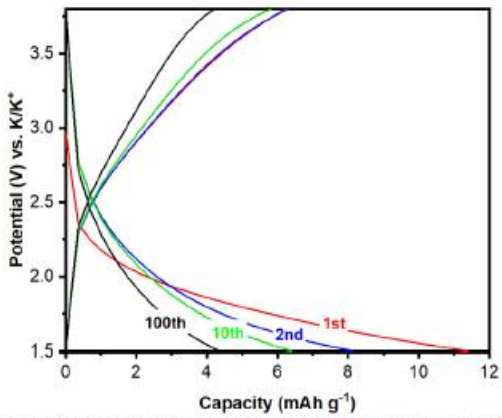

Figure S10. Selected cycles of galvanostatic cycling of the film deposited on carbon-coated Al-foil substrates at –900 mV vs. Ag/Ag^+ via PED; in the range of 1.5 – 3.8 V vs. K^+/K at 50 mA g^{-1}.

References

[1] K. Kastner, J. T. Margraf, T. Clark, C. Streb, *Chem. Eur. J.* **2014**, *20*, 12269–12273.
[2] S. Greiner, M. Anjass, C. Streb, *CrystEngComm*, **2021**, *23*, 3946–3950.
[3] Y. C. Ji, L. J. Huang, J. Hu, C. Streb, Y. F. Song, *Energy Environ. Sci.* **2015**, *8*, 776–789.

Author Contributions

All authors conceived the experiments. N. A. and S. G. performed synthesis, electrochemical characterization, and data analysis. N. A. S.G and M. S. performed the vanadate cluster electrodeposition and film characterization. T. P. performed EQCM, AFM and FTIR-ATR measurements and analysis. N. A., T. P., S. G, C. K. and M. A. concepted the experiments and revised the manuscript. N. A. and T. P. contributed equally to this study.

6.2 (NA2): Tuning the Electronic and Electrochemical Properties of 3D Porous Laser-induced Graphene by Electrochemically Induced Deposition of Polyoxovanadate Nanoclusters for Flexible Supercapacitors

Nikhil Arya, Sirshendu Dinda, Thomas Diemant, Ke Wang, Maximilian Fichtner and Montaha Anjass*

*Corresponding author

Published in: *Advanced Functional Materials* (2024): 2410943

Copyright: Arya, Nikhil, Sirshendu Dinda, Thomas Diemant, Ke Wang, Maximilian Fichtner, and Montaha Anjass. "Tuning the Electronic and Electrochemical Properties of 3D Porous Laser-Induced Graphene by Electrochemically Induced Deposition of Polyoxovanadate Nanoclusters for Flexible Supercapacitors." *Advanced Functional Materials* (2024): 2410943.

DOI: https://doi.org/10.1002/adfm.202410943

Licence: CC BY 4.0 (https://creativecommons.org/licenses/by/4.0/)

Author contribution:

N. Arya: Material synthesis and characterization, electrochemical characterization, data analysis, writing and revision of the manuscript

S.Dinda: Performed Raman measurements and analysis, writing and revision of the Manuscript

T. Diemant: Performed the XPS measurement and analysis, revision of manuscript

K. wang: Material preparation and electrochemical characterization

M. Anjass: Result discussion, writing, and revision of the manuscript

Check for updates

RESEARCH ARTICLE

ADVANCED FUNCTIONAL MATERIALS
www.afm-journal.de

Tuning the Electronic and Electrochemical Properties of 3D Porous Laser-Induced Graphene by Electrochemically Induced Deposition of Polyoxovanadate Nanoclusters for Flexible Supercapacitors

*Nikhil Arya, Sirshendu Dinda, Thomas Diemant, Ke Wang, Maximilian Fichtner, and Montaha Anjass**

The advancement of microelectronic devices mandates the development of flexible energy storage systems to enable the fabrication of miniaturized and wearable electronics. Herein, a sustainable approach is demonstrated for tuning the electronic and electrochemical properties of hierarchically porous laser-induced graphene (LIG) substrates. The methodology entails the electrochemical deposition of polyoxovanadate nanoclusters ($K_5(CH_3CN)_3[V_{12}O_{32}Cl]$ (= $K_5\{V_{12}\}$)) onto the highly porous LIG matrix. The comprehensive characterization is integrated through micro-Raman spectroscopy and in-depth X-ray photoelectron spectroscopy to elucidate the deposition mechanism and electronic properties of the fabricated electrode. The results indicate a significant correlation between the orientation of the deposited clusters and the non-crystalline regions of the LIG structure. Additionally, the cluster deposition results in a reduction of grain boundary defects in the nano-graphite lattice of LIG. The optimized electrode exhibits enhanced areal capacitance (C_A) of 125 mF cm^{-2} at a current density of 0.1 mA cm^{-2}, representing a fivefold improvement compared to the undoped LIG substrate. Furthermore, as a proof of concept, a flexible solid-state symmetrical supercapacitor device, fabricated with a PVA-H_2SO_4 gel electrolyte, demonstrates an areal capacitance of 24.92 mF cm^{-2} at current density of 0.1 mA cm^{-2} and exhibits exceptional cycling stability, enduring up to 5000 consecutive galvanostatic charge-discharge cycles.

1. Introduction

The transition from fossil-fuel-based systems to carbon-neutral and sustainable energy storage systems requires affordable modern energy storage systems with high power density and extended life cycles. The growing demand for such next-generation energy storage systems arises from their promising functionality in various applications, such as portable electronic devices, electric vehicles, energy harvesting, etc.[1–5] As a consequence, considerable research focuses on high-performance electrochemical double-layer supercapacitors (EDLSCs) due to their high power density, enhanced electrochemical stability, and remarkable charge-discharge cycle performance.[6] The working principle of EDLSCs relies on the non-faradaic fast adsorption/desorption of the electrolyte ions between the electrolyte and the highly electron/ion conductive porous electrode material. Over the past decade, graphene-based electrode materials have emerged as an

N. Arya, K. Wang, M. Anjass
Institute of Inorganic Chemistry I
Ulm University
Albert-Einstein-Allee 11, 89081 Ulm, Germany
E-mail: montaha.anjass@uni-ulm.de

The ORCID identification number(s) for the author(s) of this article can be found under https://doi.org/10.1002/adfm.202410943

© 2024 The Author(s). Advanced Functional Materials published by Wiley-VCH GmbH. This is an open access article under the terms of the Creative Commons Attribution License, which permits use, distribution and reproduction in any medium, provided the original work is properly cited.

DOI: 10.1002/adfm.202410943

N. Arya, S. Dinda, T. Diemant, M. Fichtner, M. Anjass
Helmholtz Institute Ulm for Electrochemical Energy Storage (HIU)
Helmholtzstr. 11, 89081 Ulm, Germany
T. Diemant, M. Fichtner
Karlsruhe Institute of Technology (KIT)
Institute of Nanotechnology
P. O. Box 3640, 76021 Karlsruhe, Germany
M. Anjass
Department of Chemistry
University of Sharjah
27272 Sharjah, United Arab Emirates

ADVANCED SCIENCE NEWS
www.advancedsciencenews.com

ADVANCED FUNCTIONAL MATERIALS
www.afm-journal.de

16163028, 0, Downloaded from https://onlinelibrary.wiley.com/doi/10.1002/adfm.202410943, Wiley Online Library on [21/08/2024]. See the Terms and Conditions (https://onlinelibrary.wiley.com/terms-and-conditions) on Wiley Online Library for rules of use; OA articles are governed by the applicable Creative Commons License

ideal choice for EDLSC electrodes due to their large 3D nano/microstructure surface area, excellent electronic properties, and high mechanical stability.[6] However, the intrinsic structural modification and restacking of the active graphene layers in pristine graphene-based electrodes cause poor ion and electron transport within the electrode, resulting in low theoretical capacitance and limited energy density.[7] To address these limitations, several strategies such as oxidation, exfoliation, and heteroatom insertion into graphene materials have been reported in order to enhance the pseudo-capacitive performance of graphene-based electrodes.[8–11]

Recently, laser-induced graphene has been extensively used as a promising electrode precursor for flexible supercapacitors (SCs) due to its unique physiochemical properties, good electrical conductivity, highly porous micro/nanostructure, and favorable thermal and mechanical stability.[12–14] LIG is generated by irradiating polyimide (PI) with a laser at a wavelength of about 500 nm; the high-temperature treatment and spontaneous gas formation on the PI layer result in a 3D, highly porous micro/nanostructure.[15] This method facilitates large-scale fabrication of flexible graphene materials while preserving important graphene properties for various applications such as electrocatalysis, sensors, SCs, and microfluidics.[16–20] The success of LIG as a flexible electrode matrix for application in SCs and micro-SCs has been attributed to excellent electrolyte ion diffusion within the porous LIG surface.[21–23] The capacitive performance of a pristine LIG surface is limited to less than 10 mF cm^{-2} due to the large number of non-functionalized capacitive sites.[12,13,24] Alternatively, a huge specific surface area and substantial crystallite defects enable LIG to be easily modified by functionalization and heteroatom doping. Previous reports on structural modification via heteroatom doping with boron (B), phosphorus (P), and nitrogen (N) have demonstrated an enhancement of capacitive performance by up to threefold.[25–28]

In this study, we show an easy and effective method for enhancing the capacitive charge storage performance by embedding vanadium oxide nanoclusters on hierarchical porous LIG. These molecular metal oxide structures are known as polyoxometalates (POMs). POMs are anionic metal oxoclusters of highly valent early transition metals (often Mo, W, and V) that form by self-assembly in solution.[29] POMs, specifically polyoxovanadates (POVs), have garnered attention due to their promising electrochemical properties and unique multivalent characteristics.[30] Moreover, these POV structures have set a new benchmark for successful heterometallic functionalization, opening up a systematic route to the study of controlled structural and electrochemical tuning.[31,32] Recent studies have investigated the interaction between alkali cations and POVs and demonstrated the influence of these cations on structural stability and electrochemical properties.[33] Schimpf and co-workers illustrated this influence of the concentration of the charge-balancing cation (K^+) on the coordination of the polyoxotungstate phase using the Preyssler-type polyoxoanion cluster $[NaP_5W_{30}O_{110}]^{14-}$.[34] Similarly, the Dawson-type polyoxotungstate showed cation-controlled reversible storage of up to 18 electrons in solution.[35] However, the technological application of POMs remains challenging due to the lack of a clear method to transform soluble POM species into a solid substance and immobilize them on a functional substrate. Interestingly, the cluster immobilization by electrochemical deposition leads to continuous film growth on the substrate in a more controlled manner. Hwu and co-workers, for instance, recently showed the electrochemical crystal growth of decavanadate-based organic-inorganic hybrids.[36]

Our group has recently provided the first proof of concept for a reversible electrochemically deposited thin film of the potassium-bridged molecular vanadium oxide cluster ($K_5(CH_3CN)_3$ $[V_{12}O_{32}Cl]$ (= $K_5\{V_{12}\}$)) or K-POV on a conductive surface.[37] The reduction of $K_5\{V_{12}\}$ in excess K^+ ions leads to the reduction-induced growth of a potassium-enriched homogeneous POV film on the conductive surface. Furthermore, comprehensive electrochemical studies provided in-depth understanding of the physicochemical properties, structural tuning, and redox activity of the electrochemically deposited $K_5\{V_{12}\}$-based thin film. Herein, we expand our investigation on a highly porous LIG graphene nanostructure as substrate, reporting a facile electrochemical deposition route that enables the successive deposition of reduced $K_5\{V_{12}\}$. Detailed spectroscopic investigation reveals that the deposition of $K_5\{V_{12}\}$ on the LIG nanostructure occurs via physisorption. Nevertheless, the deposited reduced $K_5\{V_{12}\}$ species exhibit high redox activity, enhancing the number of pseudocapacitive active sites and promoting reversible redox reactions and rapid charge storage capacity on the modified LIG electrode surface. During electrodeposition, reduction-induced growth of a potassium-enriched $K_x\{V_{12}\}$ film on the conductive surface occurred, facilitating the formation of mixed-valent vanadium centers V^V/V^{IV}. This unique property of POVs to change their oxidation state and incorporate transition metal has been utilized in various electrocatalysis applications.[38,39] The deposition of reduced $K_5\{V_{12}\}$ on the LIG surface enhances the electrocatalytic properties of the electrode, leading to the formation of various complexes between the vanadium oxide and electrolyte anions on the modified electrode. These vanadium-based oxosulphato/hydroxysulphato complexes prevent the LIG graphene substrate from restacking and transforming into a decomposed amorphous, soot-like carbon structure during charge-discharge cycles. Consequently, the high redox activity of the LIG electrode is sustained, enhancing the specific charge storage capacity of these $K_5\{V_{12}\}$ modified electrodes.

2. Result and Discussion

The $K_5\{V_{12}\}$ nanoclusters, employed in this study, were synthesized through a self-assembly process of two hexagonal $\{V_6\}$ rings, as depicted in **Figure 1a**. The electrochemical deposition and complex supramolecular aggregation on the porous LIG surface were initiated upon dissolving the $K_5\{V_{12}\}$ in an alkali metal salt-based supporting electrolyte of potassium hexafluorophosphate (KPF_6). The presence of a strong electropositive cation, such as K^+, in the solvent enables controlled crosslinking with the vanadium oxide framework, resulting in a homogeneous settlement within the nanoporous graphene network.[40] This potential-controlled deposition of $K_5\{V_{12}\}$ illustrates the indispensability of strong electropositive alkali metal cations for stabilizing the reduced cluster, leading to the development of highly redox-active supramolecular cluster growth on any conductive surface.[37]

© 2024 The Author(s). Advanced Functional Materials published by Wiley-VCH GmbH

ADVANCED SCIENCE NEWS
www.advancedsciencenews.com

ADVANCED FUNCTIONAL MATERIALS
www.afm-journal.de

16163028, 0, Downloaded from https://onlinelibrary.wiley.com/doi/10.1002/adfm.202410943, Wiley Online Library on [21/08/2024]. See the Terms and Conditions (https://onlinelibrary.wiley.com/terms-and-conditions) on Wiley Online Library for rules of use; OA articles are governed by the applicable Creative Commons License

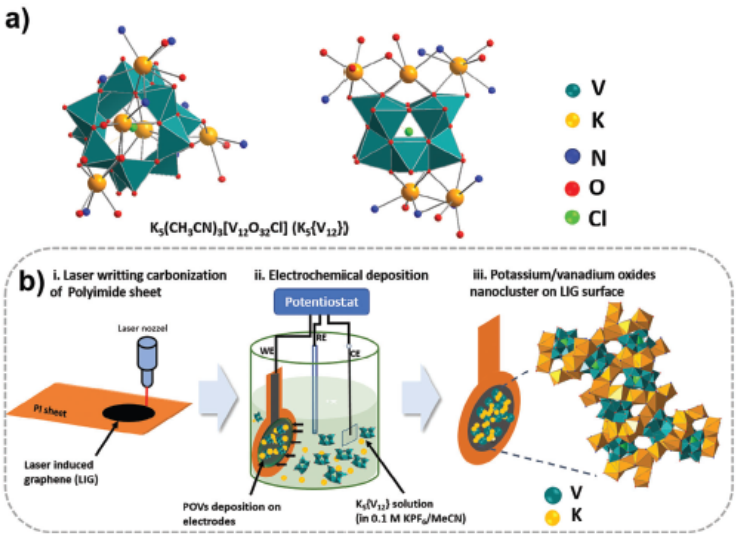

Figure 1. a) Molecular structure of the $K_5\{V_{12}\}$ cluster (left image: top view, right image: side view). b) Schematic representation of LIG electrode fabrication and electrochemical immobilization of $K_5\{V_{12}\}$. Color scheme: V (teal); O (red), N (blue), Cl (green), and K (yellow).

Figure 1b shows the main steps for preparing the K-POV/LIG electrodes. More experimental details can be found in the Supporting Information (SI). In brief, the LIG precursor was prepared by laser irradiating a polyimide sheet, generating an active area of 1 cm^2 for the deposition process.[12] The deposition of $K_5\{V_{12}\}$ was accomplished by cyclic voltammetry (CV) scans conducted within three different potential ranges: −250 – 250 mV, −500 – 500 mV, and −750 – 750 mV versus Ag^+/Ag, with the operating electrode scanned at 100 mV s^{-1} in a conventional three-electrode cell configuration using a non-aqueous ionic electrolyte solution (1 mM $K_5\{V_{12}\}$ in 0.1 M KPF_6 in MeCN). In each experiment, nine consecutive CV cycles were acquired (Figure S1a, Supporting Information). The modified LIG electrodes are labeled K-POV-250, K-POV-500, and K-POV−750 in the following, corresponding to the above-mentioned potential ranges.

To mitigate diffusion limitations during deposition, a 60-second rest period was introduced after every 3 consecutive CV cycles. The working electrode initially rested at 0 mV versus Ag^+/Ag, cycled toward the upper oxidative potential limit during the first sweep, and then reduced to the reduction potential limit. All the CVs that were measured showed a broad anodic peak at ≈220 mV versus Ag^+/Ag during the scan from the initial resting potential to the oxidative potential limit. This is in line with the solute $\{V_{12}\}$ cluster's characteristic reversible oxidation behavior.[37] Similarly, during the cathodic sweep to -500 mV versus Ag^+/Ag, a reduction process started at ≈100 mV versus Ag^+/Ag. This was caused by the partial reduction of the vanadium centers from V^{+V} to V^{+IV} oxidation state (Figure S1b, Supporting Information).[37] This reduction process facilitates stronger interaction between the reduced anionic cluster framework $\{V_{12}\}$ and dissolved K^+ ions, which enhanced the cluster's insolubility and resulted in the electrodeposition of the POVs on the LIG surface. Increasing the potential window from −500 to −750 mV versus Ag^+/Ag leads to an additional reduction feature in the CV at about −550 mV versus Ag^+/Ag, possibly representing a further reduction of the already deposited cluster species. This leads to an enhanced cathodic current observed for −750 mV versus Ag^+/Ag potential range. In addition, the following cycles observe a significant shift of the anodic peak (from 220 to 340 mV versus Ag^+/Ag), confirming that the charge compensating K^+ cations stabilized the reduced cluster, making its re-oxidation more difficult. These findings are in good agreement with a previous report.[37] The deposition of the cluster at a potential range of −750 to 750 mV versus Ag^+/Ag shows multiple redox peaks during the first CV cycle. This confirms that the $K_5\{V_{12}\}$ cluster has distinct redox-active properties in a higher potential range. To investigate the influence of the deposition of the $K_5\{V_{12}\}$ cluster on the LIG electrode, a blank CV measurement was performed on a fresh LIG electrode under similar conditions but without the $K_5\{V_{12}\}$ in the supporting electrolyte (only 0.1 M KPF_6/MeCN). More experimental details can be found in the supporting information. Figure S1c (Supporting Information) displays the comparison between the CV responses measured with and without $K_5\{V_{12}\}$ in the potential window of −750 to 750 mV versus Ag^+/Ag. In the absence of $K_5\{V_{12}\}$, the measured CV response exhibits a charge storage behavior that is completely non-faradaic and without any redox features. This confirms that there are no redox-active species in the electrolyte. As a result, after nine consecutive cycles, no obvious changes were visible in the LIG electrode's CVs. In contrast, in the presence of $K_5\{V_{12}\}$ in the supporting electrolyte, the first cycles showed multiple redox peaks due to cluster reduction on the LIG surface. Notably, the

© 2024 The Author(s). Advanced Functional Materials published by Wiley-VCH GmbH

ADVANCED SCIENCE NEWS
www.advancedsciencenews.com

ADVANCED FUNCTIONAL MATERIALS
www.afm-journal.de

16163028, 0, Downloaded from https://onlinelibrary.wiley.com/doi/10.1002/adfm.202410943, Wiley Online Library on [21/08/2024]. See the Terms and Conditions (https://onlinelibrary.wiley.com/terms-and-conditions) on Wiley Online Library for rules of use; OA articles are governed by the applicable Creative Commons License

LIG electrode with dissolved $K_5\{V_{12}\}$ exhibited two broad peaks after nine CV cycles at a reduction potential (E_1) of −300 and an oxidation potential (E_2) of 600 mV versus Ag^+/Ag, confirming quasi-reversible charge storage. Consequently, the substantial increase in the area under the CV curve signifies a noteworthy alteration in the electrochemical performance of the LIG electrode due to $K_5\{V_{12}\}$ deposition at a higher overpotential within the range of −750 to 750 mV versus Ag^+/Ag.

Next, the possible changes in the electrode morphology upon $K_5\{V_{12}\}$ deposition were analyzed by scanning electron microscopy (SEM). The surface of the pristine LIG electrode is shown in Figure S2a,b (Supporting Information), emphasizing its highly porous morphology, which is essential for the diffusion and deposition of the $K_5\{V_{12}\}$ cluster into the LIG pores upon application of cathodic potential. Figure S2c,d (Supporting Information) shows the morphology of the as-synthesized K-POV-750 electrode, revealing that the porous nanostructure of the LIG surface remains intact post-cluster deposition, with no visible aggregation of the clusters or electrolyte salt. The ultrathin, flakes-like morphology and porous nanostructure of the LIG substrate confer superior mechanical properties. Despite the $K_5\{V_{12}\}$ deposition, the LIG surface retains its inherent mechanical properties, including the retention of electronically conductive channels and a microporous architecture that facilitates enhanced electron mobility and ionic conductivity. To gain a deeper understanding of the elemental composition and validate the deposition of $K_5\{V_{12}\}$ on the LIG carbon structure, energy dispersive X-ray (EDX) spectroscopy analysis was performed for all three synthesized electrodes (K-POV-250, K-POV-500, and K-POV-750, Figure S2e-g, Supporting Information). The results confirmed the presence of the primary cluster components, vanadium (V) and potassium (K), for all synthesized electrodes. The EDX elemental analysis also revealed a slight variation in the K:V ratio, likely due to the different applied potential ranges (Table S1, Supporting Information). Therefore, the range of applied potential has a notable influence on the $K_5\{V_{12}\}$ deposition, allowing for plausible variations in the ratio of vanadium to potassium for the three synthesized samples.[37] X-ray diffraction (XRD) measurements were performed to evaluate the influence of the deposited $K_5\{V_{12}\}$ cluster on the LIG surface, as shown in Figure S2h (Supporting Information). The LIG electrode defined a distinct peak at a 2-theta value of ≈26°, corresponding to the (002) plane, which indicates a high degree of graphitization in the fabricated LIG substrate.[41] For all $K_5\{V_{12}\}$ modified electrodes, the observed peak at 26° became less prominent and gradually deteriorated with the cluster deposition at a higher potential range, confirming that the LIG structure is significantly altered by the deposition of $K_5\{V_{12}\}$ nanocluster.

Raman spectroscopy was employed to gain insights into changes in structural and electronic properties of the LIG substrate resulting from $K_5\{V_{12}\}$ deposition. The micro-Raman spectrum of pristine LIG is presented in Figure S3 (Supporting Information). Three prominent Raman bands at ≈1350 cm^{-1}, 1586 cm^{-1}, and 2695 cm^{-1} are recognized as the D, G, and 2D bands, respectively, which are commonly associated with any graphitic lattice.[42] The D band is attributed to phonons related to defects in the sp^2-carbon lattice, the G band signifies symmetric stretching of the sp^2-carbon lattice, and the 2D band originates from second-order zone-boundary phonons. The D' band, positioned at ≈1620 cm^{-1}, is also a vibrational mode related to defects and is observed as a shoulder band to the G band. It is commonly accepted that the ratio of peak intensities I_D/I_G is a measure for the disorder in the graphite layers, and the observed value of 0.72 for LIG suggests a nanocrystalline nature of the graphitic lattice.[43] Furthermore, the full width at half maximum (FWHM) of the 2D band (≈62 cm^{-1}) and the I_{2D}/I_G ratio (0.49) indicate that the pristine LIG primarily consists of randomly oriented stacks of graphene layers.[44] In addition, the presence of Raman bands such as D'' (≈1100 cm^{-1}), D' (≈1620 cm-1), D+D'' (≈2450 cm^{-1}), and D+D' (≈2940 cm^{-1}) also corroborates the presence of defective graphene lattices.[45] Given that the electrical conductivity and ion mobility of graphitic material depends on the structural properties of the sp^2 lattice, it is necessary to quantify changes in the number of defects during the electrochemical deposition of $K_5\{V_{12}\}$ and assess the overall crystallinity of the LIG electrode after cycling.

Defects within a graphite lattice can be classified into two categories: point-like defects (such as sp^3-type, vacancy-like defects, Stone-Wales defects, etc.) and line-like defects (including dislocations, grain boundaries, etc.). The quantification of defects in the graphitic lattice involves examining I_D/I_D' and D bandwidth with respect to the G-band-width.[45,46] In order to gain a better understanding of the distribution of defects in the graphitic lattice of the pristine LIG surface, Raman imaging measurements were carried out (with a spatial resolution of 1 × 1 mm^2 in a 60 × 60 mm^2 region). The results were put together in maps showing the peak intensities, positions, and widths (FWHM) of the D, G, and D' bands (Figure S4a, Supporting Information) and in histograms (Figure S4b, Supporting Information). The G band ranged from 1568 to 1586 cm^{-1}, and the D band from 1335 to 1348 cm^{-1}. It has been shown in literature that a red-shift of the bands together with a higher FWHM indicates the defect-rich regions of the LIG surface.[43,46] A prior investigation on defect-rich graphene concluded that the I_D/I_D' ratio is ≈13 for sp^3-type defects, ≈7 for vacancy-type defects, and 3.5 for boundary-type defects.[45] In our case, the pristine LIG exhibited an I_D/I_D' ratio of 3.69, suggesting a substantial influence of grain boundary-type defects on the nano-graphitic structure of LIG.[43,45] **Figure 2a** presents the development of characteristic values of the Raman spectra, namely peak positions (D, G, and D' band), FWHM of these bands, and $I_D/I_{D'}$ peak intensity ratio for pristine LIG, K-POV-500, and K-POV-750 electrodes. These values were derived by averaging the results of Raman maps. While the average peak frequency of all bands remains relatively constant, the FWHM and I_D/I_D' values exhibit a declining trend for $K_5\{V_{12}\}$ deposition at increasing overpotential. Furthermore, the decrease of the I_D/I_D' ratio after $K_5\{V_{12}\}$ deposition from 3.69 (pristine LIG) to 2.88 and 2.66 for K-POV-500 and K-POV-750 electrodes, respectively, signifies the elimination of grain boundary defects in the nano-graphite lattice, presumably leading to an improvement of the electrochemical properties of LIG. Additionally, the absence of sp^3-like defects or vacancies in LIG points to a predominant physisorption of the electrochemically deposited $K_5\{V_{12}\}$ on the LIG surface. Consequently, the deposited and reduced $K_5\{V_{12}\}$ does not form direct covalent or ionic bonds with the graphitic lattice.

Coming to the discussion of vanadate species, corresponding Raman spectra of pure $K_5\{V_{12}\}$ and K-POV-500 and K-POV-750

© 2024 The Author(s). Advanced Functional Materials published by Wiley-VCH GmbH

ADVANCED SCIENCE NEWS
www.advancedsciencenews.com

ADVANCED FUNCTIONAL MATERIALS
www.afm-journal.de

16163028, 0, Downloaded from https://onlinelibrary.wiley.com/doi/10.1002/adfm.202410943, Wiley Online Library on [21/08/2024]. See the Terms and Conditions (https://onlinelibrary.wiley.com/terms-and-conditions) on Wiley Online Library for rules of use; OA articles are governed by the applicable Creative Commons License

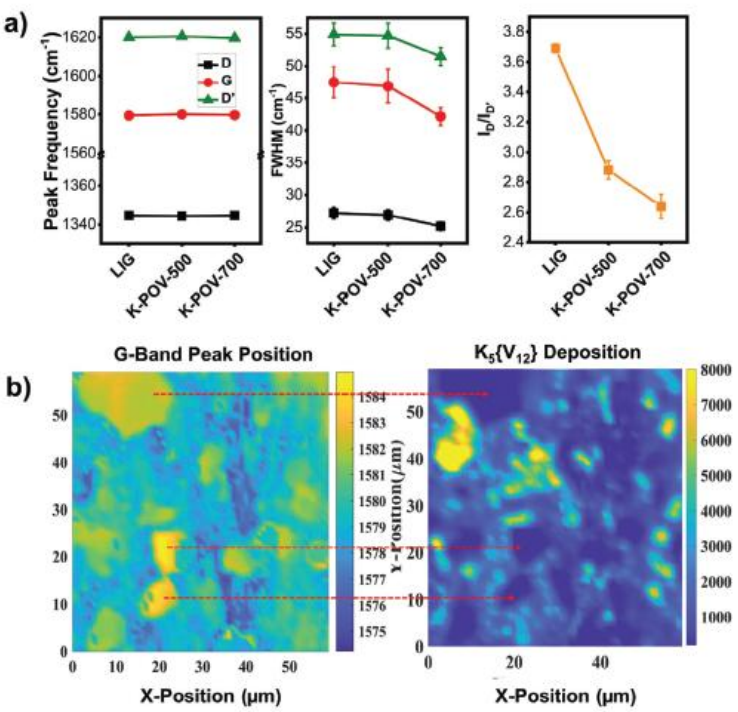

Figure 2. a) Comparison of Raman band parameters of unmodified LIG with K-POV-500 and K-POV-750 electrodes. b) Raman mapping of G band peak position and $K_5\{V_{12}\}$ deposition (from the intensity of the V-O stretch vibration at 875 cm^{-1}) for the synthesized K-POV-750 electrode, illustrating preferential deposition in the regions of low crystallinity.

electrodes are depicted in Figure S5a (Supporting Information). The intense band at ≈875 cm^{-1}, along with weaker bands at ≈938 cm^{-1} and 995 cm^{-1}, corresponds to the stretching vibration of VO_6/VO_5 units forming the polyoxovanadates.[47] Lower frequency bands at 400–600 cm^{-1} are generally assigned to the stretching vibrations of terminal V-O linkages, while bands at 200–400 cm^{-1} are associated with V-O-V bending modes. First of all, the detection of the band at ≈875 cm^{-1} confirms the presence of $K_5\{V_{12}\}$ on the K-POV-500 and K-POV-750 electrodes. Furthermore, the mapping result of this peak for the K-POV-500 electrode (Figure S5c, Supporting Information) reveals a heterogeneous spatial distribution of $K_5\{V_{12}\}$ on the surface. In addition, comparing this mapping result with that of the G-band peak position shows that $K_5\{V_{12}\}$ is preferentially situated around the regions with higher G-band peak frequencies, which are related to a higher crystallinity in the graphitic lattice (see above). Hence, the results demonstrate that electrochemical deposition favors the less crystalline regions of the LIG surface, although deposition starts initially rather at the boundary between the low- and high-crystalline regions. The mapping result for K-POV-750 exhibits a similar trend (Figure 2b), with preferred $K_5\{V_{12}\}$ deposition in the low crystallinity regions. This noteworthy behavior of preferential deposition provides further insight into the physiochemical nature of the fabricated LIG. In this context, the pristine crystalline segments of LIG maintain high electrical and ionic mobility, while the sections with deposited $K_5\{V_{12}\}$ in K-POV-750 and K-POV-500 modified the chemical inertness of the sp^2 lattice in LIG.

In the next step, X-ray photoelectron spectroscopy (XPS) was used to test the elemental composition and the chemical state of the elements in the surface layer. The results of measurements of pristine samples (LIG and K-POV-750) before cycling are shown in Figure S6 (Supporting Information). The survey spectrum of pure LIG shows dominating signals of carbon (C1s peak at ≈285 eV) and oxygen (O1s peak at ≈532 eV) (Figure S6a, Supporting Information). As expected, the deposition of $K_5\{V_{12}\}$ leads to additional features in the survey spectrum of K-POV-750, which can be attributed to potassium (K2p peak at ≈293 eV) and vanadium ($V2p_{3/2}$ peak at ≈517 eV). The detailed spectrum in the C1s region shows for pure LIG the typical features of a graphitic sample, with the dominating sp^2-C peak at 284.5 eV and the π-π^* satellite at 290.9 eV (Figure S6b, Supporting Information).[49] In addition, relatively prominent peaks at 285.1 eV, 286.6 eV, and 288.3 eV point to sizable quantities of C-C/C-H, C-O, and

© 2024 The Author(s). Advanced Functional Materials published by Wiley-VCH GmbH

ADVANCED SCIENCE NEWS
www.advancedsciencenews.com

ADVANCED FUNCTIONAL MATERIALS
www.afm-journal.de

16163028, 0, Downloaded from https://onlinelibrary.wiley.com/doi/10.1002/adfm.202410943, Wiley Online Library on [21/08/2024]. See the Terms and Conditions (https://onlinelibrary.wiley.com/terms-and-conditions) on Wiley Online Library for rules of use; OA articles are governed by the applicable Creative Commons License

C = O species on the surface, respectively. In agreement with the results in the C1s region, the main peaks in the O1s spectrum (Figure S6c, Supporting Information) are assigned to C = O (531.9 eV) and C-O (533.1 eV) groups, respectively. The C1s detail spectrum of K-POV-750 (Figure S6d, Supporting Information) shows the same C species as the pure LIG. The stronger reduction of the intensities of the C-C/C-H, C-O, and C = O contributions compared to the sp^2-C signal corroborates the preferential deposition of $K_5\{V_{12}\}$ clusters on defect sites. The C1s spectrum also includes the K2p peak doublet of the K-POV with the $K2p_{3/2}$ peak component at 293.3 eV. Similarly, the O1s and V2p peaks of K-POV-750 appear in one common binding energy region (Figure S6e, Supporting Information). The peak fit shows that most vanadium is in oxidation state +V ($V2p_{3/2}$ peak at 517.6 eV); in addition, a smaller contribution from V^{+IV} ($V2p_{3/2}$ peak at 516.3 eV) can also be discerned. For oxygen, the additional peak at 530.3 eV can be assigned to the POV oxygen atoms. The results of the quantitative analysis of pure LIG and the three K-POV electrodes are compiled in Table S2 (Supporting Information). A comparison of the K-POV electrodes shows for K-POV-750 the highest V concentration; hence, $K_5\{V_{12}\}$ deposition seems to be most effective for the largest potential window.

To investigate the electrochemical performance of pristine LIG and $K_5\{V_{12}\}$ deposited electrodes, we first performed cyclic voltammetry measurements in a typical three-electrode cell setup at a set operating potential referenced to the standard Ag/AgCl electrode (aqueous reference), using a Pt wire as counter electrode and aqueous 1 M H_2SO_4 as electrolyte. The operating potential window for the measurement ranged from −300 to 1000 mV (versus aq. Ag^+/Ag). The detailed experimental procedures are described in the supporting information. The CV curves shown in **Figure 3a** indicate that all K-POV electrodes exhibit significantly improved cyclic voltammetry responses compared to pristine LIG electrode, and thus enhanced charge storage capacity. As confirmed by Raman mapping (see above), the $K_5\{V_{12}\}$ cluster deposition preferentially takes place at regions of low crystallinity on the LIG electrode, which seems to contribute to the improved electronic and electrochemical properties of the graphitic structure. Controlled CV measurements were performed on the pristine LIG electrode in 1 M H_2SO_4 electrolyte containing the $K_5\{V_{12}\}$ cluster and showed a broad reduction peak in the range of 600–800 mV versus Ag^+/Ag, without an enhancement of the overall capacitance of LIG as in the case of K-POV modified electrodes (see Figure S7, Supporting Information). This confirms that the deposition of $K_5\{V_{12}\}$ on the LIG surface is a crucial step for the enhanced electronic and electrochemical properties of the LIG electrodes. Among all electrodes, the K-POV-750 electrode with greater content of deposited $K_5\{V_{12}\}$ demonstrates the best overall charge storage supercapacitive performance with the highest specific areal capacitance C_A (38.49 mF cm^{-2}) at a scan rate of 10 mV s^{-1}. In contrast, the undoped LIG electrode shows substantially lower C_A (approximately 10.68 mF cm^{-2}). Therefore, all other electrochemical measurements were carried out on K-POV-750 electrodes. Figure 3b illustrates the stable performance of the K-POV-750 electrode at different scan rates ranging from 10 to 100 mV s^{-1}, indicating its suitability for various operating conditions.

Next, to validate the enhanced electrochemical efficacy of the K-POV-750 electrode, the galvanostatic charge-discharge (GCD) response was recorded at various current densities ranging from 0.1 to 2 mA cm^{-2} as illustrated in Figure 3c. The GCD curves display a quasi-linear charge-discharge profile, affirming the excellent reversible supercapacitive behavior at different current densities. The K-POV-750 electrode exhibited the highest areal capacitance of 125 mF cm^{-2} at a current density of 0.1 mA cm^{-2}, a significant improvement compared to the pristine LIG electrode, which achieved a maximum areal capacitance of 25 mF cm^{-2}, i.e., only one-fifth of the K-POV-750 electrode, as depicted in Figure 3d. Similarly, the other two synthesized electrodes K-POV-500 and K-POV-250 delivered areal capacitances of 48 and 26 mF cm^{-2}, respectively, at 0.1 mA cm^{-2} (Figure 3d; Figure S8, Supporting Information). This outcome implies superior capacitive performance when the $K_5\{V_{12}\}$ molecular nanocluster was deposited on the LIG surface within a comparatively wide potential range, significantly influencing the overall electrochemical performance of the synthesized electrode. Presumably, the electrochemical deposition of the $K_5\{V_{12}\}$ within this enhanced potential window delineated the structural and chemical modification of the LIG, favoring the fast reversible Faradic response between the electrolyte and $K_5\{V_{12}\}$ modified LIG nanostructure.[50] This structural modification on the LIG surface promotes a vanadium oxide framework complex, facilitating reversible interaction/de-insertion of electrolyte ions during charging and discharging.[47,48] Additionally, the poor electrochemical performance at higher current density is in agreement with the high internal resistance, i.e., equivalent series resistance (ESR), which can be directly measured from the voltage drop V_{ESR} during the GCD cycles.[51] At a current density of 1 mA cm^{-2}, the calculated V_{ESR} for the K-POV-750 electrode is 260 mV, whereas the pristine LIG electrode exhibits a significantly higher V_{ESR} value of 1204 mV (Figure 3e). Similarly, the synthesized K-POV-500 and K-POV-250 electrodes show V_{ESR} values of 386 and 436 mV, respectively, indicating low internal resistance for the synthesized electrodes (Figure S8, Supporting Information).

To gain insight into the detailed charge storage process, the charge storage kinetics of the synthesized electrodes were explored during cyclic voltammetry sweeps. The calculated specific capacitance was interpreted quantitatively, revealing two distinct processes: the electric double-layer capacitance (EDLC), primarily a non-faradaic current response derived from capacitive performance, and the diffusion-controlled current arising from faradaic intercalation and deintercalation of the electrolyte ions, estimated by Dunn analysis.[52] The current response (I) at a fixed potential (V) is attributed to these two different charge storage mechanisms and can be expressed as:

$$I(V) = k_1 v + k_2 v^{1/2} \quad (1)$$

where v is the scan rate, $k_1 v$ defines the non-faradaic process and $k_2 v^{1/2}$ represents the diffusion-controlled contribution.[53,54] Figure 3f illustrates the voltage profile of the synthesized K-POV-750 electrode (at 10 mV s^{-1}), depicting the magnitude of the two charge storage contributions. At 10 mV s^{-1}, 95.5% of the observed current is contributed by the diffusion-controlled mechanism, showcasing significantly improved localized ion diffusivity to the carbon channel, while only a minor current response is associated with the EDLCs' capacitive behavior. Comparative analysis with the other two synthesized electrodes

© 2024 The Author(s). Advanced Functional Materials published by Wiley-VCH GmbH

ADVANCED SCIENCE NEWS
www.advancedsciencenews.com

ADVANCED FUNCTIONAL MATERIALS
www.afm-journal.de

16163028, 0, Downloaded from https://onlinelibrary.wiley.com/doi/10.1002/adfm.202410943, Wiley Online Library on [21/08/2024]. See the Terms and Conditions (https://onlinelibrary.wiley.com/terms-and-conditions) on Wiley Online Library for rules of use; OA articles are governed by the applicable Creative Commons License

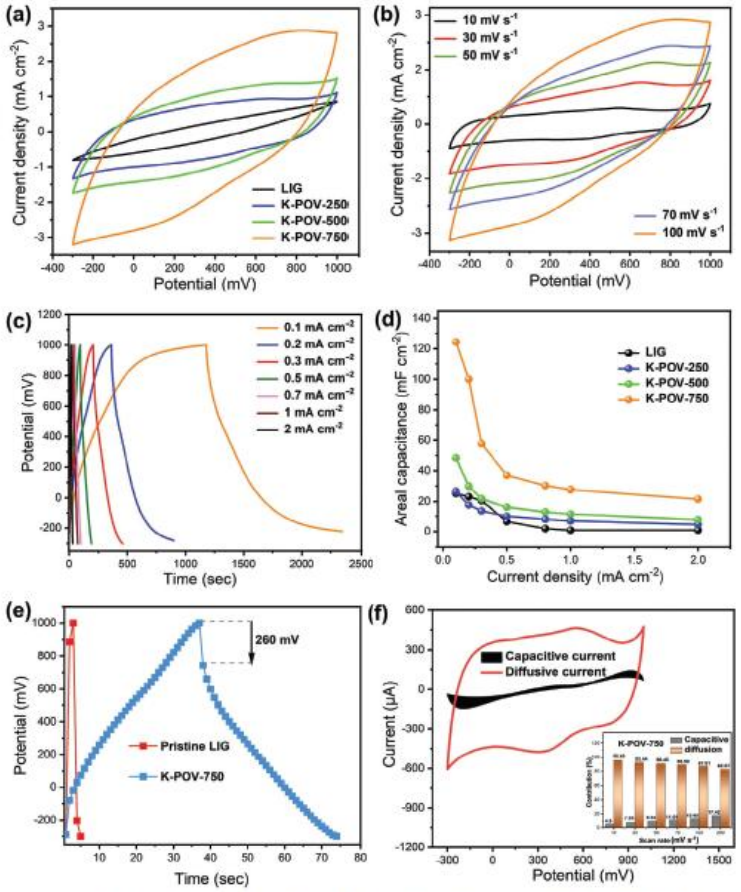

Figure 3. a) Cyclic voltammograms of K-POV-250, K-POV-500, and K-POV-750 electrodes compared with pristine LIG electrode b) CV response of K-POV-750 electrode at different scan rates from 10 mV s^{-1} to 100 mV s^{-1} c) galvanostatic charge-discharge profiles of K-POV-750 electrode at various current densities from 0.1 to 2 mA cm^{-2} d) areal capacitance (C_A) of the synthesized electrodes at different current densities e) voltage drop V_{ESR} profile of K-POV-750 and LIG electrode at 1 mA cm^{-2} and f) quantitative analysis of charge storage mechanism of K-POV-750 electrode at 10 mV s^{-1} (inset: diffusion and capacitive controlled current response at different scan rates).

(K-POV-250 and K-POV-500) suggests a predominant charge storage contribution due to the capacitive performance of the electrode when cycled from lower to higher scan rates (Figure S9, Supporting Information).

The concept's validity was ultimately shown by assembling a flexible solid-state supercapacitor (SSC-KPOV-750) using two symmetrical K-POV-750 electrodes with PVA-H_2SO_4 gel electrolyte and laboratory-grade micropores tissue paper as a separator, as illustrated in **Figure** 4a. In this study, the performance of SSC-KPOV-750 was compared with a similar SSC-LIG device based on pristine LIG electrodes. The CV performance of SSC-KPOV-750 at different scan rates, ranging from 10 to 100 mV s^{-1}, is presented in Figure 4b. The fabricated device has better pseudocapacitive performance compared to SSC-LIG, as indicated by a quasi-reversible CV within the potential range from −300 to 1000 mV. The stability of the synthesized SSC-KPOV-750 device was evaluated with the obtained CV curves at different scan rates from 10 to 100 mV s^{-1}. The two pronounced broad peaks at ≈200 and 550 mV versus Ag^+/Ag (at 30 mV s^{-1}) represent the reversible faradic reaction, contributing to excellent charge storage behavior even at a higher scan rate. Additionally, the CV of pristine SSC-LIG at 100 mV s^{-1}, when compared with SSC-KPOV-750, demonstrates significantly inferior charge storage behavior (Figure 4c). The GCDs curve for SSC-KPOV-750 (Figure 4d, Supporting Information) exhibits non-linear, asymmetrical profiles, indicative of capacitive behaviour attributed to

 © 2024 The Author(s). Advanced Functional Materials published by Wiley-VCH GmbH

ADVANCED SCIENCE NEWS
www.advancedsciencenews.com

ADVANCED FUNCTIONAL MATERIALS
www.afm-journal.de

16163028, 0, Downloaded from https://onlinelibrary.wiley.com/doi/10.1002/adfm.202410943, Wiley Online Library on [21/08/2024]. See the Terms and Conditions (https://onlinelibrary.wiley.com/terms-and-conditions) on Wiley Online Library for rules of use; OA articles are governed by the applicable Creative Commons License

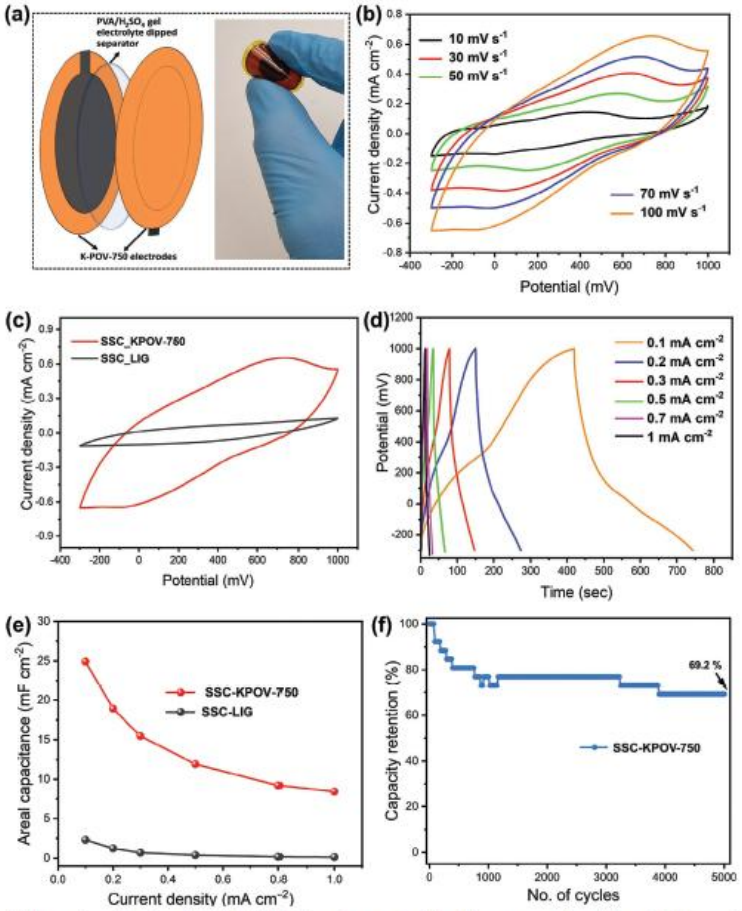

Figure 4. a) Schematic illustration of fabricated SSC-KPOV-750, inset: image of real flexible supercapacitor device; b) CV curves for SSC-KPOV-750 at different scan rates from 10 to 100 mV s^{-1}; c) comparison of the CV curve at 100 mV s^{-1} for SSC-KPOV-750 and SSC-LIG; d) GCD profiles of SSC-KPOV-750 at different current densities from 0.1 to 1 mA cm^{-2}; e) specific areal capacitance of SSC-KPOV-750 and SSC-LIG at various current densities; and f) cycling performance of SSC-KPOV-750 device during 5000 cycles at 0.8 mA cm^{-2}.

reversible Faradaic response occurring at the electrode-electrolyte interphase. For comparison, the GCD profiles of pristine LIG-based SSCs reveal a relatively short charge-discharge duration for current densities in the range from 0.1 to 0.5 $mAcm^{-2}$ (Figure S10, Supporting Information). The total areal capacitance for SSC-KPOV-750 is 24.92 mF cm^{-2} at a current density of 0.1 mA cm^{-2}, ≈11 times higher than that of the pristine LIG-based SSC (Figure 4e). Similarly, at the higher current density of 1 mA cm^{-2}, the SSC-KPOV-750 sustains a decent performance of C_A ≈8.5 mF cm^{-2}, whereas the SSC-LIG exhibits instability after 0.5 mA cm^{-2} (C_A << 1 mF cm^{-2}) due to a high internal resistance. These results confirm the better rate capability of the SSC-KPOV-750. Furthermore, the cycling stability of the SSC-KPOV-750 device was evaluated through 5000 consecutive charge-discharge cycles performed at 0.8 mA cm^{-2}, as depicted in Figure 4f.

The SSC-KPOV-750 device exhibits an initial capacity fade of ≈20% over the first few hundred cycles, potentially due to the initial activation of the electrode surface. Over the subsequent 4000 cycles, capacity fade was limited to 7%, maintaining a stable capacitive performance with 69% capacity retention. However, minor fluctuation observed at the 3200th and 4000th cycles correspond to random ruptures or crack formations within the carbon microstructure. Figure S10c (Supporting Information) presents the Ragone plot that compares the areal power density (mW cm^{-2}) and energy density (mWh cm^{-2}) of both SSC-LIG

© 2024 The Author(s). Advanced Functional Materials published by Wiley-VCH GmbH

ADVANCED SCIENCE NEWS
www.advancedsciencenews.com

ADVANCED FUNCTIONAL MATERIALS
www.afm-journal.de

16163028, 0, Downloaded from https://onlinelibrary.wiley.com/doi/10.1002/adfm.202410943, Wiley Online Library on [21/08/2024]. See the Terms and Conditions (https://onlinelibrary.wiley.com/terms-and-conditions) on Wiley Online Library for rules of use; OA articles are governed by the applicable Creative Commons License

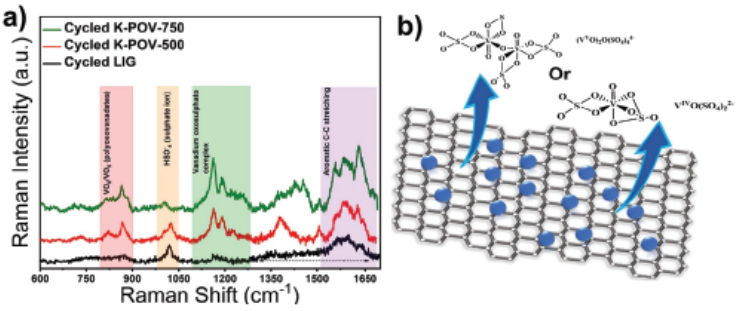

Figure 5. a) Raman spectra of LIG, K-POV-500, and K-POV-750 electrodes after 50 CVs. b) Schematic representation of the dimeric and monomeric vanadium oxosulphato complexes formed during electrochemical cycling.

and SSC-KPOV-750. The SSC-KPOV-750 had the highest areal energy density of 5.68 mWh cm^{-2} at a power density of 0.063 mW cm^{-2}, which was over 10 times more than that of SSC-LIG. Electrochemical impedance spectroscopy (EIS) measurements were conducted to comprehend the overall impedance of the fabricated solid-state devices. The Nyquist plot obtained over a frequency range from 1 Hz to 1 MHz for both SSC-KPOV-750 and SSC-LIG is shown in Figure S10d (Supporting Information). The plot of SSC-KPOV-750 consists of an almost straight line in the low-frequency region, indicative of ideal electric double-layer (EDL) capacitive behavior, while SSC-LIG displays a large Warburg response, suggesting high charge transfer resistance. Finally, the experimental data was fitted with an equivalent circuit to assess the charge transfer mechanism, with R_1 and R_2 representing the solution resistance (R_S) and charge transfer (R_{CT}), respectively. Notably, these resistances are significantly lower for SSC-KPOV-750 compared to SSC-LIG, as shown in Figure S10e,f (Supporting Information). Next, the mechanical flexibility test was conducted for the fabricated SSC-KPOV-750 device at different bending positions as shown in Figure S11 (Supporting Information). The capacitance exhibited minor variations at the initial bending angle and maintained nearly 94.2% of its original capacitance value, thereby demonstrating superior electrochemical performance and mechanical stability. These results indicate that the electrodeposited polyoxovanadates ($K_5\{V_{12}\}$) complexes were effectively introduced into the porous graphene structure and contributed to the long-term stable electrochemical performance of the SSC-KPOV-750 device.

The observed electrochemical responses of synthesized K-POV-750, K-POV-500, and K-POV-250 electrodes suggest that the deposition of reduced cluster $K_5\{V_{12}\}$ within a specific potential range enhances the electrochemical activity of the LIG electrodes. Therefore, it is important to understand the morphological and structural changes occurring in these modified electrodes during electrochemical cycling in an acidic aqueous electrolyte (1 M H_2SO_4) and compare them with the pristine LIG. We performed a post-mortem analysis of cycled K-POV-750, K-POV-500, and LIG electrodes (details of the preparation of the electrodes after cycling are given in the SI). We assessed the changes in the chemical composition of cycled electrodes by Raman and XPS analysis after performing an initial 50 CV sweeps. First, the Raman spectra of the pristine LIG electrode after cycling reveal a complete loss of the characteristic D and G bands observed in the fresh LIG electrode (**Figure 5a**). Instead, a broad Raman feature ranging from 1300 cm^{-1} to 1660 cm^{-1} is evident, resembling a highly amorphous soot-like carbon structure.[55] The electrochemical cycling in aqueous electrolyte (1 M H_2SO_4) induces oxidation of the graphitic lattice, resulting in the formation of sp^3-type defects and causing a transformation of LIG into an amorphous phase. Moreover, the distinct Raman band at ≈1019 cm^{-1} can be attributed to the stretching vibration of HSO_4^-, either intercalated or covalently bonded to the layers of LIG.[56] This substantial chemical transformation during electrochemical cycling can be interpreted as the manifestation of supercapacitive behavior in LIG.

The Raman spectra acquired from the cycled electrodes K-POV-750 and K-POV-500 (Figure 5a) reveal distinctive chemical transformations during cycling. First of all, the pronounced and convoluted Raman bands ≈1500–1650 cm^{-1} can be attributed to aromatic C-C stretching. Compared to pure LIG, two new bands at 817 cm^{-1} and 867 cm^{-1} are detected, corresponding to the polyoxovanadate VO_6/VO_5 units. It is noteworthy that these bands exhibit a red shift compared to the corresponding intense band (875 cm^{-1}) of the K-POV electrodes before cycling (Figure S5a, Supporting Information), likely due to the reduction of the vanadium core in VO_6/VO_5.[47] Additionally, a combination of bands occurs for both K-POV electrodes in the range of ≈1110-1270 cm^{-1}, with two prominent peaks at ≈1162 cm^{-1} and 1190 cm^{-1}, absent in the cycled LIG electrode (Figure S12, Supporting Information). These bands can be assigned to various vanadium oxosulphato/hydroxysulphato complexes which are formed during electrochemical cycling in 1 M H_2SO_4. Previous studies on vanadium redox flow batteries have demonstrated that the thermal stability and kinetics of the electrolyte ($VOSO_4$/3.0 M H_2SO_4) can be enhanced by organic additives with sulphonic acid (-SO_3H) or amine (-NH_2) groups.[57] It is established that the sulphate and sulphonic acid groups form solvated complexes with vanadium oxide under acidic conditions.[57] Furthermore, sulphates are able to form different types of vanadium oxosulphato complexes when vanadium oxide (V_2O_5) is melted with sulphate-containing salts.[58] In the presence of potassium sulphate, vanadium oxide forms dimeric $(V^{V}O)_2O(SO_4)_4^{4-}$ with a V-O-V bridge and a reduced monomeric $V^{IV}O(SO_4)_2^{2-}$ as shown

© 2024 The Author(s). Advanced Functional Materials published by Wiley-VCH GmbH

ADVANCED SCIENCE NEWS
www.advancedsciencenews.com

ADVANCED FUNCTIONAL MATERIALS
www.afm-journal.de

16163028, 0, Downloaded from https://onlinelibrary.wiley.com/doi/10.1002/adfm.202410943, Wiley Online Library on [21/08/2024]. See the Terms and Conditions (https://onlinelibrary.wiley.com/terms-and-conditions) on Wiley Online Library for rules of use; OA articles are governed by the applicable Creative Commons License

in the schematic in Figure 5b.[58,59] It seems plausible that the deposited and reduced $K_5\{V_{12}\}$ clusters might undergo a similar complex formation at high electrochemical potential in 1 M H_2SO_4 medium. Consequently, the Raman bands at 1190 cm^{-1} and 1162 cm^{-1} can be associated with the V^V-oxosulphato and the V^{IV}-oxosulphato complexes, respectively.[58] Interestingly, the hydrogen sulfate ion (HSO_4^-) peak at 1020 cm^{-1} is quite prominent in the Raman spectrum of the cycled K-POV-500 electrode, while it is rather weak for K-POV-750. Taken together, the electrochemical potential window along with prolonged cycling leads to a transformation of the polyoxovanadate structure to a mixture of vanadium oxosulphato complexes with V^V or V^{IV} centers.

XPS measurements were also carried out on samples that were recovered after the initial 50 CV cycles, the results for the cycled LIG and K-POV-750 electrodes are displayed in Figure S13 (Supporting Information). Starting with the LIG electrode, the detail spectrum in the C1s region shows a strong decline of the sp^2-C peak (at 284.5 eV) and the π-π^* satellite. In contrast, a strong increase in the hydrocarbon peak (C-C/C-H at 285.1 eV) is observed. These results point to a loss of graphitic material in the surface layer of the LIG electrode during electrochemical cycling, either due to reaction/etching of the graphite material by the sulphuric acid-containing electrolyte or deposition of carbonaceous species from the electrolyte. A similar development is also observed in the C1s spectrum of the K-POV-750 electrode, although the reduction of the intensity of the sp^2-C peak (and the π-π^* satellite) is not so pronounced in this case. Interestingly, the measurements for this sample showed that the vanadium and potassium content in the surface layer accessible by XPS (≈5 – 10 nm) is below the detection limit of XPS (≈0.1 to 0.3 at-% for these two elements). Since the Raman measurements demonstrated that vanadium oxides are still present in the electrodes after cycling, this finding is further evidence for the formation of a surface interlayer during cycling which covers the graphite substrate and the vanadium oxide clusters. While the S2p spectrum of cycled LIG shows a single S2p peak doublet ($S2p_{3/2}$ at 169.5 eV) which can be assigned to hydrogen sulphates/sulphates, two doublets can be discerned for K-POV-750 ($S2p_{3/2}$ at 163.9 and 168.6 eV, respectively) indicating the additional presence of reduced species in the surface layer of this sample. The oxygen atoms in the hydrogen sulphates/sulphates also contribute to the detail spectra in the O1s region. From a comparison of the peak intensities, it seems that this additional intensity goes mainly into the C-O peak at 533.0 eV. Since the O1s peak of metal sulphates is usually found at ≈531.5 eV, while the signals of hydrogen sulphates appear ≈533 eV, it follows that mainly hydrogen sulphates are captured in the surface layer of the electrodes.

A detailed post-mortem analysis of the aged SSC-KPOV-750 electrode was conducted after 5000 electrochemical cycles. At first, the morphology of the aged electrode surface was examined using the SEM analysis, which revealed a microstructure nearly identical to that of a fresh electrode, resulting in outstanding electrochemical reversibility as shown in Figure S14a,b (Supporting Information). The micro-Raman spectra gain more insight into the structural changes that occurred in the electrode after prolonged cycling, as depicted in Figure S14c (Supporting Information). The characteristic Raman band of native $K_5\{V_{12}\}$ at ≈875 cm^{-1} remained detectable, indicating the persistence of polyoxovanadate even after extensive cycling. Additionally, the spectra revealed the presence of other vanadium oxosulphato complexes with V^V or V^{IV} centers, marked by bands at 1162 and 1190 cm^{-1}, further confirming the presence of vanadium complexes. A notable Raman band at ≈1019 cm^{-1} indicated a strong interaction between sulphate ions of the electrolyte and the LIG structure. Furthermore, the XPS result of the aged K-POV-750 electrode indicated the well-maintained intensity of the sp^2-C peak and the π-π^* satellite is still observable, as confirmed by the high-resolution C1s spectrum (Figure S14e, Supporting Information). The S2p spectrum showed a single S2p peak doublet ($S2p_{3/2}$ at 169.5 eV), representing the predominated presence of hydrogen sulphates/sulphates on the electrode surface (Figure S14g, Supporting Information). However, the chemical composition of vanadium and potassium on the surface layer of the aged electrode remained undetermined due to the detection limit of XPS as described earlier, a limitation also noted for the partially cycled K-POV-750 electrode.

3. Conclusion

In summary, our study demonstrates the effective electrochemical immobilization of the potassium-bridged vanadium oxide nanocluster $K_5\{V_{12}\}$ on a highly porous graphene-like LIG substrate through a straightforward cyclic voltammetry technique. The electrochemical deposition of the nanoclusters within different potential ranges corresponds to distinct electronic and electrochemical changes in the LIG electrodes. The optimum POV deposition was achieved for electrodeposition in a potential range of −750 to 750 mV versus Ag^+/Ag, which leads to the presence of a highly redox-active and stable reduced cluster species on the LIG surface. This process also fine-tunes the electrochemical active sites on the graphene surface. The resulting K-POV-750 electrode exhibits a superior areal capacity of 125 mF cm^{-2} at a current density of 0.1 mA cm^{-2}. In comparison, the unmodified LIG electrode delivers an areal capacity of 25 mF cm^{-2} at 0.1 mA cm^{-2}. Detailed Raman measurements and XPS analysis provide insights into the deposition of POV clusters at different potential ranges and possible structural and material modifications of the LIG surface. Raman mapping reveals preferential deposition of $K_5\{V_{12}\}$ clusters in low crystallinity regions which enables high electronic conductivity of LIG after deposition. At the same time, detailed Raman analysis on the modified K-POV-750 electrode reveals the oxidation of surface sp^2 carbon centers. The deposited $K_5\{V_{12}\}$ clusters also transformed to dimeric V^V or monomeric V^{IV} polyoxovanadate centers on the modified electrode surface. Furthermore, the performance of the modified K-POV-750 electrode was evaluated in a symmetrical real supercapacitor device assembled with PVA/H_2SO_4-based gel electrolyte. The flexible symmetrical supercapacitor (SSC) with K-POV-750 sustains excellent electrochemical response with an areal capacitance of 24.92 mFcm^{-2} (at 0.1 mA cm^{-2}) and good capacity retention of 69% for up to 5000 charge-discharge cycles. The SSC-KPOV-750 device delivers an energy density of 5.68 mWh cm^{-2} and a power density of 0.063 mW cm^{-2}. In summary, this work presents a sustainable approach for introducing a highly redox-active potassium-bridged polyoxovanadate nanocluster into a graphene-like LIG framework, enhancing structural stability and improving electrochemical performance. The findings hold promise for applications in

© 2024 The Author(s). Advanced Functional Materials published by Wiley-VCH GmbH

16163028, 0, Downloaded from https://onlinelibrary.wiley.com/doi/10.1002/adfm.202410943, Wiley Online Library on [21/08/2024]. See the Terms and Conditions (https://onlinelibrary.wiley.com/terms-and-conditions) on Wiley Online Library for rules of use; OA articles are governed by the applicable Creative Commons License

micro-flexible smart devices, particularly in the fabrication of flexible micro-supercapacitors, without binders or current collectors.

4. Experimental Section

The experimental procedures and instruments used in this work are described in the supporting information

Supporting Information

Supporting Information is available from the Wiley Online Library or from the author.

Acknowledgements

This work contributes to the research performed at CELEST (Center for Electrochemical Energy Storage Ulm-Karlsruhe). Financial support by Ulm University, the Helmholtz-Gemeinschaft (HGF), and the Deutsche Forschungsgemeinschaft (DFG) within Germany's Excellence Strategy (EXC-2154/1), "POLiS" (project 390874152) and the TRR234 "CataLight" (project 364549901). M. A. thanks the State of Baden-Württemberg for a Margarete-von-Wrangell fellowship. The Baden-Württemberg Stiftung ("Elite program für Postdocs") is gratefully acknowledged. Dr. Monsur Islam is acknowledged for LIG electrode fabrication. The authors also acknowledge Dr. Bidhan Pandit for his contribution to Dunn's analysis.

Open access funding enabled and organized by Projekt DEAL.

Conflict of Interest

The authors declare no conflict of interest.

Data Availability Statement

The data that support the findings of this study are available from the corresponding author upon reasonable request.

Keywords

electrochemical deposition, flexible supercapacitors, laser-induced graphene, polyoxovanadates

Received: June 22, 2024
Revised: July 30, 2024
Published online:

[1] M. Horn, J. MacLeod, M. Liu, J. Webb, N. Motta, *Econ. Anal. Policy.* **2019**, *61*, 93.
[2] D. Wang, Y. Zhang, X. Lu, Z. Ma, C. h. Xie, Z. Zheng, *Chem. Soc. Rev.* **2018**, *47*, 4611.
[3] Z. Liu, H. Li, M. Zhu, Y. Huang, Z. Tang, Z. Pei, Z. Wang, Y. Huang, Z. Wang, Z. Shi, J. Liu, Y. Huang, C. Zhi, *Nano Energy* **2018**, *44*, 164.
[4] A. Colin, E. Ruppel, B. Lucia, In Proceedings of the Twenty-Third International Conference on Architectural Support for Programming Languages and Operating Systems, **2018**, 767.
[5] Y. Huang, W. S. Ip, Y. Y. Lau, J. Sun, J. Zeng, N. S. S. Yeung, W. S. Ng, H. Li, Z. Pei, Q. Xue, Y. Wang, J. Yu, H. Hu, C. Zhi, *ACS Nano* **2017**, *11*, 8953.
[6] Q. Ke, J. Wang, *J. Materiomics* **2016**, *2*, 37.
[7] S. Abdolhosseinzadeh, H. Asgharzadeh, H. S. Kim, *Sci. Rep.* **2015**, *5*, 10160.
[8] H. Zong, A. Zhang, J. Dong, Y. He, H. Fu, H. Guo, F. Liu, J. Xu, J. Liu, *Chem. Eng. J.* **2023**, *475*, 146088.
[9] Z. Lu, K. Zhao, H. Guo, L. Duan, H. Sun, K. Chen, J. Liu, *Small* **2024**, *20*, 2309814.
[10] A. Bahaa, M. A. Abdelkareem, A. Y. Mohamed, P. A. Shinde, B. A. A. Yousef, E. T. Sayed, H. Alawadhi, K.-J. Chae, S. Al-Asheh, A. G. Olabi, *J. of Colloid Interface Sci.* **2022**, *608*, 711.
[11] F. Clerici, M. Fontana, S. Bianco, M. Serrapede, F. Perrucci, S. Ferrero, E. Tresso, A. Lamberti, *ACS appl. Mater. Interfaces.* **2016**, *8*, 10459.
[12] J. Lin, Z. Peng, Y. Liu, F. Ruiz-Zepeda, R. Ye, E. L. G. Samuel, M. J. Yacaman, B. I. Yakobson, J. M. Tour, *Nat. Commun.* **2014**, *5*, 5714.
[13] C. Zhang, Z. Peng, C. Huang, B. Zhang, C. Xing, H. Chen, H. Cheng, J. Wang, S. Tang, *Nano Energy* **2021**, *81*, 105609.
[14] F. Clerici, M. Fontana, S. Bianco, M. Serrapede, F. Perrucci, S. Ferrero, E. Tresso, A. Lamberti, *ACS Appl. Mater. Interfaces* **2016**, *8*, 10459.
[15] Y. Zhang, L. Guo, S. Wei, Y. He, H. Xia, Q. Chen, H.-B. Sun, F.-S. Xiao, *Nano Today* **2010**, *5*, 15.
[16] R. Ye, D. K. James, J. M. Tour, *Adv. Mat.* **2019**, *31*, 1803621.
[17] C. Zhang, J. Chen, J. Gao, G. Tan, S. Bai, K. Weng, H. M. Chen, X. Ding, H. Cheng, Y. Yang, J. Wang, *Nano let* **2023**, *23*, 3435.
[18] F. M. Vivaldi, A. Dallinger, A. Bonini, N. Poma, L. Sembranti, D. Biagini, P. Salvo, F. Greco, F. D. Francesco, *ACS Appl. Mater. Interfaces* **2021**, *13*, 30245.
[19] C. Zhang, H. Chen, X. Ding, F. Lorestani, C. Huang, B. Zhang, B. Zheng, J. Wang, H. Cheng, Y. Xu, *Appl. Phys. Rev.* **2022**, *9*, 011413.
[20] M. Reina, A. Scalia, G. Auxilia, M. Fontana, F. Bella, S. Ferrero, A. Lamberti, *Adv. Sustain. Syst.* **2022**, *6*, 2100228.
[21] S. Han, C. Liu, N. Li, S. Zhang, Y. Song, L. Chen, M. Xi, X. Yu, W. Wang, M. Kong, Z. Wang, *CrystEngComm* **2022**, *24*, 1866.
[22] F. Mahmood, H. Zhang, J. Lin, C. Wan, *ACS Omega* **2020**, *5*, 14611.
[23] H. Liu, K.-s. Moon, J. Li, Y. Xie, J. Liu, Z. Sun, L. Lu, Y. Tang, C.-P. Wong, *Nano Energy* **2020**, *77*, 105058.
[24] W. Ma, J. Zhu, Z. Wang, W. Song, G. Cao, *Mater. Today Energy.* **2020**, *18*, 100569.
[25] Z. Peng, R. Ye, J. A. Mann, D. Zakhidov, Y. Li, P. R. Smalley, J. Lin, J. M. Tour, *ACS Nano* **2015**, *9*, 5868.
[26] W. Yang, Y. Liu, Q. Li, J. Wei, X. Li, Y. Zhang, J. Liu, *RSC Adv.* **2020**, *10*, 23953.
[27] K. Y. Kim, H. Choi, C. V. Tran, J. B. In, *J. Power Sources* **2019**, *441*, 227199.
[28] J. B. Lee, J. Jang, H. Zhou, Y. Lee, J. B. In, *Energies* **2020**, *13*, 6567.
[29] S. Greiner, J. Hettig, A. Laws, K. Baumgärtner, J. Bustos, A. Pöppler, C. Adam, M. Nyman, C. Streb, M. Anjass, *Angew. Chem. Int. Ed* **2022**, *61*, 20211454.
[30] M. Anjass, G. A. Lowe, C. Streb, *Angew. Chem. Int. Ed* **2021**, *60*, 7522.
[31] S. Greiner, B. Schwarz, M. Ringenberg, M. Dürr, I. Ivanovic-Burmazovic, M. Fichtner, M. Anjass, C. Streb, *Chem. Sci.* **2020**, *11*, 4450.
[32] F. Li, S. H. Carpenter, R. F. Higgins, M. G. Hitt, W. W. Brennessel, M. G. Ferrier, S. K. Cary, M. P. Shores, M. L. Neidig, S. A. Kozimor, E. M. Matson, *Inorg. Chem.* **2017**, *56*, 7065.
[33] E. Schreiber, N. A. Hartley, W. W. Brennessel, T. R. Cook, J. R. McKone, E. M. Matson, *ACS Appl. Energy Mater.* **2019**, *2*, 8985.
[34] L. Chen, M. J. Turo, M. Gembicky, R. A. Reinicke, A. M. Schimpf, *Angew. Chem.Int. Ed.* **2020**, *59*, 16609.
[35] J.-J. Chen, M. D. Symes, L. Cronin, *Nat. Chem.* **2018**, *10*, 1042.
[36] Q. Zhang, J. Ondus, J. Mills, A. Bahadori, J. Smith, T. Jordan, H. Xu, S. Hwu, *J. Solid State Chem.* **2020**, *287*, 121368.
[37] N. Arya, T. Philipp, S. Greiner, M. Steiner, C. Kranz, M. Anjass, *Angew. Chem.Int. Ed.* **2023**, *62*, 202306170.
[38] H. Lv, Y. V. Geletii, C. Zhao, J. W. Vickers, G. Zhu, Z. Luo, J. Song, T. Lian, D. G. Musaev, C. L. Hill, *Chem. Soc. Rev.* **2012**, *41*, 7572.

 © 2024 The Author(s). Advanced Functional Materials published by Wiley-VCH GmbH

[39] N. Hu, J. Du, Y.-Y. Ma, W.-J. Cui, B.-R. Yu, Z.-G. Han, Y.-G. Li, *Appl. Surface Sci.* **2021**, *540*, 148306.
[40] K. Kastner, B. Puscher, C. Streb, *Chem. Commun.* **2013**, *49*, 140.
[41] S. A. Kumar, S. Shiby, A. Sahu, P. Pachori, M. Tanwar, R. Kumar, I. A. Palani, *J. Physics D: Appl. Phys.* **2022**, *56*, 015305.
[42] M. A. Pimenta, G. Dresselhaus, M. S. Dresselhaus, L. G. Cançado, A. Jorio, R. Saito, *Phys. Chem. Chem. Phys.* **2007**, *9*, 1276.
[43] A. C. Ferrari, J. Robertson, *Phys. Rev. B* **2000**, *61*, 14095.
[44] J.-B. Wu, M.-L. Lin, X. Cong, H.-N. Liu, P.-H. Tan, *Chem. Soc. Rev.* **2018**, *47*, 1822.
[45] A. Eckmann, A. Felten, A. Mishchenko, L. Britnell, R. Krupke, K. S. Novoselov, C. Casiraghi, *Nano Lett.* **2012**, *12*, 3925.
[46] D. Sirshendu, T. Braun, F. D. Pammer, J. Choi, S. Fleischmann, M. Fichtner, *Carbon* **2024**, *218*, 118753.
[47] R. Baddour-Hadjean, A. Boudaoud, S. Bach, N. Emery, J.-P. Pereira-Ramos, *Inorg. Chem.* **2014**, *53*, 1764.
[48] X. Dong, C.-Y. Su, W. Zhang, J. Zhao, Q. Ling, W. Huang, P. Chen, L.-J. Li, *Phys. Chem. Chem. Phys.* **2010**, *12*, 2164.
[49] A. Xie, C.-A. Ma, L. Wang, Y. Chu, *Electrochim. Acta* **2007**, *52*, 2945.
[50] S. Boukhalfa, K. Evanoff, G. Yushin, *Energy Environ. Sci.* **2012**, *5*, 6872.
[51] L. Köps, P. Zaccagnini, C. F. Pirri, A. Balducci, *J. Power Sources Adv.* **2022**, *16*, 100098.
[52] J. Wang, J. Polleux, J. Lim, B. Dunn, *J. Phys. Chem. C* **2007**, *111*, 14925.
[53] N. Kumar, M. Singh, A. Kumar, T. Y. Tseng, Y. Sharma, *ACS Appl. Energ. Mater.* **2020**, *3*, 2450.
[54] T. Brezesinski, J. Wang, S. H. Tolbert, B. Dunn, *Nat. Mat.* **2010**, *9*, 146.
[55] A. Sadezky, H. Muckenhuber, H. Grothe, R. Niessner, U. Pöschl, *Carbon* **2005**, *43*, 1731.
[56] C. Schmidt, T. M. Seward, *Chem. Geol.* **2017**, *467*, 64.
[57] J. Hwang, B. Kim, J. Moon, A. Mehmood, H. Y. Ha, *J. Mat. Chem. A* **2018**, *6*, 4695.
[58] B. Soghomon, A. Chrissanthopoulos, R. Fehrmann, *J. Phys. Chem. B* **2002**, *106*, 49.
[59] B. Soghomon, *J. Chem. Soc., Faraday Trans.* **1998**, *94*, 3463.

 © 2024 The Author(s). Advanced Functional Materials published by Wiley-VCH GmbH

16163028, 0, Downloaded from https://onlinelibrary.wiley.com/doi/10.1002/adfm.202410943, Wiley Online Library on [21/08/2024]. See the Terms and Conditions (https://onlinelibrary.wiley.com/terms-and-conditions) on Wiley Online Library for rules of use; OA articles are governed by the applicable Creative Commons License

WILEY-VCH

Electronic Supporting Information

Tuning the Electronic and Electrochemical Properties of 3D Porous Laser-induced Graphene by Electrochemically Induced Deposition of Polyoxovanadate Nanoclusters for Flexible Supercapacitors

Nikhil Arya, Sirshendu Dinda, Thomas Diemant, Ke Wang, Maximilian Fichtner and Montaha Anjass

1. Sample preparation and electrochemical measurements

Chemicals and materials: V_2O_5 was purchased from Sigma Aldrich, other chemicals including acetonitrile (MeCN), diethyl ether $(C_2H_5)_2O$, sulfuric acid (H_2SO_4), polyvinyl alcohol (PVA), potassium hexafluorophosphate (KPF_6), and potassium thiocyanate (KSCN) from VWR. The Kapton sheet (304x200x0.15 mm) used for the formation of LIG was purchased from RS-online. The chemicals were used without further purification unless stated otherwise.

Synthesis of 1 mM $K_5\{V_{12}\}$/0.1 M KPF_6/MeCN electrolyte: The potassium functionalized polyoxovanadate (K-POV, $[K_{10}(V_{12}O_{32}Cl)_2]4.5\ CH_3CN$ (= $K_5\{V_{12}\}$)) cluster was synthesized by following procedures detailed in our previous work. [1] A non-aqueous supporting electrolyte of 0.1 M KPF_6/MeCN was prepared by dissolving 275.9 mg of KPF_6 salt in 15 ml of acetonitrile followed by stirring for 5 minutes until a clear solution was obtained. Subsequently, approximately 10.7 mg of $K_5\{V_{12}\}$ cluster was dissolved in the prepared supporting electrolyte (7 ml) and stirred for 30 minutes to produce a 1 mM $K_5\{V_{12}\}$/KPF_6/MeCN greenish solution. The resulting solution was then filtered to eliminate undissolved particles, yielding a clear green electrolyte solution.

LIG electrode fabrication: Laser-induced graphene (LIG) electrodes were fabricated using a 150 µm thick polyimide sheet (Kapton HN). The Kapton sheet was cleaned with ethanol to eliminate unwanted dust particles and dried under room conditions. The desired electrode shape was obtained using a programable CO_2 laser machine (ULS Versa Laser 3.50, wavelength 10.6 µm, lens 2.0 in, beam diameter 120 µm at focus) with CorelDRAW software. The LIG electrodes were fabricated with a constant power of 10 W, laser speed of 1200 RPM, and a fixed laser nozzle height of 5 mm above the Kapton sheet during raster engraving. The resulting electrodes had an active geometrical area of 1 cm^2 (and 2x0.5 cm^2 for solid-state supercapacitor electrodes).

Electrochemical deposition of $K_5\{V_{12}\}$ on LIG electrodes: The fabricated LIG electrode served as a substrate for the electrochemical deposition of the $K_5\{V_{12}\}$ cluster without further activation. Electrochemical deposition was conducted in a low-profile cell (Pine research equipment) with a conventional three-electrode setup. The fabricated LIG electrodes acted as the working electrode (WE), a platinum wire with 0.5 mm outer diameter (OD) served as the counter electrode and a silver wire in a glass frit, containing 0.1 M KPF_6/MeCN electrolyte, functioned as a quasi-reference electrode. Each deposition experiment used approximately 7 ml of freshly prepared 1 mM $K_5\{V_{12}\}$/KPF_6/MeCN electrolyte. After deposition, the modified electrodes were carefully removed from the cell and dipped several times into fresh acetonitrile (MeCN) to remove residual electrolyte salt (KPF_6) and subsequently dried in an oven at 60 °C for 3 hours to eliminate excess solvent. Finally, the mass of the dried electrode was quantified using a micro-analytical balance with a precision of up to 0.1 milligrams. Each electrode exhibited nearly uniform masses corresponding to approximately 1 mF/cm^2, validating that the cluster deposition occurred within the microgram range.

Electrochemical measurements: Cyclic voltammetry (CV), galvanostatic charge-discharge (GCD) cycling and electrochemical impedance spectroscopy (EIS) were performed using a Pine Research WaveDriver 200 electrochemical workstation with IR-compensation at 95%. Uncompensated resistance was determined by impedance measurements using the EIS-RU tool in the AfterMath software. $K_5\{V_{12}\}$ modified electrodes and pristine LIG electrodes (area: 1 cm^2) were used as working electrodes in a low-volume cell with a three-electrode configuration. A low-profile aqueous Ag/AgCl reference electrode (Pine research) with 3.5 mm OD, filled with gel electrolyte (sat. KCl), and a thin Pt wire as the counter electrode completed the circuit. All electrochemical testing of the fabricated electrodes was conducted in fresh 1 M H_2SO_4 aqueous electrolyte. The EIS measurements were performed within the frequency range from 1 Hz to 1 MHz at an AC amplitude of 10 mV. Previous reports suggested that the ion absorption/desorption properties of the LIG substrate influence the surface chemistry and relative electrochemical performance. [2,3] Therefore, the synthesized electrodes and pristine LIG electrodes were initially subjected to 30 minutes of immersion into electrolyte before the actual electrochemical testing to ensure optimal electrolyte diffusion and electrode wettability.

Flexible solid-state supercapacitor device (SSC) preparation: The real supercapacitor tests were performed on a solid-state supercapacitor device (SSC), assembled with two identical K-

POV-750 electrodes (2 x 0.5 cm^2). A gel electrolyte was prepared by dissolving 3 g of polyvinyl alcohol (PVA) in 30 ml of deionized water, followed by continuous stirring at 80 °C until a thick gel-like solution was obtained. After cooling to room temperature, 3 ml of 98% concentrated H_2SO_4 was added and stirred for 30 minutes to produce the PVA/H_2SO_4 gel electrolyte. The synthesized gel electrolyte was applied to both electrodes, which were assembled in a sandwich manner using Kimtech wipe paper (1-layer, 19 g/m^2, area: 0.5 cm^2) as a separator. The SSC device was allowed to rest for 24 hours before electrochemical measurements were conducted.

Electrochemical calculations:

The areal capacitance (C_A) of the fabricated electrodes was calculated from the CV and GCD results as follows:

From measured CV response:

$$C_A\,(mF/cm^2) = \frac{1}{2vS\Delta V} \int I(V)dV, \quad (1)$$

Where C_A is the areal capacitance (mF/cm^2), ν scan rate (V/s), S active area (cm^2), ΔV potential window (V), and I(V) area under CV curve.

From GCD response:

$$C_A\,(mF/cm^2) = \frac{I x \Delta t}{A x \Delta V}, \quad (2)$$

Where I is the discharge current (A), Δt total discharge time (s) A active area (cm^2), and ΔV potential window (V).

Furthermore, the energy density (E) and power density (P) of the fabricated symmetric devices were calculated as follows:

$$E_A\,(mWh/cm^2) = \frac{1}{2} x\, C_A\, x \frac{(\Delta V)^2}{3600}, \quad (3)$$

And,

$$P_A\,(mW/cm^2) = \frac{E_A \times 3600}{t}, \quad (4)$$

Where C_A is the areal capacitance (mF/cm^2) of SSC device at different current densities, t total discharge time (s), and ΔV potential window (V).

Electrochemically cycled electrodes for post-mortem analysis: The pristine LIG electrode, along with synthesized K-POV-750, and K-POV-500 electrodes (area: 1 cm^2), were vacuum dried at 60 °C for 3 hours before electrochemical testing. The dried electrodes served as working

electrodes in low-volume cells (Pine research) with a three-electrode configuration: a low-profile aqueous Ag/AgCl reference electrode (with 3.5 mm OD, Pine research) filled with gel electrolyte (saturated KCl), and a thin Pt wire counter electrode. The cell was filled with fresh 1 M H_2SO_4 aqueous electrolyte and each electrode was immersed for approximately 30 minutes before measurement. Cyclic voltammetry was performed within a potential window from 0 to 900 mV vs. Ag^+/Ag with a scan rate of 200 mVs^{-1} for 50 consecutive cycles. After measurement, the electrode was removed, dried at 60°C for 3 hours, and subjected to further characterization.

2. Morphological and structural characterization

Scanning electron microscopy (SEM) and energy-dispersive X-ray spectroscopy (EDX) measurements were conducted utilizing a Zeiss Gemini Leo 1550 VP instrument equipped with a silicon drift detector (OXFORD Instruments) and employing a 10 keV electron beam.

X-ray diffraction (XRD) patterns were acquired using an STOE STADI-P diffractometer, equipped with a DECTRIS MYTHEN 1K strip detector, employing Mo Kα1 radiation (0.70932 Å) over a 2θ range of 5°–60°. Measurements were conducted in reflection mode, with the electrode mounted on copper adhesive tape. The recorded 2θ values were subsequently converted to Cu Kα1 radiation (1.54056 Å) using Origin2021 software.

Raman spectroscopy: Micro Raman spectra of the synthesized electrodes and pristine LIG were collected in the spectral range of 200–3200 cm^{-1} by using an inVia™ confocal Raman microscope (RENISHAW) with a 532 nm excitation laser. In the confocal system, a grating was used as dispersion element with a groove density of 2300 mm^{-1} which produced a spectral resolution of 1 cm^{-1}, while a 50X (0.75 NA) objective was used in back scattering geometry to collect the Raman spectra. The average laser power was kept at ~1mW, which produced optimal signal-to-noise ratio without damaging the samples. To assess the comprehensive structural integrity of the LIG (pristine and $K_5\{V_{12}\}$ modified) samples, an area of 60X60 μm^2 of the graphene surface was selected and raster scanned with a spatial resolution of 1 × 1 μm^2. A spectral range from 475 cm^{-1} to 1675 cm^{-1} was selected, keeping all the other measurement parameters unchanged. To further increase the signal-to-noise ratio, the spectral acquisition time was increased to 10s. The cosmic rays and the background of all the spectra were then removed using Renishaw WiRE™ 4.0 software. The modified Raman spectra were deconvoluted in individual spectral components (D, G and D′) using Lorentzian line-shape

functions in the MatLab platform and surface-analyzed plots were generated in a homebuilt MatLab script.

X-ray photoelectron spectroscopy (XPS) was performed in a Specs XPS system using monochromatized Al K_α (1486.6 eV) radiation. The measurements were performed with pass energies at the analyzer of 90 and 30 eV for survey and detail spectra, respectively. Charging effects were in general rather small, the C1s peak of sp^2-C at 284.5 eV was used for binding energy calibration. The peak fit was carried out with CasaXPS software, applying Shirley-type background subtraction and (except of sp^2-C) Gaussian-Lorentzian peak shapes. In case of sp^2-C, an asymmetric peak shape was inserted which was adapted from previous measurements of pure graphite powder. For the 2p peaks, the expected intensity ratio (viz., 2:1) and spin-orbit splitting was used for the peak fit.[4]

3. Electrochemical deposition of $K_5\{V_{12}\}$ on the LIG electrode

Figure S1 illustrates the measured cyclic voltammetry (CVs) response during the in-situ reduction of clusters and their electrochemically induced deposition on the fabricated LIG substrate within specified potential ranges of -250 to 250 mV, -500 to 500 mV and -750 to 750 mV vs. Ag^+/Ag to synthesize three different electrodes called K-POV-250, K-POV-500, and K-POV-750, respectively. To ascertain the stability of the electrochemical cells, the open circuit potential (OCP) was measured prior to the experiment. Each deposition experiment comprised a total of 9 cyclic voltammetry repetitions, with a 60-second resting interval after every 3 CV cycles to mitigate diffusion limitation.

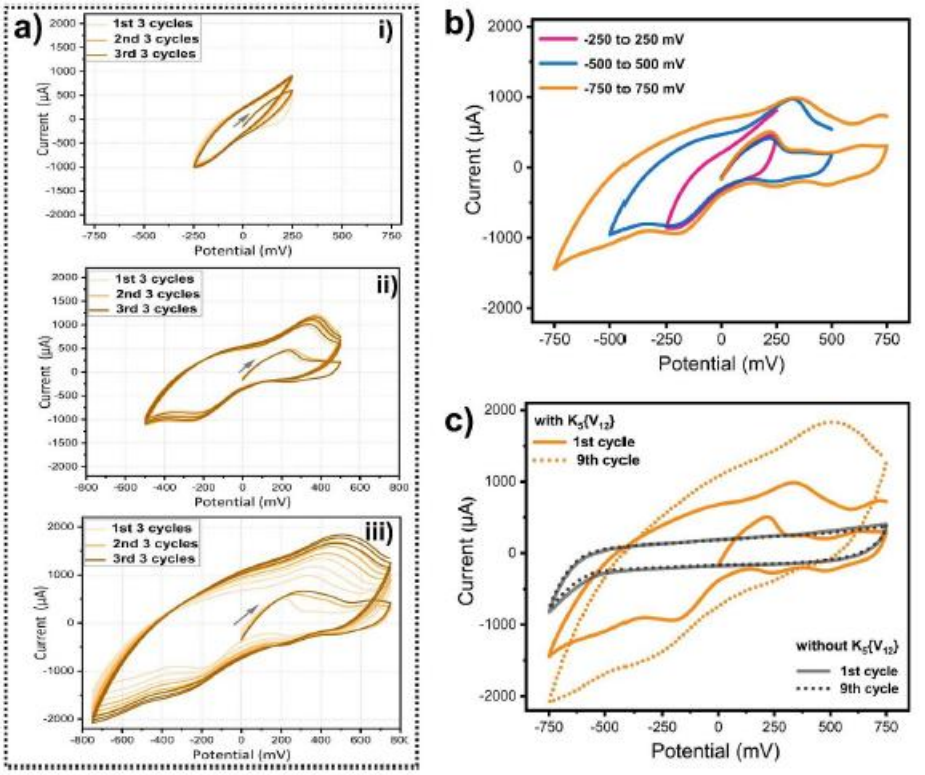

Figure S1 **(a)** Cyclic voltammetry response during $K_5\{V_{12}\}$ deposition on LIG for three different potential windows: **(i)** -250 to 250 mV, **(ii)** -500 to 500 mV, and **(iii)** -750 to 750 mV (all potentials vs. Ag^+/Ag) (conditions: electrolyte: non-aqueous 1 mM $K_5\{V_{12}\}$/0.1 M KPF_6/MeCN, WE: LIG with 1 cm^2 surface area, RE: silver wire in 0.1 M KPF_6/MeCN, CE: Pt wire). **(b)** First cyclic voltammetry response at each given potential range of -250 to 250 mV, -500 to 500 mV, and -750 to 750 mV vs. Ag^+/Ag. **(c)** Comparison of first and ninth CV response of pristine LIG and K-POV-750 electrodes.

4. Material characterization

Scanning electron microscopy (SEM) and energy-dispersive X-ray spectroscopy (EDX) results for pristine LIG and $K_5\{V_{12}\}$ modified LIG electrodes

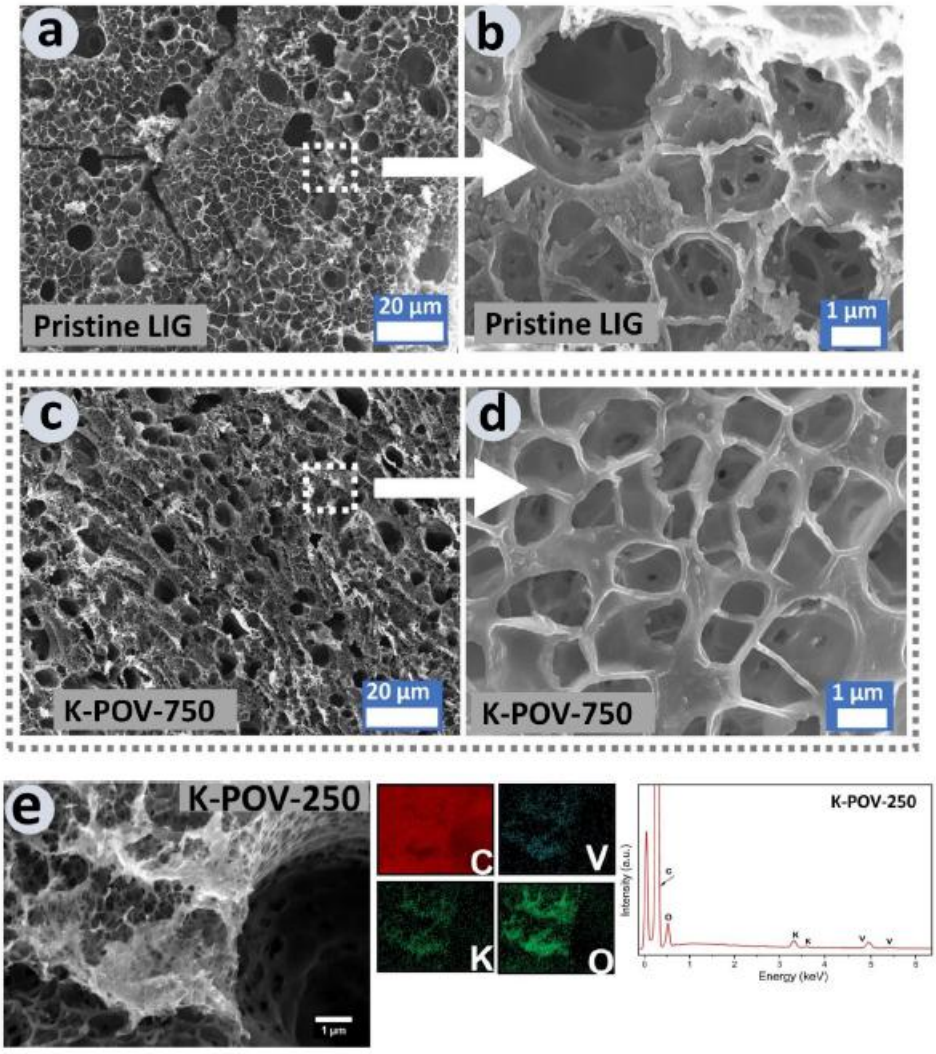

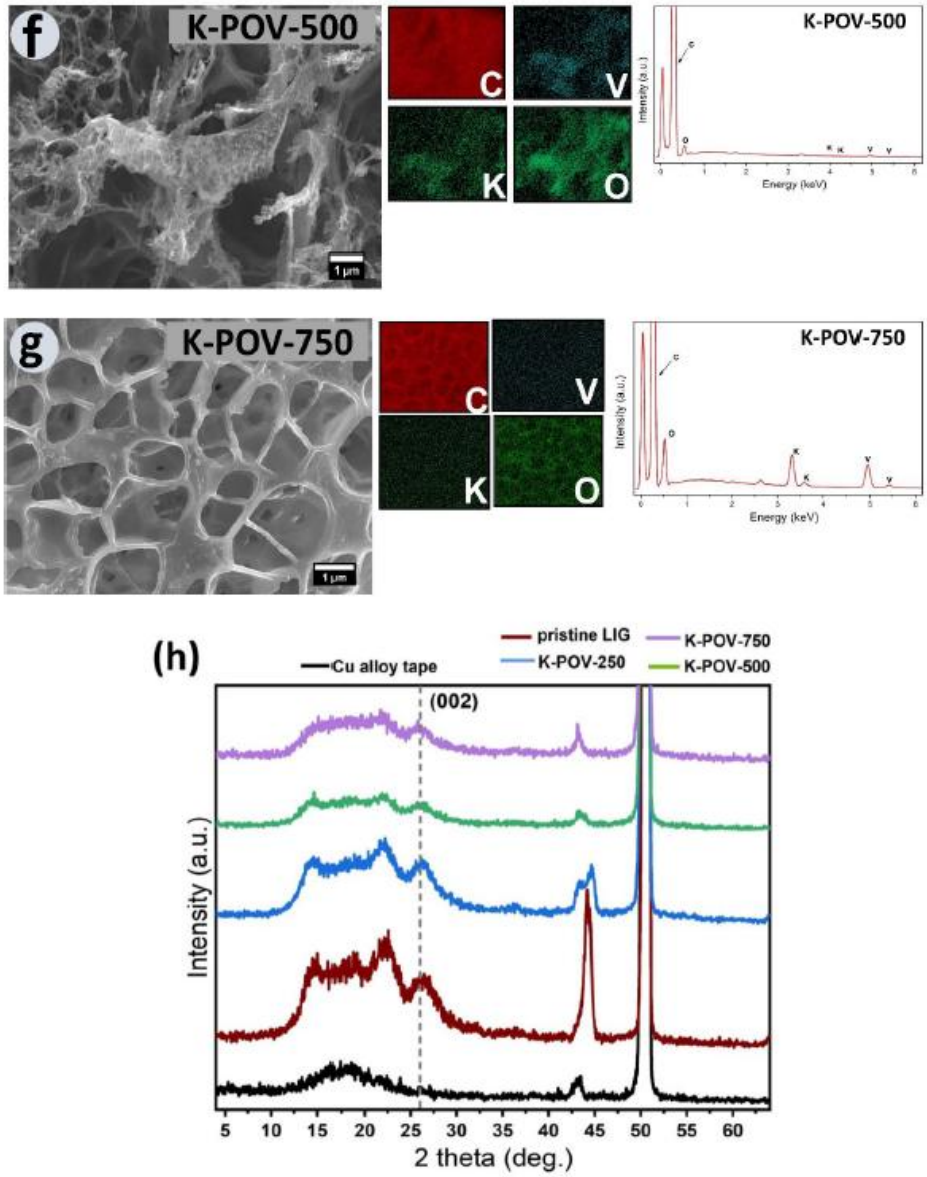

Figure S2 SEM images of (**a, b**) pristine LIG electrode and (**c, d**) K-POV-750 electrodes. EDX elemental mapping of $K_5\{V_{12}\}$ modified LIG electrodes: (**e**) K-POV-250, (**f**) K-POV-500 and (**g**) K-POV-750 (**h**) XRD pattern of pristine LIG and $K_5\{V_{12}\}$ modified electrodes at different potential ranges.

Table S1. Results of EDX analysis of synthesized K-POV electrodes.

Sample	K: V (Atomic %)
K-POV-250	0.45:1
K-POV-500	0.50:1
K-POV-750	0.52:1

5. Raman measurements

5.1 Micro Raman spectrum of pristine LIG

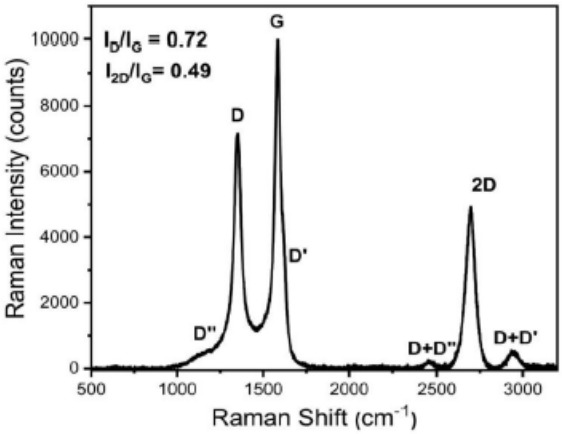

Figure S3. Micro-Raman spectrum of pristine LIG.

5.2 Raman map of pristine LIG electrode

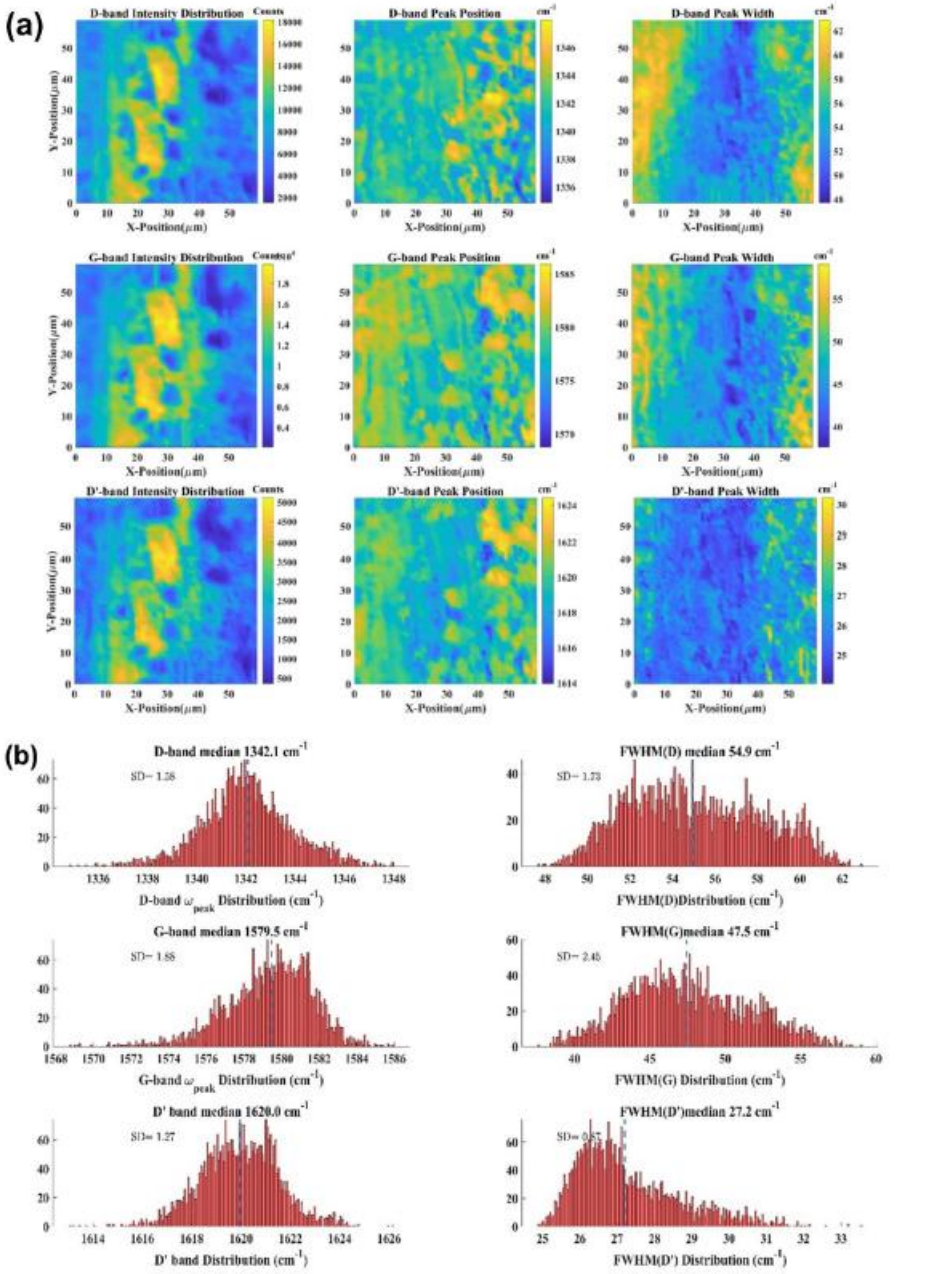

Figure S4. Results of Raman mapping of pristine LIG electrode: **(a)** band intensities, peak positions, and peak widths (FWHM) of the D, G, and D' bands, respectively. **(b)** Histogram plot of peak positions and bandwidths (FWHM).

5.3 Raman spectrum & map electrodes after $K_5\{V_{12}\}$ deposition

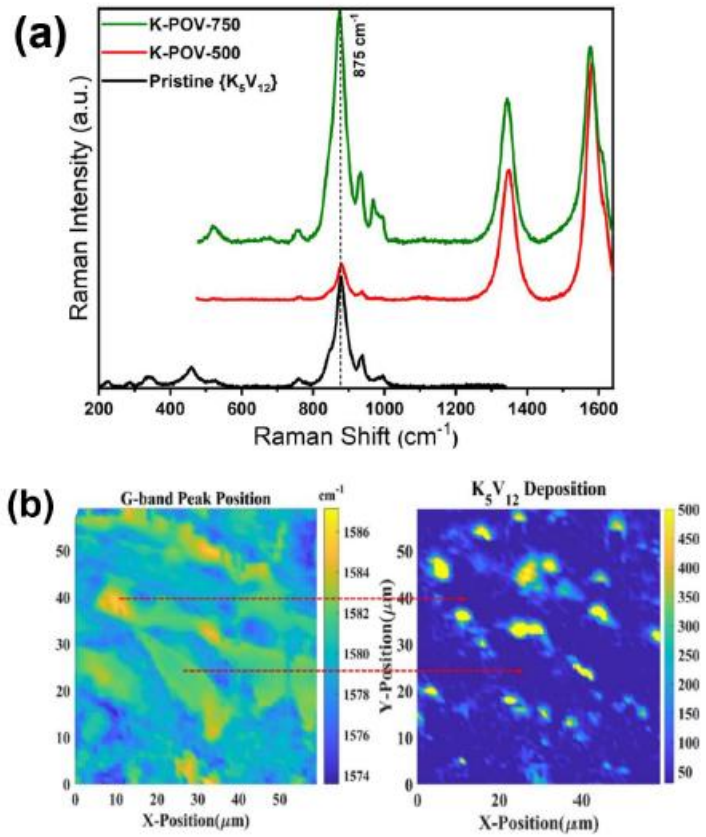

Figure S5. **(a)** Raman spectra of pristine $K_5\{V_{12}\}$ cluster and K-POV-500 and K-POV-750 electrodes. **(b)** Results of Raman mapping of K-POV-500 electrode: G-band peak position and $K_5\{V_{12}\}$ deposition (from the intensity of the V-O stretch vibration at 875 cm^{-1}).

6. XPS Analysis

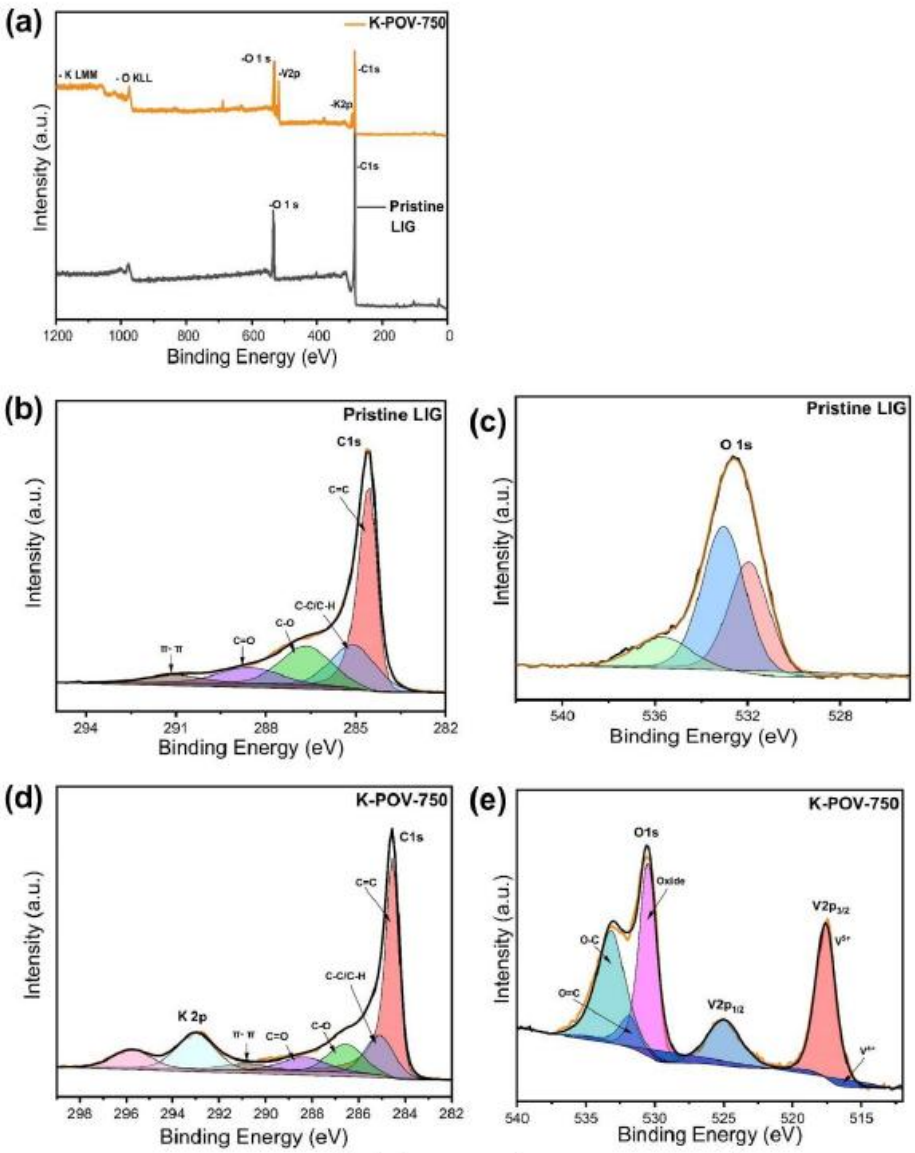

Figure S6. XPS measurements of pristine LIG and K-POV-750 electrodes. **(a)** XPS survey spectra, detail spectra in the C1s and O1s region of **(b, c)** pristine LIG and **(d, e)** K-POV-750 electrodes.

Table S2. Results of quantitative XPS analysis for the expected elements in LIG and K-POV electrodes.

Sample	C1s (%)						O1s (%)				V2p (%)			K2p (%)
	C=C	C-C/C-H	C-O	O-C=O	Pi-Pi*	sum	C=O	C-O	oxide	sum	V^{5+}	V^{4+}	sum	
LIG	40.53	18.42	11.69	9.66	4.66	84.96	4.95	6.80	0	11.75	-	-	-	-
K-POV-750	33.83	10.63	9.09	5.77	2.81	62.13	2.06	10.59	11.44	24.09	7.64	0.16	7.80	3.66
K-POV-500	62.85	8.40	2.58	4.21	3.59	81.63	3.33	7.94	1.34	12.61	1.19	0.14	1.32	1.16
K-POV-250	50.41	12.52	3.74	5.42	3.07	75.16	5.47	7.50	3.42	16.39	2.55	0.37	2.92	2.03

7. Electrochemical measurements

Electrochemical measurement of pristine LIG electrode in pure 1 M H_2SO_4 electrolyte and 1mM $K_5V\{V_{12}\}$/ 1 M H_2SO_4.

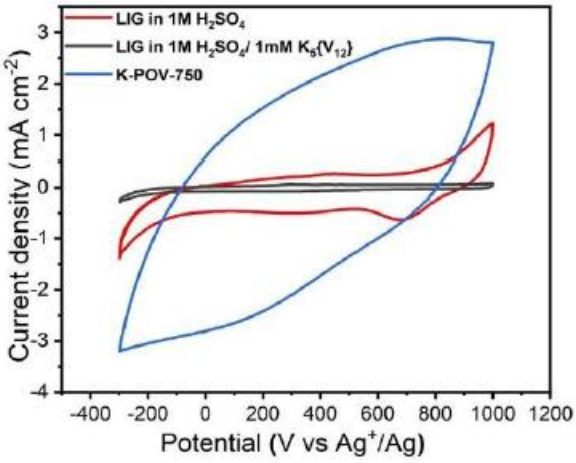

Figure S7 CVs response of pristine LIG electrode in 1 M H_2SO_4 and 1 mM $K_5\{V_{12}\}$/ 1 M H_2SO_4 electrolytes, compared with K-POV-750 electrode in 1 M H_2SO_4. (CV scan rates: 100 mV/s)

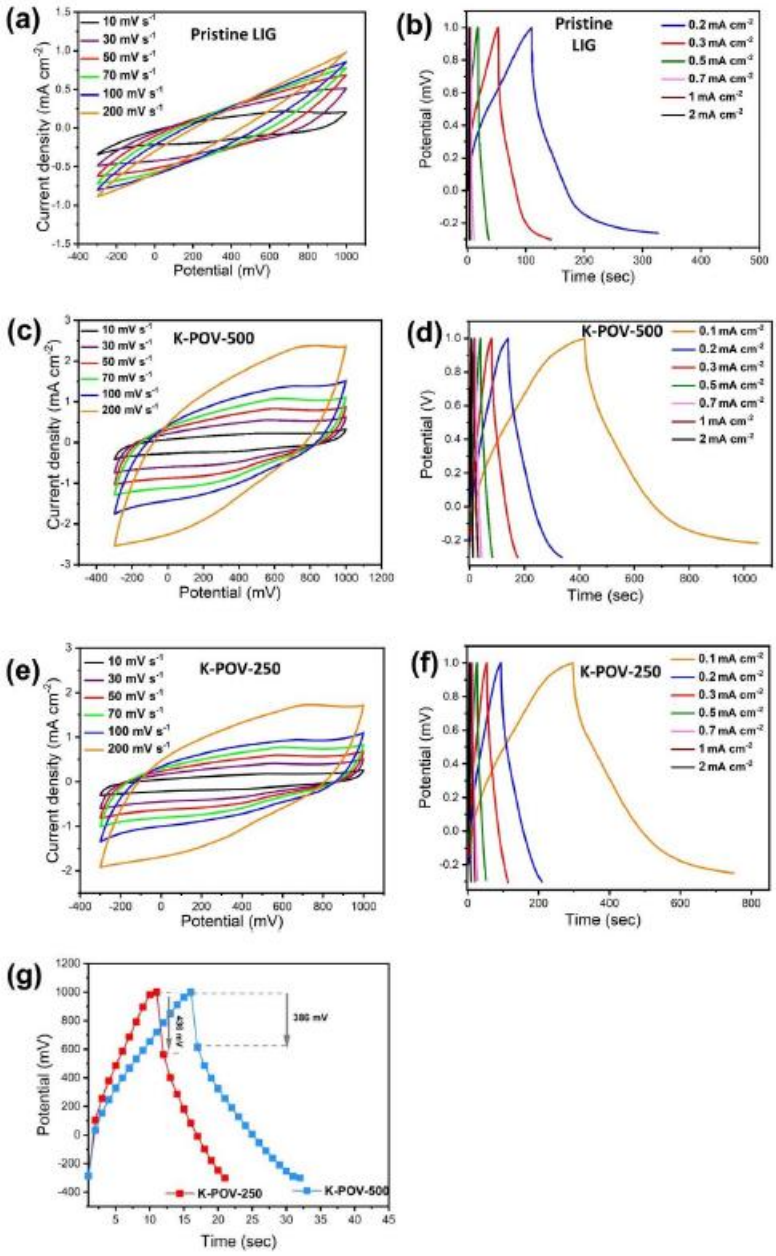

Figure S8 CVs at different scan rates and GCD profiles at various current densities for (**a-b**) pristine LIG electrode, (**c-d**) K-POV-500, (**e-f**) K-POV-250, (**g**) voltage drop V_{ESR} profile of K-POV-500 and K-POV-250 electrodes at 1 mA cm^{-2}.

8. Dunn analysis

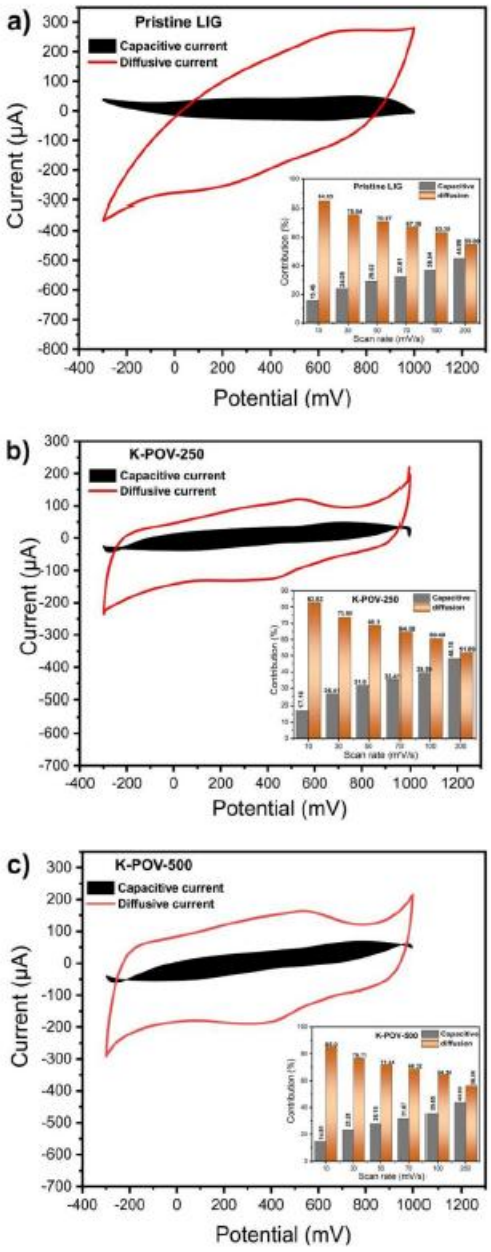

Figure S9 Quantitative analysis of charge storage mechanism at 10 mVs^{-1} of **(a)** pristine LIG electrode, **(b)** K-POV-250, and **(c)** K-POV-500, (inset: diffusion and capacitive controlled current response at different scan rates)

9. Solid-state supercapacitor (SSCs) electrochemical measurements:

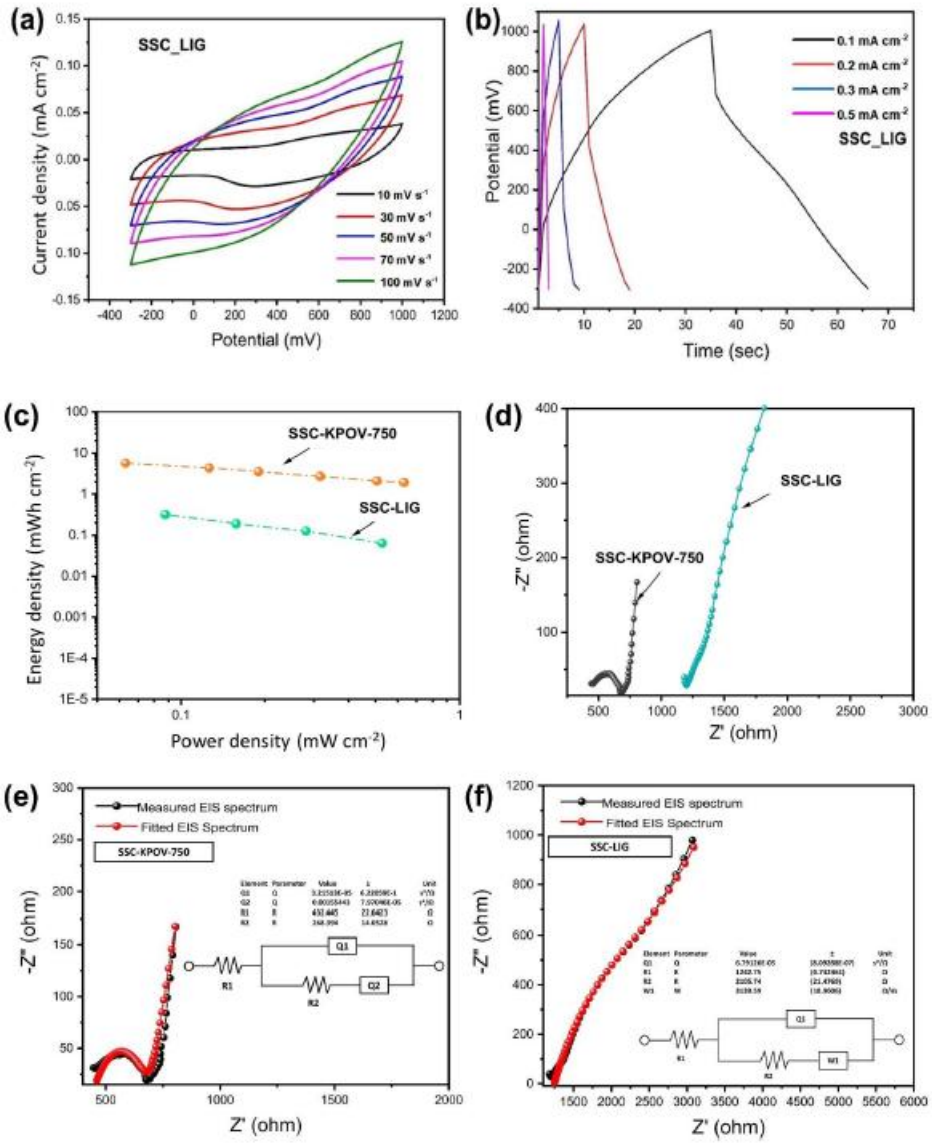

Figure S10 (a) CVs of SSC-LIG device at various scan rates; **(b)** GCD profiles of SSC-LIG at different current densities; **(c)** Ragone plot for SSC-KPOV-750 and SSC-LIG; **(d)** Nyquist plots of EIS results of SSC-KPOV-750 and SSC-LIG in the frequency range from 1 Hz to 1 MHz; and **(e, f)** fits of the EIS data (inset: equivalent circuit used for fit).

10. Bending test of SSC-KPOV-750 device

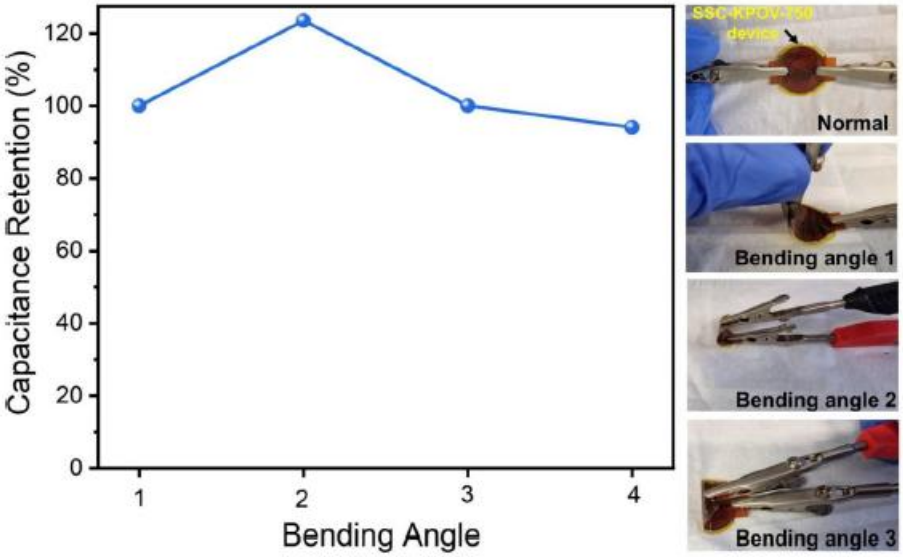

Figure S11. The measured capacitance retention of the SSC-KPOV-750 device (at left) and different bending angles (at right).

11. Post-mortem Electrode Analysis

11.1 Raman spectra of K-POV-750 electrodes before and after cycling

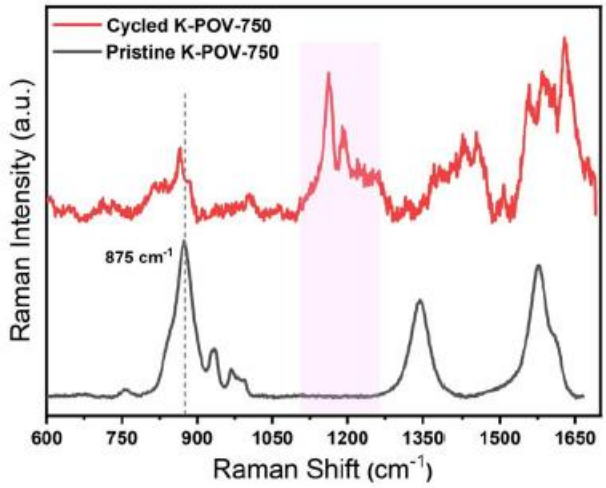

Figure S12. Raman spectra of K-POV-750 electrodes before and after cycling.

11.2 XPS Analysis

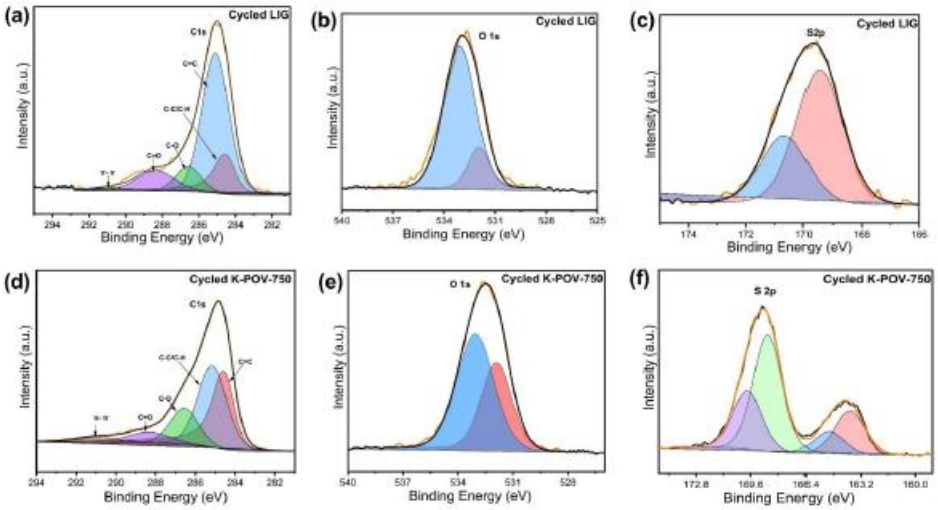

Figure S13. XPS measurements of LIG and K-POV-750 electrodes after 50 CV cycles. Detail spectra in the C1s, O1s, and S2p region of (a-c) LIG electrode (d – f) and K-POV-750 electrode.

12. Post-mortem analysis of aged SSC-KPOV-750 electrode

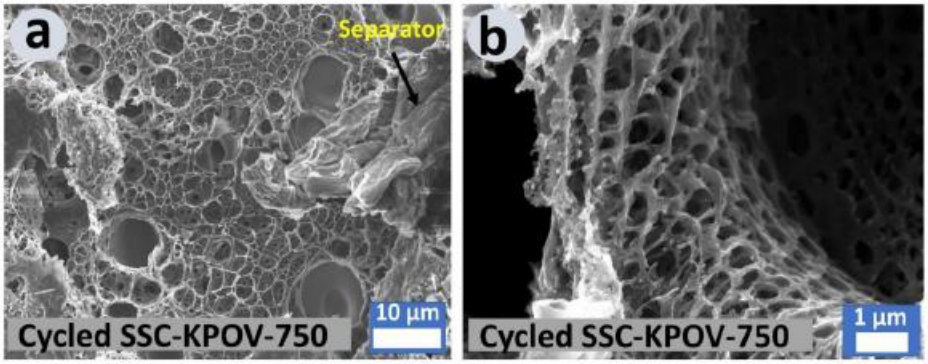

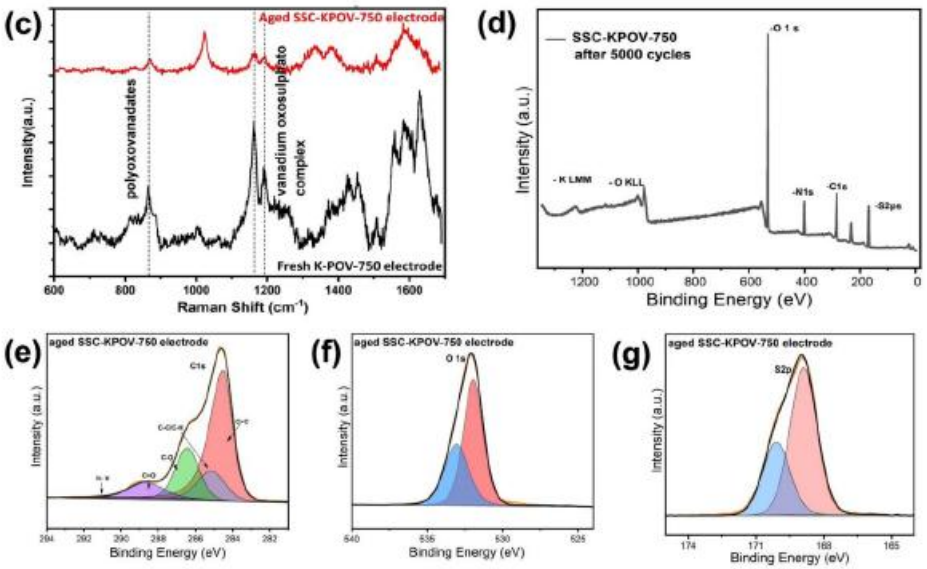

Figure S14. (a, b) SEM images of aged SSC-KPOV-750 electrode after 5000 cycles (c) Comparative micro-Raman spectra of pristine and after 5000 cycled K-POV-750 (d) XPS survey spectra of aged SSC-KPOV-750 electrode (e) detail spectra in C1s, (f) O1s and (g) S2p.

References

[1] Arya Nikhil, Tom Philipp, Simon Greiner, Michael Steiner, Christine Kranz, and Montaha Anjass. "Reversible Electrodeposition of Potassium-bridged Molecular Vanadium Oxides: A New Approach Towards Multi-Electron Storage." *Angew. Chem. Int. Ed.* (2023): e202306170.

[2] Wang, Yanan, Guantao Wang, Meihong He, Fu Liu, Mingguang Han, Tan Tang, and Sida Luo. "Multifunctional laser-induced graphene papers with combined defocusing and grafting processes for patternable and continuously tunable wettability from superlyophilicity to superlyophobicity." *Small* 17, no. 42 (2021): 2103322.

[3] Rathinam, Karthik, Swatantra P. Singh, Yilun Li, Roni Kasher, James M. Tour, and Christopher J. Arnusch. "Polyimide derived laser-induced graphene as adsorbent for cationic and anionic dyes." *Carbon* 124 (2017): 515-524.

[4] J. F. Moulder, W. F. Stickle, P. E. Sobol, K. D. Bomben, Handbook of X-ray Photoelectron Spectroscopy, Perkin Elmer Corp., Eden Prairie (USA), 1992.

6.3 (NA3): Enabling Si-Dominant Anodes: Influence of Neutralization Degree of Polyacrylic Acid on Low-Cost Micron-Sized Silicon Anode in High-Energy Li-Ion Full Cell

Gabriele Kloker*, Dragoljub Vrankovic, Nikhil Arya, Thomas Diemant, Montaha Anjass*

*Corresponding author

Published in: *Batteries & Supercaps*: e202400330

Copyright: Kloker, Gabriele, Dragoljub Vrankovic, Nikhil Arya, Thomas Diemant, and Montaha Anjass. "Enabling Si-dominant Anodes: Influence of Neutralization Degree of Polyacrylic Acid on Low-Cost Micron-Sized Silicon Anode in High-Energy Li-Ion Full Cell." *Batteries & Supercaps*: e202400330.

DOI: https://doi.org/10.1002/batt.202400330

Licence: CC BY 4.0 (https://creativecommons.org/licenses/by/4.0/)

Author contribution:

G. Gabriele: Material synthesis and characterization, battery testing and data analysis, writing and revision of the manuscript

V. Dragoljub: Material characterization and analysis, writing and revision of the manuscript

N. Arya: Material preparation for the XPS measurement and analysis, revision of manuscript

T. Diemant: Performed the XPS measurement and analysis, revision of manuscript

M. Anjass: Result discussion, writing, and revision of the manuscript

Check for updates

Batteries & Supercaps

Research Article
doi.org/10.1002/batt.202400330

Chemistry Europe
European Chemical Societies Publishing

www.batteries-supercaps.org

Enabling Si-Dominant Anodes: Influence of Neutralization Degree of Polyacrylic Acid on Low-Cost Micron-Sized Silicon Anode in High-Energy Li-Ion Full Cell

Gabriele Kloker,*[a, c] Dragoljub Vrankovic,[a] Nikhil Arya,[c, d] Thomas Diemant,[d] and Montaha Anjass*[b, c, d]

Micron-sized silicon is a promising low-cost, abundant material to increase the energy density of lithium-ion batteries. Nevertheless, significant volume change and therefore excessive solid electrolyte interphase (SEI) growth lead to fast capacity fading. In this work, polyacrylic acid (PAA) with different neutralization degrees is used for the fabrication of Si anodes for practical applications. The electrochemical performance in full pouch cells reveals that the increase in neutralization degree of PAA up to 70% enhances the overall performance by improved electrode properties, higher first cycle efficiency (FCE up to 78.1% at C/3) and better capacity retention (85.4% after 150 cycles at 1 C) over cycling, while with even higher neutralization degrees (such as 80%) the performance declines. Since proper mixing of the slurry is another important factor, we optimized the mixing procedure by increasing the solid content of the slurry, which has shown positive influence on the electrochemical performance and electrode properties. To summarize, this work shows full cell 1 C cycling until capacity retention of 85% after 150 cycles with pure Si microparticle anodes for 70% neutralized PAA as well as increased C-rate performance up to 5 C. Post-mortem, less degradation on electrode and particle level is observed.

1. Introduction

Silicon (Si) possesses a high theoretical capacity of $>3500\ mAh\,g^{-1}$ at room temperature, which is almost ten times higher than graphite ($372\ mAh\,g^{-1}$), and a low discharge potential of about 0.37 V with respect to lithium metal. Together with its abundance, environmental friendliness and low cost, it is recognized as next-generation anode material for lithium-ion batteries (LIBs).[1–5] Nevertheless, metallurgical micron-sized Si has not yet been investigated to large extent due to numerous intrinsic issues. Foremost significant volume expansion of Si during the lithiation process of more than 300% causes cracks formation throughout the particle and electrode as well as loss of electrical contact with the current collector and between particles. Moreover, excessive solid electrolyte interphase (SEI) growth due to continuous exposure of fresh active material surface to electrolyte leads to loss of active lithium (Li) due to side reactions[1,2,5,6] and Li trapping.[7–9] In order to enable the application of Si in industrial cells to boost energy density, several strategies were followed and investigated in detail. Most prominent has been using nanostructures, surrounding Si with a shield of carbon or developing new binder systems.[2,5,6,10–13] Up to now, most studies still focus on electrodes based on Si and graphite with different ratios, often containing only low amount of Si nanoparticles (SiNPs) in order to avoid the fracturing of the particles.[14–16] Even though nanoparticles prevent particle cracking, the enlarged surface area leads to more electrolyte degradation and therefore lower first cycle efficiency (FCE). Electrode processing, especially proper mixing, is also tedious and results in electrodes with low density.[14] In contrast, Si microparticles (SiMPs) offer a cost-effective alternative with higher tap density, less side reactions due to reduced surface area and easier processing. However, increased internal strain and therefore particle fracture is the main drawback in comparison to SiNPs.[17] Therefore, custom-fit binder systems as mitigation strategy are especially important for SiMP-based anodes. A big variety of different approaches has already been described in literature, leading from the more commonly used linear binders like polyacrylic acid (PAA), over cross-linked binders to systems with self-healing ability. In all cases the main requirements for industrial application are low cost and aqueous processing.[18–22] The most prominent binder used for Si anodes is PAA, which offers abundant carboxyl (COOH) groups that can interact with the functional groups of the Si surface such as silanol (Si–O–H) groups. An important modification is the partial neutralization of PAA, which

[a] G. Kloker, D. Vrankovic
Mercedes-Benz AG, Mercedesstraße 130/6, 70327 Stuttgart, Germany
E-mail: gabriele.kloker@mercedes-benz.com
gabriele.kloker@uni-ulm.de

[b] M. Anjass
University of Sharjah, Department of Chemistry, Sharjah-27272 Sharjah, United Arab Emirates
E-mail: malmasri@sharjah.ac.ae

[c] G. Kloker, N. Arya, M. Anjass
Ulm University, Institute of Inorganic Chemistry I, Albert-Einstein-Allee 11, 89081 Ulm, Germany

[d] N. Arya, T. Diemant, M. Anjass
Helmholtz Institute Ulm (HIU), Helmholtzstr. 11 89081 Ulm, Germany

Supporting information for this article is available on the WWW under https://doi.org/10.1002/batt.202400330

© 2024 The Authors. Batteries & Supercaps published by Wiley-VCH GmbH. This is an open access article under the terms of the Creative Commons Attribution License, which permits use, distribution and reproduction in any medium, provided the original work is properly cited.

© 2024 The Authors. Batteries & Supercaps published by Wiley-VCH GmbH

Batteries & Supercaps | Research Article doi.org/10.1002/batt.202400330 | Chemistry Europe European Chemical Societies Publishing

2366023, 2024, 12, Downloaded from https://chemistry-europe.onlinelibrary.wiley.com/doi/10.1002/batt.202400330 by EZZ der Universität Ulm, Wiley Online Library on [24/04/2025]. See the Terms and Conditions (https://onlinelibrary.wiley.com/terms-and-conditions) on Wiley Online Library for rules of use; OA articles are governed by the applicable Creative Commons License

influences the properties strongly. Not only the chemical interaction changes, but also the conformation of the polymer, therefore the homogeneity of polymer around the particles.[23–26] A further important aspect is the ratio of Si to graphite inside the electrode, as this affects the interaction with the binder enormously. A small ratio of Si within the active material of the anode will not help to push boundaries for energy density and will affect the understanding of the interaction between PAA and Si. In such anodes the majority of the active material is graphite, which behaves differently with PAA than Si, what also reveals in the electrochemical data, as PAA is not an optimum binder for graphite.[27] Those effects may overlap the influence on the electrochemistry originating from the interaction of PAA with Si. While most literature states how PAA and lithiated/neutralized PAA (Li_xPAA) is acting in the electrode and how it is expected to be distributed around the Si particles, this work actually visualizes the binder using transmission electron microscopy - electron energy loss spectroscopy (TEM-EELS), even though the binder has no specific heteroatoms to enable detection via the common analytical methods. In addition, the influence of the neutralization degree on the electrochemical performance and degradation is studied in detail in both half and full cell in this work.

In total, this work shows an optimized pure micron-sized Si anode with industrial-relevant composition and loading, which features a drastically improved overall performance with higher neutralization degree of the PAA until $Li_{0.7}PAA$, as shown in electrode properties and electrochemical data.

2. Results and Discussion

Silicon, being an abrasive material with a surface offering a large amount of functional groups, allows for significantly more interactions with the other components in the slurry (such as binder) while also preventing agglomerates from being destroyed by conventional methods during electrode processing. First, we tested the effect of solids content (SC) during the mixing phase on the electrochemical performance of samples with the $Li_{0.3}PAA$ binder. The mentioned SC during mixing means the highest SC within the mixing procedure, which occurs after the addition of all the silicon and carbon black to the binder solution, before adding the SWCNTs and diluting the slurry for better coating ability. For the tests, either low SC (approx. 50%) or high SC mixing (approx. 64%) were used. Figure 1a reveals that by increasing the SC during mixing the capacity retention got improved by almost 10% (from 72.9%–82.5%) at 150th cycle at C/3 rate. Interestingly, the SC during preparation also had influence on the C-rate performance, viz., the electrodes with higher SC showed slightly higher capacities for all C-rates with stronger effect for higher C-rates (Figure 1b).

The neutralization of PAA helps in a large extend to ease processing of the pure Si anode slurry regarding viscosity/rheological properties. Nevertheless, it needs to be considered that also the pH of the slurry rises with increasing neutralization degree of the PAA, as the Li^+ ions of the dissolved LiOH interact with the carboxylic acid groups of the PAA forming COOLi, at the same time leaving OH^- anions into the solution. Hydrogen formation is enabled and accelerated with increasing pH based on the reactions at the Si surface, meaning dissolution of the silica hydrogel and therefore facilitated hydrolysis of Si. Furthermore, the oxidation of Si can be additionally accelerated in presence of carbon black.[28,29] Overall, these effects can lead to reduced stability of the slurry especially in larger batches due to gassing. However, the effect is reduced for SiMPs due to lower surface area ratio. The change in processing of the pure silicon anode slurry originates from the different interactions between binder and particles/substrate, and both influence the electrode properties, therefore the adhesion is one measure to show the differences. The results of the 90° peel test in Figure 2a show an increasing adhesion with increased partial neutralization of PAA. Previous work[30] showed that the interaction between binder and copper current collector is reduced with higher neutralization degree, while this work showed a higher adhesion for the electrodes with higher neutralization degree. On the one hand this might be counter-intuitive, as the partial neutralization prevents a corresponding amount of carboxylic acid groups from bonding with the particle surface groups and substrate, on the other hand this observed trend fits together with the explanation of polymer conformation, meaning stretched and decoiled PAA chains due to partial neutralization.[31,32] The change to a stretched conformation of the polymer would then lead to a much higher interaction ability between polymer chain and surface as in a coiled conformation where most functional groups are blocked by intramolecular interactions. Additionally, the type of bonding is changed due to changes in the pH value.[23,26] Therefore, more chemical bonds are formed than in acidic conditions. Also, the comparison between samples with different SC surprisingly shows lower adhesion for the $Li_{0.3}PAA$ with high SC, almost as low as for the acidic sample. The binder distribution/influence seems to be quite different in those two cases, as the cohesion contrariwise is higher for the sample mixed with high SC, and even higher as for the more neutralized samples, where the cohesion seems to even decline slightly with higher neutralization degree. Together with the differences in electrochemical performance between the two different mixing routines, cohesion seems to be the more influencing factor than adhesion. Next, we measured the electronic resistivity at room temperature on three different spots of each electrode using a Hioki device. In order to avoid randomness in laboratory mixing, both adhesion and electronic resistivity were measured not only with three samples of one electrode, but also with different coatings on different days to assure repeatability. As shown in Figure 2b the interface resistances between coating and copper substrate are comparable for $Li_{0.3}PAA$ (0.0081 Ωcm^2) and $Li_{0.7}PAA$ (0.0042 Ωcm^2), while the one for Li_0PAA (0.055 Ωcm^2) is much higher, and $Li_{0.8}PAA$ (0.031 Ωcm^2) is lying in between. Notably, the interface resistance for the $Li_{0.3}PAA$ containing electrode with high SC of 0.0045 Ωcm^2 is as low as the one of $Li_{0.7}PAA$ (0.0042 Ωcm^2) with standard mixing. While the interface resistance of $Li_{0.7}PAA$ seems to be most beneficial, it changes when checking the composite volume resistivity. In this case, electrodes with Li_0PAA (0.835 Ωcm) and $Li_{0.3}PAA$

© 2024 The Authors. Batteries & Supercaps published by Wiley-VCH GmbH

Batteries & Supercaps | Research Article
doi.org/10.1002/batt.202400330
Chemistry Europe
European Chemical Societies Publishing

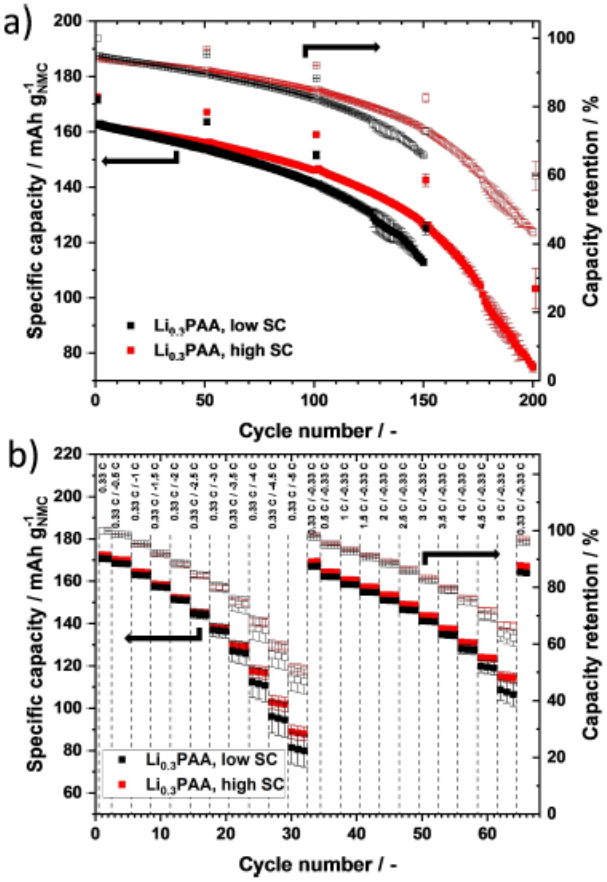

Figure 1. Electrochemical performance of $Li_{0.3}$PAA-containing electrodes with different solids contents during mixing (low SC ~50% and high SC ~64%). a) Capacity retention at 1 C cycling with C/3 check-up cycles each 50th cycle and b) C-rate performance in Si||NMC811 full pouch cell. The C-rates given on top of the graph show the variation of the discharge rate in the first half and variation of the charge rate in the second half of cycles. The charge rate in the first half and the discharge rate in the second half were kept constant at C/3. The end of the test consists of C/3 cycles to check how well the initial capacity is maintained.

(0.802 Ωcm) show the lowest composite volume resistivity, which increases for $Li_{0.3}$PAA with high SC and $Li_{0.7}$PAA, offering the highest values of 1.499 Ωcm and 2.052 Ωcm, respectively. Finally, the $Li_{0.8}$PAA containing electrode does not follow the trend, as its value (1.489 Ωcm) is slightly lower than $Li_{0.7}$PAA, but still higher than the value of Li_0PAA and $Li_{0.3}$PAA. As this effect is expected to be mostly influenced by the conductive additives' dispersion, it will be discussed in more detail later. Therefore, based on the measured resistances, especially for interface resistances clear overall improvements are shown by using partially neutralized PAA in comparison to Li_0PAA. Among the different neutralization degrees, $Li_{0.3}$PAA shows the optimum combination of respective interface and composite volume resistivity.

To get an overview of the surface morphology of the silicon electrodes with different partial neutralization of the binder, scanning electron microscope focused ion beam (SEM FIB)-cross section images were recorded. Figure S1 shows the morphology of pristine electrodes. It can be seen that due to slight calendering the surface of the electrodes is quite smooth and homogenous, as well the distribution of silicon particles, but still not so densified that the porous electrode structure is lost. At some spots the carbon black looks agglomerated, which is known as well for pure graphite electrodes. There are no major differences observed in the different samples.

In order to comprehend the properties and performance of the anode depending on variations in the degree of neutralization of PAA, it is essential to gain an understanding of the

© 2024 The Authors. Batteries & Supercaps published by Wiley-VCH GmbH

2366023, 2024, 12, Downloaded from https://chemistry-europe.onlinelibrary.wiley.com/doi/10.1002/batt.202400330 by EZZ der Universitat Ulm, Wiley Online Library on [24/06/2025]. See the Terms and Conditions (https://onlinelibrary.wiley.com/terms-and-conditions) on Wiley Online Library for rules of use; OA articles are governed by the applicable Creative Commons License

Batteries & Supercaps | Research Article
doi.org/10.1002/batt.202400330
Chemistry Europe
European Chemical Societies Publishing

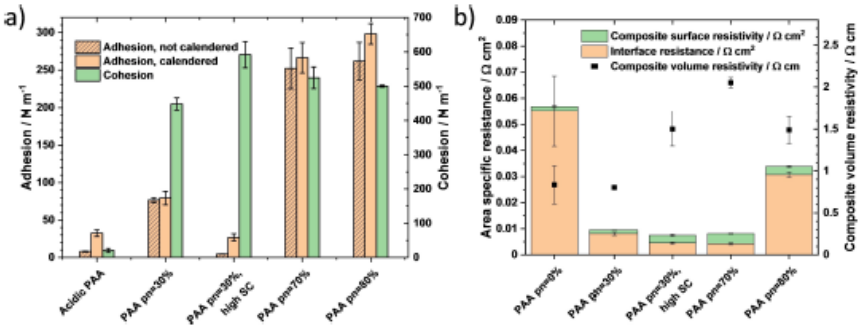

Figure 2. a) Adhesion of non-calendered (orange, shaded) and calendered (orange) electrodes with different PAA neutralization degree and cohesion (green), all measured in 90° peel tests. b) Measured resistances of calendered electrodes with different PAA neutralization degree showing composite surface resistivity (green) and interface resistance (orange) as bars and composite volume resistivity as dots (black).

particle-binder interaction. Although it has been demonstrated in literature how the interaction changes with variation of the pH value or neutralization degree, more research is still required to gain more insight into the particle-binder interaction. Since this binder does not contain any heteroatom to distinguish it from the carbon of carbon additives and the oxygen and hydrogen of the native oxide layer on the Si surface, the usage of SEM-EDX is not suitable for that purpose and the analytical techniques to investigate the particle-binder interaction are limited. CryoTEM-EELS is a potential technique, that offers a differentiated view on the respective elements based on their (bonding) state. In this work, cross-section TEM-EELS spectrum mapping images for the Li_0PAA, $Li_{0.3}$PAA and $Li_{0.7}$PAA containing electrodes were collected. During mapping, it is possible to distinguish between the different states of carbon in carbon black and binder, demonstrating the uniformity of the binder coating around the particle. Furthermore, the oxygen state can be distinguished between oxygen at the interface and oxygen in the bulk of the binder in principle. Unfortunately, the signal was rather noisy due to overlapping signals in our case. Therefore, the different oxygen states could not be mapped reliably. Nevertheless, the mapping of the carbon assigned to the binder enables us to draw conclusions about the structural differences of the samples with different neutralization degree. The cross-section TEM images of the Li_0PAA electrode shown in Figure 3a give insight into the binder/conductive additive phase between the silicon particles. Not only the elemental distribution of silicon, carbon and oxygen is shown, but as well the different states of carbon (Figure 3b), which can be attributed to carbon black and binder by EELS spectra (Figure 3c). Based on that, the binder looks to be rather inhomogeneously distributed and especially concentrated around the carbon black instead of a homogenous distribution on the silicon particle surface. This is also visible in another part of the same electrode, shown in Figure S2. Therefore, carbon black agglomerates in the space between the particles, forming conductive paths, which are weakly attached to the Si particles. Nevertheless, they may could lead to a conductive network in between the particles, resulting in lower composite volume resistivity for Li_0PAA as shown in Figure 2b, but inefficient conductive particle connection.

In contrast, the cross-section TEM-EELS results of $Li_{0.7}$PAA (Figure 4) show that the carbon attributed to carbon black is embedded in the one assigned to the binder, the latter simultaneously appearing to be homogeneously covering the Si particle surface. Hence, this technique allows to compare the distribution of the binder in electrodes with different binder modifications, concluding that the partial neutralization of PAA leads to a more homogenous distribution around the silicon particles due to the decoiled, stretched conformation.[31,32] In addition, the carbon black accumulation by the binder seems to be much reduced with partial neutralization of the binder, leading to higher composite volume resistivities as shown in Figure 2b, but also conductive paths attached to the Si particles, therefore efficiently connecting Si particles. Finally, a similar investigation of the $Li_{0.3}$PAA electrodes (Figure S3), shows an intermediate result between both extremes. It should be noted that due to the porous nature of the pure Si anode the sample preparation gets much more complicated, as the generated lamella need to be thinned, causing breaking off from parts of the structure. Therefore, the images seem to include a lot of voids, which is the result of the remaining part of thin lamella. For mapping the different (bonding) states of oxygen the resolution of this method is too low. Therefore, we further studied the electrodes by using X-ray photoelectron spectroscopy (XPS) to gain insight into the elemental composition and distinguish between the different states of oxygen.

XPS survey spectra of the pristine Li_0PAA, $Li_{0.3}$PAA and $Li_{0.7}$PAA electrodes show peaks corresponding to C, O, and Si as major components (Figure S4). In addition, a small Cu contribution (from the Cu foil) could also be detected in some cases. The Si 2p detail spectra in Figure S5 (left column) of the Li_0PAA, $Li_{0.3}$PAA and $Li_{0.7}$PAA electrodes show three features which can be assigned to elemental Si^0 (Si $2p^{3/2}$ peak at binding energy of 99.0 eV), intermediate SiO_x (100.5 eV) and SiO_2 (103.1 eV).[33,34] Comparison of the three Si 2p spectra shows a significant

© 2024 The Authors. Batteries & Supercaps published by Wiley-VCH GmbH

25662223, 2024, 12, Downloaded from https://chemistry-europe.onlinelibrary.wiley.com/doi/10.1002/batt.202400330 by KIT, der Universität Uni, Wiley Online Library on [24/06/2025]. See the Terms and Conditions (https://onlinelibrary.wiley.com/terms-and-conditions) on Wiley Online Library for rules of use; OA articles are governed by the applicable Creative Commons License

Batteries & Supercaps | Research Article
doi.org/10.1002/batt.202400330
Chemistry Europe
European Chemical Societies Publishing

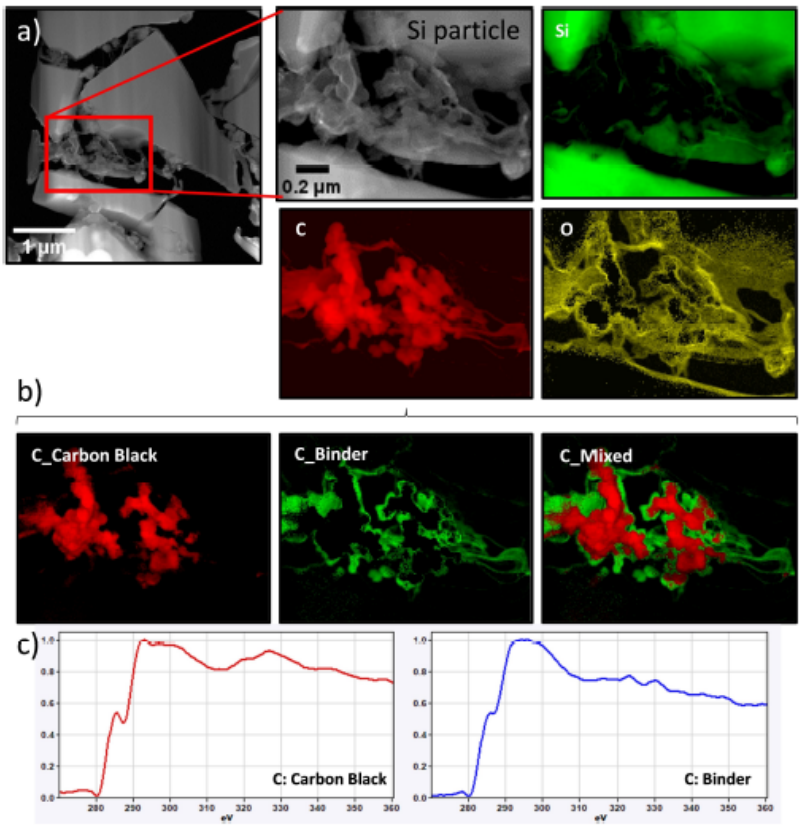

Figure 3. a) Cross-section TEM image of the Li_0PAA electrode showing Si particles and the binder/conductive additive mixture in between with the elemental mapping of silicon (green), carbon (red) and oxygen (yellow). b) Differentiated carbon states by EELS for carbon black (red) and binder (green). c) Spectra for carbon which can be attributed either to carbon black or PAA binder.

reduction of the intensity for $Li_{0.3}$PAA and $Li_{0.7}$PAA compared to Li_0PAA. The Si species show slightly higher ratio of SiO_x/SiO_2 for the partially neutralized samples due to higher pH value during slurry fabrication. The reduced general intensity of the Si 2p peaks for the partially neutralized samples can be explained by the more homogeneous coverage of the Si particle by the binder, this can be also observed in the O 1s region with reduced SiO_2 contribution for the partially neutralized samples and fits to the conclusion drawn from the TEM-EELS. Four contributions can be discerned in the C 1s spectra (Figure S5, middle column), which can be assigned to conductive carbon (284.4 eV), as well as C–C/C–H (285.0), C–O (286.3 eV) and O–C=O (288.8 eV) species.[33–35] A clear increase of the C–O contribution can be observed with increasing neutralization, while the O–C=O signal stays almost constant. Furthermore, a change of the main C contribution from the signal of C–C/C–H to conductive carbon occurs with increasing neutralization, which could be a result of the changing interaction between (neutralized) binder and conductive carbon. Finally, the spectra in the O 1s region (Figure S5, right column) reflect more or less the findings of the measurements in the Si 2p and C 1s region. First, the reduction of the SiO_2 signal in the Si 2p spectra of $Li_{0.3}$PAA and $Li_{0.7}$PAA translates to the intensity of the corresponding peak in the O 1s spectra at 532.6 eV. Second, an increase in the O–C peak intensity is observed with increasing neutralization.[34–36]

Even though the interaction of particles with binder is challenging to analyze, the variation of the neutralization degree of the binder has quite pronounced consequences for the electrochemical behavior. The electrochemical properties of Li_0PAA, $Li_{0.3}$PAA and $Li_{0.7}$PAA electrodes were investigated in coin-cell configuration with Si anode against Li metal, cycling between 0.01–1.5 V vs Li^+/Li at C/3 (after formation) in three cells to test reproducibility. A comparison of voltage profile and FCE for the Si electrodes with different degree of PAA neutralization (Figure 5) reflects the variation in SEI formation.

© 2024 The Authors. Batteries & Supercaps published by Wiley-VCH GmbH

2366023, 2024, 12, Downloaded from https://chemistry-europe.onlinelibrary.wiley.com/doi/10.1002/batt.202400330 by ICGC, the University of Lleida, Wiley Online Library on [24/04/2025]. See the Terms and Conditions (https://onlinelibrary.wiley.com/terms-and-conditions) on Wiley Online Library for rules of use; OA articles are governed by the applicable Creative Commons License

Batteries & Supercaps | Research Article
doi.org/10.1002/batt.202400330
Chemistry Europe
European Chemical Societies Publishing

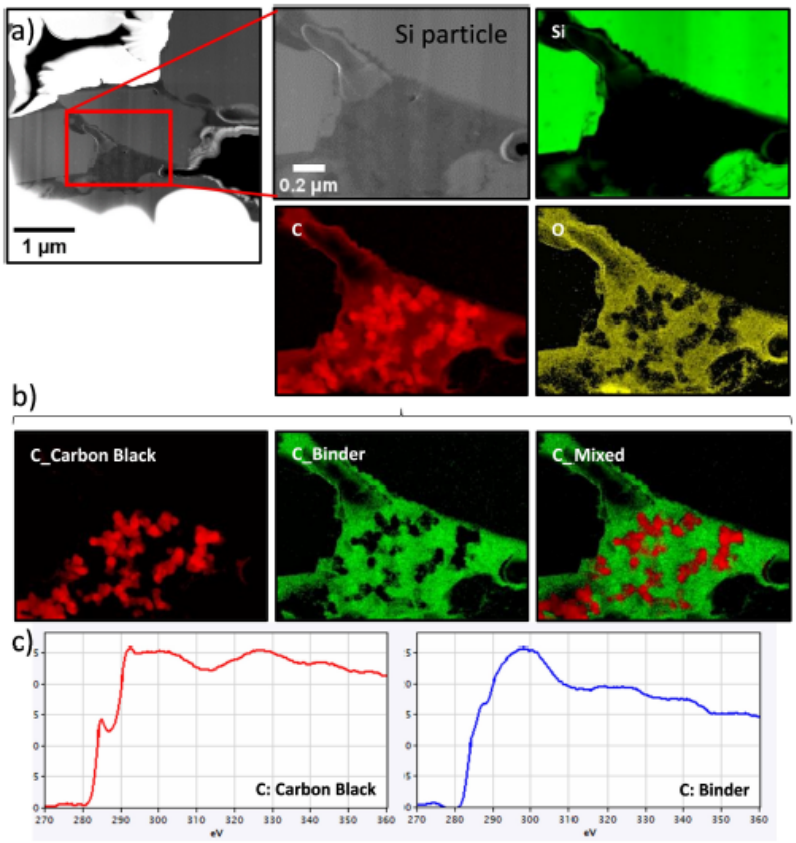

Figure 4. a) Cross-section TEM images of the $Li_{0.7}$PAA electrode showing Si particles and the binder/conductive additive mixture in between with the elemental mapping of silicon (green), carbon (red) and oxygen (yellow). b) Differentiated carbon states by EELS shown for carbon black (red) and binder (green c) Spectra for carbon which can be attributed either to carbon black or PAA binder.

While the FCE of the Li_0PAA electrodes in half cells is 89.3%, it increases to 92.2%, 94.4% and 94.9% for $Li_{0.3}$PAA, $Li_{0.7}$PAA and $Li_{0.8}$PAA electrodes, respectively. Amongst others this trend can be attributed to less electrochemical lithiation of the binder during first cycle.[34,37] Therefore, the partial neutralization has a beneficial influence on the SEI formation in the first cycle, while leading to less consumption of active Li within the cell than Li_0PAA, where the lithiation happens fully electrochemically. This can be seen in the respective voltage range for SEI formation during Si lithiation, which shows a changed capacity profile. The beneficial SEI properties based on partial neutralization of the binder also go beyond the first cycles. The half-cell cycling with limited capacity of 1500 mAh g_{Si}^{-1} in Figure 5e shows stable cycling for all electrodes with different neutralization degrees. However, the cumulative irreversible capacity shows a quite differentiated picture of the different binder modifications. While for the Li_0PAA electrode, the cumulative irreversible capacity increases quite linearly and much more than for the rest, the partially neutralized ones show less cumulative irreversible capacity with a short increase in the beginning, then much reduced increase during cycles 10–20, followed by an increase again. Both $Li_{0.3}$PAA and $Li_{0.7}$PAA show the same development, but with lower values for $Li_{0.7}$PAA, showing a smaller Li loss not only in the beginning for the SEI formation, but overall cycles. Interestingly, the $Li_{0.8}$PAA electrode does not show the plateau with distinct reduced increase, but more of a constantly growing cumulative irreversible capacity, ending up with roughly the same values after 30 cycles like $Li_{0.3}$PAA, therefore showing no distinct stabilization. Based on that, it looks like the increasing partial neutralization does not lead to a linear improvement of beneficial properties, therefore the improved performance cannot be only attributed to the increased lithium-ion amount in the binder. Half-cell C-rate tests were conducted as well (Figure S6), giving a small

© 2024 The Authors. Batteries & Supercaps published by Wiley-VCH GmbH

Batteries & Supercaps | Research Article doi.org/10.1002/batt.202400330 | Chemistry Europe European Chemical Societies Publishing

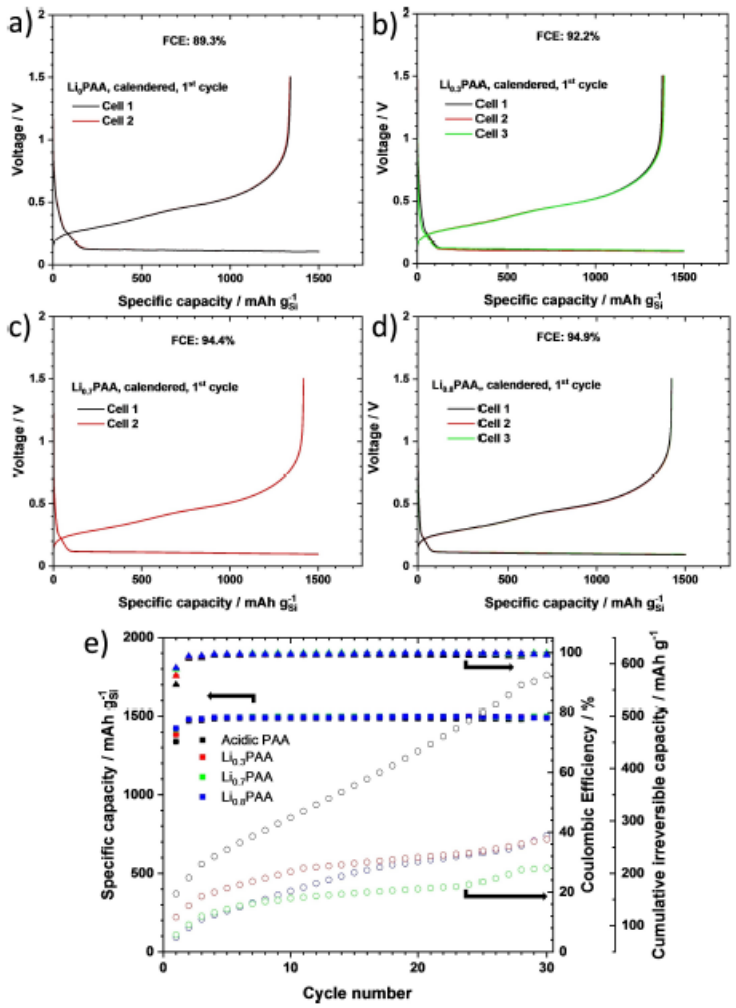

Figure 5. First cycle of half cells with Si anodes containing PAA binder with different neutralization degree (**a**) Li_0PAA, **b**) $Li_{0.3}$PAA, **c**) $Li_{0.7}$PAA and **d**) $Li_{0.8}$PAA). Tested against Li metal in the range of 0.01–1.5 V vs Li^+/Li at C/20 first formation. **e**) Specific capacity (triangles) and cumulative irreversible capacity (circles) of half-cells with Si anodes containing Li_0PAA (black), $Li_{0.3}$PAA (red), $Li_{0.7}$PAA (green) and $Li_{0.8}$PAA (blue) at limited charge capacity of 1500 mAh g^{-1}.

glimpse on the influence of partial neutralization on the fast charge behavior, but due to the stronger overpotentials at high currents on lithium metal the results are not as reliable.[38] To understand the electrode stability, and other properties of the electrodes better, full cell cycling was conducted in small pouch cells.

The positive influence of increasing partial neutralization on the FCE directly transfers to full-cell measurements, where the same FCE increase between Li_0PAA, $Li_{0.3}$PAA, $Li_{0.7}$PAA and $Li_{0.8}$PAA is observed like in the half-cell measurements. In full cell a maximum FCE of ~80% in the first formation cycle is reached for the $Li_{0.8}$PAA variation, which is comparable to literature, when taking into account the narrower voltage range of 3–4.2 V vs. Li^+/Li used in this work.[39–41] As can be seen in the first formation cycle of the respective variations shown in Figure 6, the difference in SEI formation is clearly visible with faster increasing voltage upon lithiation of the anodes with higher neutralization degree of the PAA.

While taking into account, that due to 100% ratio of silicon as active material significant electrolyte degradation takes place in the first cycle, it nevertheless gives a fast rise of CE in the next few following cycles. The cycle life test at 1 C with C/3

© 2024 The Authors. Batteries & Supercaps published by Wiley-VCH GmbH

2/06/2025, 20:44, 12, Downloaded from https://chemistry-europe.onlinelibrary.wiley.com/doi/10.1002/batt.202400330 by EZZ der Universität Ulm, Wiley Online Library on [24/06/2025]. See the Terms and Conditions (https://onlinelibrary.wiley.com/terms-and-conditions) on Wiley Online Library for rules of use; OA articles are governed by the applicable Creative Commons License

Batteries & Supercaps | Research Article
doi.org/10.1002/batt.202400330
Chemistry Europe
European Chemical Societies Publishing

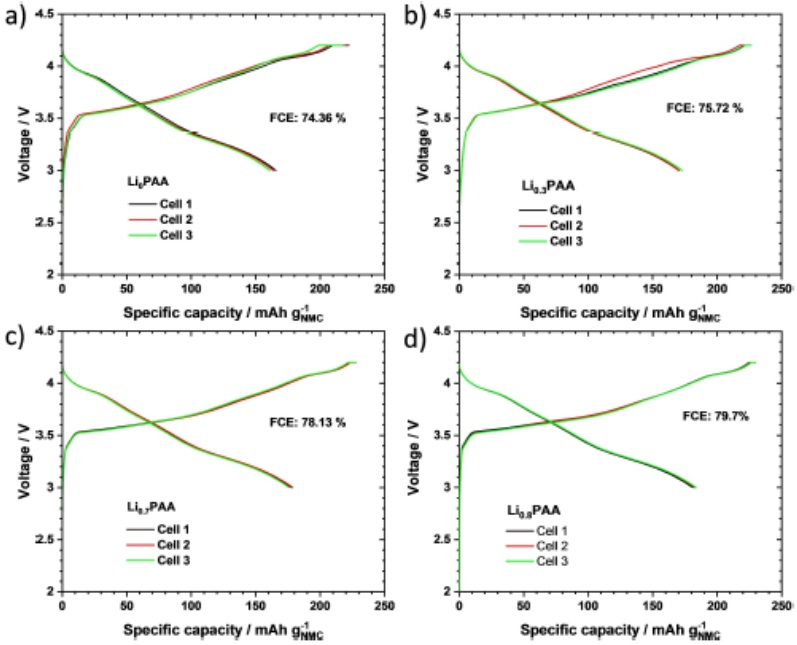

Figure 6. First formation cycle of full cells with Si anodes containing PAA binder with different neutralization degree (Li_0PAA, $Li_{0.3}$PAA, $Li_{0.7}$PAA and $Li_{0.8}$PAA). Measured in full pouch cells against NMC811 cathodes in a voltage window of 3.0–4.2 V vs. Li^+/Li at C/10.

check-up cycles each 50th cycle shown in Figure 7a shows that the partial neutralization helps substantially to enlarge the capacity retention. While the Li_0PAA-based electrodes allow cycling only up to 100 cycles until SOH = 80 % is reached, the $Li_{0.3}$PAA and $Li_{0.8}$PAA electrodes reach 150 cycles and $Li_{0.7}$PAA 200 cycles until that threshold. However, all of the synthesized electrodes undergo fast degradation after that point and eventually break down.

To gain further insights into the performance of the respective electrodes, a C-rate test was conducted with C-rate variation first in discharge direction, then in charge direction. As it can be seen in Figure 7b, the electrodes based on higher neutralization degree show better performance in both discharge and charge C-rate variation. Interestingly, the $Li_{0.8}$PAA-based electrode shows slightly lower performance in the fast-charging test, but even more pronounced in the discharge direction compared to the best-performing $Li_{0.7}$PAA. The electrode properties shown in Figure 2 indicate not only worse adhesion, but also higher resistivity values for $Li_{0.8}$PAA compared to $Li_{0.7}$PAA. This could be causing the lower C-Rate performance. Even though $Li_{0.3}$PAA shows better resistivity values than $Li_{0.8}$PAA, this is most probably based on the already described carbon black agglomeration, leading to an inefficient conductive network, which doesn't connect active material particles beneficially. For that reason, $Li_{0.8}$PAA with rather stretched PAA conformation and resulting less agglomerated conductive additives offers better C-Rate performance than $Li_{0.3}$PAA. Nevertheless, the C/3 capacity retention after the C-rate variation test in Figure 7b shows that the Li_0PAA electrode cannot maintain the initial capacity at C/3 and shows a much faster degradation than the $Li_{0.7}$PAA electrode, which still provides almost the same C/3 capacity after the C-rate variation test.

After the standard cycling test in Figure 7a, the post-mortem analysis was performed to investigate the morphological and structural changes of the used electrodes at SOH = 70–80 % with SEM-EDX, as shown in Figure S7 (SEM) and Figure S8 (EDX mapping). Based on top view SEM images of the electrodes in Figure S7a it can be seen that with increasing neutralization degree the number of cracks increases, but the intensity of the cracks gets less, meaning that they are finer. In FIB cross-sections of the cycled electrodes in Figure S7b, one can clearly observe severe degradation of the Li_0PAA electrode, not only showing cracks, but even voids throughout the electrode thickness. The $Li_{0.3}$PAA electrode already shows less distributed damage across the electrode, but even though there are no voids visible, the cracks are still severe. The cross-section image of the $Li_{0.7}$PAA electrode reveals a mild damage and only fine cracks are visible within the coating, but unlike the $Li_{0.3}$PAA electrode, no delamination of the coating from the current collector is observed. The cross-section images also reveal different ageing of the particles throughout the electrode and

© 2024 The Authors. Batteries & Supercaps published by Wiley-VCH GmbH

Batteries & Supercaps | Research Article
doi.org/10.1002/batt.202400330
Chemistry Europe
European Chemical Societies Publishing

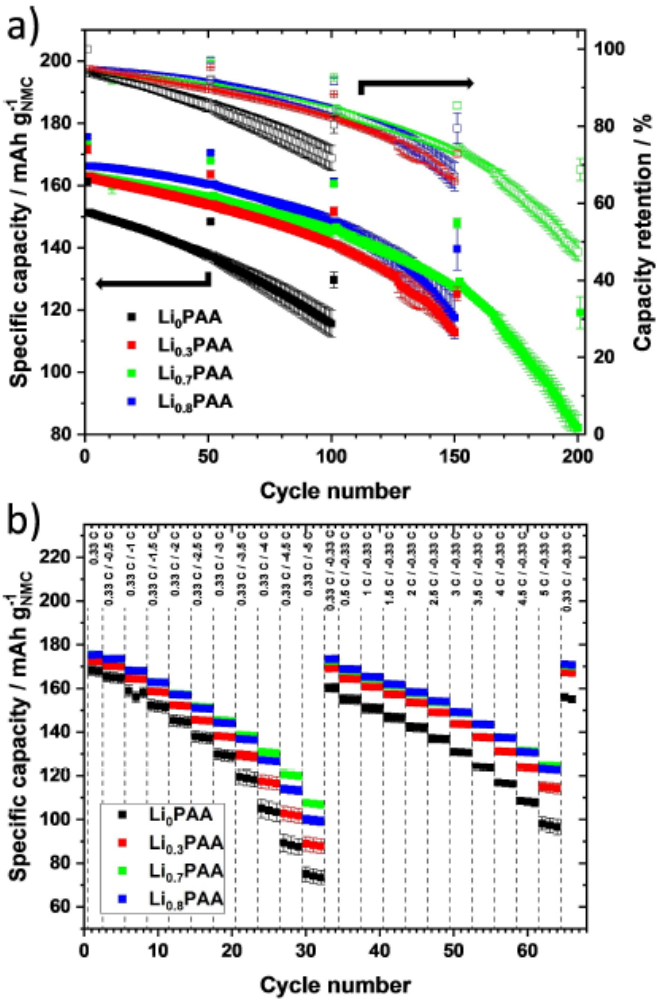

Figure 7. a) Cycling performance at 1 C cycling with C/3 check-up cycles each 50th cycle. The left y-axis shows the specific cathode capacity and the right y-axis the capacity retention with the threshold value of SOH = 80% as end criterion. b) C-rate performance of the different binder variations (Li_0PAA, $Li_{0.3}$PAA and $Li_{0.7}$PAA). The C-rates given on top of the graph show variation of the discharge rate in the first half and variation of the charge rate in the second half of cycles. The charge rate in the first half and the discharge rate in the second half were kept constant at C/3. The end of the test consists of C/3 cycles to check how well the initial capacity is maintained.

show that the particles degradation was less pronounced close to the current collector and more significant towards the thick SEI layer (dark seam) at the top of the electrode. Closer inspection of the Si particles in Figure S9 reveals differences in the size and shape of the particles in the electrode with varying neutralization degree. While for the Li_0PAA electrodes the particles seem to get smaller and irregularly shaped, the particles of the $Li_{0.3}$PAA and $Li_{0.7}$PAA remain with a round shape and comparable size to the pristine electrodes. Additionally, a dark seam is visible around the bright Si particles. EDX analysis (Figure S9b) indicates the presence of fluorine and phosphorous in this parts, typical for electrolyte degradation products. Hence, these darker parts constitute the SEI layer around the Si particles. Not only does the SEI differ in thickness with varied PAA neutralization degree, but also in fluorine and phosphorous concentration. It shows a much sharper defined concentration for the $Li_{0.7}$PAA, but more pronounced as well, which

© 2024 The Authors. Batteries & Supercaps published by Wiley-VCH GmbH

Batteries & Supercaps | Research Article doi.org/10.1002/batt.202400330 | Chemistry Europe European Chemical Societies Publishing

25666223, 2024, 12, Downloaded from https://chemistry-europe.onlinelibrary.wiley.com/doi/10.1002/batt.202400330 by KIT-Bibliothek, Wiley Online Library on [24/06/2025]. See the Terms and Conditions (https://onlinelibrary.wiley.com/terms-and-conditions) on Wiley Online Library for rules of use; OA articles are governed by the applicable Creative Commons License

can indicate more inorganic SEI for higher neutralization degrees.

In the next step, XPS measurements were also conducted with the cycled electrodes to get more insight into the elemental composition and the chemical species in the top layer of the SEI. The corresponding results are presented in Figure S10 and S11. The XPS survey spectra in Figure S10a show peaks for C and O from the binder, but as well from degradation products of the organic electrolyte solvents. P and F signals can be observed, which can be attributed to the electrolyte salt ($LiPF_6$) and its decomposition products, the electrolyte additive fluoroethylene carbonate (FEC) is another potential F source. Coming to the detail spectra, a pronounced reduction of the intensity is observed in the Si 2 p region (Figure S11a) for the cycled compared to the pristine samples of Li_0PAA, $Li_{0.3}$PAA and $Li_{0.7}$PAA, which indicates the formation of a SEI layer with an average thickness of several nanometers (i.e., slightly less than the sampling depth of the XPS experiment). Furthermore, it is interesting to note that an additional feature is detected at lower binding energy (Si $2p_{3/2}$ peak at 96.2 eV) for all samples, which is most probably related to Si–Li alloy(s). On the other hand, the feature due to SiO_2 disappears at the high binding energy side. The C 1s detail spectra (Figure S11b) are dominated by the contribution from conductive carbon, while the C–C/C–H peak of the PAA backbone has comparatively low intensity for all cycled samples. Interestingly, the C–O contribution for $Li_{0.7}$PAA is reduced compared to the others, i.e., the development is reversed to the pristine samples. Finally, a new feature can be noted at 290.7 eV which is due to carbonate(s) as decomposition products coming from the electrolyte. The reduced C–O content for $Li_{0.7}$PAA is also corroborated by the O 1s detail spectra (Figure S11c). The other peak in the O 1s spectra (at 531.8 eV) contains in addition to the C=O signal also the contribution from phosphate, which is the final decomposition product of the $LiPF_6$ electrolyte salt. The phosphate is also detected in the P 2p spectra (P $2p^{3/2}$ peak at 133.4 eV, Figure S11b. In addition, a further peak doublet due to partly decomposed $LiPO_xF_y$ (P $2p^{3/2}$ peak at 136.2 eV) appears for all samples, while the signal of intact $LiPF_6$ (P $2p^{3/2}$ peak at 137.7 eV) is only found for the Li_0PAA sample. Correspondingly, the $LiPF_6$ peak (688.5 eV) is most clearly seen in the F 1s spectrum of the Li_0PAA sample, while its intensity is only small for the other two samples. The two other signals in the F 1s spectra (Figure S11d) can be assigned to $LiPO_xF_y$ (687.1 eV) and LiF (685.0 eV), respectively. Most importantly, a successive increase of the LiF contribution with increasing neutralization is obvious. Therefore, it seems likely that the higher amount of Li^+ ions in partially neutralized PAA enables the decomposition of FEC. The higher ratio of inorganic SEI compounds like LiF, which is rather rigid, can be one reason for the improved cycle life, as it is less prone to be harmed during cycling and shows higher Li^+ ion conductivity, at the same time passivating the Si surface.[42–45]

3. Conclusions

In summary, we have demonstrated how the partial neutralization of the PAA improves the processability of the pure silicon-based anode and also enhances the overall electrochemical and physicochemical properties of the synthesized anodes. Nevertheless, an excessive neutralization degree above 70% is not favorable, as it diminishes the battery cycle life and also gassing of the slurry occurred as a major challenge. Therefore, a simple increase in neutralization degree does not necessarily improve all the important properties and performance of the anode, but rather resembles the search of the best compromise. Additionally, higher SC during mixing changes electrode and electrochemical properties and gives improvement in cycle life. This influence needs further investigation in future studies to understand underlying mechanisms and dependencies between SC and neutralization degree. Furthermore, a detailed TEM-EELS and XPS analysis shows the interaction between Si particles and binder, as well as the polymer distribution within the electrodes. Overall, this work shows the outstanding performance of Si-dominant anodes with limitation of Si capacity by oversizing of the anode (high N/P ratio). It is important to note that the active material was only based on pure SiMPs. Additionally, the best performing cells showed the least degradation in SEM on electrode and particle level and indicated a different SEI composition with a higher contribution of stable inorganic LiF in the SEI. Literature shows that modification of the binder towards more stable and/or self-healing networks is crucial to stabilize the SiMP-based anode. Therefore, the partial neutralization of PAA should be taken into account when introducing crosslinkers. The use of multivalent cations can be an important benefit to gain self-healing properties without need for very complex binder systems. Also, as the capacity limitation plays a crucial role in further development of SiMPs-based anodes, experiments are ongoing which will show the impact of lower cutoff voltage variation.

Experimental Section/Methods

Experimental details are provided in the supporting information (SI).

Detailed description of the methods and instruments used in this work is provided in the Supporting Information.

Supporting Information Summary

Supporting Information is available from the Wiley Online Library or from the corresponding authors.

Experimental Section, SEM-EDX images of pristine and cycled electrodes, TEM-EELS images of pristine Li_0PAA and $Li_{0.3}$PAA electrode, XPS survey and detail measurements of pristine and cycled electrodes based on Li_0PAA, $Li_{0.3}$PAA, $Li_{0.7}$PAA, half-cell C-rate test.

The following files are available free of charge.

Supporting Information (PDF).

© 2024 The Authors. Batteries & Supercaps published by Wiley-VCH GmbH

Batteries & Supercaps | Research Article
doi.org/10.1002/batt.202400330
Chemistry Europe
European Chemical Societies Publishing

Abbreviations

CB	carbon black
CCCV	constant current constant voltage
DCIR	direct current internal resistance
DMC	dimethyl carbonate
EC	ethylene carbonate
EDX	energy-dispersive X-ray spectroscopy
EELS	electron energy loss spectroscopy
EMC	ethyl-methyl carbonate
FCE	first cycle efficiency
FEC	fluoroethylene carbonate
FIB	focused ion beam
FTIR	Fourier-transform infrared spectroscopy
LIB	lithium ion battery
LiOH	lithium hydroxide
Li_xPAA	lithiated PAA to degree x
M_w	average molar mass
NMC811	lithium nickel manganese cobalt oxide (8:1:1)
N/P	negative to positive ratio
PAA	polyacrylic acid
PVDF	polyvinylidene fluoride
R2R	roll to roll
SC	solids content
SEI	solid electrolyte interphase
SEM	scanning electron microscopy
SiMP	silicon microparticle
SiNP	silicon nanoparticle
SOH	state of health
SWCNTs	single-wall carbon nanotubes
TEM	transmission electron microscopy
VC	vinylene carbonate
wt.%	weight percent
XPS	X-ray photoelectron spectroscopy

Author Contributions

The manuscript was written through contributions of all authors. All authors have given approval to the final version of the manuscript.

Acknowledgements

We acknowledge the financial support of Mercedes-Benz AG, (Stuttgart, Germany). M.A. gratefully acknowledges the financial support from the Deutsche Forschungsgemeinschaft (DFG, German Research Foundation) under Germany's Excellence Strategy – EXC 2154 – Project number 390874152 (POLiS Cluster of Excellence). Financial support by Ulm University and the Helmholtz-Gemeinschaft (HGF) is gratefully acknowledged. G.K. thanks Philipp Bellucci from Mercedes-Benz AG for the preparation of FIB cross-sections of the samples and SEM/EDX measurements. Clementine Warres from NMI Tübingen is acknowledged for the lamella preparation and measurement of TEM-EELS spectra. This work contributes to the research performed at CELEST (the Center for Electrochemical Energy Storage Ulm-Karlsruhe). Open Access funding enabled and organized by Projekt DEAL.

Conflict of Interests

The authors declare no conflict of interest.

Data Availability Statement

The data that support the findings of this study are available from the corresponding author upon reasonable request.

Keywords: Silicon anode · Micron-sized metallurgical silicon · Partially neutralized polyacrylic acid · Binder distribution · TEM-EELS

[1] M. N. Obrovac, *Curr. Opin. Electrochem.* **2018**, *9*, 8–17.
[2] K. Feng, M. Li, W. Liu, A. G. Kashkooli, X. Xiao, M. Cai, Z. Chen, *Small* **2018**, *14*, 1702737.
[3] M. N. Obrovac, V. L. Chevrier, *Chem. Rev.* **2014**, *114*, 11444–11502.
[4] M. Armand, P. Axmann, D. Bresser, M. Copley, K. Edström, C. Ekberg, D. Guyomard, B. Lestriez, P. Novák, M. Petranikova, W. Porcher, S. Trabesinger, M. Wohlfahrt-Mehrens, H. Zhang, *J. Power Sources* **2020**, *479*, 228708.
[5] X. Zuo, J. Zhu, P. Müller-Buschbaum, Y.-J. Cheng, *Nano Energy* **2017**, *31*, 113–143.
[6] C. Zhang, F. Wang, J. Han, S. Bai, J. Tan, J. Liu, F. Li, *Small Structures* **2021**, *2*, 2100009.
[7] B. Zhu, G. Liu, G. Lv, Y. Mu, Y. Zhao, Y. Wang, X. Li, P. Yao, Y. Deng, Y. Cui, J. Zhu, *Sci. Adv.* **2019**, *5*, eaax0651.
[8] Y. Li, X. Zheng, Z. Cao, Y. Wang, Y. Wang, L. Lv, W. Huang, Y. Huang, H. Zheng, *Energy Storage Mater.* **2023**, *55*, 660–668.
[9] D. Rehnlund, F. Lindgren, S. Böhme, T. Nordh, Y. Zou, J. Pettersson, U. Bexell, M. Boman, K. Edström, L. Nyholm, *Energy Environ. Sci.* **2017**, *10*, 1350–1357.
[10] X. Su, Q. Wu, J. Li, X. Xiao, A. Lott, W. Lu, B. W. Sheldon, J. Wu, *Adv. Energy Mater.* **2014**, *4*, 1300882.
[11] G. G. Eshetu, H. Zhang, X. Judez, H. Adenusi, M. Armand, S. Passerini, E. Figgemeier, *Nat. Commun.* **2021**, *12*, 5459.
[12] F. Li, J. Xu, Z. Hou, M. Li, R. Yang, *ChemNanoMat* **2020**, *6*, 720–738.
[13] H. Wu, Y. Cui, *Nano Today* **2012**, *7*, 414–429.
[14] X. Zhao, V.-P. Lehto, *Nanotechnology* **2021**, *32*, 42002.
[15] Y. Yang, W. Yuan, W. Kang, Y. Ye, Y. Yuan, Z. Qiu, C. Wang, X. Zhang, Y. Ke, Y. Tang, *Nanoscale* **2020**, *12*, 7461–7484.
[16] X. H. Liu, L. Zhong, S. Huang, S. X. Mao, T. Zhu, J. Y. Huang, *ACS Nano* **2012**, *6*, 1522–1531.
[17] G. Zhu, D. Chao, W. Xu, M. Wu, H. Zhang, *ACS Nano* **2021**, *15*, 15567–15593.
[18] F. Zou, A. Manthiram, *Adv. Energy Mater.* **2020**, *10*, 2002508.
[19] Y.-M. Zhao, F.-S. Yue, S.-C. Li, Y. Zhang, Z.-R. Tian, Q. Xu, S. Xin, Y.-G. Guo, *InfoMat* **2021**, *3*, 460–501.
[20] G. G. Eshetu, E. Figgemeier, *ChemSusChem* **2019**, *12*, 2515–2539.
[21] J.-T. Li, Z.-Y. Wu, Y.-Q. Lu, Y. Zhou, Q.-S. Huang, L. Huang, S.-G. Sun, *Adv. Energy Mater.* **2017**, *7*, 1701185.
[22] D. Bresser, D. Buchholz, A. Moretti, A. Varzi, S. Passerini, *Energy Environ. Sci.* **2018**, *11*, 3096–3127.
[23] J. Xiong, N. Dupré, D. Mazouzi, D. Guyomard, L. Roué, B. Lestriez, *ACS Appl. Mater. Interfaces* **2021**, *13*, 28304–28323.
[24] K. A. Hays, R. E. Ruther, A. J. Kukay, P. Cao, T. Saito, D. L. Wood, J. Li, *J. Power Sources* **2018**, *384*, 136–144.
[25] Z. Li, W. Tang, Y. Yang, G. Lai, Z. Lin, H. Xiao, J. Qiu, X. Wei, S. Wu, Z. Lin, *Adv. Funct. Mater.* **2022**, *32*, 2206615.
[26] D. Dang, Y. Wang, M. Wang, J. Hu, C. Ban, Y.-T. Cheng, *ACS Appl. Energ. Mater.* **2020**, *3*, 10940–10949.

© 2024 The Authors. Batteries & Supercaps published by Wiley-VCH GmbH

2366625, 2024, 12, Downloaded from https://chemistry-europe.onlinelibrary.wiley.com/doi/10.1002/batt.202400330 by KIT - Universitaet Ulm, Wiley Online Library on [24/06/2025]. See the Terms and Conditions (https://onlinelibrary.wiley.com/terms-and-conditions) on Wiley Online Library for rules of use; OA articles are governed by the applicable Creative Commons License

Batteries & Supercaps | Research Article doi.org/10.1002/batt.202400330 | Chemistry Europe European Chemical Societies Publishing

[27] N. Hamzelui, G. G. Eshetu, E. Figgemeier, *J. Energy Storage* **2021**, *35*, 102098.
[28] M.-T. F. Rodrigues, S. E. Trask, I. A. Shkrob, D. P. Abraham, *J. Power Sources* **2018**, *395*, 289–294.
[29] K. A. Hays, B. Key, J. Li, D. L. Wood, G. M. Veith, *J. Phys. Chem. C* **2018**, *122*, 9746–9754.
[30] B. Hu, S. Jiang, I. A. Shkrob, J. Zhang, S. E. Trask, B. J. Polzin, A. Jansen, W. Chen, C. Liao, Z. Zhang, L. Zhang, *J. Power Sources* **2019**, *416*, 125–131.
[31] Z.-J. Han, K. Yamagiwa, N. Yabuuchi, J.-Y. Son, Y.-T. Cui, H. Oji, A. Kogure, T. Harada, S. Ishikawa, Y. Aoki, S. Komaba, *Phys. Chem. Chem. Phys.* **2015**, *17*, 3783–3795.
[32] M. K. Burdette-Trofimov, B. L. Armstrong, A. M. Rogers, L. Heroux, M. Doucet, G. Yang, N. D. Phillip, M. K. Kidder, G. M. Veith, *J. Phys. Chem. C* **2020**, *124*, 13479–13494.
[33] Z.-Y. Wu, L. Deng, J.-T. Li, S. Zanna, A. Seyeux, L. Huang, S.-G. Sun, P. Marcus, J. Światowska, *Batteries* **2022**, *8*, 271.
[34] C. C. Nguyen, T. Yoon, D. M. Seo, P. Guduru, B. L. Lucht, *ACS Appl. Mater. Interfaces* **2016**, *8*, 12211–12220.
[35] J. He, C. Das, F. Yang, J. Maibach, *Electrochim. Acta* **2022**, *411*, 140038.
[36] T. R. Martin, R. T. Pekarek, J. E. Coyle, M. C. Schulze, N. R. Neale, *J. Mater. Chem. A* **2021**, *9*, 21929–21938.
[37] W. Porcher, S. Chazelle, A. Boulineau, N. Mariage, J. P. Alper, T. van Rompaey, J.-S. Bridel, C. Haon, *J. Electrochem. Soc.* **2017**, *164*, A3633–A3640.
[38] R. Nölle, K. Beltrop, F. Holtstiege, J. Kasnatscheew, T. Placke, M. Winter, *Mater. Today* **2020**, *32*, 131–146.
[39] F. Maroni, M. Spreafico, A. Schönecker, M. Wohlfahrt-Mehrens, M. Marinaro, *J. Electrochem. Soc.* **2022**, *169*, 80506.
[40] N. P. Wagner, K. Asheim, F. Vullum-Bruer, A. M. Svensson, *J. Power Sources* **2019**, *437*, 226884.
[41] F. Reuter, A. Baasner, J. Pampel, M. Piwko, S. Dörfler, H. Althues, S. Kaskel, *J. Electrochem. Soc.* **2019**, *166*, A3265–A3271.
[42] X.-Q. Zhang, X.-B. Cheng, X. Chen, C. Yan, Q. Zhang, *Adv. Funct. Mater.* **2017**, *27*, 1605989.
[43] T. Jia, G. Zhong, S. Lu, X. Ren, Y. Lv, N. Li, R. Yin, G. Kang, K. Cai, F. Kang, Y. Cao, *Chem. Eng. J.* **2023**, *454*, 140397.
[44] P. Parikh, M. Sina, A. Banerjee, X. Wang, M. S. D'Souza, J.-M. Doux, E. A. Wu, O. Y. Trieu, Y. Gong, Q. Zhou, K. Snyder, Y. S. Meng, *Chem. Mater.* **2019**, *31*, 2535–2544.
[45] H. Shin, J. Park, S. Han, A. M. Sastry, W. Lu, *J. Power Sources* **2015**, *277*, 169–179.

Manuscript received: May 17, 2024
Revised manuscript received: June 27, 2024
Accepted manuscript online: July 11, 2024
Version of record online: September 3, 2024

© 2024 The Authors. Batteries & Supercaps published by Wiley-VCH GmbH

25666223, 2024, 12, Downloaded from https://chemistry-europe.onlinelibrary.wiley.com/doi/10.1002/batt.202400330 by KIT - Universitat Ulm, Wiley Online Library on [24/06/2025]. See the Terms and Conditions (https://onlinelibrary.wiley.com/terms-and-conditions) on Wiley Online Library for rules of use; OA articles are governed by the applicable Creative Commons License

Batteries & Supercaps

Supporting Information

Enabling Si-Dominant Anodes: Influence of Neutralization Degree of Polyacrylic Acid on Low-Cost Micron-Sized Silicon Anode in High-Energy Li-Ion Full Cell

Gabriele Kloker,* Dragoljub Vrankovic, Nikhil Arya, Thomas Diemant, and Montaha Anjass*

WILEY-VCH

Supporting Information

Enabling Si-Dominant Anodes: Influence of Neutralization Degree of Polyacrylic Acid on Low-Cost Micron-Sized Silicon Anode in High-Energy Li-Ion Full Cell

Gabriele Kloker, Dragoljub Vrankovic, Nikhil Arya, Thomas Diemant, Montaha Anjass**

G. Kloker, D. Vrankovic
Mercedes-Benz AG, Mercedesstraße 130/6, 70327 Stuttgart, Germany
E-mail: gabriele.kloker@mercedes-benz.com, gabriele.kloker@uni-ulm.de

M. Anjass
University of Sharjah, Department of Chemistry, Sharjah-27272, Sharjah, United Arab Emirates
E-mail: malmasri@sharjah.ac.ae

G. Kloker, N. Arya, M. Anjass
Ulm University, Institute of Inorganic Chemistry I, Albert-Einstein-Allee 11, 89081 Ulm, Germany

N. Arya, T. Diemant
Helmholtz Institute Ulm (HIU) Electrochemical Energy Storage, Helmholtzstr. 11 89081 Ulm, Germany

1. Experimental

All mentioned steps were done under ambient conditions, if not stated otherwise. Glove box conditions means an argon atmosphere with O2 < 10 ppm and H2O < 1 ppm. Dry room conditions indicates a dew point of less than -50 °C. All reagent-grade chemicals were purchased from Sigma-Aldrich and were used without further purification. Weight percentages (wt.%) of electrode components are given based on the dry electrode.

Preparation of partially neutralized PAA

The 10 weight percent (wt.%) PAA solution was prepared using PAA powder from Sigma-Aldrich (average molar mass M_w ~ 450,000) and deionized water, dissolved by a magnetic stirrer. Partial neutralization of the solution was done by calculating the neutralization degree as one mol lithium hydroxide (LiOH) neutralizing one mol –COOH functional groups. To enable precise control over added lithium ions, they were added as 1 mol L^{-1} LiOH solution to the PAA solution. 2 mol L^{-1} LiOH solution was only used to reach higher desired solids contents during mixing of the $Li_{0.3}$PAA electrode within the solids content variation of that sample. Since the equilibrium between –COOH and –COOLi groups is reached slowly, the partially neutralized PAA solution was left for at least 1 h and checked several times via measurement of pH comparing to a neutralization curve, which was obtained before by titration. PAA was neutralized to 30%, 70% and 80%, the received samples are referred to as $Li_{0.3}$PAA, $Li_{0.7}$PAA and $Li_{0.8}$PAA.

Fabrication of electrodes containing PAA and partially neutralized PAA

Electrodes were manufactured by preparing batches of ca. 80 g slurry, starting with pre-mixing the powders. For this purpose, 88.5 wt.% pestled silicon microparticles (Elkem e-Si 703, d_{50} = 3.59 µm) and 3 wt.% carbon black (Imerys, Super C45) were mixed by using a helix-type stirrer with an overhead-mixer. The pre-mixed powder was then added in several steps to the binder solution and mixed with a planetary centrifugal mixer (Speedmixer™ DAC 700.2 VAC-P) in a 150 mL cup. The pH value of the slurry was constantly monitored during the addition of the powders to the binder solution. If necessary, some deionized water was added in between. As last step, 0.5 wt.% single wall carbon nanotubes (SWCNTs) (Tuball) were added to the slurry and mixed thoroughly. Then the slurry was degassed in the Speedmixer and rheology (rheometer Anton Paar MCR 302) as well as solids content was measured and adapted to be ~40 %. In addition, a test on the Hegman gauge/grindometer was done before coating to check

for large agglomerates. The slurry was then cast on a 10 µm thick copper foil with a doctor blade on a coating table. The used thickness was selected based on the solids content of the slurry and ranged from 75 to 100 µm. After casting, the coatings were dried under vacuum at 80 °C overnight (~ 16 h). After drying, the electrode sheets were calendered using an Ingecal lab calender with preheating of 80 °C. Electrode thickness was measured with a micrometer gauge (Mitutoyo high accuracy). The adhesion of the electrodes was measured via 90° peel test (ZwickRoell) electrode pieces with comparable loading. For the adhesion test, the electrode coating was put on the adhesive tape and the copper foil was pulled from the coating. For cohesion, the copper foil was put on the adhesive tape and another one was glued on the electrode coating, which was then pulled with the aim to create mechanical failure within the coating layer.

Hioki measurement of electronic resistivity

Electronic resistances were obtained by use of HIOKI RM2610 and measuring three different spots for each electrode. The device contains a 46-point probe head, which is placed carefully on top of the electrode.

Cell preparation and electrochemical testing

Electrochemical tests were conducted in half coin cells at room temperature (25 °C) as well as in full pouch cells in Memmert chamber at 25 °C. In both cases, an electrolyte containing 1.2M $LiPF_6$/ethylene carbonate (EC):ethyl methyl carbonate (EMC):dimethyl carbonate (DMC) +1% vinylene carbonate (VC)+7% fluoroethylene carbonate (FEC) was used together with polyethylene-based and ceramic coated tri-layer separator (21µm thick). For the half coin cell tests, 2016 housings were filled with anode coin (Ø = 15 mm), separator (Ø = 21 µm), 75 µL electrolyte, 250 µm thick lithium coin (Ø = 16 mm) and spacer and crimped in glove box. The full pouch cells were stacked sandwich-type with double-sided, roll-to-roll (R2R)-coated cathodes based on single-crystal NMC811 (94.5% commercial active material, 1% Super C65 carbon black, 1% MWCNTs, and 3.5% polyvinylidene fluoride PVDF) in the middle and two single-sided, table-coated anodes as described above. With a cathode area of 4.8x4.8 cm^2 and an areal capacity of ~3 mAh cm^{-2}, the resulting capacity of those cells is ~150 mAh. The oversized anodes (5x5 cm^2), limited to a capacity of 1500 mAh g_{Si}^{-1} by calculation, were coated with a loading that leads to a negative/positive (N/P) ratio of ~1.1. After filling with electrolyte, the cells were put under vacuum (40 mbar) and sealed in a subsequent step in the glove box.

Before cycling, they were pressed between acrylic glass plates by two foldback clamps and left to rest for 2 h.

A Basytec tester was used for the electrochemical measurements. All cells were subjected to initial formation (2x C/10, 2x C/5, 3x C/3, discharge CC) before cycling. Half-cell cycling was done at 0.01-1.5 V vs. Li^+/Li at a C-rate of C/3 after one C/20 and one C/10 formation cycle (lithiation CCCV, delithiation CC).

Half-cell C-rate tests were done with the same voltage range with two additional C/10 formation cycles, followed by C-rate variation in lithiation direction (C/2, 1C, 1.5C, 2C, 3C – 5x each) and ending with 5x C/3 cycles. The delithiation rate was kept constant and lithiation was done with CCCV, while delithiation was measured with CC. All C-rates were chosen to avoid too fast charge/discharge, which could lead to detrimental effects based on Li stripping/plating. During lithation of the Si in half cell tests (both normal and C-rate variation) the capacity was limited to 1500 mAh g^{-1} within the program.

Full cell cycling was conducted at 3.0-4.2 V with 1C cycling including check-up cycles with C/3 after every 50 cycles. The latter were used to determine state of health (SOH) of the cell based on measured C/3 capacity compared to first C/3 cycle directly after formation (all cycles charge CCCV, discharge CC) to cycle it until SOH=80%. Within the check-up cycles a direct current internal resistance (DCIR) test was included as well. Full cell C-rate testing was done with two C/3 cycles in the beginning, followed by C-rate variation in discharge direction (C/2, 1C, 1.5C, 2C, 2.5C, 3C, 3.5C, 4C, 4.5C, 5C – 3x each) while keeping charge direction at C/3. After another two C/3 parallel cycles the charge direction was varied the same way while discharge direction was kept constant at C/3. Two C/3 parallel cycles marked the end of the test to check again the capacity retention. All C/3 charging steps were conducted CCCV, the rest only CC.

Characterization

Scanning electron microscopy (SEM)

SEM images were taken with a TESCAN Mira3 at 15 kV. A Hitachi IM 4000 Plus with cross section milling was used as ion-polisher.

Cryo transmission electron microscopy (TEM)-electron energy loss spectroscopy (EELS)

CryoTEM images were taken with a Zeiss Crossbeam 550 JEOL ARM 200F instrument with probe corrector and equipped with a Gatan Quantum ER EELS. The samples were prepared via focused ion-beam (FIB) under cryo condition. The commonly used platinum/carbon protection

stripe could not be used because carbon of the sample was the aim of investigation, therefore the protection stripe would have influenced the results. Therefore, deposition of a thin gold/palladium layer (~100 nm) on the particle surface via sputtering was used instead. A FIB lamella was cut, thinned, attached to the TEM grid and transferred to the TEM chamber with minimum exposure to ambient condition. TEM analysis was carried out in cryo conditions as well to minimize knock-on damage of the sample by electron beam.

X-ray photoelectron spectroscopy (XPS)

X-ray photoelectron spectroscopy (XPS) measurements were carried out with a Specs XPS system using monochromatized Al Kα (1486.6 eV) radiation. The measurements were done pass energies at the analyzer of 90 and 30 eV for survey and detail spectra, respectively. The samples were neutralized with electrons from a flood gun to compensate for charging effects at the surface. For binding energy calibration, the C 1s peak of conductive carbon was set to 284.4 eV. CasaXPS was used for peak fitting with Shirley-type backgrounds and Gaussian-Lorentzian peak shapes (GL30). For the Si 2p spectra, a peak doublet (Δ = 0.61 eV) was inserted for elemental Si, while a (broader) single peak was adopted for the oxidized Si species (SiOx an SiO_2). A peak due to SiO_2 was added at 532.7 eV in the O 1s spectra of the pristine samples, its intensity was derived from the SiO_2 Si 2p signal taking into account stoichiometry and the atomic sensitivity factors of Si 2p and O 1s peaks.

2. Results and Discussion

2.1. Scanning electron microscopy (SEM) and energy-dispersive X-ray spectroscopy (EDX) maps

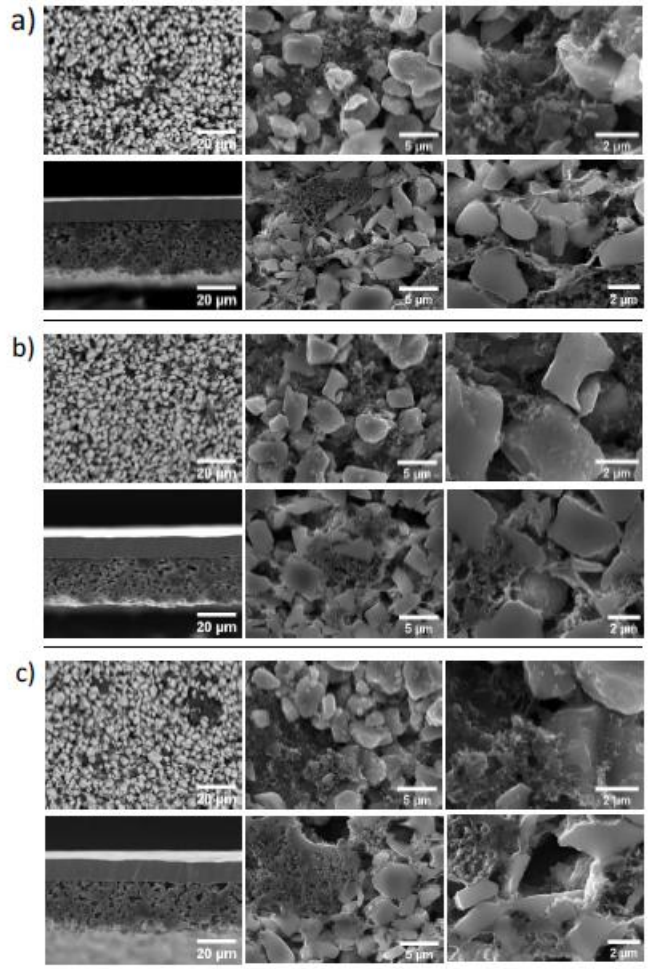

Figure S1. SEM images from top-view perspective (top line) and cross-section (bottom line) with different magnifications of pristine electrodes containing: **a)** Li_0PAA, **b)** $Li_{0.3}PAA$ and **c)** $Li_{0.7}PAA$.

2.2. Transmission Electron Microscopy - Electron Energy Loss Spectroscopy (TEM-EELS)

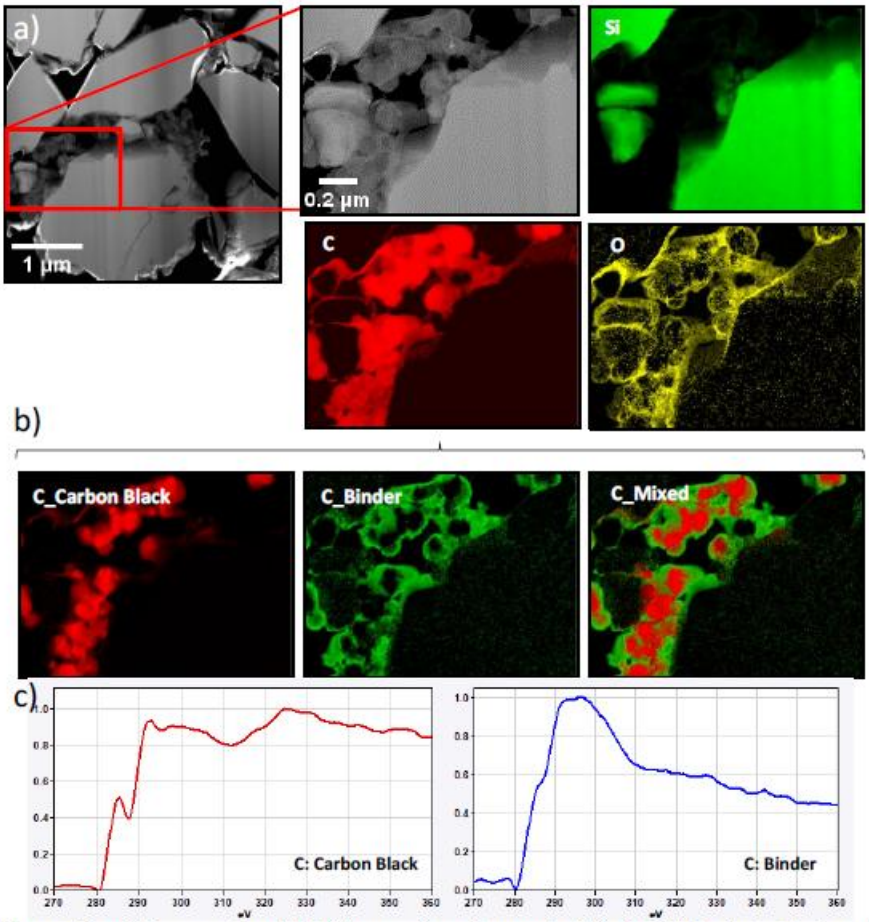

Figure S2. a) Cross-section TEM image of another part of the Li_0PAA electrode showing Si particles and the binder/conductive additive mixture in between with the elemental mapping of silicon (green), carbon (red) and oxygen (yellow). b) Differentiated carbon states by EELS for carbon black (red) and binder (green) c) Spectra for carbon which can be attributed to carbon black or PAA binder.

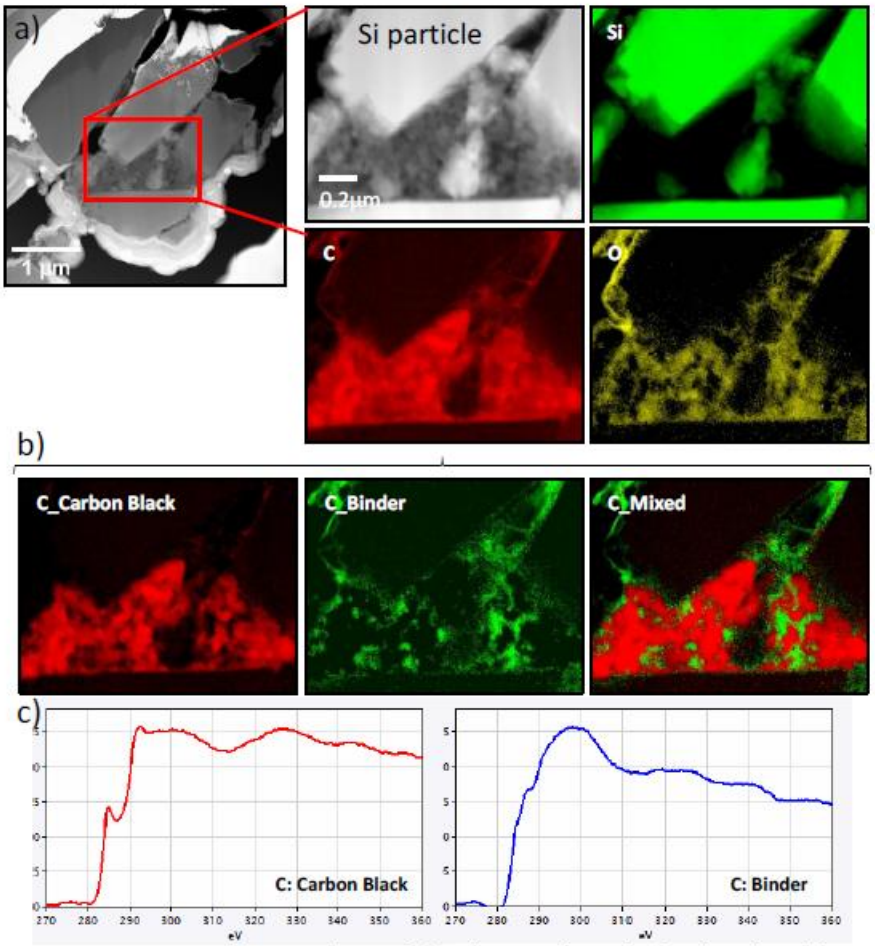

Figure S3. a) Cross-section TEM image of the $Li_{0.3}$PAA electrode showing Si particles and the binder/conductive additive mixture in between with the elemental mapping of silicon (green), carbon (red) and oxygen (yellow). **b)** Differentiated carbon states by EELS for carbon black (red) and binder (green). **c)** Spectra for carbon which can be attributed either to carbon black or PAA binder.

2.3. X-ray photoelectron spectroscopy (XPS) for pristine electrodes

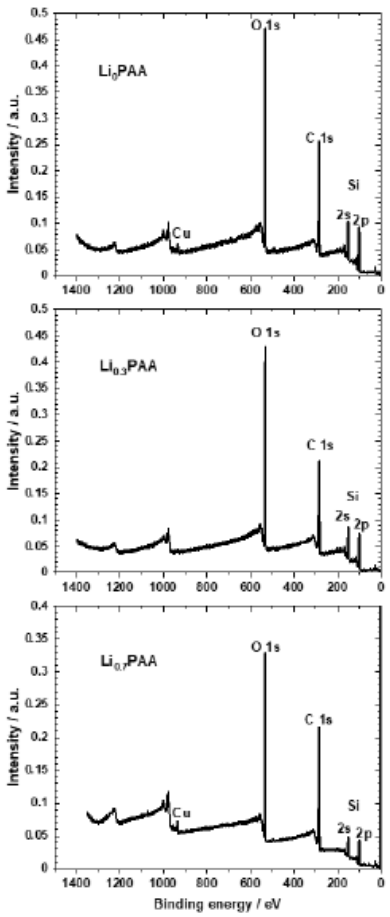

Figure S4. XPS survey spectra of pristine electrodes containing PAA binder with different neutralization degree: Li_0PAA (top), $Li_{0.3}$PAA (middle) and $Li_{0.7}$PAA (bottom).

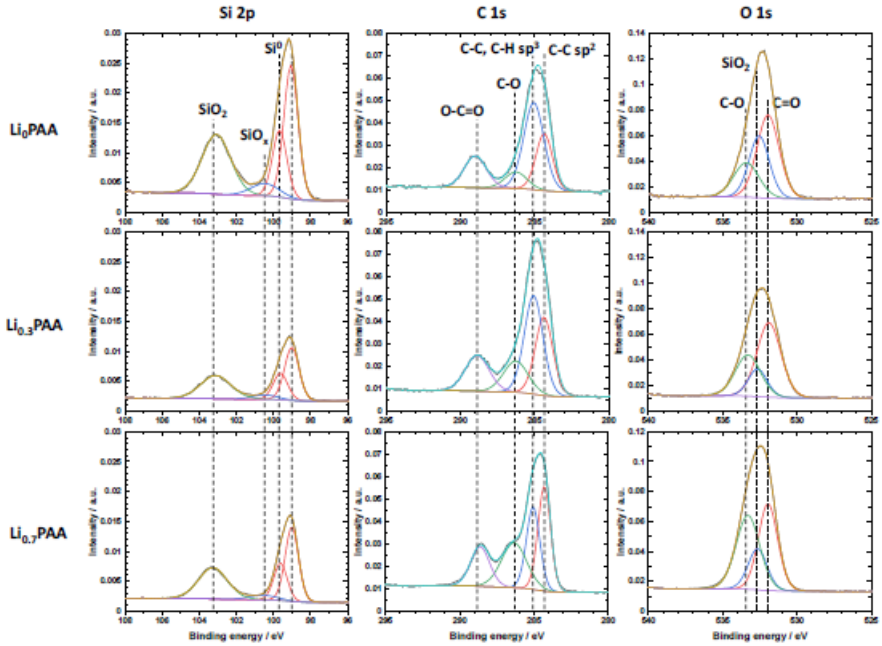

Figure S5. XPS detail measurements in the Si 2p, C 1s and O 1s regions from pristine electrodes containing PAA binder with different neutralization degree: Li_0PAA (top row), $Li_{0.3}PAA$ (middle row) and $Li_{0.7}PAA$ (bottom row).

2.4. C-rate test

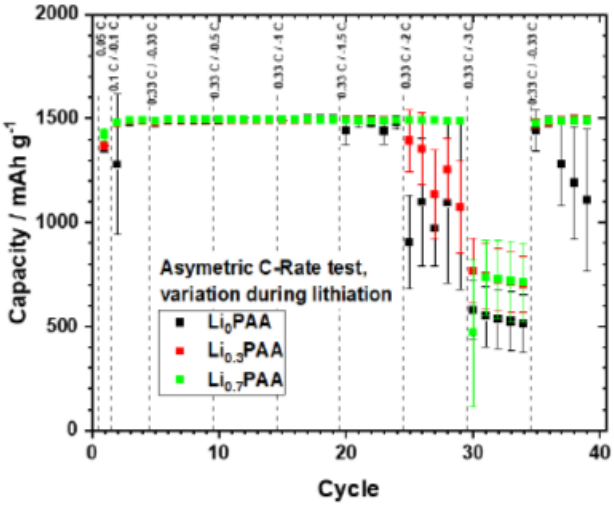

Figure S6. Asymmetric half-cell C-rate test of electrodes containing Li_0PAA (black), $Li_{0.3}PAA$ (red) and $Li_{0.7}PAA$ (green) at limited capacity of 1500 mAh g_{Si}^{-1}. The C-rate was varied in lithiation direction, the corresponding values are given above the dotted lines showing delithiation first and lithiation direction second. It needs to be considered that the lithium stripping/plating is the limiting factor for testing C-rates in half cell configuration.

2.5. Scanning electron microscopy (SEM) and energy-dispersive X-ray spectroscopy (EDX) maps of the cycled electrodes

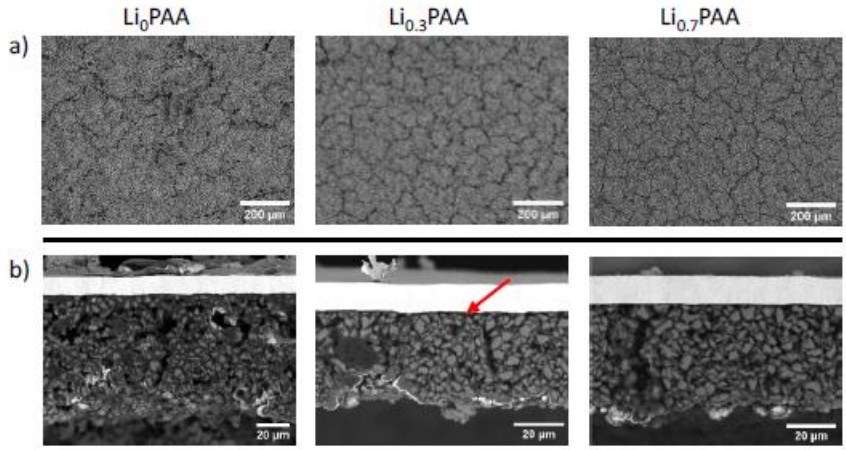

Figure S7. SEM images of post-mortem electrodes (SOH=70-80%) with Li_0PAA (left column) after 100 cycles, $Li_{0.3}PAA$ (middle column) after 150 cycles and $Li_{0.7}PAA$ (right column) after 200 cycles. **a)** Top-view perspective , **b)** cross-section of the electrodes (red arrow indicates delamination).

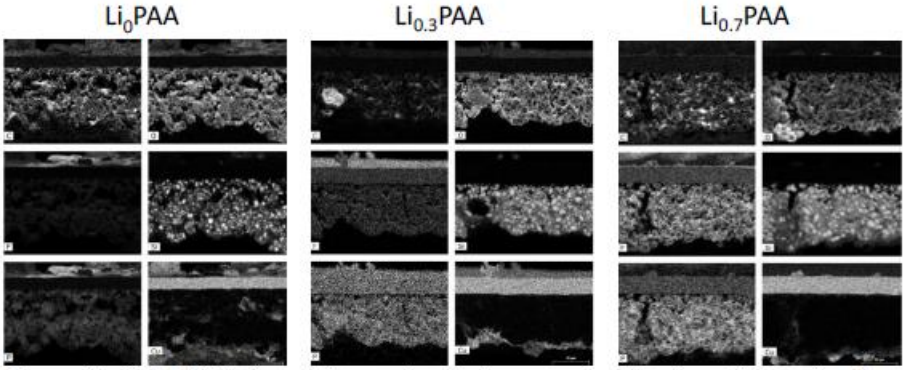

Figure S8. SEM-EDX elemental mapping (carbon, oxygen, fluorine, silicon, phosphorous, copper) of post-mortem electrodes (SOH=70-80%) with Li_0PAA (left column) after 100 cycles, $Li_{0.3}PAA$ (middle column) after 150 cycles and $Li_{0.7}PAA$ (right column) after 200 cycles in cross-section perspective.

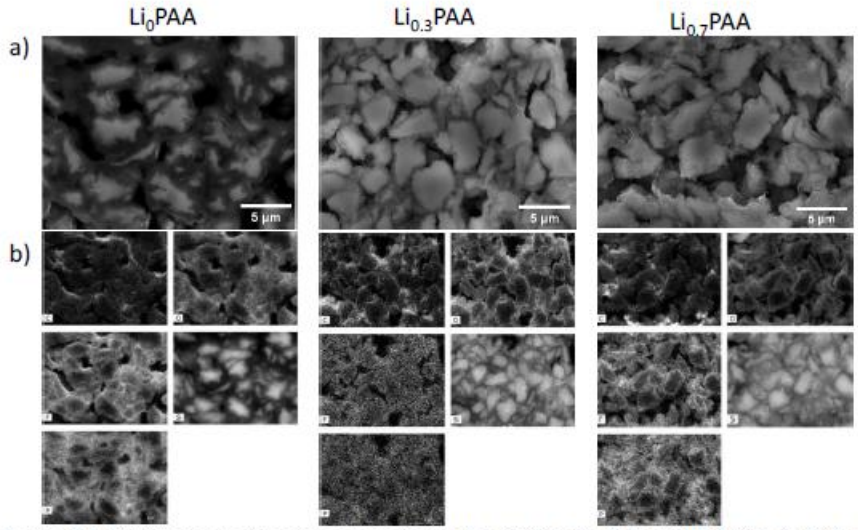

Figure S9. SEM images of post-mortem electrodes (SOH=70-80%) with Li_0PAA (left column) after 100 cycles, $Li_{0.3}$PAA (middle column) after 150 cycles and $Li_{0.7}$PAA (right column) after 200 cycles. **a)** Cross-section of the particles, **b)** corresponding EDX mapping of carbon, oxygen, fluorine, silicon and phosphorous.

2.6. X-ray photoelectron spectroscopy (XPS) for the cycled electrodes

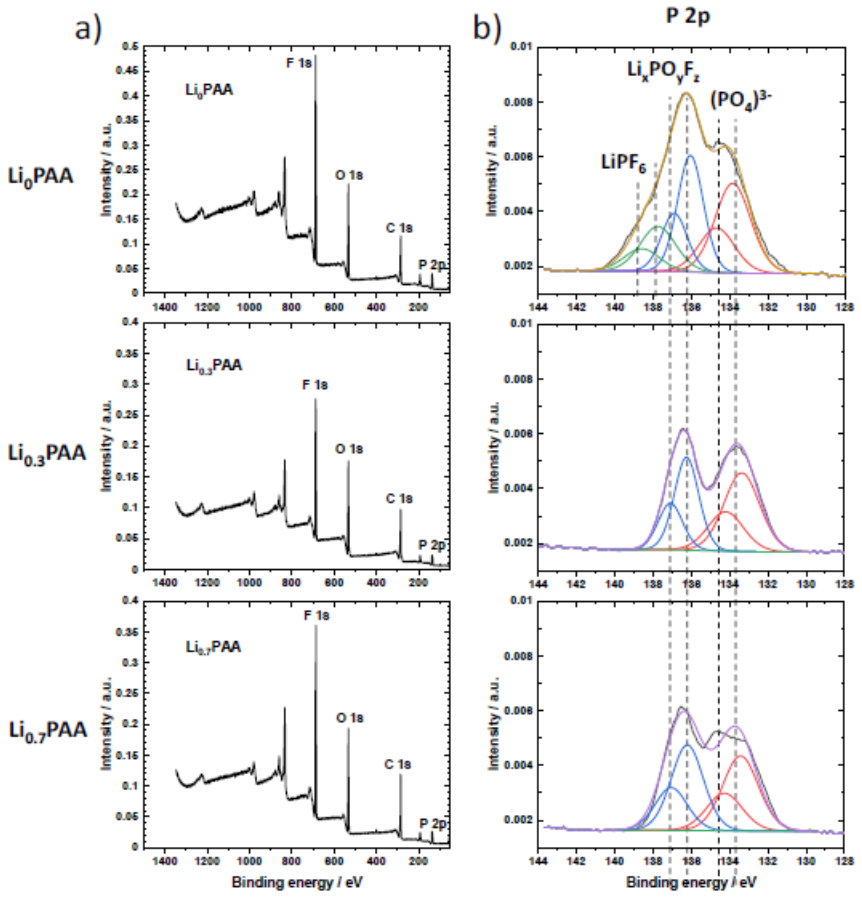

Figure S10. a) XPS survey spectra of cycled electrodes containing PAA binder with different neutralization degree: Li_0PAA (top row), $Li_{0.3}$PAA (middle row) and $Li_{0.7}$PAA (bottom row). **b)** XPS detail measurements in the P 2p region.

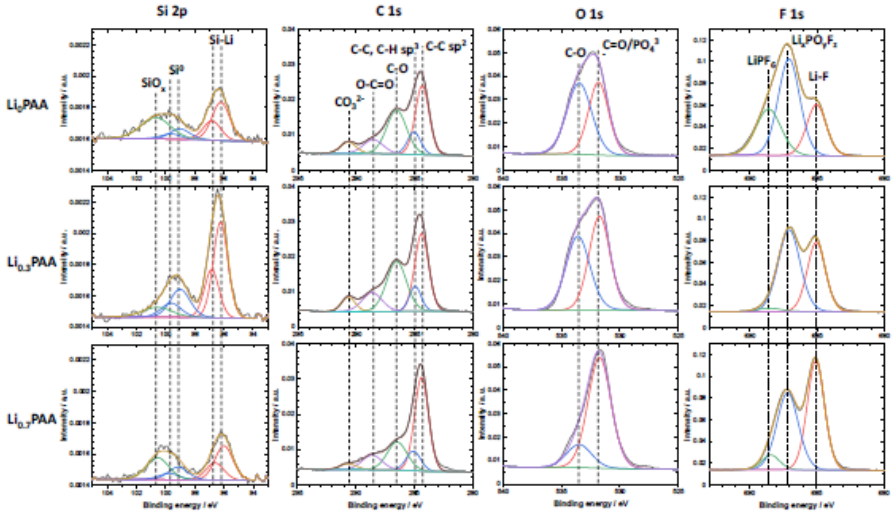

Figure S11. XPS detail measurements in the Si 2p, C 1s, O 1s and F 1s regions from cycled electrodes containing PAA binder with different neutralization degree: Li_0PAA (top row), $Li_{0.3}$PAA (middle row) and $Li_{0.7}$PAA (bottom row).

6.4 (NA4): Boosting Mg Deposition and Dissolution from Ionic liquids – The Role of Different Additives for Applications in Mg-ion Batteries

Omar W. Elkhafif, Hagar K. Hassan*, Motahira Hashmi, Nikhil Arya, Montaha Anjass, Timo Jacob*

*Corresponding author

Published in: Journal of Energy Storage

Copyright: Elkhafif, Omar W., Hagar K. Hassan, Motahira Hashmi, Nikhil Arya, Montaha Anjass, and Timo Jacob. "Boosting Mg deposition and dissolution from ionic liquids–The role of different additives for applications in Mg-ion batteries." *Journal of Energy Storage* 105 (2025): 114636.

DOI: https://doi.org/10.1016/j.est.2024.114636

Licence: As the author of this Elsevier article, you retain the right to include it in a thesis or dissertation, provided it is not published commercially. Permission is not required, but please ensure that you reference the journal as the original source. For more information on this and on your other retained rights, please visit: https://www.elsevier.com/about/our-business/policies/copyright#Author-rights (*2024 Elsevier Ltd.)*

Author contribution:

O. W. Elkhafif: Material synthesis and characterization, battery testing and data analysis, writing and revision of the manuscript

H. K. Hassan: Result discussion, writing, and revision of the manuscript

M. Hashmi: Performed Material preparation and characterization

N. Arya: Material preparation for the Raman measurement and analysis, revision of manuscript

M. Anjass: Result discussion, writing, and revision of the manuscript

T. Jacob: Data analysis, result discussion, writing, and revision of the manuscript

Journal of Energy Storage 105 (2025) 114636

Contents lists available at ScienceDirect

Journal of Energy Storage

journal homepage: www.elsevier.com/locate/est

Research Papers

Boosting Mg deposition and dissolution from ionic liquids – The role of different additives for applications in Mg-ion batteries

Omar W. Elkhafif [a], Hagar K. Hassan [a,b,c,*], Motahira Hashmi [d], Nikhil Arya [d], Montaha Anjass [d,e], Timo Jacob [a,b,c,*]

[a] Institute of Electrochemistry, Ulm University, Albert-Einstein-Allee 47, 89081 Ulm, Germany
[b] Helmholtz-Institute-Ulm (HIU), Helmholtzstr. 11, 89081 Ulm, Germany
[c] Karlsruhe Institute of Technology (KIT), P.O. Box 3640, 76021 Karlsruhe, Germany
[d] Institute of Inorganic Chemistry I, Ulm University, Albert-Einstein-Allee 11, 89081 Ulm, Germany
[e] Department of Chemistry, University of Sharjah, Sharjah 27272, Sharjah, United Arab Emirates

ARTICLE INFO

Keywords:
Ionic liquid
Mg batteries
Co-solvent
Additives
Mg deposition
WS_2/PANI

ABSTRACT

In this work, Mg deposition from 0.1 M $Mg(TFSI)_2$ dissolved in a hydrophobic ionic liquid (IL) is found to occur, regrettably at very high overpotential, which is accompanied by electrolyte decomposition. To address this issue, we have systematically improved the electrochemical performance of the Mg-IL system through three stages of electrolyte optimization. The first two stages involved investigating the effects of different co-solvents and Mg $(BH_4)_2$ as electrolyte additives, while the third stage comprised a detailed study of various ratios between the ionic liquid and different co-solvents to achieve an optimized system. Notably, a ratio of 1:3 MPPip-TFSI to diglyme exhibited higher cathodic and anodic currents, lower overpotential, and improved cycling stability compared to other co-solvents. Scanning electron microscopy micrographs and X-ray diffraction revealed uniform and reversible Mg deposition and dissolution. The optimized electrolyte was tested with WS_2/PANI as cathode material to validate our electrolyte system in a Mg battery application, achieving a specific capacity of 197 $mAh \cdot g^{-1}$ at 20 $mA \cdot g^{-1}$ at room temperature.

1. Introduction

Rechargeable magnesium-ion batteries (RMBs) have great potential as *post*-lithium-ion technology, owing to their abundance, high volumetric capacity, low cost, and safety compared to Li-ion batteries. However, numerous challenges persist in the development of a Mg battery, including finding electrolytes that are stable and compatible with the Mg anode as well as identifying high voltage cathodes that can accommodate the divalent Mg ions [1]. Various solvents including glymes, ionic liquids, and ethers have been investigated to achieve compatible electrolytes [2]. Although ionic liquids (ILs) offer remarkable properties such as wide electrochemical stability windows, thermal stability, high ionic conductivity, low vapor pressure, and high salt solubility, achieving reversible Mg deposition and dissolution remains challenging [3]. After the addition of Mg triflates to the ionic liquid electrolytes, Mg deposition could be realized on different substrates, while even 100 % reversibility could be realized on Ag substrates [4–7]. On the contrary, dissolving different Mg salts in miscellaneous ionic liquids did not promote any successful Mg deposition/dissolution. The difficulty for Mg deposition from ILs is related to the strong association of the salt anion with the Mg^{2+} cations [8]. In order to overcome this limitation, co-solvents are added to the ILs, in particular ethereal-based solvents such as tetrahydrofuran (THF), dimethoxyethane (DME), cyclic ether, and tetraglyme [7,9–12]. For instance, the addition of THF to the IL enhanced ionic conductivity and improved Mg deposition/dissolution reversibility [7]. Similarly, the addition of cyclic ethers has proven effective in promoting the reversibility of Mg deposition and dissolution [12]. Furthermore, adding a mixture of DME and tetraglyme to the IL enhanced the electrolyte's ionic conductivity, anodic stability, and cycling efficiency, while demonstrated good compatibility with TiO_2 and Mo_6S_8 [11]. However, the impact of using a high concentration of Li (BH_4)—equivalent to that of the Mg salt—in the optimized electrolyte is ambiguous, and requires further investigations.

On the other hand, utilizing cathode materials for RMBs with compatible reversible Mg intercalation at elevated potentials and a significant rate of cation migration for effective operation at higher

* Corresponding author at: Institute of Electrochemistry, Ulm University, Albert-Einstein-Allee 47, 89081 Ulm, Germany.
E-mail address: hagar.ibrahim@kit.edu (H.K. Hassan).

https://doi.org/10.1016/j.est.2024.114636
Received 5 September 2024; Received in revised form 26 October 2024; Accepted 11 November 2024
Available online 25 November 2024
2352-152X/© 2024 Elsevier Ltd. All rights are reserved, including those for text and data mining, AI training, and similar technologies.

power levels remains a great obstacle towards a practical battery [13]. Meanwhile, there are three types of intercalation cathode materials reported for Mg batteries with 3D, 2D, and 1D diffusion channels. Chevrel phase, Mo_6S_8, along with spinel oxides and sulfides, *e.g.* Mn_2O_4, are known to have 3D diffusion channels [14,15]. On the other hand, layered sulfides and selenides, including WS_2, TiS_2, and $TiSe_2$, are designated for 2D diffusion channels [16]. As for polyanions such as silicates and phosphates, *e.g.* $FePO_4$, are the most common cathodes with 1D diffusion channels [17]. The sulfide structures have attracted great interest due to their favorable Mg mobility compared to slow diffusion and conversion reactions in the oxide-based structures [16]. Interestingly, WS_2 is recognized as preferred intercalation host for Mg batteries due to its weaker ionic bonds and van der Waals forces in comparison to other transition metal sulfides as well as its loosely stacked layer structure [18]. Motivated by this aspect, WS_2 was studied in different electrolytes, *i.e.* all-phenyl complex (APC) in THF, $Mg(TFSI)_2$ and $MgCl_2$ in DME, magnesium aluminium chloride complexes (MACC)-based electrolytes and $Mg(NO_3)_2{\cdot}6H_2O$ dissolved in ACN/G4 [18–20]. Additionally, polyaniline (PANI), as an inexpensive, easy-to-synthesize conductive polymer is utilized as additive to WS_2 in order to increase the interlayer distance of layered WS_2 and thus improve the ionic mobility [21,22].

Despite numerous efforts to enhance the electrochemical efficiency of ionic liquid (IL)-based electrolytes for magnesium ion batteries, a dearth of comprehensive and systematic investigations still remains. Thus, in the present study we present an inaugural systematic exploration of the influence of additives on the electrochemical performance of IL-based Mg electrolytes, examining the individual contributions of each additive and their combined synergistic effects. Additionally, we unveil the significance of the IL itself in the performance of Mg-ion batteries. Furthermore, the optimized electrolyte has been evaluated with WS_2/PANI composites as cathode material to affirm its compatibility in a full magnesium battery configuration.

2. Experimental

2.1. Chemicals

1-Methyl-1-propylpiperidinium bis(trifluoromethylsulfonyl)imide (MPPip-TFSI) was purchased from lolitec with purity >99 % (water <100 mg·L^{-1} and halides <100 mg·L^{-1}). Magnesium(II) bis(trifluoromethanesulfonyl)imide ($Mg(TFSI)_2$, 99.5 %) was obtained from Solvionic. Additionally, monoglyme (G1) (99.5 %), diglyme (G2) (99.5 %), triglyme (G3) (≥ 98 %), tetraglyme (G4) (≥ 99 %), 1,2-difluoro benzene (98 %) and magnesium borohydride ($Mg(BH_4)_2$, 95 %) were bought from Sigma Aldrich. Further, tetrafluoroethyl tetrafluoropropyl ether (99 %) was purchased from Apollo Scientific. Diethylene glycol diethyl ether (+99 %) was obtained from Alfa Aesar. Tungsten disulfide (WS_2, 99 %), aniline (with purity ≥99.5 %) and ammonium persulfate ($(NH_4)_2S_2O_8$, ≥ 98 %) were purchased from Sigma Aldrich.

2.2. Electrolyte preparation

All solvents were dried using 4 Å molecular sieves (Sigma Aldrich) using the same procedures as described in our previous study [23]. $Mg(TFSI)_2$ was dried under vacuum at 80 °C for 16 h and $Mg(BH_4)_2$ was used as received. Mg salts were dissolved in MPPip-TFSI at 80 °C for 2 h inside the glovebox (MBRAUN LABStar) with N_2 (5.0, MTI IndustrieGase AG) and atmosphere of O_2 and $H_2O \leq 0.5$ ppm. Additionally, Mg salts were dissolved with different ratios of various co-solvents (1,2-difluorobenzene (dFBn), tetrafluoroethyl tetrafluoropropyl ether (TTE), and diethylene glycol diethyl ether (DEGDE), mono-, di-, tri-, and tetraglymes) at 40 °C for 2 h inside the glovebox, and then stored inside it for further use.

2.3. Synthesis of WS_2/PANI composites

WS_2 nanosheets were produced by liquid exfoliation of WS_2 powders (1 mg• mL^{-1}) in DMF. The mixture was sonicated for 30 min. The resultant dispersions were centrifuged at 6000 rpm for 30 min. *In situ* polymerization was performed to synthesize the PANI/WS_2 composite. Solution (a) was prepared by dissolving 1 mL of 0.1 M aniline monomer in 50 mL of 1.0 M HCl and stirred well to form aniline hydroxide. WS_2 was added to the solution while continuously stirring to form a homogeneous mixture. Solution (b) was prepared by dissolving 2.5 g of ammonium persulfate [$(NH_4)_2S_2O_8$] in 50 mL of 1.0 M HCl. Polymerization was achieved by adding solution (b) to solution (a) under robust stirring for 5–6 h in an ice bath (0–5 °C). The obtained PANI/WS_2 composite was then vacuum filtered and washed with deionized water and then dried at 40 °C for 24 h. For electrode preparation, the active material (PANI/WS_2), Ketjenblack, and poly(vinylidene difluoride) (PVDF) binder with a weight ratio of 70:20:10 were homogeneously blended in *N*-methyl-2-pyrrolidine (NMP) using a planetary mixer. The slurry was coated on an aluminium foil by the doctor-blade technique. The coated foil was subsequently dried overnight under vacuum for solvent evaporation and punched into electrode discs of 12 mm diameter. The electrodes were further dried overnight at 40 °C or 70 °C under vacuum using a Büchi glass oven to get rid of humidity prior to storage in a glovebox for cell assembly. The obtained electrodes are designated as WS_2/PANI-40 and WS_2/PANI-70, respectively.

2.4. Structural characterisation

X-ray data were acquired using STOE Stadi P diffractometer under the following parameters: 40 kV, 40 mA, utilizing Cu-Kα radiation (λ = 0.154 nm) in reflection mode for Mg deposition detection, while Mo-Kα radiation (λ = 0.0709 nm) was used for WS_2/PANI samples in transmission mode for the powder samples and in reflection mode for the electrodes. The electrodes were disassembled in an Ar-filled glovebox (O_2, $H_2O \leq 0.1$ mg •L^{-1}) and covered with Kapton® tape to avoid air exposure. Scanning electron microscopy (SEM) micrographs and energy-dispersive X-ray spectroscopy (EDX) were conducted using the Zeiss LEO 1550VP field emission scanning electron microscope (FESEM, Carl Zeiss, Germany). To prevent exposure to air, a transfer box was employed to move samples from the glovebox to the SEM chamber.

Raman measurements were performed in a Reinshaw Raman imaging microscope, where for excitation a He—Ne laser with 532 nm and an output power of 1 % was used. The location for laser excitation and collection of the Raman spectra was monitored using a 50× objective lens. The Raman spectra of the electrodes in their original state were acquired without undergoing any further processing. Raman measurements of the cycled electrodes were performed under argon conditions. The Raman spectra were normalized (0,100) and analyzed using the Gauss model in the OriginPro 2021 software. This analysis determined the precise peak position, bandwidth, and FWHM values for each spectrum.

2.5. Electrochemical characterisation

Electrochemical quartz crystal microbalance (EQCM) measurements were carried out inside the glovebox using a Pt-coated 5.0 MHz quartz crystal as working electrode having a contact area of 0.324 cm^2 inside a temperature-controlled cell set to 60 °C to overcome the high viscosity of MPPip-TFSI. Further, a Mg meshed wire as well as a pure Mg wire were used as counter and reference electrodes, respectively. A quartz crystal microbalance with dissipation (QCM-D) (Micro Vacuum, Budapest, Hungary) connected with a Gamry potentiostat (Gamry Instruments) was employed. Cyclic voltammetry (CV) was carried out in a three-electrode BOLA cell, similar to the Swagelok setup but with the outer lining being made of Teflon. A Pt foil (MaTeck GmbH, 99.9 %) with a diameter of Ø12 mm and a thickness of 0.025 mm was used as

working and counter electrodes, respectively, while a magnesium wire was used as reference electrode. Two glass fiber separators (Whatman GF/B) soaked with 140 µL of the electrolyte were used as separator between the working and the reference electrodes as well as the counter and the reference electrodes. All measurements were carried out at room temperature and after resting at open circuit voltage (OCV) for 3 h by using a BioLogic Potentiostat. For the symmetric cell investigations, magnesium sheets (HMW Hauner GmbH, 99.8 %, Ø12 mm, and 0.1 mm thick) were used as working and counter electrodes after polishing both surfaces using sandpaper to remove the oxide layer and one glass fiber separator soaked with 70 µL of (MPPip-TFSI: diglyme (1:3) + 0.1 M Mg $(TFSI)_2$ and 0.01 M $Mg(BH_4)_2$) was used between them. Additionally, in cathode material investigations, a magnesium sheet (Ø12 mm and 0.1 mm thick) after polishing with sand paper was used as counter electrode and the WS_2/PANI cathode was used as working electrode with a glass fiber separator soaked with 70 µL of (MPPip-TFSI: diglyme (1:3) + 0.1 M $Mg(TFSI)_2$ and 0.01 M $Mg(BH_4)_2$) placed between both electrodes. The cells were kept at OCV overnight and ran at room temperature.

3. Results and discussion

Mg deposition/dissolution was studied with $Mg(TFSI)_2$ salts in a MPPip-TFSI ionic liquid, which has already been proven to facilitate Mg deposition using $Mg(OTF)_2$ [4]. Upon testing different electrochemical potential windows to track any changes in the current validating the Mg deposition, no significant increase in the current was observed until reaching a potential around −2.0 *V vs.* Mg/Mg^{2+}, as shown in Fig. 1a. Deposition of Mg at such potentials may lead to the decomposition of $TFSI^-$ anions. This makes Mg deposition from pure ILs highly challenging. To substantiate this assumption, the electrochemical quartz crystal microbalance (EQCM) technique was used. As shown in Fig. 1b, at around −2.0 *V vs.* Mg/Mg^{2+}, a significant increase in current density along with a change in the frequency by 500 Hz is observed, revealing changes in the mass taking place. Following the Sauerbrey equation, fluctuations in frequency are directly related to shifts in the mass of the quartz [24,25].

By using the Sauerbrey equation in combination with Faraday's law, the change in mass is calculated as shown in eq. 1.

$$\frac{M}{Z} = -\frac{FA\sqrt{\rho_q \mu_q}}{2f_0^2}\frac{df}{dQ} \quad (1)$$

where F is Faraday's constant, A is area of the quartz crystal, ρ_q and μ_q are the density and shear modulus of the quartz crystal, respectively, while f_0 is the change in resonance frequency of the crystal.

The electro reduction of Mg^{2+} ions to metallic Mg resulting in a $\frac{M}{Z}$ value of 12 g/mol. However, a higher $\frac{M}{Z}$ value of 21.8 g/mol was obtained from the Δf *vs.* Q diagram as shown in Fig. 1c. This possibly indicating another process to take place at the same potential such as the decomposition of $TFSI^-$ anions or $MPPI^+$ cations [26,27]. Furthermore, as shown in Fig. 1d, the SEM micrograph illustrates the presence of inhomogeneous Mg islands. The EDS shown in the inset of Fig. 1d reveals the presence of comparable percentages of F and S that might be attributed to $TFSI^-$ decomposition or the deposition of Mg-complexes.

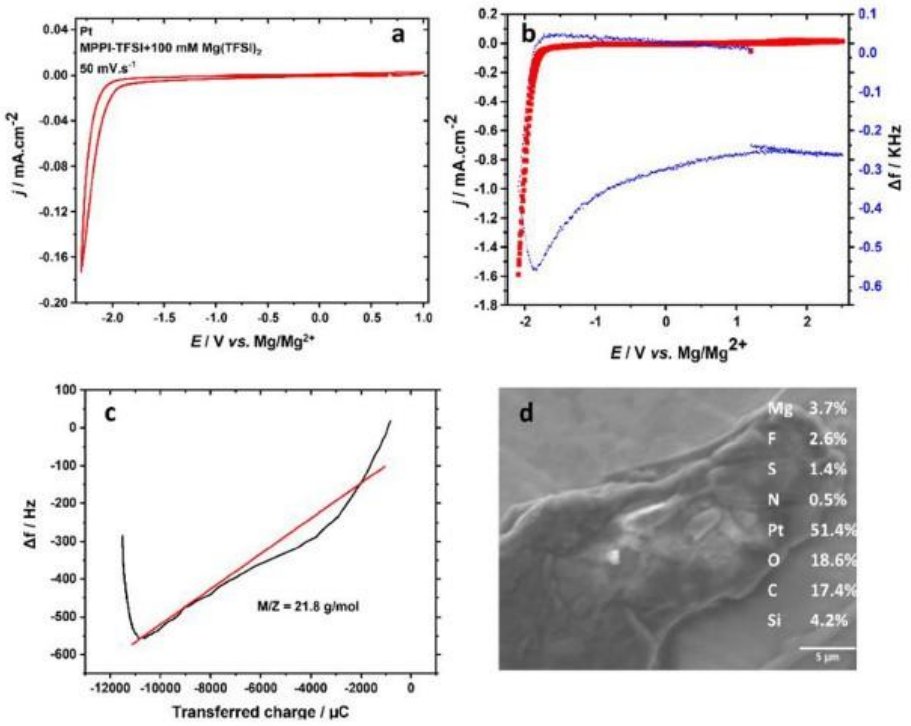

Fig. 1. a) Cyclic voltammetry of Mg deposition from 0.1 M $Mg(TFSI)_2$ in a dried MPPip-TFSI IL on a Pt working electrode at a scan rate of 50 $mV{\cdot}s^{-1}$ *vs.* Mg/Mg^{2+}, b) EQCM measurement recorded during Mg deposition, c) EQCM measurement showing the change in frequency *versus* charge during Mg deposition, and d) SEM micrograph for Mg deposition at −2.0 V *vs.* Mg/Mg^{2+} (inset: EDS data).

Therefore, we can conclude that Mg deposition from the pure ionic liquid, MPPip-TFSI, might occur accompanied by other products at very high overpotentials ≥2.0 *V*, which makes it practically infeasible.

Aiming to overcome the high overpotential of Mg deposition from IL-based electrolytes, different additives were investigated. Firstly, $Mg(BH_4)_2$ was considered as salt additive. The presence of BH_4^- in the electrolyte system acts as a water scavenger as well as a complexing agent and also eliminates or diminishes the interaction between Mg and the ionic liquid components [28–31]. No significant influence was observed upon the addition of 0.01 M $Mg(BH_4)_2$ to pure MPPip-TFSI with 0.1 M $Mg(TFSI)_2$ (see Fig. S1a). A potential explanation for the limited electrochemical deposition of magnesium from ILs is their high viscosity [32,33]. Therefore, various co-solvents, such as ether-based solvents, have been explored to reduce the IL's viscosity and the overpotential as well as to obtain higher columbic efficiencies [7,9–11,34–37].

In this study, the effect of adding monoglyme in a ratio of 1:1 with MPPip-TFSI in the presence of 0.1 M $Mg(TFSI)_2$ with and without 0.01 M $Mg(BH_4)_2$ has been initially investigated, but no significant changes were observed after the addition of monoglyme. On the other hand, interestingly, upon the addition of 10 mM $Mg(BH_4)_2$, a significant change is observed (see Fig. S1b), where Mg deposits at around −0.5 *V vs.* Mg/Mg^{2+} and dissolves at around 0.2 V *vs.* Mg/Mg^{2+}. Co-solvents such as 1,2-difluorobenzene (dFBn), tetrafluoroethyl tetrafluoropropyl ether (TTE), and diethylene glycol diethyl ether (DEGDE) have been explored in combination with the ionic liquid in Li-ion batteries to investigate their impact on promoting Li^+ ion transport [38–40]. 1,2-difluorobenzene was employed to improve Li-ion transport and enhance the electrode/electrolyte interface through the formation of LiF that lead to a stable interphase [38]. On the other hand, TTE was utilized not only to reduce charge transfer impedance but also to stabilize the solid electrolyte interphase and to enhance ion conduction within the electrolyte [39]. Further, DEGDE showed good cyclic stability [38,40,41]. Therefore, in addition to the four known glymes (mono-, di-, tri-, and tetra-glymes), in our study we also selected dFBn, TTE, and DEGDE as co-solvents and analyzed their impact on Mg^{2+} ion transport. The previously mentioned co-solvents were dried with a 4 Å molecular sieve for 1 week and were afterwards added to the pre-dried MPPip-TFSI ionic liquid in a 1:1 volume ratio. Subsequently, MPPip-TFSI +0.1 M $Mg(TFSI)_2$ + 0.01 M $Mg(BH_4)_2$ was dissolved in the resulting mixture by stirring at a temperature of 40 °C for 2 h. The electrochemical performance of the resulting electrolytes has been investigated in a three-electrode setup using Pt as a working electrode (WE). As shown in Fig. 2, the effect of each co-solvent on the electrochemical performance of the IL-based electrolytes seems to be different. For instance, adding TTE as co-solvent did not alter the electrochemical performance significantly, while adding dFBn or DEGDE showed an effect on the Mg deposition feasibility as well as the Mg deposition/dissolution reversibility. In case of dFBn, magnesium deposition is observed at approximately −1.0 *V vs.* Mg/Mg^{2+}, with no dissolution detected up to 1.0 V. Thus, dFBn appears to facilitate magnesium deposition from this ionic liquid, although the dissolution process remains uncertain. Conversely, with DEGDE magnesium deposition occurs around −1.5 V *vs.* Mg/Mg^{2+}, and magnesium dissolution takes place near 0.0 V *vs.* Mg/Mg^{2+}, while during the backward scan, an ambiguous oxidation process appears at approximately −0.5 V *vs.* Mg/Mg^{2+}. Notably, DEGDE forms moderately stable complexes with magnesium ions, enhancing the reversibility of magnesium deposition and dissolution processes but still to a lesser extent compared to what has been obtained with glyme co-solvents [30]. Therefore, further investigations are needed to gain more insights into the effects of both DEGDE and dFBn, which are not within the scope of this study but will be explored in our future research endeavours.

Meanwhile, the addition of glymes to the IL resulted in a better electrochemical performance compared to the other co-solvents. Mg deposition occurs at around −0.5 *V vs.* Mg/Mg^{2+} and dissolution at around 0.1 V *vs.* Mg/Mg^{2+}. The main cause for the significant improvement is the high tendency for glymes to form Mg complexes which are not too stable compared to the co-solvents facilitating the Mg deposition/dissolution processes. Those complexes are crucial factors for improving Mg deposition/dissolution [30].

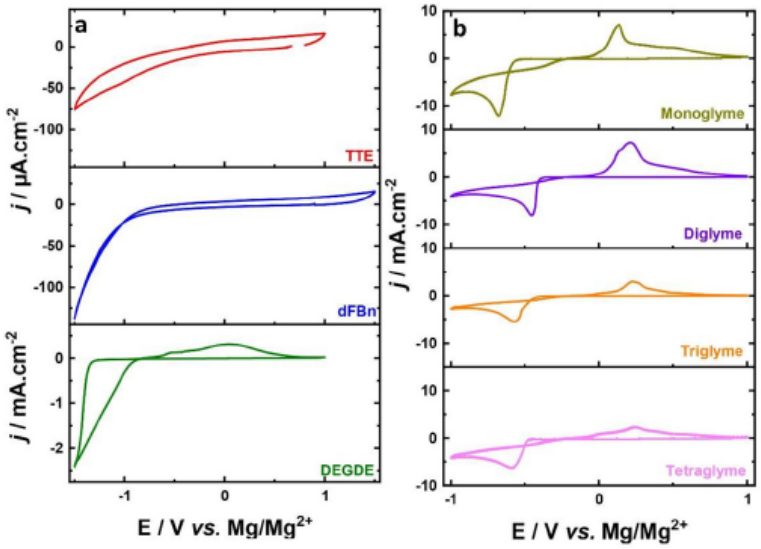

Fig. 2. Cyclic voltammograms of Mg deposition on a Pt WE from 0.1 M $Mg(TFSI)_2$ + 0.01 M $Mg(BH_4)_2$ in MPPip-TFSI IL: different co-solvents (1:1); a) tetrafluoroethyl tetrafluoropropyl ether (TTE), difluorobenzene (dFBn), and diethylene glycol diethyl ether (DEGDE), and b) monoglyme, diglyme, triglyme, and tetraglyme at a scan rate of 50 $mV \cdot s^{-1}$. *vs.* Mg/Mg^{2+}.

In the next step, a systematic study was carried out to investigate the optimum ratio of MPPip-TFSI to the different four glymes (3:1, 2:1, 1:1, 1:2, and 1:3). Fig. S2 illustrates the cyclic voltammograms for the comparison between the five ratios of MPPip-TFSI with the four glymes. From the cyclic voltammograms, four different properties affecting the electrochemical performance (such as Mg deposition overpotential, Coloumbic efficiency, anodic current peak, and cathodic current peak) were extracted and compared in histograms, as depicted in Fig. 3. Fig. 3a shows that the Mg deposition overpotential decreases with increasing the ratio of the glymes until it reaches the optimum overpotential at around −0.35 to −0.4 *V vs.* Mg/Mg^{2+}. While all different glymes have a similar impact on the Coulombic efficiency, the ratios of 1:2 and 1:3 show the highest efficiency (around 60 %), especially for G1 and G2 as shown in Fig. 3b.

Alternatively, the length of the glyme has been demonstrated to have a notable impact on both cathodic and anodic currents (see Fig. 3c and d), with the most pronounced effect at a ratio of 1:3 IL:G. This suggests that the 1:3 ratio displays a kinetic preference over 1:2. Remarkably, the length of the glyme appears to influence the Mg deposition/dissolution kinetics, where longer glyme lengths lead to slower transport kinetics in the Mg deposition and stripping.

Additionally, the 1:3 ratio exhibited the highest anodic and cathodic current peaks, while G1 and G2 showed competitive results. Therefore, concentrating on this 1:3 ratio, in the next step the different cosolvents were compared. Thus, cyclic stabilities for the 1:3 systems that contain G1 or G2 were studied. A narrower electrochemical window from −0.5 to 1.0 *V vs.* Mg/Mg^{2+} was selected to avoid any further process that may take place at potentials above −0.5 *vs.* Mg/Mg^{2+} as suggested by the subsequent increase in cathodic currents (see Fig. 2). The cyclic voltammograms for both glyme-containing systems were recorded for 50 cycles with a Pt WE at a scan rate of 50 mV/s *vs.* Mg/Mg^{2+} (see Fig. 4).

In the case of monoglyme, the cathodic currents for Mg deposition as well as the anodic current for the dissolution sharply decrease upon cycling till the cell reaches total passivation and blocking of the Mg electrode after only 20 cycles. On the other hand, the cell operated with diglyme as co-solvent showed better cyclic stability compared to monoglyme for up to 50 cycles. Following, an increase in the ratio of G1 and G2 to 4:1 was also investigated in order to check for possible enhancements. As observed in Fig. S4, the current peak for G2 is decreased compared to the 3:1 ratio, confirming again the 3:1 ratio to be optimal.

Among the other glymes, G2 stands out due to the formation of structures with different motifs compared to G1, G3, and G4. This distinction is evidently influenced by the number of oxygen atoms in the glyme chain that significantly affects the resulting Mg complexes. Two oxygen atoms (in G1) and four oxygen atoms (in G3) appear to be preferred for stabilizing solvated Mg complexes. The presence of additional oxygen atoms in G4 provides further stabilization of the structural motif initiated by G3. In contrast, G2 has three oxygen atoms, which are insufficient for full solvation in the same manner. Moreover, the ligand deficit in G2 is too small to benefit from additional G2 molecules, thereby prompting the system to create distinct structures [42]. This may elucidate the distinct electrochemical behavior of G2-based electrolytes, characterized by higher kinetics and enhanced stability. The preference of diglyme over the other glymes has also been reported in

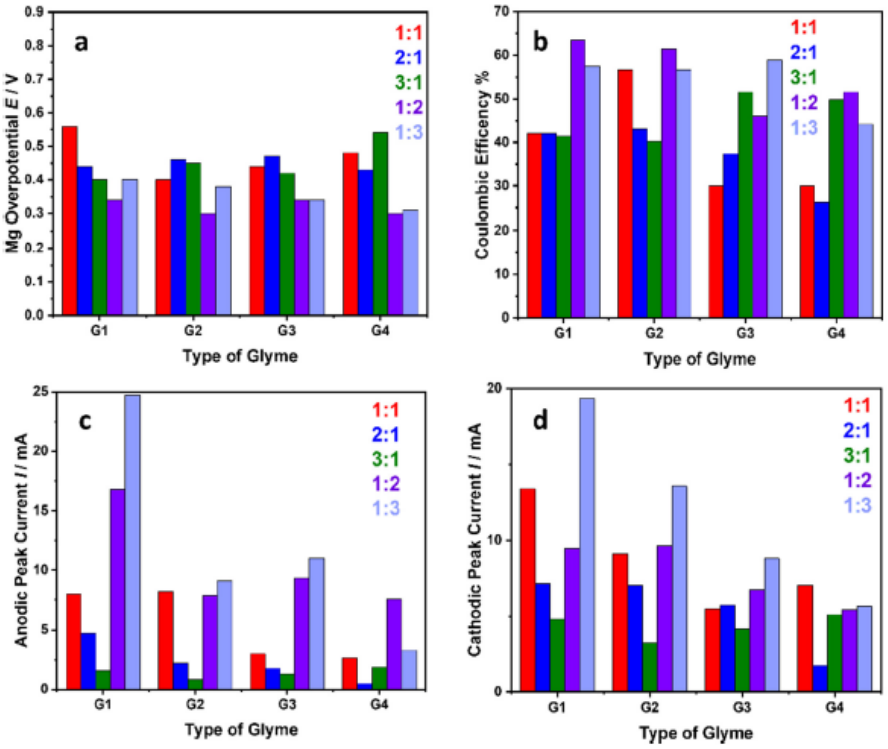

Fig. 3. Histograms, comparing the four glymes (monoglyme, diglyme, triglyme, and tetraglyme) as an additive with different ratios to MPPip-TFSI: a) overpotential of Mg deposition, b) Coulombic efficiency (in %), c) anodic current peak, and d) cathodic current peak.

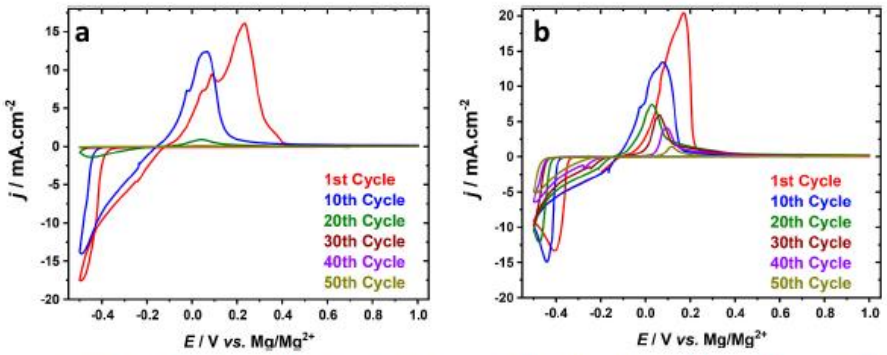

Fig. 4. Cyclic voltammograms showing the cyclic stability of Mg deposition from; a) 0.1 M $Mg(TFSI)_2$ + 0.01 M $Mg(BH_4)_2$ in MPPip-TFSI:G1 (1:3), b) 0.1 M Mg $(TFSI)_2$ + 0.01 M $Mg(BH_4)_2$ in MPPip-TFSI:G2 (1:3) with a Pt counter electrode at a scan rate of 50 mV/s *vs.* Mg/Mg^{2+}.

the literature for $Mg[Al(HFIP)_4]_2$ salts and has been attributed to the enhanced Mg^{2+} diffusivity and notable interfacial kinetics [43,44].

After the optimization of the electrolyte for Mg deposition/dissolution, scanning electron microscopy (SEM) and X-ray diffraction (XRD) were used to confirm Mg deposition and dissolution on a Pt disk. As shown in Fig. 5a, the bare Pt disk exhibits a uniform microstructure and its EDS spectra confirm its purity. After magnesium deposition at a constant current of −0.05 mA for 6 h, island-shaped magnesium deposits (29.1 wt%) were observed and confirmed by EDS analysis and elemental mapping as shown in Fig. 5b and d. Subsequently, a current of +0.05 mA was applied for another 6 h to dissolve the deposited magnesium, resulting in nearly complete dissolution where EDS shows only a 0.5 wt % residue of magnesium remaining on the surface, likely originating from the residual electrolyte (Fig. 5c). Additionally, XRD characterization was carried out for the bare Pt disk, after Mg deposition as well as after dissolution, see Fig. 5e. From the analysis of the XRD pattern, metallic Mg was deposited, which was assigned to the diffraction peaks at around 33° and 34.5° corresponding to Mg(100) and Mg(002), respectively. Furthermore, EQCM measurements were conducted and a mass of 15.16 g/mol was achieved, which is comparable to the expected mass change during Mg deposition as shown in Fig. S5.

Successively, galvanostatic cycling of a symmetric Mg cell was performed using the optimized electrolyte at 0.1 mA for 120 h, as illustrated in Fig. 6a. Initially, Mg deposition/dissolution took place at around

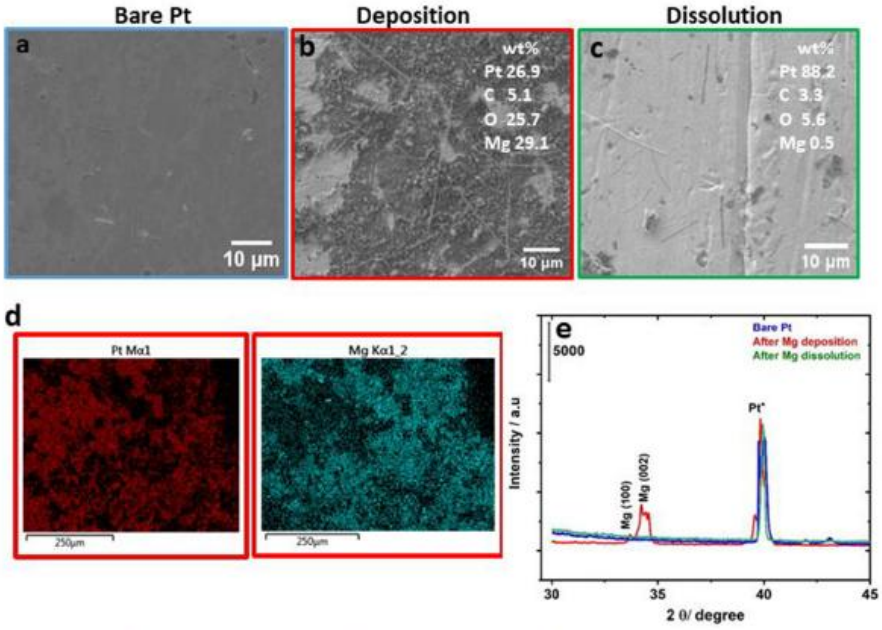

Fig. 5. SEM micrographs and EDS spectra of a) bare Pt sheet at OCV, b) after Mg deposition for 6 h at −0.05 mA, c) after Mg dissolution for 6 h at 0.05 mA from MPPip-TFSI + G2 (1:3) +0.1 M $Mg(TFSI)_2$ + 0.01 M $Mg(BH_4)_2$, d) the corresponding elemental mapping, and e) the corresponding XRD patterns for Mg deposition, dissolution and bare Pt.

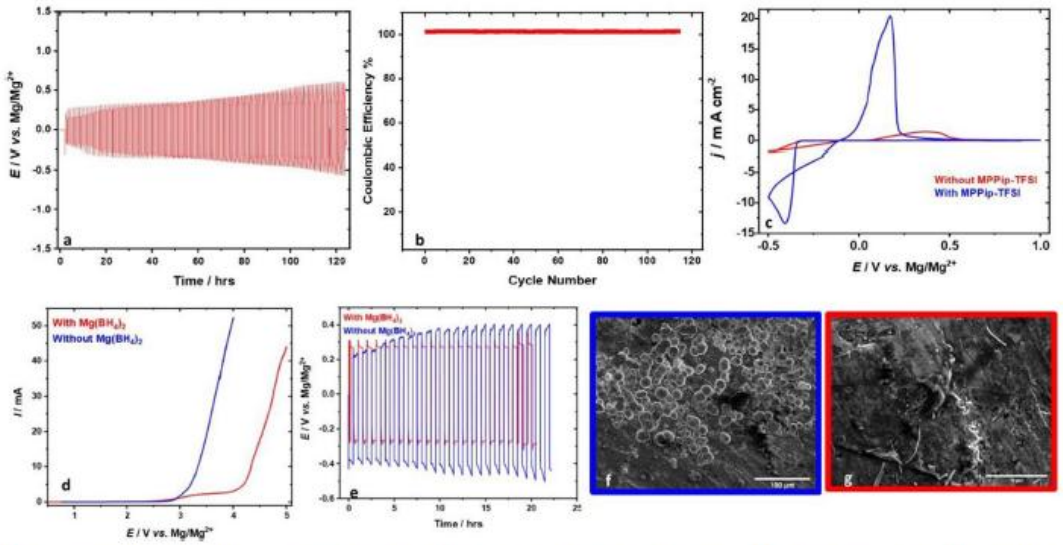

Fig. 6. a) Galvanostatic cycling of Mg symmetric cell at 0.1 mA with the optimized electrolyte for 120 cycles, b) Coulombic efficiency *vs.* number of cycles, c) CV of Mg deposition on Pt with the optimized electrolyte and in the absence of MPPip-TFSI with scan rate 50 mVs^{-1} *vs.* Mg/Mg^{2+}, d) Linear sweep voltammetry of optimized electrolyte in the presence and absence of the $Mg(BH_4)_2$, e) Influence of the presence of 0.01 M $Mg(BH_4)_2$ on the galvanostatic cycling of Mg symmetric cell at 0.05 mA, f-g) SEM micrograph for Mg deposition in the absence and presence of $Mg(BH_4)_2$ respectively.

±0.15 mV *vs.* Mg/Mg^{2+}, indicating a high stability of the optimized electrolyte in presence of the Mg anode. Additionally, the coulombic efficiency of the galvanostatic cycling was around 100 % as observed in Fig. 6b. On the other hand, the dynamic viscosity of the IL was measured after the addition of G2 in a 1:3 ratio (1 IL: 3 G2). It is observed that the dynamic viscosity of the MPPip-TFSI IL has sharply dropped from 124 to 3.22 mPa•s after the addition of G2. Lowering the viscosity of the IL-based electrolytes enhances the deposition overpotential as well as the reversibility of Mg deposition and dissolution.

From an application point of view, it was essential to investigate the role of each electrolyte component in detail, especially the highly-expensive ionic liquid. Therefore, the influence of the role of MPPip-TFSI and $Mg(BH_4)_2$ on the electrochemical performance of the suggested electrolyte was further investigated.

As shown in Fig. 6c, the presence of MPPip-TFSI results in higher kinetics, indicating the increase in current density by 10 orders of magnitude compared to the pure G2-based electrolyte. This is attributed to the inherent characteristics of the IL, such as higher ionic conductivities and low volatility compared to pure glymes.

The EIS spectra of the optimized electrolyte and in the absence of MPPip-TFSI is resembled in Fig. S6a. The solution resistance as well as the charge transfer resistance of the optimized electrolyte are very low compared to the pure diglyme was determined from fitting the EIS results using equivaled circuit shown in Fig. S6b. The results of the fitting process are shown in Table S1. The ionic conductivity values were then calculated from the solution resistances using eq. (2):

$$\sigma = \frac{L}{R.A} \tag{2}$$

where σ is the ionic conductivity, L is the distance between the electrodes (the thickness of the soaked separator), R is the solution resistance, and A is the electrode area. The calculated ionic conductivity in the presence of MPPip-TFSI is 8.53 mS cm^{-1} compared to 0.61 mS cm^{-1} in pure diglyme.

Afterwards, the role of $Mg(BH_4)_2$ was investigated in detail. Since it was previously reported that $Mg(BH_4)_2$ reduces the anodic stability [45], it was essential to study its effect on the anodic stability of the optimized electrolyte. Therefore, the anodic stability of the optimized electrolyte, with and without $Mg(BH_4)_2$, was investigated using linear sweep voltammetry (*LSV*). As shown in Fig. 6d, the optimized electrolyte exhibited anodic stability up to 4.2 V, compared to 3.0 V in its absence. This improvement can be attributed to changes in the solvation structure (complexation) in the presence of the IL-glyme mixture, compared to the pure glyme.

From the galvanostatic cycling shown in Fig. 6e, the impact of BH_4^- anions become evident, reducing the overpotential of Mg deposition by 68.42 % upon addition of 10 mM. Moreover, the absence of $Mg(BH_4)_2$ altered the morphology of the deposited magnesium, as illustrated in Fig. 6e. The deposited magnesium has a spherical shape in the absence of $Mg(BH_4)_2$, compared to smooth and uniform deposit when $Mg(BH_4)_2$ is added (see Fig. 6f), suggesting a change in the nucleation and growth mechanisms of the deposited Mg.

As a proof of principle we demonstrated the performance of the optimized electrolyte in a Mg full cell, where WS_2/polyaniline (WS_2/PANI) composites were used as cathode. The integration of polyaniline (PANI) led to an enhanced ionic conductivity and suppresses restacking and agglomeration [46]. The WS_2/PANI composites were prepared as discussed in the experimental section and characterized by SEM and powder XRD. Figs. S7a and S7b show a flake-like morphology of the WS_2, while Fig. 7c represents the morphology of PANI which resembles interconnected nanofibers. The SEM picture of the WS_2/PANI composite is shown in Fig. S7d, confirming the formation of the exfoliated WS_2/PANI composite. Fig. S8 shows the XRD patterns of the WS_2 and WS_2/PANI samples, confirming the purity of WS_2 (ICSD_CollCode56014). The existence of the majority of WS_2 reflections in the WS_2/PANI pattern suggests that the composite was successfully formed. A decrease in peak positions was observed after WS_2 exfoliation in DMF and following PANi insertion, confirming an increase in the interlayer distance. The TGA analysis shown in Fig. S9 indicates that the compositions of WS_2 and

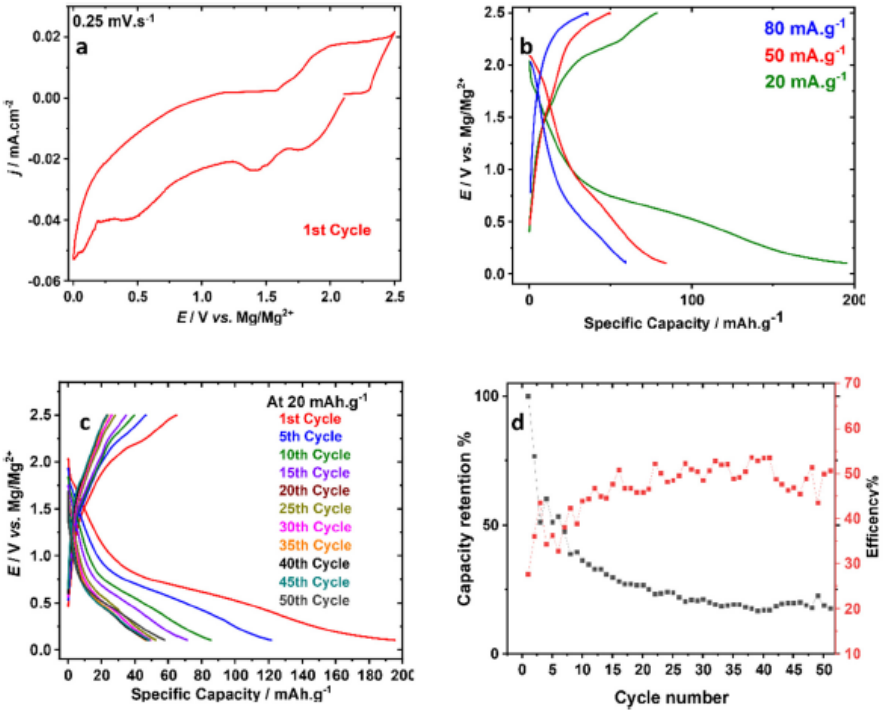

Fig. 7. a) CV of WS_2/PANI-40 | 0.1 M $Mg(TFSI)_2$+ 0.01 M $Mg(BH_4)_2$ in MPPip-TFSI IL: G2 (1:3) | Mg at scan rate 0.25 $mV{\bullet}s^{-1}$, b) Charge–discharge profile of WS_2/PANI-40 at different specific current, c) stability of the WS_2/PANI-40 electrode up to 50 cycles at 20 $mA{\bullet}g^{-1}$, d) Capacity retention and coulombic efficiency *vs.* number of cycles.

PANI are comparable, with 35 wt% and 46 wt% calculated for PANI and WS_2, respectively. The remaining weight is attributed to adsorbed moisture and low molecular weight PANI fragments.

The prepared WS_2/PANI composite was dried at 40 °C (labeled as WS_2/PANI-40) overnight before storing in an Ar-filled glovebox for the electrochemical measurements. Asymmetric WS_2/PANI | optimized electrolyte | Mg cells were assembled and left to rest at OCV (1.9 V) overnight. To study the intercalation and deintercalation of Mg^{2+} ions, cyclic voltammograms were recorded (at a scan rate of 0.25 $mV{\bullet}s^{-1}$), as shown in Fig. 7a. A cathodic peak at around 0.5 V *vs.* Mg/Mg^{2+} and an anodic peak at around 2.0 V *vs.* Mg/Mg^{2+} were observed, corresponding to intercalation and deintercalation, respectively [20]. Two more cathodic peaks at 1.5 and 2.0 V *vs.* Mg/Mg^{2+} were observed which might be related to the reduction of PANI [47].

The electrochemical reaction steps during the insertion and removal of Mg^{2+} within WS_2/PANI are summarized in eqs. 3–5 [18,20,48].

$$\text{Anode}: 4\,Mg \leftrightarrow 4\,Mg^{2+} + 8e^- \quad (3)$$

$$\text{Cathode}: 6\,WS_2 + 4\,Mg^{2+} + 8e^- \leftrightarrow Mg_4W_6S_{12} \quad (4)$$

$$\text{Overall}: 6\,WS_2 + 4\,Mg \leftrightarrow Mg_4W_6S_{12} \quad (5)$$

Subsequently, the performance of WS_2/PANI-40 composites in the optimized electrolyte at different specific currents was investigated. The first cycle capacities obtained at 80, 50, and 20 $mA{\bullet}g^{-1}$ are 84, 60, 197 $mAh{\bullet}g^{-1}$, respectively, as observed in Fig. 7b. Thus, the achieved capacity at 20 $mA{\bullet}g^{-1}$ is 2.5 times higher than what was reported with WS_2/graphene in a MAAC electrolyte [20]. Fig. 7c and d, display the cyclic stability of WS_2/PANI-40 at 20 $mA{\bullet}g^{-1}$ for 50 cycles and the capacity retention as well as the coulombic efficiency, respectively. After 50 cycles, around 25 % of the initial capacity is retained. However, the coulombic efficiency is enhanced upon cycling until it reaches 50 % at the 50th cycle. One possible reason for the low capacity retention obtained at 20 $mA{\bullet}g^{-1}$ could be attributed to the partial degradation of PANI upon cycling. Previously reported work showed that the electroactivity of PANI is influenced by the heat treatments, specifically above 70 °C [49]. To demonstrate this, WS_2/PANi was investigated after drying at 70 °C before the measurements (labeled as WS_2/PANi-70). This process induced partial degradation and cross-linking prior to our measurements. After drying the WS_2/PANI composites at 70 °C, the charge/discharge profile was investigated successively at different specific currents of 80, 50, 30, 20, 10, 8 and 5 $mA{\cdot}g^{-1}$ in the optimized electrolyte (see Fig. 8a and b). The achieved capacities in the first cycle are 2, 48, 60, 61, 600, 590 and 430 $mAh{\cdot}g^{-1}$, respectively. The increase in capacity at a relatively low specific current (10 $mA{\cdot}g^{-1}$) indicates a change in the charging/discharging mechanism. Further, Fig. 8c and d show the cyclic stability at 20 $mA{\cdot}g^{-1}$ and the capacity retention after 50 cycles, where 85 % of the initial capacity is retained. Surprisingly, at 20 $mA{\cdot}g^{-1}$ the initial capacity of WS_2/PANi-70 is nearly the same as the specific capacity of WS_2/PANi-40 at 25th cycle, indicating that the substantial loss in capacity is mainly attributed to the PANI partial degradation upon cycling. Surprisingly, a specific capacity of 600 $mAh{\cdot}g^{-1}$ at 10 $mA{\cdot}g^{-1}$ was achieved for the electrode dried at 70 °C. However, when the specific current is reduced to 5 $mA{\cdot}g^{-1}$, the capacity begins to decrease instead of increasing. These results suggest that this capacity value is not solely due to Mg intercalation; it also involves

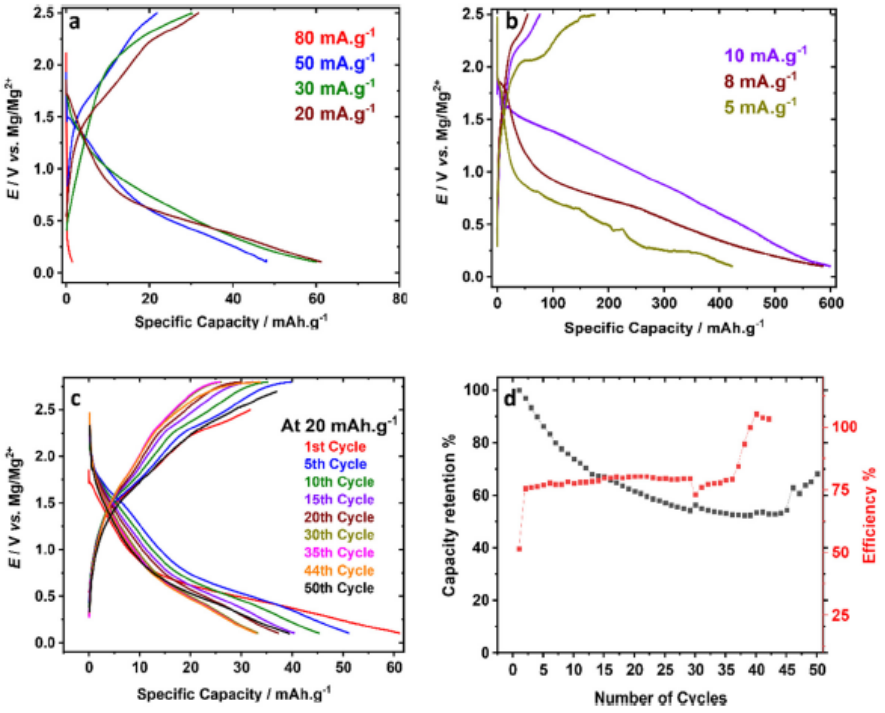

Fig. 8. a) and b) Charge–discharge profile of WS_2/ PANI-70 in 0.1 M $Mg(TFSI)_2$ + 0.01 M $Mg(BH_4)_2$ in MPPip-TFSI IL: G2 (1:3) electrolyte at different specific current (the measurements shown in b have been conducted successively), c) stability of the WS_2/PANI-70 electrode up to 50 cycles at 20 $mA{\bullet}g^{-1}$, d) capacity retention and efficiency *vs.* number of cycles.

contributions from side reactions, such as partial polymer degradation during cycling and cross-linking. Furthermore, capacity retention decreases with increasing specific currents. This is demonstrated by < 10 % capacity retention after 50 cycles at 80 $mA{\cdot}g^{-1}$, as shown in Fig. S10. Therefore, it can be concluded that high specific currents may accelerate polymer degradation."

To further understand the intercalation and deintercalation of Mg^{2+} in the WS_2/PANI cathode and the reasons behind the capacity fading, Raman spectroscopy was performed. The Raman spectra of carbon black, WS_2/PANI-40, and WS_2/PANI-70 were examined within the frequency range of 200 to 2000 cm^{-1}, as shown in Fig. 9a. For comparison, the spectrum of the reference carbon black electrode was compared with the synthesized WS_2/PANI electrode under distinct heat treatment conditions. The reference carbon black electrode has a higher crystalline carbonaceous component, confirmed by the relative intensity bands at 1593 and 1361 cm^{-1}, corresponding to the G and D peaks, respectively [50].

The electrode incorporating WS_2/PANI has a comparable spectrum, showing prominent G and D band peaks at 1599 and 1340 cm^{-1} for the WS_2/PANI-70 electrode, and at 1606 and 1346 cm^{-1} for the WS_2/PANI-40 electrode. The apparent change in peak position might be attributed to the impact of the heat-treatment on WS_2/PANI at varying temperatures. The Raman spectra of WS_2/PANI-70 and WS_2/PANI-40 showed strong bands at around 1495 cm^{-1} and 1522 cm^{-1}, which are attributed to the C═N stretching vibrations in quinoid diimine units [51]. The red shift observed in the bands of the WS_2/PANI-70 electrode is most likely due to the cross-linking and phenazine-like structures induced by heating [51,52]. The increase in the band intensity at 1495 cm^{-1} for WS_2/PANI-70 indicates an increase in the concentration of quinoid units [51,53,54]. Nevertheless, the fluctuation in these peak intensities corresponds to potential structural alterations when the temperature rises from 40 to 70 °C (refer to Table S2 and S3) [51].

To understand the reasons behind the significant capacity fading observed with the WS_2/PANI-40 electrode, Raman spectra were also acquired during the first cycling process (Fig. 9b) at fully charged and discharged states. A small shift towards higher wavenumber was observed in almost all peaks after the discharge process due to structural alterations caused by the insertion of Mg cations. However, a shift to a higher wavenumber is observed for the C—H bending band at 1168 cm^{-1}, shifting to 1170–1173 cm^{-1} after cycling compared to the pristine electrode. This shift is associated with the transformation from quinoid to benzenoid units. An additional peak is observed at 1405 cm^{-1} after cycling and becomes pronounced after the charging process, indicating the formation of phenazine-like structures and the partial degradation as well as deprotonation of emeraldine salt [55]. The appearance of a strong band at 580 cm^{-1} after 50 successive galvanostatic cycles indicates the cross-linking of the polymer [51,54,55]. Moreover, it was difficult to distinguish the characteristic bands of WS_2 (at 350 and 420 cm^{-1}) from those of PANI at 414–418 cm^{-1}, making it challenging to comment on them.

On the other hand, SEM and XRD shown in Fig. 9e–f did not show any significant changes in the morphology or peak positions of WS_2/PANI-40 and WS_2/PANI-70 electrodes before and after cycling. These findings indicate that WS_2 preserves its structure during cycling, confirming the increase in interlayer spacing due to PANI prior to the measurements.

All these results indicate that the capacity fading observed during

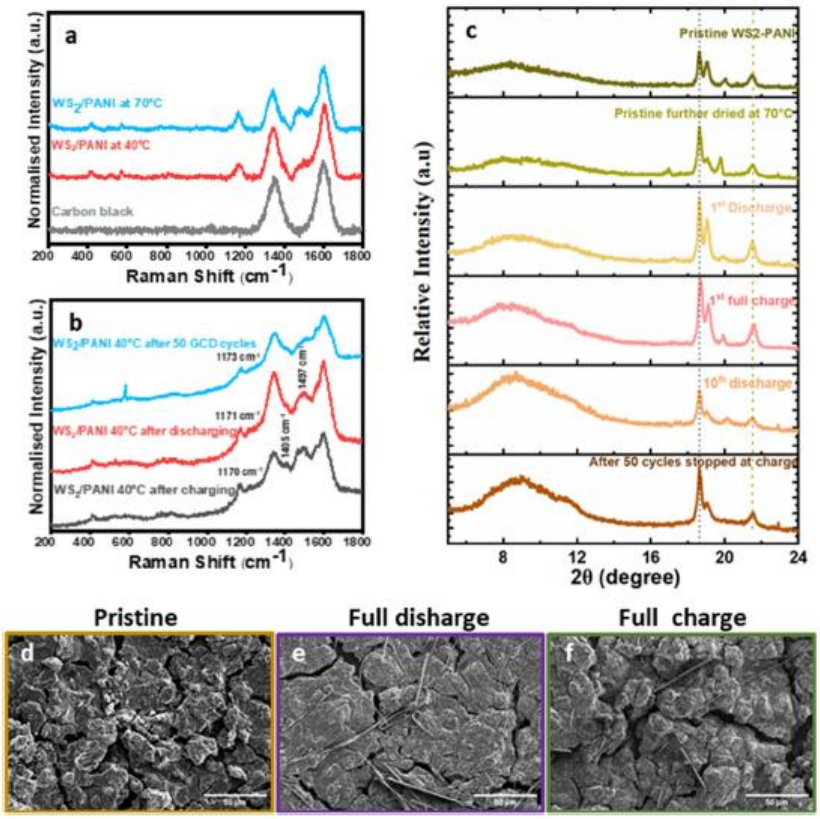

Fig. 9. a) Raman spectra of carbon black, WS_2/PANI-70 and WS_2/PANI-40 electrode, b) Raman spectra of WS_2/PAN-40 electrode at charged, at discharged state and after 50 cycles, c) XRD pattern for the pristine WS_2/PANI without any drying, pristine heat treated at 70 °C, after a full discharge, after full charge, after the 10th discharge and after 50 cycles stopped after full charge all dried at 40 °C, d)-f) the corresponding SEM micrographs, respectively.

cycling of WS_2/PANI-40 is most likely attributed to the cross-linking of PANI and partial degradation during cycling. Therefore, we can conclude that the addition of PANI to the layered structure of WS_2 might expand the interlayer spacing (see Fig. S8), thereby could promote Mg diffusion during intercalation and deintercalation without altering the crystalline structure of WS_2. However, due to PANI cross-linking during cycling, alternative interlayer spacers will be explored in our future studies.

4. Conclusion

In conclusion, our electrochemical characterization using EQCM and *post-mortem* analyses highlighted the complexities and challenges of Mg deposition from pure MPPip-TFSI, which is impeded by significant electrolyte decomposition and high overpotential requirements. To address these issues, we systematically developed an optimized electrolyte system incorporating Mg salt additives and a co-solvent strategy. Among various co-solvents, glyme-based co-solvents notably enhanced electrochemical Mg deposition and dissolution. Through a detailed investigation of different co-solvent ratios, we identified that a 1:3 ratio of MPPip-TFSI to G2 yielded the highest cathodic and anodic peak currents and the lowest Mg deposition overpotential. Further analysis revealed that the ionic liquid MPPip-TFSI improved electrolyte conductivity and electrochemical kinetics, while the co-solvent reduced electrolyte viscosity, thereby lowering deposition overpotential and enhancing the reversibility of Mg deposition and dissolution. Additionally, the inclusion of $Mg(BH_4)_2$ decreased the Mg deposition overpotential by 68.42 % and allowed the use of higher current densities. As a proof of concept, this optimized electrolyte was investigated in a Mg metal battery using WS_2/PANI as cathode material. Our findings demonstrated a substantial improvement in initial capacity, achieving 197 $mAh \bullet g^{-1}$ at 20 $mA \bullet g^{-1}$, which is 2.5 times higher than previously reported values with WS_2/graphene in a MAAC electrolyte. However, significant capacity fading of 75 % after 50 cycles at 20 $mA \bullet g^{-1}$ was observed, likely due to PANI cross-linking during heat treatment and subsequent cycling, in particular at higher specific currents.

CRediT authorship contribution statement

Omar W. Elkhafif: Writing – original draft, Visualization, Methodology, Investigation, Formal analysis, Data curation. Hagar K. Hassan: Writing – review & editing, Validation, Supervision, Methodology, Investigation, Data curation, Conceptualization. Motahira Hashmi: Writing – review & editing, Validation, Formal analysis. Nikhil Arya: Writing – review & editing, Visualization, Formal analysis. Montaha Anjass: Writing – review & editing, Validation, Investigation, Data

curation. Timo Jacob: Writing – review & editing, Validation, Supervision, Project administration, Funding acquisition.

Declaration of competing interest

The authors declare the following financial interests/personal relationships which may be considered as potential competing interests: Timo Jacob reports financial support was provided by Deutsche Forschungsgemeinschaft (DFG). Timo Jacob reports a relationship with Deutsche Forschungsgemeinschaft (DFG) that includes: funding grants. If there are other authors, they declare that they have no known competing financial interests or personal relationships that could have appeared to influence the work reported in this paper.

Acknowledgement

The authors gratefully acknowledge funding from the Deutsche Forschungsgemeinschaft (DFG) through the priority program SPP 2248 Polymer-based Batteries (Project ID 441209207) and through the individual project with ID 501805371.

Appendix A. Supplementary data

Supplementary data to this article can be found online at https://doi.org/10.1016/j.est.2024.114636.

Data availability

Data will be made available on request.

References

[1] R. Deivanayagam, B.J. Ingram, R. Shahbazian-Yassar, Energy Storage Materials 21 (2019) 136–153.
[2] R. Attias, M. Salama, B. Hirsch, Y. Goffer, D. Aurbach, Joule 3 (2019) 27–52.
[3] A.P. Abbott, K.J. McKenzie, Phys. Chem. Chem. Phys. 8 (2006) 4265.
[4] Y. Nuli, J. Yang, J. Wang, J. Xu, P. Wang, Electrochem. Solid-State Lett. 8 (2005) C166.
[5] P. Wang, Y. Nuli, J. Yang, Z. Feng, Surf. Coat. Technol. 201 (2006) 3783–3787.
[6] Y. Nuli, J. Yang, P. Wang, Appl. Surf. Sci. 252 (2006) 8086–8090.
[7] Q. Zhao, Y. Nuli, T. Naiman, J. Yang, J. Wang, Int. J. Electrochem. 2012 (2012) 1–8.
[8] G. Vardar, A.E.S. Sleightholme, J. Naruse, H. Hiramatsu, D.J. Siegel, C.W. Monroe, A.C.S. Appl, Mater. Interfaces 6 (2014) 18033–18039.
[9] Z. Ma, M. Forsyth, D.R. MacFarlane, M. Kar, Green Energy & Environment 4 (2019) 146–153.
[10] W. Ren, D. Wu, Y. Nuli, X. Zhang, J. Yang, J. Wang, A.C.S. Appl, Mater. Interfaces 13 (2021) 32957–32967.
[11] S. Su, Y. Nuli, N. Wang, D. Yusipu, J. Yang, J. Wang, J. Electrochem. Soc. 163 (2016) D682–D688.
[12] I. Weber, J. Ingenmey, J. Schnaidt, B. Kirchner, R.J. Behm, ChemElectroChem 8 (2021) 390–402.
[13] A. Ponrouch, M.R. Palacín, Phil. Trans. R. Soc. A 377 (2019) 20180297.
[14] Z. Rong, R. Malik, P. Canepa, G. Sai Gautam, M. Liu, A. Jain, K. Persson, G. Ceder, Chem. Mater. 27 (2015) 6016–6021.
[15] M.D. Levi, E. Lancry, H. Gizbar, Z. Lu, E. Levi, Y. Gofer, D. Aurbach, J. Electrochem. Soc. 151 (2004) A1044.
[16] X. Sun, P. Bonnick, L.F. Nazar, ACS Energy Lett. 1 (2016) 297–301.
[17] M. Mao, T. Gao, S. Hou, C. Wang, Chem. Soc. Rev. 47 (2018) 8804–8841.
[18] W. Guo, D.A.H. Hanaor, D. Kober, J. Wang, M.P. Bekheet, A. Gurlo, Batteries 8 (2022) 116.
[19] M. Alahmadi, E. El-Dek, A. Mostafa, A. Moselhy, S. AbdelMonem, H.S. Naeer, M. Refai, X.-Y. El-Desoky, E. Sheha Yang, Tungsten Disulfide Coupling with Halogen Free Electrolyte for Magnesium Battery Applications, SSRN, 2024.
[20] M. Latha, S. Biswas, J.V. Rani, Ionics 26 (2020) 3395–3404.
[21] P. Wang, C. Tang, H. Song, L. Zhang, Y. Lu, F. Huang, ACS Appl. Mater. Interfaces 16 (2024) 14082–14092.
[22] H. Sade, J.-P. Lellouche, Nanomaterials 8 (2018) 156.
[23] O.W. Elkhafif, H.K. Hassan, M.U. Ceblin, A. Farkas, T. Jacob, ChemSusChem 16 (2023) e202300421.
[24] G. Sauerbrey, Z. Phys. 155 (1959) 206–222.
[25] D. Aurbach, M. Moshkovich, Y. Cohen, A. Schechter, Langmuir 15 (1999) 2947–2960.
[26] P.C. Howlett, E.I. Izgorodina, M. Forsyth, D.R. MacFarlane, Z. Phys. Chem. 220 (2006) 1483–1498.
[27] T. Pajkossy, C. Müller, T. Jacob, Phys. Chem. Chem. Phys. 20 (2018) 21241–21250.
[28] M. Eckardt, D. Alwast, J. Schnaidt, R.J. Behm, ChemSusChem 13 (2020) 3919–3927.
[29] M. Kar, Z. Ma, L.M. Azofra, K. Chen, M. Forsyth, D.R. MacFarlane, Chem. Commun. 52 (2016) 4033–4036.
[30] Y. Shao, T. Liu, G. Li, M. Gu, Z. Nie, M. Engelhard, J. Xiao, D. Lv, C. Wang, J.-G. Zhang, J. Liu, Sci. Rep. 3 (2013) 3130.
[31] H. Wang, X. Feng, Y. Chen, Y.-S. Liu, K.S. Han, M. Zhou, M.H. Engelhard, V. Murugesan, R.S. Assary, T.L. Liu, W. Henderson, Z. Nie, M. Gu, J. Xiao, C. Wang, K. Persson, D. Mei, J.-G. Zhang, K.T. Mueller, J. Guo, K. Zavadil, Y. Shao, J. Liu, ACS Energy Lett. 5 (2020) 200–206.
[32] N.N. Rajput, X. Qu, N. Sa, A.K. Burrell, K.A. Persson, J. Am. Chem. Soc. 137 (2015) 3411–3420.
[33] J. Drews, P. Jankowski, J. Häcker, Z. Li, T. Danner, J.M. García Lastra, T. Vegge, N. Wagner, K.A. Friedrich, Z. Zhao-Karger, M. Fichtner, A. Latz, ChemSusChem 14 (2021) 4820–4835.
[34] G.T. Cheek, W.E. O'Grady, S.Z. El Abedin, E.M. Moustafa, F. Endres, J. Electrochem. Soc. 155 (2008) D91.
[35] A. Kitada, Y. Kang, Y. Uchimoto, K. Murase, J. Electrochem. Soc. 161 (2014) D102–D106.
[36] T. Kakibe, J. Hishii, N. Yoshimoto, M. Egashira, M. Morita, J. Power Sources 203 (2012) 195–200.
[37] Y. Bi, S. He, C. Fan, J. Luo, B. Yuan, T.L. Liu, J. Mater. Chem. A 8 (2020) 12301–12305.
[38] X. Liu, A. Mariani, T. Diemant, M.E.D. Pietro, X. Dong, M. Kuenzel, A. Mele, S. Passerini, Adv. Energy Mater. 12 (2022) 2200862.
[39] H. Lu, Z. Chen, Y. Yuan, H. Du, J. Wang, X. Liu, Z. Hou, K. Zhang, J. Fang, Y. Qu, J. Electrochem. Soc. 166 (2019) A2453–A2458.
[40] S.-M. Han, J.-H. Kim, D.-W. Kim, J. Electrochem. Soc. 162 (2015) A3103–A3109.
[41] H. Lu, Z. Chen, H. Du, K. Zhang, J. Wang, Z. Hou, J. Fang, Ionics 25 (2019) 2685–2691.
[42] P. Jankowski, J.M.G. Lastra, T. Vegge, Batteries & Supercaps 3 (2020) 1350–1359.
[43] T. Mandai, Y. Youn, Y. Tateyama, Mater. Adv. 2 (2021) 6283–6296.
[44] T. Pavčnik, M. Lozinšek, K. Pirnat, A. Vizintin, T. Mandai, D. Aurbach, R. Dominko, J. Bitenc, ACS Appl. Mater. Interfaces 14 (2022) 26766–26774.
[45] X. Li, Y. Yan, T.R. Jensen, Y. Filinchuk, I. Dovgaliuk, D. Chernyshov, L. He, Y. Li, H.-W. Li, J. Mater. Sci. Technol. 161 (2023) 170–179.
[46] M. Iqbal, N.G. Saykar, P.S. Alegaonkar, S.K. Mahapatra, New J. Chem. 46 (2022) 7043–7054.
[47] A. Watanabe, K. Mori, M. Mikuni, Y. Nakamura, M. Matsuda, Macromolecules 22 (1989) 3323–3327.
[48] B. Liu, T. Luo, G. Mu, X. Wang, D. Chen, G. Shen, ACS Nano 7 (2013) 8051–8058.
[49] R. Ansari, W.E. Price, G.G. Wallace, Polymer 37 (1996) 917–923.
[50] T. Jawhari, A. Roid, J. Casado, Carbon 33 (1995) 1561–1565.
[51] J.E. Pereira da Silva, D.L.A. de Faria, S.I. Córdoba de Torresi, M.L.A. Temperini, Macromolecules 33 (2000) 3077–3083.
[52] I. Šeděnková, M. Trchová, J. Stejskal, Polym. Degrad. Stab. 93 (2008) 2147–2157.
[53] G. Ćirić-Marjanović, M. Trchová, J. Stejskal, J. Raman Spectrosc. 39 (2008) 1375–1387.
[54] J. Zhang, G. Liu, G. Shi, J. Appl. Polym. Sci. 96 (2005) 732–739.
[55] G.M. do Nascimento, M.L.A. Temperini, J. Raman Spectrosc. 39 (2008) 772–778.

Supporting Information

Boosting Mg Deposition and Dissolution from Ionic liquids – The Role of Different Additives for Applications in Mg-ion Batteries

Omar W. Elkhafif[1], Hagar K. Hassan*[1,2,3], Motahira Hashmi[4], Nikhil Arya[4], Montaha Anjass[4,5], Timo Jacob*[1,2,3]

[1] Institute of Electrochemistry, Ulm University, Albert-Einstein-Allee 47, 89081 Ulm, Germany.
[2] Helmholtz-Institute-Ulm (HIU),Helmholtzstr. 11, 89081 Ulm, Germany.
[3] Karlsruhe Institute of Technology (KIT), P.O. Box 3640, 76021 Karlsruhe, Germany
[4] Institute of Inorganic Chemistry I, Ulm University, Albert-Einstein-Allee 11, 89081 Ulm, Germany
[5] Department of Chemistry, University of Sharjah, Sharjah-27272, Sharjah, United Arab Emirates

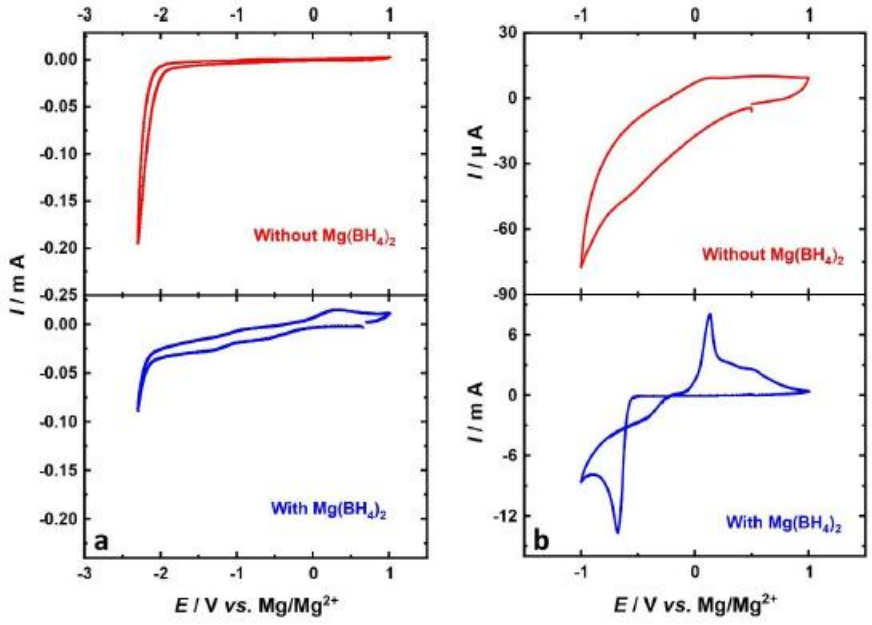

Figure S1: Cyclic voltammograms of Mg deposition from a) pure MPPip-TFSI +0.1 M $Mg[TFSI]_2$ in the presence and absence of 0.01 M $Mg(BH_4)_2$ and b) MPPip-TFSI + Monoglyme (1:1) +0.1 M $Mg[TFSI]_2$ in the presence and absence of 10 mM $Mg(BH_4)_2$ on a Pt with a scan rate 50 m·Vs^{-1}.

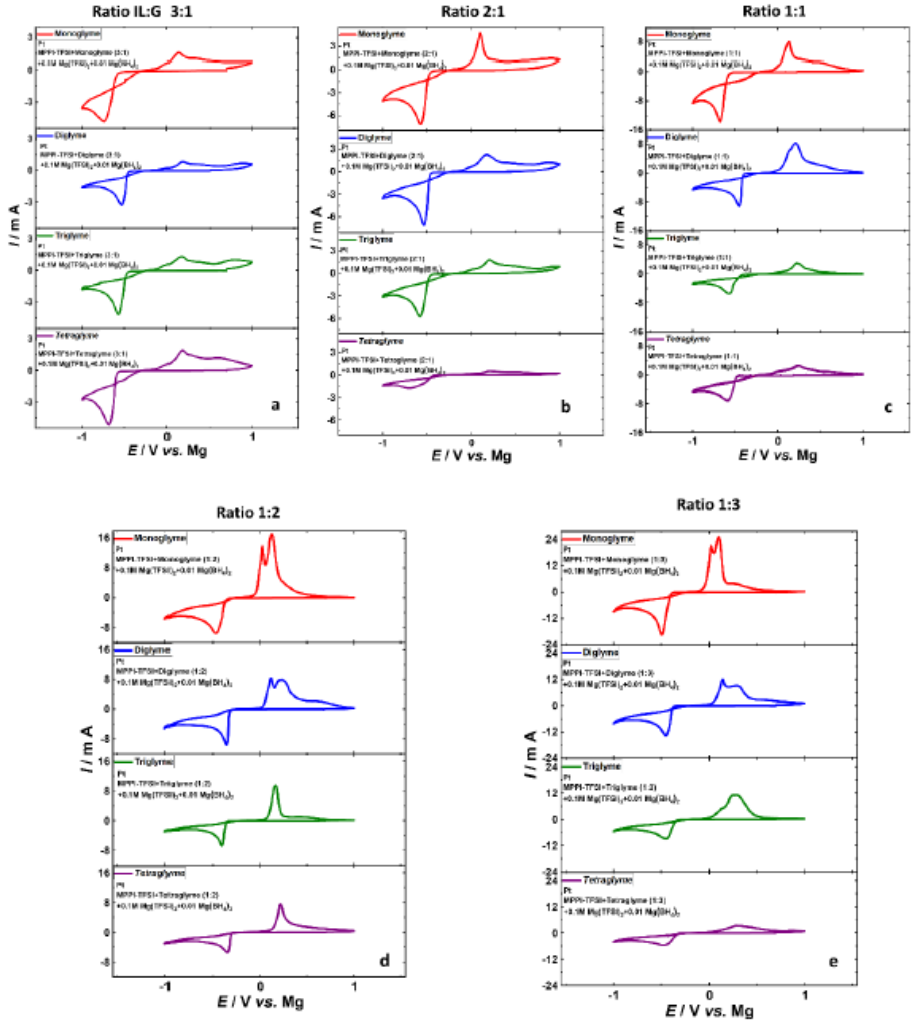

Figure S2: Cyclic voltammograms of Mg deposition of MPPip-TFSI and four glymes (monoglyme, diglyme, triglyme and tetraglyme)+0.1 M $Mg[TFSI]_2$+0.01 M $Mg(BH_4)_2$ with different ratios; a) 3:1, b) 2:1, c) 1:1, d) 1:2, e) 1:3 on a Pt with a scan rate 50 $mV \cdot s^{-1}$.

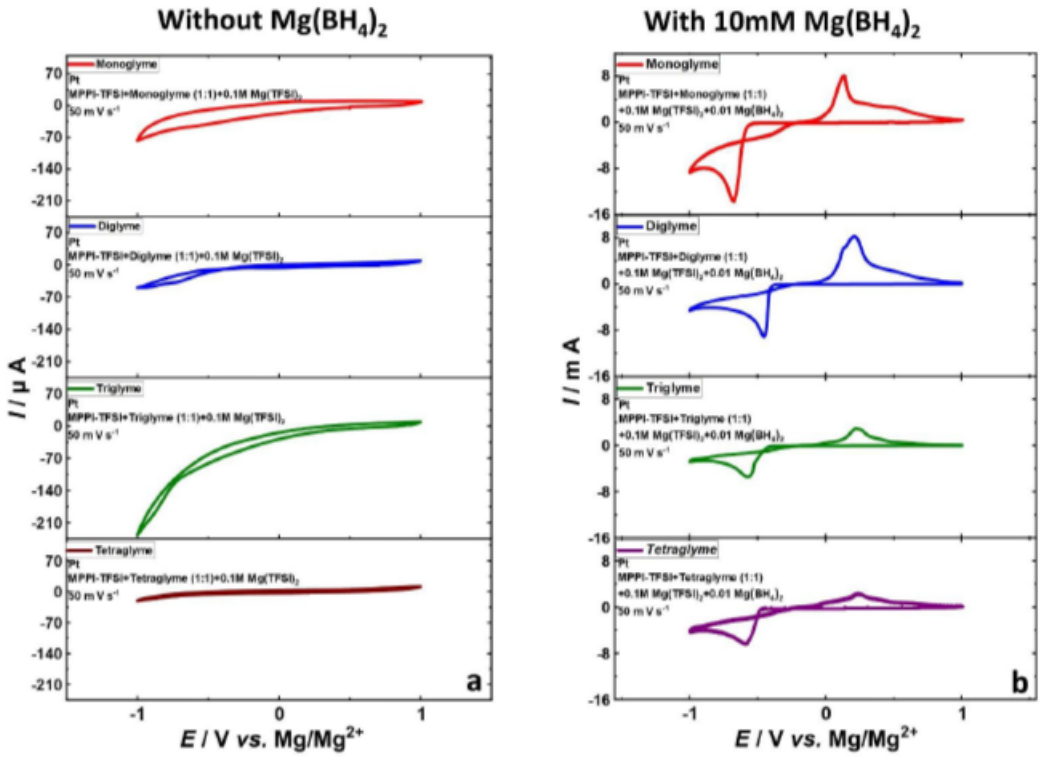

Figure S3: Cyclic voltammograms of Mg deposition with ratio (1:1) of MPPip-TFSI and four glymes (monoglyme, diglyme, triglyme and tetraglyme)+0.1 M $Mg[TFSI]_2$; a) without the addition of $Mg(BH_4)_2$, b) with the addition of 0.01 M $Mg(BH_4)_2$on a Pt with a scan rate 50 m·Vs^{-1}.

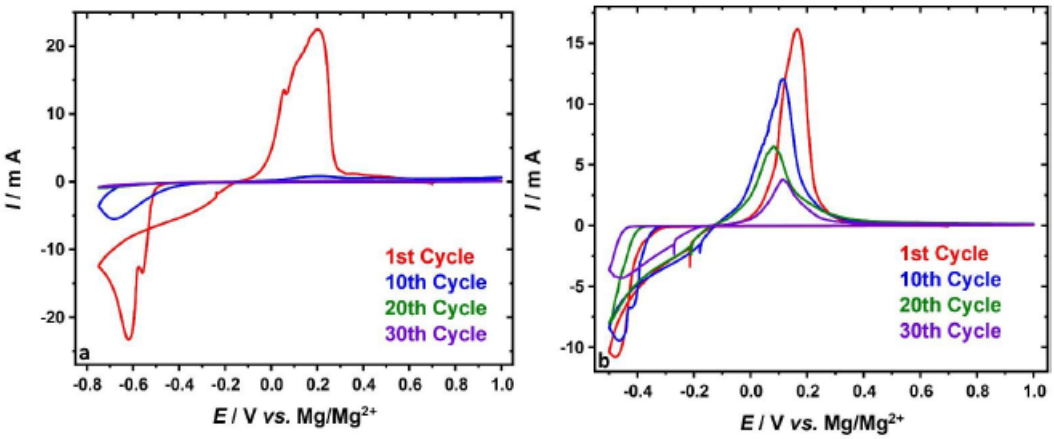

Figure S4: Cyclic voltammograms showing Mg deposition from; a) monoglyme (G1), b) diglyme (G2) +(4:1) MPPip-TFSI+0.1 M $Mg[TFSI]_2$ +0.01 M $Mg(BH_4)_2$ on a Pt at a scan rate 50 $mV{\cdot}s^{-1}$.

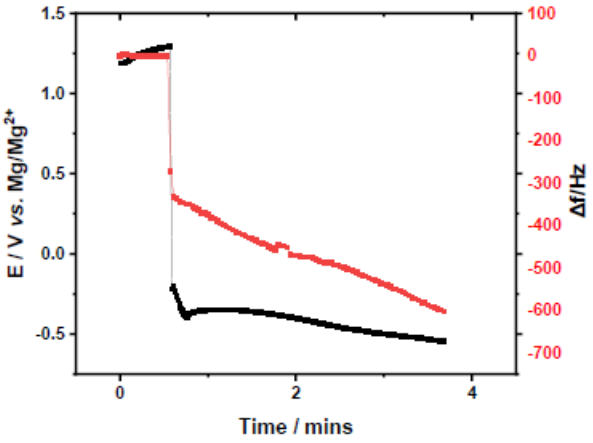

Figure S5: Chronopotentiometry measurement at -0.05 mA for 3 min. *vs.* frequency change.

$$\frac{M}{Z} = -\frac{FA\sqrt{\rho_q \mu_q}}{2f_*^2}\frac{df}{Idt} \qquad \textbf{equation 1}$$

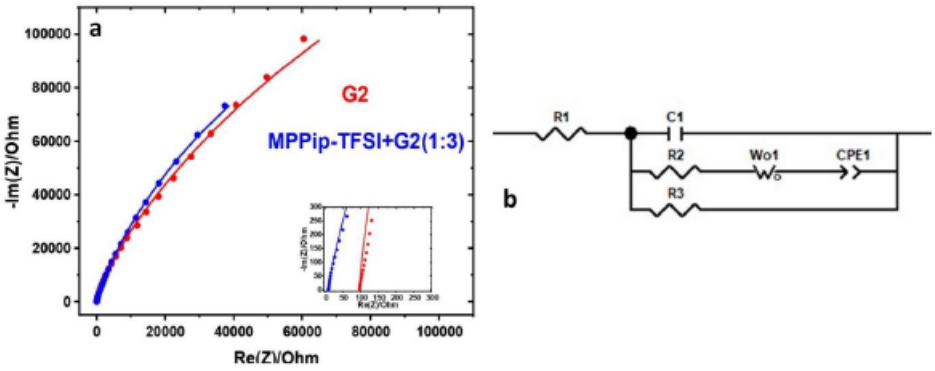

Figure S6: a) EIS spectra of the optimized electrolyte and in the absence of MPPip-TFSI (blue and red balls show the experimentally obtained data while the lines represent the fit results (inset: zoom-in of the high-frequency region), b) Equivalent circuit used to fit the results.

Table S1: The EIS fitting parameters of the optimized electrolyte in the presence and the absence of MPPip-TFSI.

Circuit Component	0.1 M $Mg[TFSI]_2$-0.01 M $Mg(BH_4)_2$ in MPPip-TFSI+G2 (1:3)	0.1 M $Mg[TFSI]_2$-0.01 M $Mg(BH_4)_2$ in G2
R_1 (Ω)	7.0268	96.880
C_1 (μF cm^{-2})	4.2785	3.9013
R_2 (Ω)	2.2370	233.85
W_o-R (KΩ)	9.3578	19.162
W_o-T (Ω $s^{-1/2}$)	3.4698	1.8602
CPE_1-T ($\mu S\ s^n$)	0.12853	8.1096
CPE_1-P	0.7942	0.6487
R_3 (R_{ct}) (KΩ)	35.035	50.916

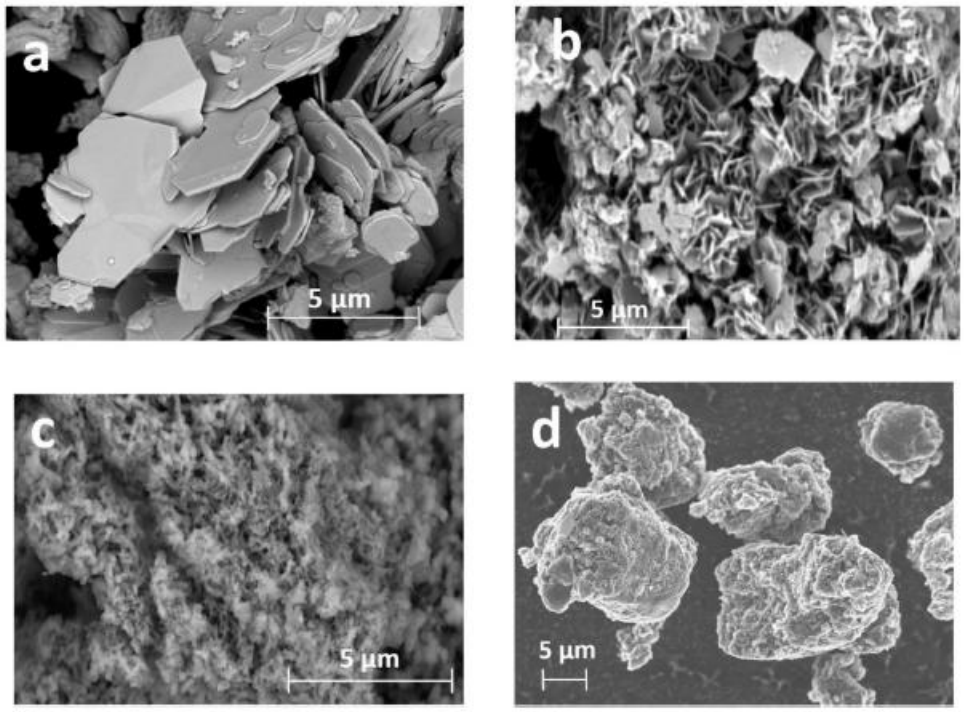

Figure S7: SEM images of a) bulk WS_2, b) exfoliated WS_2, c) PANI and d) WS_2/PANI composite

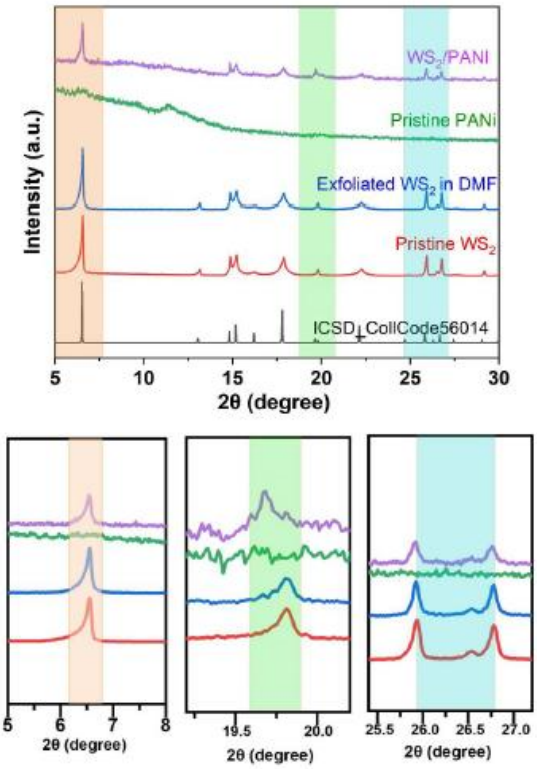

Figure S8: XRD pattern of WS_2, PANI and WS_2/PANI composites.

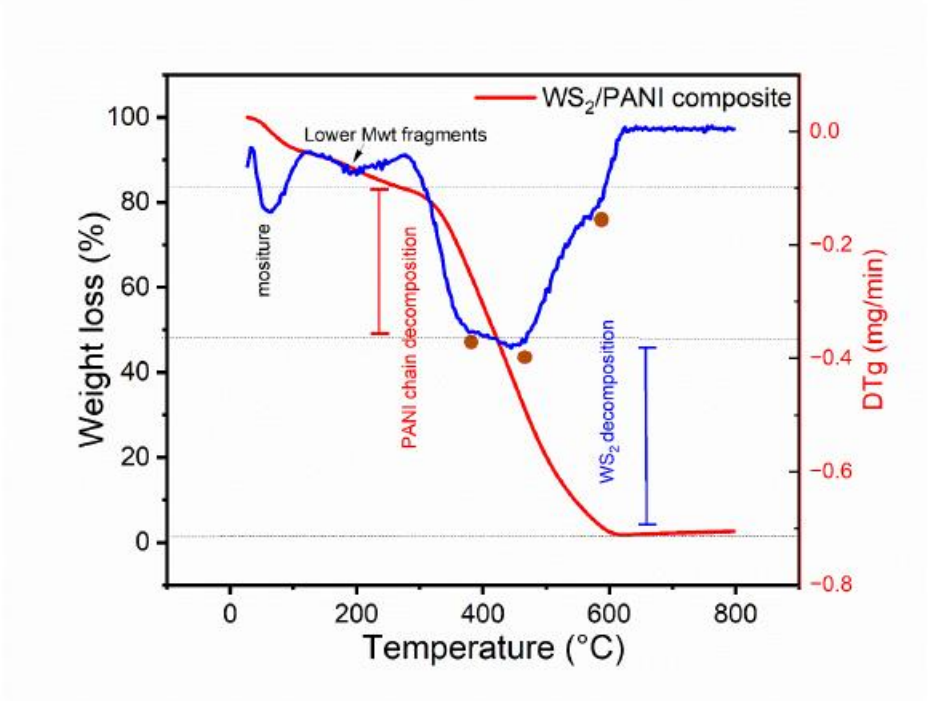

Figure S9: TGA of WS_2/PANI composite measured in O_2 atmosphere. PANI decomposition starts at 300 °C until almost 500 °C while the WS_2 starts decomposition at 500-600 °C due to the oxidative atmosphere. The calculated percentages are 35% PANI, 46 wt% WS_2 and almost 10 wt% of small molecular weight PANI fragments.

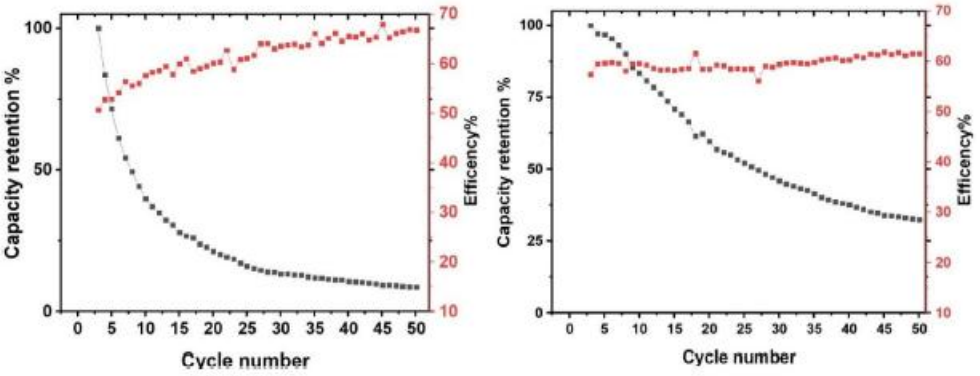

Figure S10: Capacity retention and efficiency of WS_2/PANI at 80 mA (left) and 50 mA (right) after 50 cycles.

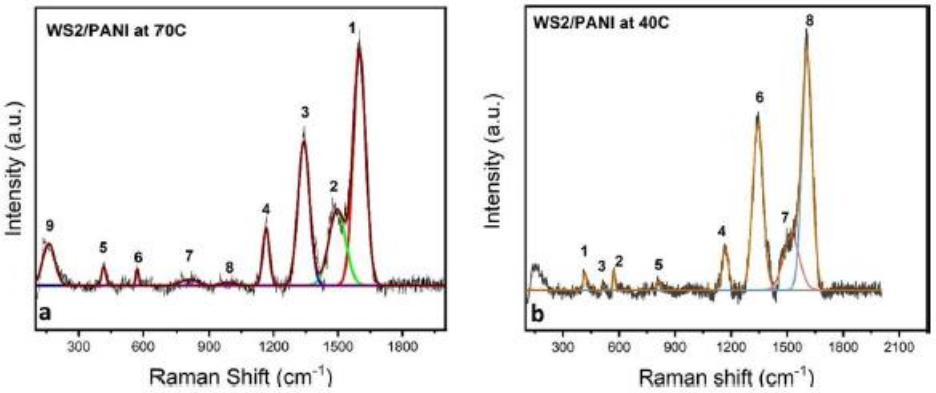

Figure S11: Peak fitting value of obtained Raman spectra for WS_2/PANI, a)70 °C, b) 40 °C.

Table S2: Summary of peak fitting value of obtained Raman spectra for WS_2/PANI at 70 °C.

Model	Gauss								
Equation	y=y0 + (A/(w*sqrt(pi/2)))*exp(-2*((x-xc)/w)^2)								
Plot	Peak1	Peak2	Peak3	Peak4	Peak5	Peak6	Peak7	Peak8	Peak9
X_c	1599.49331 ± 0.23759	1495.79062 ± 0.85367	1340.36685 ± 0.26184	1165.0344 8 ± 0.49359	416.66662 ± 1.29183	573.09677 ± 1.20894	807.25493 ± 7.14858	986.91301 ± 14.37938	160.52605 ± 0.99095
FWHM	67.78456 ± 0.53106	92.02709 ± 2.17216	64.32414 ± 0.6381	36.42351 ± 1.18102	24.67159 ± 3.07199	16.23739 ± 2.86577	86.22702 ±17.3928	73.88028 ± 34.83681	66.66361 ± 2.45087
A	3655.92288 ± 29.7804	1611.708 ± 33.2392	2135.907± 19.1328	484.3352 ± 14.0213	108.72555 ± 11.94964	61.37359 ± 9.50301	125.0320 ± 23.2394	48.681 ± 21.0044	646.65816 ± 21.1003
Reduced Chi-Sqr	1.87078								
R-Square (COD)	0.98141								
Adj. R-Square	0.9811								

Table S3: Summary of peak fitting value of obtained Raman spectra for WS_2/PANI at 40 °C.

Model	Gauss							
Equation	y=y0 + (A/(w*sqrt(pi/2)))*exp(-2*((x-xc)/w)^2)							
Plot	Peak1	Peak2	Peak3	Peak4	Peak5	Peak6	Peak7	Peak8
X_c	417.59219 ± 1.38044	572.5083 ±0.97851	517.9678 ± 4.86729	1168.428 ± 0.7144	814.2523 ± 2.6979	1343.7143 ± 0.237	1522.182 ± 2.511	1606.340 ± 0.351
FWHM	21.81492 ± 3.27032	14.95685 ± 2.314	16.996 ± 11.5164	38.19789 ± 1.7020	21.60697 ± 6.3932	65.71606 ± 0.57286	101.08572 ± 4.9621	63.82147 ± 0.653
A	100.75085 ± 13.235	79.84482 ± 10.7872	19.5166 ± 11.56031	427.9016± 16.8879	49.44562 ± 12.82768	2880.495 ± 22.4593	1429.532 ± 74.470	3910.469 ± 69.4892
Reduced Chi-Sqr	2.65381							
R-Square (COD)	0.98086							

7. Curriculum Vitae

This page has been removed for reasons of data protection.

Acknowledgment

This page has been removed for reasons of data protection.

Declaration of honesty in academic work

The present dissertation, titled *"A Detailed Investigation of Heterometal-Incorporated Polyoxovanadate Nanocluster-Based Films: Material Properties and Sustainable Applications for Energy Storage Systems,"* was conducted between March 2021 and September 2024 at the Institute of Inorganic Chemistry I (AC-1), under the supervision of Prof. Dr. Sven Rau and Dr. Montaha Anjass.

I hereby declare that this work is entirely my own, and no sources have been used other than those properly cited. Furthermore, the content of this dissertation has not been submitted for any other degree or qualification.

Additionally, I confirm my awareness of and compliance with the current version (16.10.2009) of the University of Ulm's guidelines on maintaining good scientific practice.

Ulm, 11.12.2024 ……

Nikhil Arya